Structure and Dynamics of Ge-Se Liquids and Glasses under Pressure

A thesis presented for the degree of
Doctor of Philosophy
by

Can Yıldırım

Université de Liège - SPIN Laboratory
Université Pierre et Marie Curie Paris 6 - LPTMC
September 2016

Abstract-Résumé

Structure and Dynamics of Ge-Se Liquids and Glasses under Pressure

Among network forming glasses, chalcogenide glasses are of great importance not only for their optoelectronic applications, but also for the network structure that displays enhanced structural variability due to the covalent bonding network. In this project, we study the Ge-Se binary alloy as the target system in order to investigate the structure and dynamics of the liquid and glassy phases under pressure by using a combination of *ab initio* molecular dynamics (AIMD) simulations and X-ray scattering experiments. The wide glass forming range of the $\mathrm{Ge_xSe_{100-x}}$ system allows one to tune the stiffness of the network structure by increasing the mean coordination number with the Ge content which affects the macroscopic material properties such as resistance to aging, hardness, conductivity, and fragility. In this respect, we study 10 different AIMD generated and 5 experimentally produced (i.e melt quenching) compositions spanning the flexible-to-rigid elastic phase transitions according to Maxwell's isostatic stability criterion. As for the liquid state, after having validated the structural models by comparing the experimental findings available, we examine the dynamics of Ge-Se melts at ambient pressure. The investigations on the diffusion coefficients and viscosity at 1050 K showed clear anomalies, departing from the expectation that atomic mobility should decrease as the system becomes more and more rigid. Furthermore, the relaxation behavior at 1050 K also shows similar anomalies when intermediate scattering factors are examined at q vector corresponding to the principal peak position of the total structure factor. To elucidate this anomaly, we discuss the effect of the topological constraints on the dynamics in liquid state. The results show that the isostatic systems have slower dynamics as compared to flexible and stressed rigid phases. Moreover, we speculate that the reason of this anomaly may originate from the distribution of the topological bond bending constraints of the higher coordinated species (i.e. Ge) results. In particular, the flexible, and stressed rigid compositions showed a high variance in the Ge bond bending constraints whereas the isostatic composition forms a network in which the bond bending constraints are homogeneously distributed. We link this behavior with a global fragility concept for network forming liquids in such a way that fragility minima are obtained both by experimental findings and the calculated fragility values of the AIMD generated compositions (i.e. VFT or MYEGA fits) when scaled to the isostatic composition for a number of different systems. As for the glassy phase, the AIMD generated structural models show good agreement in both real and reciprocal space. The equation of state and normalized stress-strain curves are compared to the available experiments in order to verify the pressure behavior of the simulations. The results show a good agreement. In addition to the simulations under pressure, we show results of X-ray absorption spectroscopy (XAS) and X-ray diffraction (XRD) experiments under pressure. Both simulations and the experiments show that there are no sign of crystallization during compression up to 42 GPa. One of the main important finding is the evolution of the Ge-Se bond length for the compositions studied. We observe a bond compression in the early stages of densification in the phase identified as low density amorphous (LDA), which is followed by an abrupt jump starting in pressures around 10-15 GPa, both in simulations and experiments. Furthermore, a semiconductor to metal transition is identified with the red shift in Ge K edge energy. The features of polyamorphism was also detected from the pressure evolution of the principal peak position of the structure factor which show two distinct slopes indicating different structural response to the applied pressure. In order to have a deeper understanding of the densification mechanisms, we apply neighbor analyses to our atomic trajectories and show that the tetrahedral to octahedral transformation (i.e LDA to HDA) starts to take place when the fifth and sixth neighbors effectively become the part of first shell neighbors, where the bond angles adapt themselves to 90° degrees. We furthermore speculate the effect of network rigidity of the glasses at ambient conditions onto the kinetics of the amorphous-amorphous transitions. It appears that the polyamorphic transitions are more sluggish as the network rigidity (i.e Ge content) increases. Finally we show that there is a universal threshold value in coordination change from LDA to HDA phases $\mathrm{Ge_xSe_{100-x}}$ (where $\mathrm{x} \leq 25$) when scaled to reduced densities.

Keywords

Ge-Se glasses, AIMD, high pressure, EXAFS, XANES, CPMD, rigidity, topological constraints

La Structure et la Dynamique des Liquids et des Verres Chalcogénures sous Pression

Les verres de chalcogénure sont ont une grande importance dans des applications optoélectroniques, mais aussi pour leur réseau covalent qui leur procure une “variabilité structurale” accrue. Ce projet étudie des alliages Ge-Se et utilise l’association d’analyses dynamique moléculaire (AIMD), de simulations et de diffusion des rayons X afin de déterminer la structure et la dynamique des phases liquide et vitreuse sous pression. Les alliages de Ge-Se permettent la “formation de verre” sur une large gamme de conditions, ce qui permet de contrôler la rigidité du réseau en augmentant le nombre moyen de coordination en fonction de la teneur en Ge ce qui affectera les propriétés macroscopiques du matériau, comme la résistance au vieillissement, la dureté, la conductivité et la fragilité. Dans cette optique, nous étudions 10 compositions générées/calculées par AIMD, et 5 autres compositions déterminées expérimentalement (i.e par trempe) couvrant les domaines transitions élastiques souple-rigide suivant les critères de stabilité isostatique de Maxwell. Dans le cas de l’état liquide, la comparaison au préalable des données de la expérimentale permet de valider les modèles structuraux, pour ensuite examiner la dynamique des liquides de Ge-Se à pression ambiante. En partant du postulat que la mobilité atomique du système décroit en devenant plus rigide, l’étude des coefficients de diffusion et de la viscosité à 1050 K a montré des anomalies flagrantes. De plus, le comportement en relaxation à 1050 K a révélé des déviations semblables lorsque les facteurs intermédiaires de diffusion sont examinés avec un facteur q correspondant à la position du pic de référence de la structure factorielle. Afin d’expliciter cette anomalie, nous nous intéressions aux effets des contraintes topologiques sur la dynamique à l’état liquide. Les systèmes isostatiques ont des dynamiques plus lentes par rapport aux phases rigides souples et sollicitées . Nous supposons que cette anomalie puisse provenir des résultats de distribution des contraintes topologiques de déformation des liaisons des espèces les plus coordonnées (i.e Ge). En particulier, les compositions rigides souples et sollicitées montrent une grande variabilité des contraintes de déformation des liaisons de Ge, alors que la composition isostatique forme un réseau où les contraintes de déformation des chaines sont distribuées uniformément. Nous expliquons ce comportement par une fragilité globale des liquides formant des réseaux. Nos constatations expérimentales ainsi que les compositions générées par AIMD (i.e. VFT or MYEGA fits) appliquées à différents systèmes à composition isostatique ont permis de déterminer les minima de fragilité. Les modèles structuraux de la phase vitreuse, générés par AIMD concordent en espace réel comme en espace réciproque. Afin de vérifier le comportement en pression de nos simulations, la concordance entre l'équation d'état et les courbes normalisées contrainte-déformation aux résultats connus a été vérifiée. Par ailleurs, des mesures de spectroscopie d'absorption et de diffraction des rayons X (XAS, et XRD respectivement) ont été réalisées sous pression. Ces mesures ainsi que les simulations ont montré qu'il n'y aucune trace de cristallisation pour des compressions inférieures à 42 GPa. L'évolution de la longueur de la liaison Ge-Se pour les compositions étudiées constitue un des résultats majeurs de ces travaux. Dans les premiers instants du phénomène de densification de la phase identifiée comme amorphe et de faible densité (LDA), nous observons expérimentalement et par simulation une compression de la liaison, suivie d'une hausse soudaine à des pressions entre 10 et 15 GPa. De plus, une transition metal-semiconducteur est identifiée grâce à "red shift in Ge K edge energy ". Un phénomène de polyamorphisme a aussi été décelé de l'évolution du pic de référence de la structure factorielle en fonction de la pression appliquée qui montre l'existence de deux pentes distinctes. Afin de mieux comprendre le mécanisme de densification, des analyses du plus proche voisin à nos trajectoires atomiques montrent que des transformations d'une conformation tetraédrique à une conformation octaédrique (i.e. LDA to HDA) se produisent lorsque les cinquième et sixième plus proches voisins deviennent partie intégrante de la première écorce voisine , lorsque les liaisons se réorientent naturellement à 90°. Nous supposons aussi l'existence d'un effet de la rigidité du réseau vitreux en conditions ambiantes sur la cinétique des transitions amorphe-amorphe/polyamorphiques. Ces transitions sont plus molles lorsque la rigidité du réseau augmente. (i.e. le taux de Ge). Enfin, nous montrons l'existence d'un valeur maximale universelle dans le changement de coordination entre les phases LDA et HDA $\mathrm{Ge_xSe_{100-x}}$ (où $x \leq 25$) lorsque les densités sont réduites.

Mots-clés

Ge-Se verres, AIMD, haute pression, EXAFS, XANES, CPMD, rigidité, contraintes topologiques

"The more you've found the less you've have been around."

Acknowledgements

I think it would be a fair statement if I say that my PhD years have been the most intense years of my life in many aspects. Since this project is a joint program between Liège, and Paris, I had the chance to enjoy tremendously -well, not always. I am not one of the Teletubbies after all, regular human being- in both places. Indeed, through these years, I met great people who helped me complete this thesis work. I would like to take the chance to mention them here.

First of all, I would like to mention my supervisor in Liège, professor Jean-Yves Raty for being amazing all the time even at the job interview. It is with immense gratitude that I acknowledge his support, honesty and patience during my PhD years, and for his complete trust in me, even at times where I questioned myself. I am indebted to my supervisor in Paris, professor Matthieu Micoulaut for his guidance, discussions and encouragement. I learned a great deal from him and he always motivated me in a positive manner.

I am thankful to the International Doctoral School of Funtional Materials (IDS Funmat) for the financial support for this PhD project (Project 2013-05-EM) and also to Pierre Noé from CEA Grenoble for the EDS analyses as the industrial partner of the project. I am indebted to Consortium des Equipements de Calcul Intensif (CECI, funded by F.N.R.S) is acknowledged for supercomputing access. I also thank professor Boolchand for providing us the Ge-Se samples. I would like to thank professor Jaakko Akola and professor Tanguy Rouxel for agreeing to be the reviewers, and also professor Frédéric Decremps, professor Peter Schlagheck, and professor Duy Ngoc Ngyuen for being the examiners of this thesis.

The experiments at the ESRF would not have been possible without the help of the Innokenty Kantor, Olivier Mathon, Rafaella Torchio, Angelika Rosa, Sakura Pascarelli for the X-ray absorption experiments and Sofia-Michaela Souliou and Valentina Giordano for the inelastic X-ray scattering experiments. It was indeed a blessing to work with you, thank you. I also should express my gratitude to professor Jean Pierre Gaspard for helping with the experiments, for enjoyable discussions not only scientific but also about basically anything, and of course for the amazing photos he took.

I would like to mention my colleagues from each institution. First of all I thank my friend Begüm for all the good times we had in Liège. I thank my lab-mate in Paris, Axelle, who helped me for many things and with whom we spent enjoyable time at work. Also, I would like to thank Annie and Boris, for being super friendly and making me feel comfortable at work. I am thankful to my friend Medhi for his kind help for the abstract.

Apart from work, I thank my friend Alban for being there and for never withholding his help in my time of need since the beginning of my stay in Paris. I also would like to mention Anouschka the Siberian Duchesse for making Paris even more fun and full of enjoyable rituals, thank you for all.

Last but not least, I would like to thank my parents for their unconditional support and love, and believing in me through these years, as they always did. I owe you the most.

Contents

Résumé-Abstract **i**

Dedication **v**

Acknowledgements **vii**

List of Figures **xiii**

List of Tables **xxv**

Abbreviations and symbols **xxvii**

1 General Introduction **1**

1.1 A Brief Overview of Glasses 1

1.2 Glass Formation 2

1.3 Topological Constraints and Rigidity 9

1.4 Chalcogenide Glasses 15

1.4.1 Germanium Selenide Glasses 16

1.4.2 Effects of Pressure on Glassy Ge_xSe_{1-x} 18

1.5 Motivations and Thesis Organization 24

2 Theory **27**

2.1 Density Functional Theory 27

2.1.1 Why Using the DFT Scheme ? 27

2.1.2 Historical Overview 28

2.1.3 Many-Body Equations 29

2.1.4 The Schrödinger Equation and Many-Body Wavefunction 30

2.1.5 Hohenberg and Kohn Theorem 30

2.1.6 Kohn-Sham Formalism 31

2.2 Practical Approximations 33

2.2.1 Local Density Approximation 33

2.2.2 Generalized Gradient Approximation 34

2.2.3 Plane-Wave Basis Set 34

2.2.4 Pseudopotentials 35

2.3 Ab initio Molecular Dynamics 36

2.3.1 Car-Parrinello Molecular Dynamics 36

2.4 Our Simulations 38

2.5 Atomic Scale Simulations of $\mathrm{Ge_xSe_{1-x}}$ 40

2.6 Data Processing 50

2.6.1 Radial Distribution Function 51

2.6.2 Structure Factor 53

2.6.3 Bond Angle Distribution 54

2.6.4 Constraint Counting 54

2.6.5 Mean Square Displacement 56

2.6.6 Intermediate Scattering Function 57

3 Experimental Techniques **61**

3.1 Phenomenology of XAS 61

3.2 XANES 63

3.3 EXAFS 64

3.4 Data Analysis 65

3.5 Experimental Details 67

3.6 Sample Preparation and Characterization 69

4 Study of Liquid Ge-Se **75**

4.1 Introduction 75

4.2 Structural Properties 76

4.3 Anomalous Dynamics and Relaxation 80

4.4 Role of with Molecular Rigidity on Fragility 83

4.4.1 Relaxation and interaction range 91

4.5 Summary and Conclusions 97

5 Pressure Induced Polyamorphism in Vitreous Ge-Se **99**

5.1 Introduction 99

5.2 XRD 100

5.3 EXAFS 101

5.4 Equation of State 105

5.5 Pair Distribution Functions 106

5.6 Neighbor Distances and Bond Angle Distributions 109

5.7 Octahedrality and Coordination Numbers 112

5.8 Discussion 114

5.9 Conclusions 116

6 Polyamorphism and Rigidity **119**

6.1 Introduction 119

6.2 Reciprocal Space Properties 120

6.3 Real Space Properties 123

6.3.1 Discussions and Conclusions 128

7 General Conclusions and Future Directions **133**

Appendix A Liquid State **139**

Appendix B Glassy State **143**

Appendix C List of Scientific Contribution **149**

C.0.2 Publications in International Journals 149

C.0.3 Oral Presentation 149
C.0.4 Poster Presentations and Scientific Visits 150

List of Figures

1.1 The changes in specific volume or enthalpy upon cooling from liquid state. Two different cooling rates, a and b, result in different glass transition temperatures. Adopted from [12]. 4

1.2 T_g scaled temperature dependence of viscosity showing Arrhenius (strong liquids) and non-Arrhenius (fragile liquids) behavior of liquids upon cooling. The inset shows the heat capacity change, ΔC_p, for selected strong and fragile liquids. Adopted from [15]. 5

1.3 A summary of the main concepts in glass formation. a) the divergence in the relaxation times as reaching to the glass transition, b) the disappearance of the excess entropy, c) energy minima in potential energy surface d) temperature dependence of energy showing the amorphous megabasin at T_K. Adopted from[18] 6

1.4 Energy landscape representations of glassed quenched from a) fragile b) strong liquids. Adopted from[20] 7

1.5 Comparison of VFT, AM, and MYEGA models A) viscosity as a function of T_g scaled temperature assuming m=60 and $\log \eta_\infty$ = -4. B) The Adam-Gibbs equation, the AM equation diverges at the high temperature limit. C) VFT model assumes a vanishing configurational entropy at low temperature limit. Reproduced from [23]. 8

1.6 Elastic modulus of three network glasses as a function of the average coordination number. the inset shows the average number of zero-frequency modes of the three glasses compared to the line that represents the prediction by the mean field theory. Adopted from [29]. 11

1.7 The composition dependence of non-reversing heat flow ΔH_{nr} and molar volume in Ge$_x$Se$_{100-x}$ glasses showing the intermediate phase can be defined between x=20-26 %. Adopted from [49]. 13

1.8 Raman mode frequencies for a) corner-sharing (CS) and b) edge sharing (ES) tetrahedra as a function of Ge composition in Ge_xSe_{100-x}. The CS frequencies remain nearly constant in the IP region while ES frequencies show an abrupt increase, deviating from the linear behavior observed in the flexible region. Adopted from [50]. 13

1.9 Fourier Transform Raman profiles of vitreous $Ge_{19}Se_{81}$ collected at 9 different points from the quenched glass rod showing the effect of melt homogenization time at a) 6h b) 24h c) 96h d) 168h. Adopted from [45]. 14

1.10 Schematics of structural units and possible network connections in Ge_xSe_{1-x} glasses. Adopted from [49]. 17

1.11 Bhatia-Thornton number-number structure factor for different Ge_xSe_{1-x} along with Se glasses at room temperature measured using neutron diffraction. Adopted from [73]. 18

1.12 The total structure factor for $GeSe_2$ at different pressures measured by high energy X-ray diffraction. The dashed lines corresponds to the Fourier transforms of the total pair distribution functions. Adopted from [76]. 19

1.13 Densification mechanisms suggested by acoustic measurements in $GeSe_2$.Se atoms are shown in orange an Ge atoms in blue. Adopted from [83]. . . 20

1.14 Specific volume relaxation of $GeSe_2$ at different pressures. The orange curve corresponds to the relaxation for GeS_2. The inset provides the pressure dependence of relaxation rate on different Ge-Se glasses. Reproduced from [88]. 21

1.16 Electricial resistivity of glassy $GeSe_4$ under pressure. The inset shows the variation of the resistivity with reciprocal of pressure, showing a threshold around $\sim$ 11 GPa. Reproduced from [77]. 21

1.15 X-ray absorption spectroscopy results of $GeSe_2$ under pressure. The panels show the pressure dependencies of various properties (in descending order), band gap energy, Ge-Se distance, Debye Waller factor, and coordination number of Ge-Se. Reproduced from [90]. 22

1.17 The pressure dependence of (a) the mean nearest neighbor distance $\bar{r}$ as measured in (i) the X-ray diffraction work of Skinner et al. [93] [(blue) solid circles with vertical error bars] and Kalkan et al. [77] [(magenta) open squares], (ii) the neutron diffraction work [(black) solid squares with error bars], and (iii) as calculated by ab initio Molecular Dynamics (AIMD) simulations [solid (green) curve]; (b) the mean coordination number $\bar{n}$ as measured in (i) the X-ray diffraction work of Skinner et al. [93] (blue) solid circles with vertical error bars] and Kalkan et al. [77] [(magenta) open squares], (ii) the present neutron diffraction work [(black) solid squares with error bars], and (iii) as calculated by AIMD [solid (green) curve], where the latter is broken down into its contributions from $\bar{n}_{Ge}$ [(red) upward-pointing triangles] and $\bar{n}_{Se}$ [(magenta) downward-pointing triangles]; and (c) the AIMD results for the fractions of Ge [(black) open circles] and Se [(red) open squares)] atoms involved in homopolar bonds, and the fractions of Ge atoms involved in corner-sharing [(green) leftward-pointing triangles] and edge-sharing [(blue) rightward-pointing triangles] tetrahedra. Reproduced from [94]. 23

2.1 The cooling regime for obtaining glassy Ge$_x$Se$_{1-x}$ with AIMD simulations. 1050 K represents the quenching point from the lowest liquid temperature attained. 39

2.2 a) Ge-Ge partial pair distribution of Ge$_{22}$Se$_{78}$ at 300 K obtained by 3 quenches from 1050 K. The snapshot represents the Ge-Ge homopolar bonding where green atoms are Ge and yellow atoms are Se. b) Schematic Potential energy of a glass, defining basins, transition states, and minima. Adapted from [12] 40

2.3 Calculated vibrational density of states (solid curve) for glassy GeSe$_2$ are compared to the experimental data (open circles). Adapted from [125] 41

2.4 Computed structure factors for liquid (solid curve) and glassy (broken lines) GeSe$_2$. Note that the lack of the reproduction of the FSDP in $S_{\mathrm{CC}}(\mathbf{k})$. Adapted from [126] 42

2.5 Calculated Bhatia-Thornton structure factors for liquid GeSe$_2$ (solid lines) compared to experiment (dots with error bars). Adapted from [127] . . . 42

2.6 Calculated structure factors for liquid $GeSe_2$ using GGA (upper solid curve) and LDA (lower curve with dots) approaches compared to experimental findings (open circles). Adapted from [128] 43

2.7 Contour plots of the electronic charge density for a tagged Se-Ge-Se trimer in liquid GeSe2 calculated using LDA (upper left) and GGA (upper right) approaches in atomic units. The lower panel shows the difference plot (GGA-LDA). Adapted from [128] 44

2.8 Ge-Se-Ge (upper) and Se-Ge-Se (lower) Bond angle distributions of liquid $GeSe_2$ with BLYP (black) and PW (red) schemes. Adapted from [130] . 45

2.9 Partial Bhatia-Thornton structure factors calculated with 120 atoms (black) and 480 atoms (red) are compared experimental results (open circles). The right panels zoom to the low wave vector region of the spectrum. Adapted from [134]. 46

2.10 Comparison of calculated diffusion coefficients of liquid GeSe (Se and Ge species) using BLYP, PBE, and PW schemes. Adapted from [138]. . . 47

2.11 Calculated NMR chemical shifts in $GeSe_2$ (upper) and $GeSe_4$ (lower) compared to experiment. Adapted from [141]. 48

2.12 Computed partial pair distribution functions for $GeSe_4$ (upper) and GeS_4 (lower) for 120 (green continuous lines) and for 480 (blue broken lines). The inset highlights the Ge-Ge correlations and homopolar bonds observed in 480 atoms case. Adapted from [143]. 49

2.13 Comparison of the standard deviation of the Ge centered partial bond angle distributions, σ_{Ge}, within tetrahedra as a function of composition. The shaded zone corresponds to the reported IP phase for Ge-Se system [50]. Adapted from [144]. 50

2.14 Neighbor distribution as a function of distance around a central Ge atom for glassy $GeSe_4$ (red: neighbors 1-4, green : neighbors 5-9). The black curve is the sum of all neighbor contributions. The inset shows the peak positions of each neighbor for different chalcogenide and oxide compounds. Adapted from [144]. 51

2.15 Calculated total structure factors of different Ge_xSe_{1-x} compounds (black) are compared with the experimental results(red lines and blue circles) in the upper panel. The lower panel shows the distribution of the standard deviation of the Ge centered angular constraints. The continuous lines represent the Gaussian fits to the data points. The broken curves are the fits to calculate the population of the broken bond-bending constraints for the stressed rigid compositions. Reproduced from [145]. 52

2.16 Schematics of MD based constraints counting method. a) Bond stretching b) bond bending constraints. The large excursions are set to be broken while the small excursions are enumerated as intact constraints. Adapted from[30]. 55

2.17 Enumerating the neighbors of a central atom labeled as 0. The angle that correspond to 102 is emphasized in red. 55

2.18 Standard deviation σ_θ of Ge centered partial bond angle distributions as a function of angle number. The horizontal dashed line indicates the fixed angular cut-off for σ_θ 56

2.19 Time dependence of mean-square-displacement in a Lennard-Jones liquid at different temperatures. Three different mobility regimes are observed. Here the longest time attained in simulation corresponds to 30 ns in real time. Reproduced from[149]. 57

2.20 Self part of the intermediate scattering function for a Lennard-Jones liquid. Here the longest time attained in simulation corresponds to 30 ns in real time. Reproduced from [153]. 59

3.1 a) X-ray absorption spectrum of Pb element. Here K, L, and M radiations refer to different quantum number n being 1, 2, and 3,respectively. The inset shows L subshell radiations corresponding to $2s$ and $2p$ orbitals. b) X-ray emission lines of different shells. Adapted from [154] 62

3.2 Se K edge absorption spectrum of $Ge_{10}Se_{90}$ showing the XANES (from the edge to $\sim$ 12.68 keV) and EXAFS parts separated by the vertical line. 63

3.3 Schematic representation of single and multiple scattering of a photoelectron due to an incident X-ray beam. Reproduced from [156]. 64

3.4 k dependence of EXAFS parameters calculated by FEFF. Adapted from [160] 66

3.5 Measured absorption spectrum at Ge K edge for $Ge_{20}Se_{80}$ (black). a) Normalization of the measured $\mu(E)$ is done with the post and pre-edge lines having cubic spline fits (red). b) normalized absorption spectra with edge step equal to 1 (black arrows). 67

3.6 Schematic of the standard EXAFS data reduction. Reproduced from [156] 68

3.7 k^2 weighted EXAFS signals at the Ge K edge of amorphous $Ge_{20}Se_{80}$ (black), the calculated best fit (red) and the window function (blue) together with b) the Fourier transforms at ambient pressure. Note that the phase shifts are not corrected here 69

3.8 Schematics of a typical synchrotron ring showing its essential components. Adapted from [165] 70

3.9 Schematics of XAS beamline optics. 70

3.10 BM23 XAS beamline at ESRF, Grenoble, France. 71

3.11 Lower half of the diamond anvil cell (DAC) having the rhenium gasket with a 120μm diameter hole (left). Inside the DAC with sample and ruby placed in the 35μm thick hole. 72

3.12 EDXS spectrum of $Ge_{25}Se_{75}$ at 15 keV. The inset shows the corresponding image where the spectrum was collected. 73

4.1 Composition dependence of molar volume of Ge-Se liquids at 1073 K. The red curve represents the polynomial fit applied to the experimentally measured data [124] (diamond symbols). Black symbols shows the extrapolated data for other compositions used in our simulations. 76

4.2 Calculated static structure factors $S(\mathbf{k})$ (red curves) for selected compositions at 300 K (a) and in the liquid state (b), and comparison with experimental neutron diffraction results in panel a: blue circles [170], black circles : $Ge_{20}Se_{80}$ [140], $Ge_{33}Se_{67}$ [171], and in panel b: Green circles $Ge_{20}Se_{80}$ [175], $Ge_{33}Se_{67}$ at 1050 K [172], and at 1373 K [176]. The yellow curve corresponds to a system with 120 atoms [173]. Note that the experimental data of $Ge_{20}Se_{80}$ have been duplicated in order to be compared with the simulated $Ge_{22}Se_{78}$. 78

4.3 Calculated total pair distribution functions (red curves) for selected compositions at 300 K (a) and in the liquid state (b), compared to neutron diffraction experiment results (black lines): $Ge_{20}Se_{80}$ [73] and $Ge_{33}Se_{67}$ at 300 K [140], $Ge_{33}Se_{67}$ at 1050 K [172] and 1373 K [176]. The calculations are also compared to previous simulation results (blue curves) on 120 atom systems for 1373 K ($GeSe_2$) [175] and 300 K [140, 145]. 79

4.4 Total mean square displacement (msd) as a function of simulation time for $Ge_{20}Se_{80}$ at different temperatures. The broken line shows the behavior of $\langle r_\alpha^2(t) \rangle$ in the diffusive regime. 81

4.5 Total mean square displacement (msd) as a function of simulation time for different compositions at 1050 K. 82

4.6 Calculated self diffusion coefficients D_{Se} (red) and D_{Ge} (black) as a function of composition at 1050 K. 83

4.7 a) Arrhenius plot of the diffusion constant for selected compositions. The solid lines represent the Arrhenius fits. (b) Diffusion activation energy E_A of Ge (red) and Se (black) as a function of Ge content. 84

4.8 Self part of van Hove correlation function of Ge atoms, showing the atomic displacements at different simulation times. 85

4.9 Composition dependence of the jump probabilities of atoms that have jumped r>2.88 Å within 20 ps at 1050K (filled circles) and 1373 K (open circles). 86

4.10 (a) Global MD constraint count of the liquid (1050 K), compared with a count in the glassy state (300 K). The broken line represents the Phillips–Thorpe constraint count $n_c = 2 + 5x$ [29]. (b) Contourplots of the Ge BB constraint distribution among the structure for selected compositions. They have been generated by focusing on the constraint distribution inside a slab of 3.2 ± 0.2 Å(c) Calculated Ge BB (black) and BS (red, right axis) constraint density as a function of Ge content. (d) Variance $\sigma_{n_c}^2$ of the Ge BB constraint population. 87

4.11 SE estimated viscosities at 1050 K (black) and 1373 K (red) as a function of Ge content (upper panel). Fitted fragility values using MYEGA (equation 4.4.3)(black) and VFT functional (equation1.2.4) forms (red), as a function of Ge content (lower panel). 88

4.12 Comparison between the Stokes–Einstein calculated (filled symbols) viscosities at various Ge–Se compositions and experimental measurements of viscosity (open symbols) from Stolen et al. [185] Senapati et al [187] and Guegen et al. [186] Note that only Stolen et al. have investigated the high temperature region where numerical data can be directly compared. The solid lines correspond to fits using the Mauro–Yue–Ellison–Gupta–Allen (MYEGA) equation4.4.3 that describes with an increased accuracy the high temperature viscosities as compared with alternative fitting functionals (for example, Vogel–Fulcher–Tamman, VFT) 1.2.4. 90

4.13 A summary of experimentally measured fragilities in glass network-forming melts. Experimental fragilities as a function of a rescaled composition corresponding to the centroid of the corresponding isostatic window (or Boolchand phase): Ge–S [191], Ge–Se [189], As–Se [192], Ge–Sb–Se [193], Si–Ge–Te. All display a minimum at or close to . Note that the minimum for Ge–Si–Te is clearly visible if represented on an appropriate scale [194]. The trend in composition for TeO_2–V_2O_5 is highlighted by a thin broken line (P. Boolchand, unpublished results). The solid line is a global quadratic fit to the whole data sets, and serves only as guide. Stoichiometric compounds are signaled. 91

4.14 Reciprocal space vector dependence of $F_s(k,t)$ of $Ge_{20}Se_{80}$ at 1050 K for Ge (solid curves) and Se (broken curves). 92

4.15 Reciprocal space vector dependence of $F_s(k,t)$ of $Ge_{20}Se_{80}$ at 1050 K for Ge (solid curves) and Se (broken curves). 93

4.16 Self part of intermediate scattering function $F_s(k,t)$ of Ge (a) and Se (b) at 1050 K and k=2.10Å^{-1} for selected compositions. The horizontal solid line in panel a corresponds to the value e^{-1}, whereas the broken line in panel b shows the Kohlrausch fit at the long time limit of $F_s(k,t)$ for $Ge_{25}Se_{75}$ 94

4.17 Fitted relaxation times τ_α (a) and stretched exponent β (b) of the (Ge,Se) species as a function of Ge content from the KWW fits. The open circles represents a simple estimate using $F_s(k,\tau_\alpha) = e^{-1}$. Error bars are of the size of the symbols. The green horizontal lines are predicted values for β from trap models of relaxation (3/7, 3/5) REF (see text for details). . . 95

5.1 a) X-ray diffraction patterns of $Ge_{25}Se_{75}$ with increasing pressure (written on the continuous curves in GPa unit) and of the measured empty cell (red dashed line). b) The pressure dependence of the principal peak position of the XRD patterns for Ge_xSe_{1-x}. The black solid lines are guides to the eye, marking the high and low pressure regimes while the dashed lines indicate the transition in $Ge_{17}Se_{83}$ glass. 101

5.2 Normalized X-ray absorption spectra at the a) Ge K edge and b) at the Se K edge of amorphous $\mathrm{Ge_xSe_{1-x}}$ at ambient pressure. EXAFS oscillations of $Ge_{17}Se_{83}$ at the c) Ge K edge and d) at the Se K edge under selected pressure points collected using DAC. 102

5.3 a) Evolution of the Ge-Se interatomic distance as a function of increasing pressure. The filled symbols represent $Ge_{17}Se_{83}$ (black) and $Ge_{20}Se_{80}$ (red). The open diamond symbols are AIMD results for $Ge_{18}Se_{82}$. The estimated error bars are shown separately in the graph. The red dashed line corresponds to the intercept of low and high pressure regimes shown by the pressure dependence of the PP position in Fig. 5.1 b). b) Energy decrease in the Ge K absorption edge position with increasing pressure of $Ge_{17}Se_{83}$. In the inset, the XANES spectra of selected pressures are compared to illustrate the edge shift. 104

5.4 The pressure-volume equation of state for amorphous Ge_xSe_{1-x}. The results obtained by AIMD (filled diamond symbols) are compared to the measured data of $Ge_{20}Se_{80}$ [77, 93], $Ge_{17}Se_{83}$ and Ge_8Se_{92}[88] (open symbols) The solid lines represent third-order Birch-Murnaghan equation of state fits to the simulation data and the corresponding data are presented with 10% internal displacement in the reduced volume axis. . 106

5.5 AIMD results of $Ge_{25}Se_{75}$. a) The reduced density dependence of the coordination number. Here, the cut-off distances for the calculation of the coordination numbers are defined by the position of the first minimum of the total pair distribution functions, $r = 2.85$ Å. The gradual increase in the coordination of Ge and Se atoms becomes pronounced around $\rho/\rho_0 = 1.4$. The calculated partial pair distribution functions b), c) and d) as a function of pressure. Note that the evolution of Ge-Se bond length could also be traced in a trend similar to what is observed in Fig. 5.3 107

5.6 a) Calculated interatomic distances evolution of selected compositions as a function of ρ/ρ_0 the filled squares shows the average distances within the first shell consisting of 4 neighbors while the half filled circles show the average distances of the 5th and the 6th neighbors. The dashed red line corresponds to the minimum r_{min} of the pair correlation function, and serves to split the first from the second shell of neighbors. b) Computed bond angle distributions Ge-Se-Ge with increasing pressure for $Ge_{20}Se_{80}$ c) Reduced density dependence of the angle distributions split into neighbor number of the selected compositions obtained from CPMD simulations. Here 0 stands for a central Ge atom in a tetrahedron and the numbers 1,2,3,4,5 and 6 represent the neighbors (i.e. 102 indicates the angle between the first and 2nd neighbor of the central Ge atom labeled 0. d) Computed bond angle distributions Se-Ge-Se with increasing pressure for $Ge_{20}Se_{80}$. The color code in panel b) is the same as in panel d). 110

5.7 Evolution of 6 fold coordinated Ge atoms as a function of reduced density. The inset shows the changes of various Ge environment in $Ge_{18}Se_{82}$ over the whole pressure range of the AIMD simulations. 112

5.8 Normalized total coordination number as a function of the reduced density for the selected compositions of Ge_xSe_{1-x} obtained from CPMD calculations. Here the y axis represents the total coordination number at a given ρ divided by the total coordination number at ambient pressure. A global behavior is clearly observed for all the compositions with a marked increase in the coordination number starting around $\rho/\rho_0 = 1.4$. 113

5.9 Atomic configurations of $Ge_{20}Se_{80}$ for LDA (right panel) and HDA (left panel) phases where Ge atoms are pink and Se atoms are yellow. The bars are drawn to highlight tetrahedral (right panel) and octahedral (left panel) coordination environment of a selected Ge atom. 115

6.1 Pressure dependence of the total structure factor for $Ge_{20}Se_{80}$. AIMD computed results (black curves) are compared to neutron diffraction (red curves) [94] and X-ray [77] diffraction (blue diamonds) results. Here, the first pressure value indicated corresponds to the simulations while the second is for the experimental pressure points. 121

6.2 Computed pressure dependence of the principal peak position of the total structure factor (black spheres) compared to the experimental results of Kalkan [77] et al during compression (filled red diamond symbols) and decompression (open red diamond symbols). The solid black lines are the linear fits marking two different pressure while dashed vertical line is a guide to the eye for critical pressure. The inset shows the calculated normalized stress G as a function of normalized strain g (see text for details) compared to X-ray diffraction experiments by Kalkan et al.[77] (open red diamond symbols) and Skinner et al. [93] (open blue diamond symbolds). 122

6.3 Pressure dependence of computed (black curves) total pair distribution function for $Ge_{20}Se_{80}$ are compared to neutron diffraction experiments [94] (red curves). 124

6.4 The calculated pressure dependence of partial pair distribution functions for $Ge_{20}Se_{80}$ (from upper panel to lower $g_{\mathrm{GeGe}}(r)$, $g_{\mathrm{GeSe}}(r)$, and $g_{\mathrm{SeSe}}(r)$). 126

6.5 Computed pressure dependence of computed coordination number for $Ge_{20}Se_{80}$ (filled spheres) are compared to AIMD and ND work of Bouzid et al. [94] (open squares and magenta open circles, respectively), XRD work of Skinner et al. [93] (orange open pentagons) and XRD work of Kalkan et al. [77] (green open diamons). On the top left and bottom right snapshots of typical structural units are represented for LDA and HDA phases 127

6.6 Calculated fraction of Ge-Se and Se-Se bonds as a function of pressure for $Ge_{20}Se_{80}$. Cut-off values for each pressure point was taken from the minimum of the corresponding pdf. (i.e 2.8 Å at ambient pressure). The inset shows the faction of Ge-Ge homopolar bonds. 129

6.7 Composition dependence of the critical pressure found by the onset of the Ge-Se bond length increase. The inset shows the pressure dependence of the AIMD calculated Ge-Se bond length for a number of compositions ranging the rigidity transitions. The open red square data is taken from the EXAFS work of Properzi et al.[90] 130

A.1 Calculated self diffusion coefficients D_{Se} (red) and D_{Ge} (black) using glass and liquid densities as a function of composition at 1050 K. 139

A.2 Stress evolution in the simulation cells having liquid densities as a function of simulation time for selected compositions at 1050 K. 140

A.3 A Number of constraints n_c Total and Ge related constraints calculated for five independent configurations at 1050 K for the 22% system for cells having glass densities. 141

A.4 Total pair distribution functions of the 22% system at 1050 K for five independent configurations for cells having glass densities. 142

B.1 Calculated vibrational density of states for $Ge_{10}Se_{90}$ at 300 K compared to inelastic neutron scattering measurement Ge_8Se_{92} (ref. [220]). 144

B.2 Calculated energy normalized VDOS as a function of energy for $Ge_{14}Se_{86}$ (continuous lines) and for $Ge_{18}Se_{82}$ under pressure (broken lines) at 300 K. The inset shows the total VDOS as a function of energy for $Ge_{14}Se_{86}$. . 144

B.3 Experimental XANES spectra (continuous curves) for $Ge_{25}Se_{75}$ under pressure at Ge K edge compared to FEFF calculations using the AIMD simulated atomic trajectories (broken curves). 145

B.4 a) Calculated intermediate scattering functions for selected compositions of Ge_xSe_{100-x} at 300 K. b) The non-ergodicity parameter as a function composition. 146

B.5 Calculated average Ge-Se-Ge and Se-Ge-Se bond angle distributions of (BAD) $Ge_{10}Se_{90}$ under pressure at annealed or cold compression conditions. 147

B.6 Measured pressure dependence of Ge K edge shift energy in XANES spectra of $Ge_{20}Se_{80}$ compared to AIMD simulations from the ref [94]. . . 148

List of Tables

1.1 Comparison of some physical properties of selected glass families. Reproduced from [63]. 15

1.2 Inter-atomic distances, coordination numbers and densities of different Ge-Se compounds at different temperatures measured by neutron diffraction studies. Reproduced from [73]. 17

2.1 Calculated coordination numbers with PW and BLYP schemes compared to neutron diffraction experiment [70]. Note the bimodal distribution in the Ge-Se-Ge due to ES and CS contribution. Reproduced from [130]. 45

Abbreviations and Symbols

AIMD	First-principles molecular dynamics
GFA	Glass Forming Ability
SRO	Short Range Order
IRO	Intermediate Range Order
DFT	Density Functional Theory
HK	Hohenberg Kohn
KS	Kohn Sham
LDA	Local Density Approximation
GGA	Generalized Gradient Approximation
PBE	Perdew, Burk, and Ernzerhof
BLYP	Becke Lee Yang Parr
PW-PP	Plane-wave pseudopotentials
FSDP	First Sharp Diffraction Peak
RDF	Radial Distribution Function
PDF	Pair Distribution Function
MSD	Mean-Square Displacement
XAS	X-ray Absorption Spectroscopy
XRD	X-ray Diffraction
XANES	X-ray Absorption Near Edge Structure
EXAFS	Extended X-ray Absorption Fine Structure
EDXS	Energy Dispersive X-ray Spectroscopy
ND	Neutron Diffraction
IXS	Inelastic X-ray Scattering

Chapter 1

General Introduction

Abstract

In this chapter, the fundamentals of glass formation in both thermodynamic and kinetic aspects will be covered. A short description of the topological constraints and its link with glass formation will be provided. In the following sections, after touching briefly upon the general features of chalcogenide glasses, the focus will be given to a detailed structural description of Ge-Se glassy networks, the target system of this thesis. Finally, one can find the thesis motivation and the organization at the end of this chapter.

1.1 A Brief Overview of Glasses

The history of glass making traces back to an era around 3500 - 4000 B.C. in ancient Egypt and Mesopotamia region [1]. The word glass was derived from a Latin word meaning a transparent material. Albeit being more of a luxury product in the beginning, glass-making techniques have been improved through years and glassy materials have been used in many areas. Since then, examples can be followed from ancient Roman products to medieval churches. In today's world, glassy materials are used in vast amount in everyday life for a large variety of purposes ranging from beverage containers to high-technology optical fibers for communication.

The endeavors for understanding the nature of glasses have engaged many scientists over the last hundred years. Even though many developments have been achieved in understanding these materials, many issues still remain unsolved regarding the structure and dynamics of glasses. Glasses are amorphous materials with lack of long range order in their atomic structure unlike crystals. The structure of glasses has been shown to be very similar to that of the liquids by Zachariasen's work in 1932 [2]. However, glasses exhibit various different short range structures, leading to many diverse material properties.

1.2 Glass Formation

If a liquid in thermal equilibrium is cooled down to its melting temperature at cooling rates high enough to avoid crystallization, it reaches an undercooled state with an increase of its viscosity. At sufficiently fast cooling rates, the increased viscosity hinders the atomic mobility that is required for structural rearrangements, and, results in a decrease of the attachment frequency of the atoms in such a way that the critical nuclei size for crystallization is no longer attainable. Upon further cooling of the undercooled liquid, the viscosity continues to increase until a typical value at which the liquid becomes a non-flowing rigid solid. This critical temperature is called the glass transition temperature, T_g. Although there are number of different approaches to define the glass transition temperature, it is often defined as the temperature at which viscosity becomes 10^{12} Pas. Another commonly used description of glass transition is the value of the Deborah number which is given as;

$$D = \frac{t_{observation}}{t_{relaxation}} \tag{1.2.1}$$

According to the above equation, when the observation time of flow [3] is much shorter than the internal relaxation time, glass formation is favored [4, 5, 6]. Therefore, a glass structure is a frozen configuration of the undercooled liquid in which the ergodicity (i.e. ability to visit all possible configurations at observable experimental time scales [7]) is broken. In this respect, glasses are non-equilibrium materials and non-ergodic thermo-systems having a frozen-in structure of the parent liquid phase.

Using basic hydrodynamics, the shear viscosity of a liquid can be described by the product of the shear modulus, G_∞ in the long wavelength limit and the shear relaxation time, τ, as shown by Maxwell :

$$\tau G_\infty = \eta \tag{1.2.2}$$

In an ordinary fluid such as water, the relaxation times are of the order of picoseconds. However, for a liquid that approaches its glass transition, typical relaxation times are on the order of 1000 seconds [8]. In this respect, the value of τ is indicative of the time required for a molecule to move over one inter-molecular distance. Yet, the molecular motion in a liquid approaching to the glass transition is so slow that the average velocities remain ineffective, thus, vibrational motion dominates. These vibrations explore different energy minima in the configurational space before any hopping or jumping could occur by a neighboring distance. The jumps that occur represent the elementary process contributing to the actual flow of the liquid. However, these events are so rare at the glass temperature that the liquid appears as a solid on the observation time scales.

Unlike crystallization that gives rise to changes in the first order in thermodynamic quantities such as enthalpy H, entropy S, and specific volume V, the glass transition exhibits discontinuities in the second order quantities such as heat capacity, thermal expansion coefficient, and isothermal compressibility. However, it was shown that the glass transition can not be considered as a second order transformation due to the deviation of the Prigiogine-Defay ratio which defines the jump of second order thermodynamic quantities from unity [9, 10]. Earlier studies have shown that the glass transition is governed by the arrested kinetics instead of a thermodynamic origin [11]. Notably, the cooling rate directly affects T_g. Fig.1.1 illustrates the effect of the cooling rate on glass transition temperatures.

In theory, any liquid can form a glass if cooled fast enough to bypass crystallization, in other words, if the relaxation time is much larger than the observation time (i.e. $D << 1$). However, liquids can be classified according to their glass forming tendencies. As mentioned above, viscosity of undercooled liquids increases continuously as the temperature is lowered as contrast to the sudden jump observed in the case of a crystallization event. The temperature dependence of viscosity η varies for different liquids, i.e. Arrhenius-like and non-Arrhenius-like behaviors. In the first category the liquids are called *strong* and have higher GFA in contrast with the second category of liquids which are called *fragile* and have low GFA. To asses the GFA of a liquid numerically, a crucial parameter called *fragility* [13, 14] is used. Fragility, m, is a property of glass forming melts defined by the temperature dependence of viscosity around the glass transition temperature T_g and given by

$$m(x) = \frac{\partial \log\ \eta(T,x)}{\partial (T_g(x)/T)}\Big|_{T=T_g} \tag{1.2.3}$$

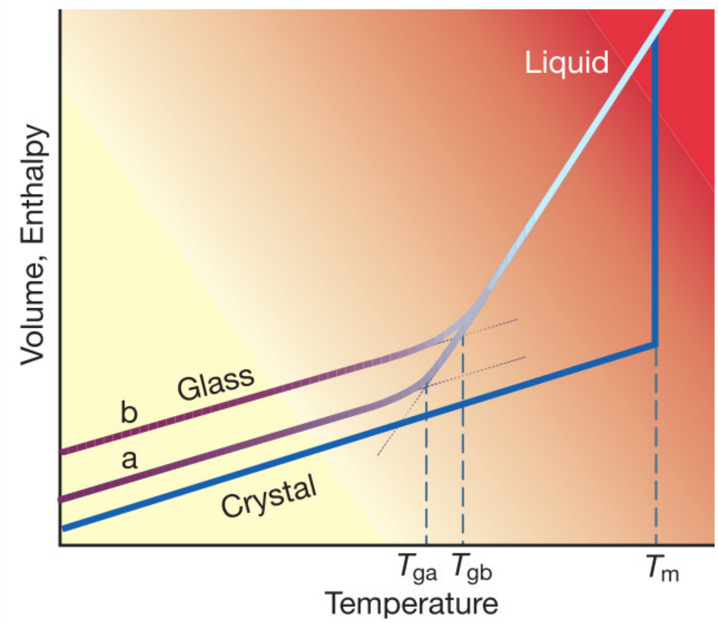

Figure 1.1: The changes in specific volume or enthalpy upon cooling from liquid state. Two different cooling rates, a and b, result in different glass transition temperatures. Adopted from [12].

Fragility is a unitless steepness index of viscosity as a function of inverse temperature scaled to T_g/T. Materials having lower m values have higher GFA. Fig.1.2 shows the viscosity dependence of different type of liquids.

It can be seen that the oxide glasses such as silica and germania exhibit a strong behavior while organic glasses prominently deviate from the Arrhenius relation. Strong glasses usually have small jumps in heat capacity upon glass transition whereas fragile (or sometimes called marginal) glass formers show much more sensible changes. The origin of the changes in the heat capacity at the onset of the glass transition lies in the c excess entropy. In 1948, Kauzmann mentioned the paradox that for glassy materials, extrapolating the entropy difference between the liquid and the crystal phases (or the most organized state of the system) leads zero entropy at finite temperatures above 0 K [16]. To overcome this unphysical picture, Kauzmann suggested a pseudo-critical temperature below which there is no distinction between an undercooled liquid and the glass itself. This temperature is called the Kauzmann temperature, T_K. About ten years later, in 1958, Gibbs and Di Marzio suggested that in order to observe a phase transition at the temperature T_K, the difference between configurational entropy of the undercooled liquid and the entropy of the phonons of a crystal, that is called the *residual* or *excess entropy*, should vanish [17]. Thus, the transformation manifests itself with abrupt changes in the heat capacity along with a divergence of the relaxation time which goes beyond the experimental observation times.

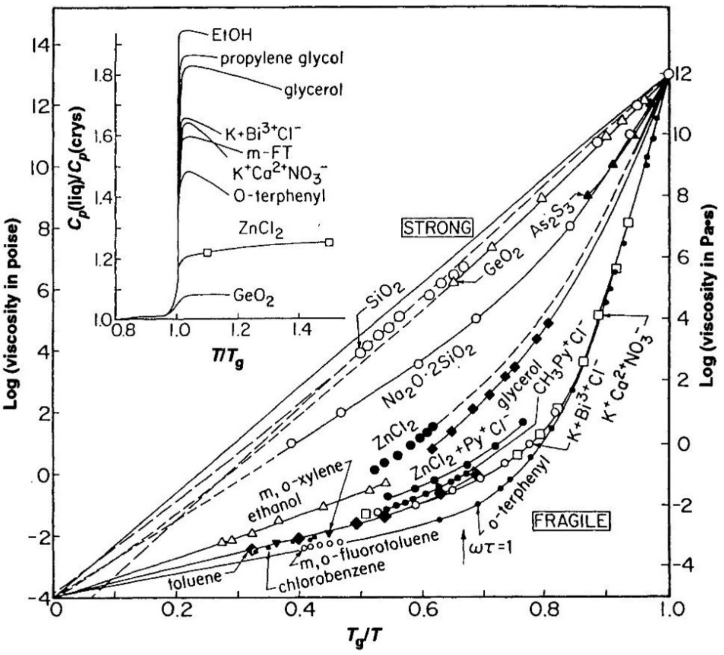

Figure 1.2: T_g scaled temperature dependence of viscosity showing Arrhenius (strong liquids) and non-Arrhenius (fragile liquids) behavior of liquids upon cooling. The inset shows the heat capacity change, ΔC_p, for selected strong and fragile liquids. Adopted from [15].

The correlation between the glass transition, relaxation, and fragility can also be expressed using a qualitative energy landscape approach [12]. Considering a potential energy map as a function of particle coordinates, a glassy system, indeed, will fall into a basin in the energy surface, which is the local minimum for a given configuration of the glass. In the presence of a thermal activation such as annealing at temperatures below T_g, the system displays excursions around the energy minimum. On the other hand, at elevated temperatures, system has a relaxation mechanism that it is not sensitive to the wells at the energy surface. The relation between the relaxation times and vanishing of the excess entropy landscape paradigm are summarized in Fig.1.3.

In contrast to strong liquids which are generally composed of tetrahedral units with iono-covalent bonds, non directional Coulomb and van der Waals interactions usually lead to liquids with a more fragile behavior. [19]. Considering the energy landscape approach, a fragile liquid has many degenerate minima with small thermal activation barriers to move from one to another. In contrast, a strong liquid has comparably less number of minima that are well separated with large energy barriers. Fig. 1.4 illustrates the differences of energy landscape maps between strong and fragile liquids.

The most popular equation to describe the temperature dependence of the viscosity of liquids that deviate from an Arrhenius behavior is the Vogel-Fulcher-Tamann (VFT)

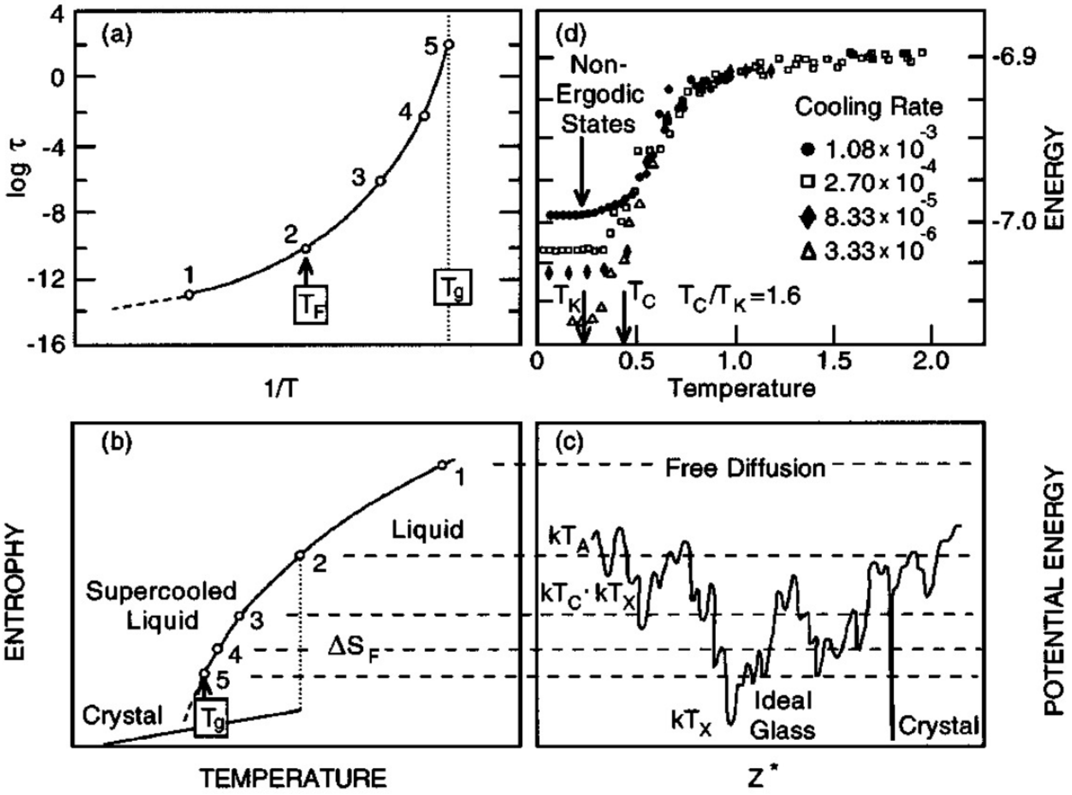

Figure 1.3: A summary of the main concepts in glass formation. a) the divergence in the relaxation times as reaching to the glass transition, b) the disappearance of the excess entropy, c) energy minima in potential energy surface d) temperature dependence of energy showing the amorphous megabasin at T_K. Adopted from[18]

equation which is given by

$$\log \eta(T,x) = \log \eta_\infty + \frac{A(x)}{T - T_0(x)}, \tag{1.2.4}$$

where T is temperature, x is composition, η_∞, A, and T_0 are the constants. The VFT equation has been used extensively for many systems and it has shown to be successful in describing the temperature dependence of viscosity for a large number of different systems. However, some reports indicated that at low temperatures, the VFT equation fails to describe the viscous behavior of undercooled liquids [21, 22].

Another approach for modeling viscosity is the Avramov-Milchev (AM) equation

$$\log \eta(T,x) = \log \eta_\infty(x) + \left[\frac{\tau(x)}{T}\right]^{\alpha(x)}, \tag{1.2.5}$$

where η_∞, τ, and α are fitting parameters.

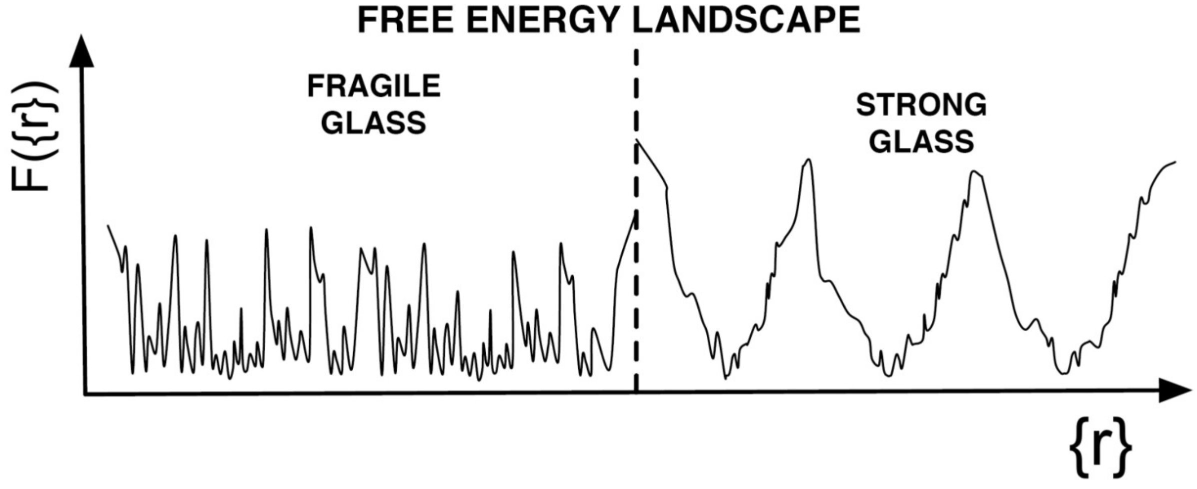

Figure 1.4: Energy landscape representations of glassed quenched from a) fragile b) strong liquids. Adopted from[20]

In a recent study, a new model was proposed for modeling the dynamics of viscous liquids based on configuration entropy and atomic constraints which is called Mauro-Yue-Ellison-Gupta-Allan (MYEGA) equation [23] (detailed information on constraints will be given in the following sections of this chapter). Recalling the Adam-Gibbs equation [24] which relates thermodynamic and kinetic aspects of the glass transition

$$\log \eta(T,x) = \log \eta_{\infty}(x) + \frac{B(x)}{TS_c(T,x)}, \tag{1.2.6}$$

where $B(x)$ is a fitting parameter related with the effective activation barrier and $S_c(T,x)$ is the configuration entropy. It was shown that the latter term can be related to the topological degrees of freedom $f(T,x)$ (see section 1.3) per atom with the given equation

$$S_c(T,x) = f(T,x)Nk \ln \Omega, \tag{1.2.7}$$

where, $f(T,x)$ is the number of degrees of freedom per atom, N is the total number of atoms, k is the Boltzmann constant, and Ω is the number of degenerate configurations per floppy mode [25] (see section 1.3). Defining two parameters; $K(x)$ which is given by $B(x)/3Nk \ln \Omega$ and $C(x)$, which is a term defining the energy difference between intact and broken topological constraints, the three parameter MYEGA model

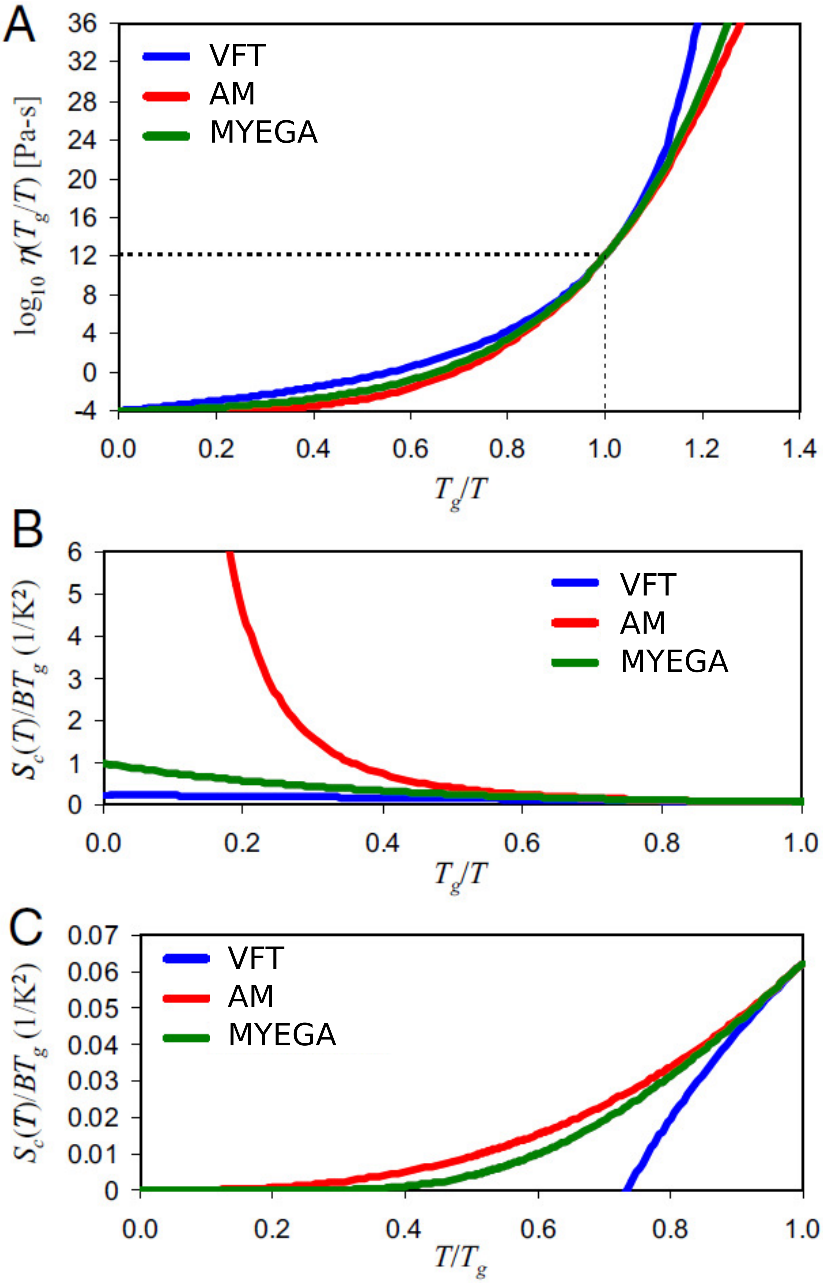

Figure 1.5: Comparison of VFT, AM, and MYEGA models A) viscosity as a function of T_g scaled temperature assuming m=60 and $\log \eta_\infty$ = -4. B) The Adam-Gibbs equation, the AM equation diverges at the high temperature limit. C) VFT model assumes a vanishing configurational entropy at low temperature limit. Reproduced from [23].

is given as

$$\log \eta(T,x) = \log \eta_\infty(x) + \frac{K(x)}{T}\exp\Big(\frac{C(x)}{T}\Big). \tag{1.2.8}$$

Incorporating the fragility term, the VFT equation becomes

$$\log \eta(T) = \log \eta_\infty + \frac{(12-\log\eta_\infty)^2}{m(T/T_g)+(12-\log\eta_\infty)}, \tag{1.2.9}$$

the AM equation becomes

$$\log \eta(T) = \log \eta_\infty + (12-\log\eta_\infty)\Big(\frac{T_g}{T}\Big)^{m/(12-\log\eta_\infty)} \tag{1.2.10}$$

and finally the MYEGA equation becomes

$$\log \eta(T) = \log \eta_\infty + (12-\log\eta_\infty)\frac{T_g}{T}\exp\Big[\Big(\frac{m}{12-\log\eta_\infty}-1\Big)\Big(\frac{T_g}{T}-1\Big)\Big]. \tag{1.2.11}$$

Fig.1.5 shows the comparison of the viscosity models for different cases. The differences of these three models are visible especially at high temperature and low temperature limits. We can see that the AM model fails to describe the high temperature configurational entropy variations whereas VFT function struggles with assessing the correct configurational entropy at some finite temperature T_0.

1.3 Topological Constraints and Rigidity

In the 19th century, Maxwell examined the mechanical structures consisting of bar and node network. The essence of his stability criterion was based on *constraint counting*, effectively deciding how many independent deformations could be associated to a mechanical system without costing energy (i.e. zero frequency modes). The constraint counting suggested by Maxwell relies on the estimation of the rank of a dynamical matrix which gives the the number of floppy modes (zero frequency modes). The floppy modes in a system can be given as the difference between the total number of degrees of freedom (that is Nd, for N sites and d dimensions) and the number of independent constraints, n_c. A change in a dependent (redundant) constrain does not affect the number of the floppy modes but induces a strengthening to the network that cannot be accommodated unless the bonding distances and geometry are changed.

One can define the quantity f, that is the number of floppy modes per atom obtained by the normalization through the total number of degrees of freedom (i.e. $f =$

F/Nd). Therefore, for a three dimensional network the number of floppy modes per atom can be given as;

$$f = 3 - n_c \tag{1.3.1}$$

The above equation indicates that a network will have an elastic phase transition from a floppy to a constrained state as f reaches zero.

About a century later, Phillips applied this method on network glasses to provide an insight of the glass forming ability. He built an analogy between the mechanical structure having bars and nodes and the glass network structure which can be described by stretching and bending interactions of bonds. In his work [26], he speculates that for a liquid to form a glass, the covalent forces constraining the neighbors with local bonding must be in a micro mechanical equilibrium. The glass forming ability is optimized when this mechanical equilibrium is reached via the equality of the number of degrees of freedom and the number of constraints for atom (i.e n_c=3 in three dimensions) [27]. The rigidity theory was later made more rigorous by Thorpe[28] for covalent systems in which local forces between neighbors are subject to small fluctuations

$$V = \frac{\alpha}{2}(\Delta l)^2 + \frac{\beta l}{2}(\Delta\theta)^2 \tag{1.3.2}$$

where l is the mean bond length and Δl and $\Delta\theta$ are the changes in the bond length and the bond angle. β represents the bond-bending (BB) force while α represents the bond-stretching (BS) term. In Thorpe's work in 1983, he examined Ge$_x$As$_y$Se$_{1-x-y}$ compound, where Ge, As, and Se are 4, 3, and 2 fold coordinated atoms, the coordination number bieng noted r. Assuming that there is no space for isolated pieces in the system nor a surface, the total number of atoms is;

$$N = \sum_{r=2}^{4} n_r \tag{1.3.3}$$

Thus, the mean coordination number can be defined as;

$$\langle r \rangle = \frac{\sum\limits_{r=2}^{4} r n_r}{\sum\limits_{r=2}^{4} n_r} = 2 + 2x + 2y \tag{1.3.4}$$

The implementation of the Maxwell constraint counting method to covalent networks suggested by Thorpe is as follows ; for each r fold coordinated atom, the number of bond stretching and bending constraints are equal to $r/2$ and $2r - 3$, respectively [8]. Thus, the total number of constraints is

$$n_c = \frac{\sum\limits_{r=2}^{N} n_r[r/2 + 2r - 3]}{\sum\limits_{r=2}^{N} n_r}. \tag{1.3.5}$$

Finally, combining with the equation1.3.1 we have

$$f = 6 - \frac{5}{2}\langle r \rangle. \tag{1.3.6}$$

Solving the above equation results in an optimally rigid (i.e isostatic) network at $\langle r \rangle = 2.4$, where the number of degrees of freedom is equal to the number of constraints per atom. Thus, a network is said to be *flexible* or *rigid* depending on whether $\langle r \rangle$ of the network is below or above the threshold value of 2.4, respectively. Philips showed that among chalcogenide liquids, the compositions at the mean coordination number $\langle r \rangle$ are the optimum glass-formers [26]. Since the network is stress-free at $\langle r \rangle$ = 2.4, the resulting glass is not as far from thermodynamic equilibrium as compared to its crystal counterpart. In addition to this, albeit being stress free, the network is still rigid which prevents the excursions in different configurations as compared to a flexible system. As a results, due to both thermodynamic and kinetic results, liquids, whose resulting glasses have $\langle r \rangle$ = 2.4, possess higher glass forming tendencies.

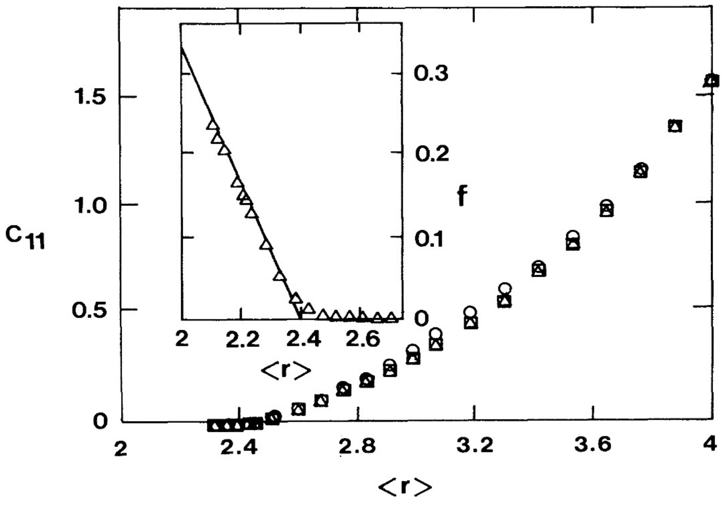

Figure 1.6: Elastic modulus of three network glasses as a function of the average coordination number. the inset shows the average number of zero-frequency modes of the three glasses compared to the line that represents the prediction by the mean field theory. Adopted from [29].

This threshold value of rigidity percolation has been shown to be related with many material properties (including fragility, elastic constants, hardness, fracture toughness, and electrical conductivity) not only for glasses but also for proteins and structural materials such as binding phases of concrete [**? ? ?** 30, 31, 32]. The link between the network rigidity and macroscopic properties of network glasses can be used as a design criterion. For example, the Gorilla©Glass 3 designed by the Corning company can be seen as one of the major contributions of rigidity theory to the design of new materials with specific properties, the atomic scale modeling from constraints being used to establish the composition before anything was experimentally cast.

During a long period, the topological constraints and their link with material properties have been shown to reflect a single threshold. However, this single threshold behavior was challenged recently with the observation of surprising features using various experimental techniques such as temperature modulated differential scanning calorimetry (MDSC), Raman, and Mössbauer spectroscopy in oxide and chalcogenide glasses [33, 34, 35, 36]. The experiments showed the existence of a finite mean coordination number region where the glass is isostatic instead of a single threshol. Many intriguing material properties such as weak aging [37, 38], low internal stress [39] and space-filling tendencies [40, 41] emerge. Since this region lies between flexible and rigid phases of a network, it is often called the *intermediate phase* (IP) or sometimes referred as the *reversibility window* given its detection from calorimetry. One of the most common feature of the IP is indeed the vanishing of the non-reversing enthalpy at the glass transition observed by MDSC (Fig.1.7) In a standard DSC, the heat flow ($\Delta Q/\Delta T$) is measured through heating a sample simultaneously with a reference at the same heating rate ($\Delta T/\Delta t$). It is important to note that the heating rate affects the results in T_g measurements performed by conventional DSC.

Fortunately, improvement to this issue can be circumvented by MDSC which is a complementary method to DSC in such a way that the heat flow is deconvoluted into reversing and non-reversing components. The former follows the temperature variations and measures the heat capacity C_p while the latter monitors the irreversible kinetic processes around the glass transition, T_g. Therefore, the MDSC-measured T_g is nearly free of kinetic effects [42]. In this respect, MDSC gives an access to more detailed information on the slow dynamic processes occurring near T_g [43].

The observation of the IP have been a controversial since its discovery. The debate on this issue has mostly raised from the MDSC measurements, especially the incorporation of the non-reversing heat flow with the reversibility window, regardless of the fingerprints of this phase tracked by other conventional methods such as Raman scattering (Fig.1.8). Contradictory results have been reported even for the same systems

[44]. However, it was also reported that there are important criteria to be met for observing the IP. In particular, sample homogeneity [45, 46, 47], especially when it comes to aging, and dryness [48] have been shown to affect the observation of the IP. Fig.1.9 illustrates the importance of the duration of melt homogenization prior to quenching.

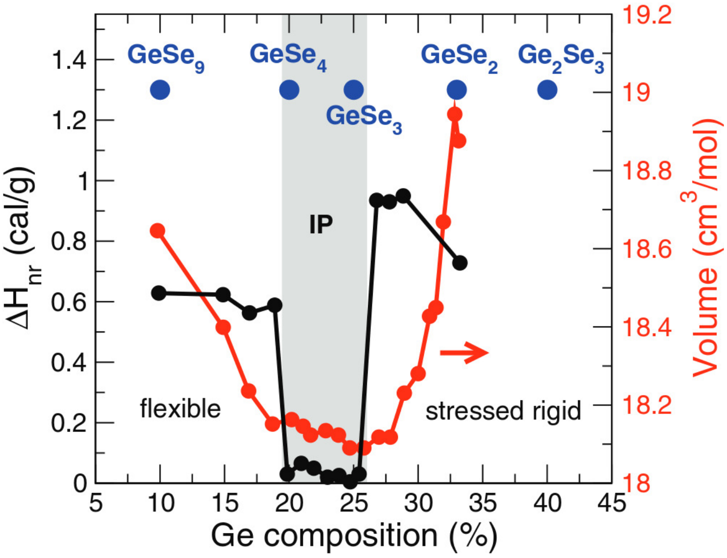

Figure 1.7: The composition dependence of non-reversing heat flow ΔH_{nr} and molar volume in Ge_xSe_{100-x} glasses showing the intermediate phase can be defined between x=20-26 %. Adopted from [49].

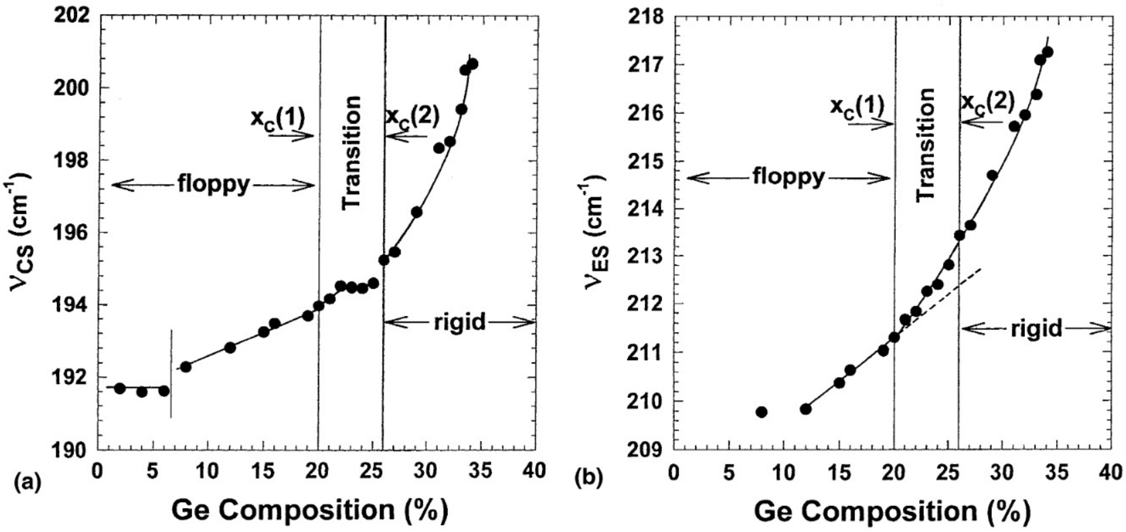

Figure 1.8: Raman mode frequencies for a) corner-sharing (CS) and b) edge sharing (ES) tetrahedra as a function of Ge composition in Ge_xSe_{100-x}. The CS frequencies remain nearly constant in the IP region while ES frequencies show an abrupt increase, deviating from the linear behavior observed in the flexible region. Adopted from [50].

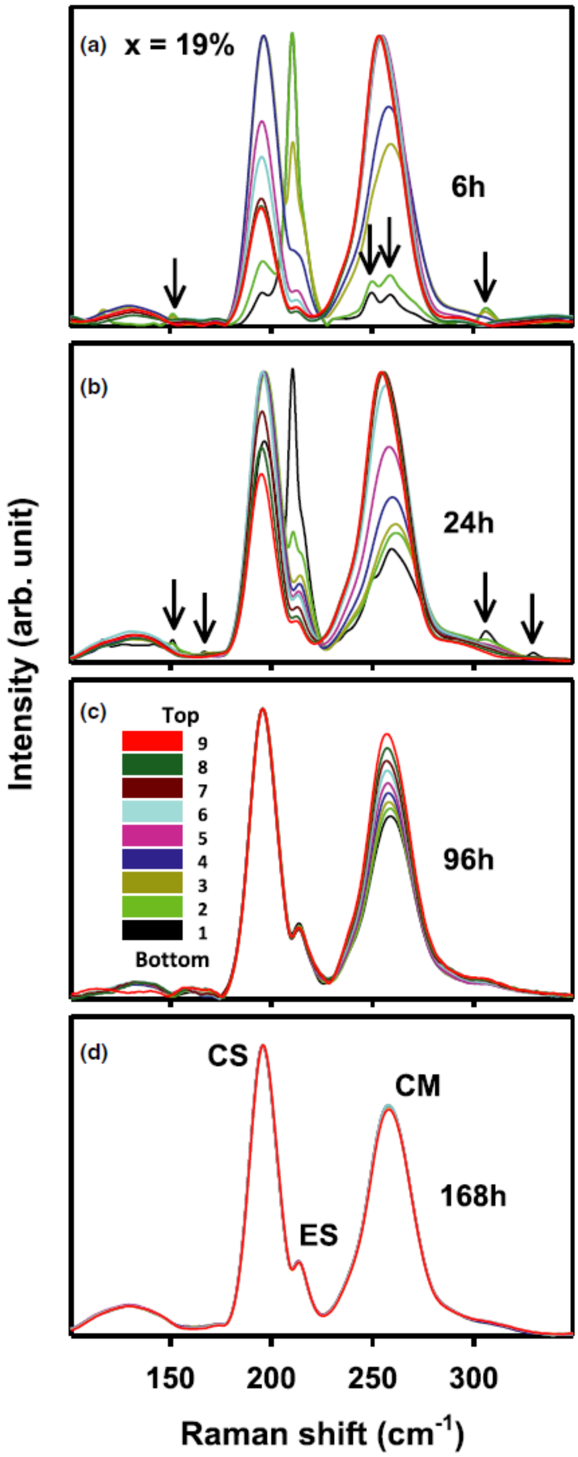

Figure 1.9: Fourier Transform Raman profiles of vitreous $Ge_{19}Se_{81}$ collected at 9 different points from the quenched glass rod showing the effect of melt homogenization time at a) 6h b) 24h c) 96h d) 168h. Adopted from [45].

1.4 Chalcogenide Glasses

Chalcogenide glasses (CGs) consist of a base chalcogen element such as S, Se, and T belonging to VI-A subgroup of the periodic table, alloyed with electropositive elements or with organic radicals. The word chalcogenide is derived from a combination of the following Greek words: "copper", "born", and "type", since the very first chalcogenide minerals that were found to contain copper along with S, Se, and Te [51]. Among inorganic glasses, chalcogenide glasses constitutes an important class due to their technological applications in wide range of areas such as bio-sensors [52, 53, 54] and night vision [55, 56] cameras, electric switches, microelectronic for infrared devices [57, 58]. The first commercially synthesized chalcogenide glass was As_2S_3, produced by Servo Corporation in 1957 for a bulk optical component in mid-IR range [59]. This composition is the most studied system in CGs due to its remarkable IR transmission, high GFA, and resistance to chemicals [60]. Soon after this, the idea of having Se as the base glass former came into play and allowed the synthesis of compounds such as As-Se, P-Se, and Ge-Se. In the following twenty years, many S and Se based glasses were produced along with Se-Te glasses which were used commercially [61, 62].

A variety of different techniques are used in the preparation of CGs. These glasses can be produced in bulk, fibre or film forms. The most commonly used method is the quenching technique with the use of rapid cooling from a liquid which is kept in a protective atmosphere within a quartz ampule. Other frequently used preparation methods include splat cooling, sputtering, chemical vapor deposition, glow discharge decomposition, and thermal evaporation techniques [63].

Table 1.1: Comparison of some physical properties of selected glass families. Reproduced from [63].

Glass	Phonon energy cm^{-1}	Transmission energy μm	Refractive index
Chalcogenide	330-380	0.5-10.0	2.3-2.7
Fluoride	440-650	0.25-6.50	1.52
HMO	590-850	0.4-7.0	2.65

As opposed to their oxide counterparts, the heavy chalcogen elements in chalcogenide glasses allow low phonon energy which makes them good candidates for sensor applications. CGs are amorphous semiconductors having a band gap of 1-3 eV. In this respect, Te based CGs possess the widest whereas S based CGs possess the smallest band gap. As for their optical properties, there are a number of distinct photoinduced phenomena that take place in CGs. These phenomena can be divided into two sub groups; heat-mode and photon-mode, respectively. One of the most interesting photon-mode phenomena is photo-darkening [64, 65]. This effect occurs when sample illumination causes red shift in the optical absorption edge and therefore the sample becomes darker. Other photo-induced phenomena are explained in detail in the references [66, 63] and therein.

Structural properties of CGs are characterized through the short range order (SRO) and intermediate range ordering (IRO) as for the case of other glassy materials due to lack of long range ordering in the amorphous nature of these materials. The two fold coordinated chalcogenide elements provide flexibility to these semiconducting glasses. Although for some CGs the SRO resembles to its crystal counterpart with slight distortion such as in As_2Se_3 [67]. However, binary CGs having Ge as the alloying element contradict this behavior[68].

1.4.1 Germanium Selenide Glasses

Ge_xSe_{1-x} glasses hold an important place among CGs not only for being a good starting material for optoelectronic applications, but also for serving as an archetypical system for studying covalently bonded networks [69]. In contrast to to their oxide counterparts, a considerable amount of homopolar bonds exist in the structure of these glasses, enhancing the structural variability [70]. The binary Ge_xSe_{100-x} system exhibits a wide glass forming range ($0 \leq x \leq 0.43$ [71]) that allows the tuning of the topological properties linked with short and intermediate range atomic ordering provided by the stiffening of the network structure [72]. With the increasing Ge content, the system becomes more rigid and exhibits three elastic phases within the glass forming region; flexible, isostatic, and stressed rigid (Fig. 1.8). As Ge atoms adopt a 4 fold coordination while Se atoms have 2 neighbors, the average coordination number of Ge_xSe_{100-x} glasses is given by $\langle r \rangle = 2 + 2x$, and at $x = 20\%$ corresponding to $\langle r \rangle = 2.4$ the rigidity percolation occurs. As mentioned above, it was reported that Ge_xSe_{1-x} glasses feature an IP between $20 \leq x \leq 26\%$ [45, 50]. The inter-atomic forces in this system can be tuned to a significant level by changing composition, temperature or pressure [73]. Therefore, by altering the average coordination number, the network properties can be controlled. The main building blocks of the network in Ge-Se glasses are $GeSe_4$ tetrahedra, which are connected either by edges or corners [74, 75, 76] (Fig. 1.10). A prototype material is $GeSe_2$, the most studied compound within the Ge-Se system, where the network consists of edge and corner sharing $GeSe_4$ tetrahedra along

Table 1.2: Inter-atomic distances, coordination numbers and densities of different Ge-Se compounds at different temperatures measured by neutron diffraction studies. Reproduced from [73].

System	r_1 (Å $^{-1}$)	r_2/r_1	$\bar{n}$	T (°C)	ρ (Å $^{-3}$)
l-GeSe	2.66(2)	2.37	5.8(4)	1000(3)	0.0456(3)
l-GeSe	2.52(2)	1.452	3.5(3)	727(2)	0.0387(2)
l-$GeSe_{1.5}$	2.41(2)	1.618	2.8(2)	728(3)	0.0336(2)
l-$GeSe_2$	2.38(2)	1.609	2.6(1)	784(3)	0.0311(2)
g-$GeSe_{1.5}$	2.37(2)	1.616	2.81(5)	26(1)	0.0341(1)
g-$GeSe_2$	2.35(2)	1.647	2.69(5)	26(1)	0.0334(1)
g-$GeSe_3$	2.35(2)	1.609	2.51(5)	26(1)	0.0339(1)
g-$GeSe_4$	2.34(2)	1.583	2.44(6)	26(1)	0.0339(1)

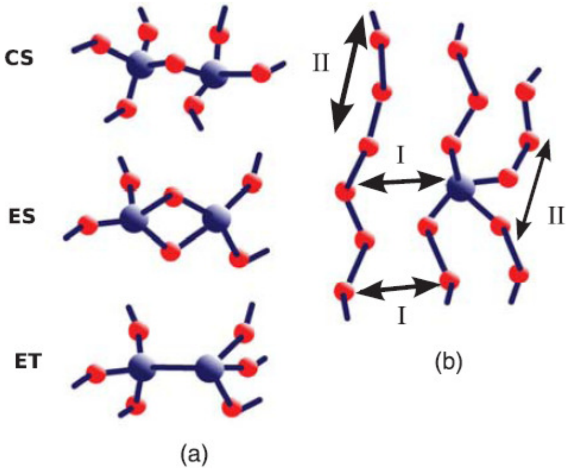

Figure 1.10: Schematics of structural units and possible network connections in Ge_xSe_{1-x} glasses. Adopted from [49].

with a substantial amount of Ge-Ge and Se-Se homopolar bonds ([75] and therein). In $GeSe_2$, the IRO results from the network structure and manifests itself by an internal first sharp diffraction peak (FSDP) in the diffraction pattern around ~ 1 Å^{-1}. An inspection of Fig.1.11 shows that the FSDP gradually decreases as the Ge concentration is lowered and eventually vanishes for pure Se. Another interesting feature that is absent pure Se is the shoulder peak at k = 7 Å $^{-1}$, which may be related with network rigidity, as it was suggested for the $GeSe_4$ system under pressure [77].

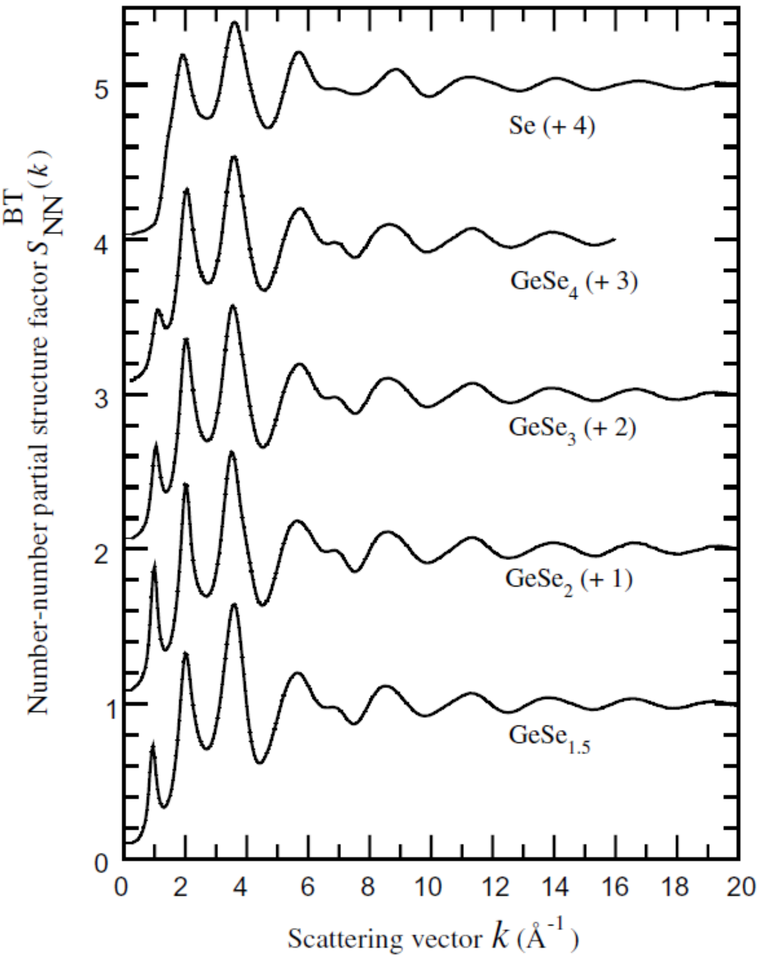

Figure 1.11: Bhatia-Thornton number-number structure factor for different Ge_xSe_{1-x} along with Se glasses at room temperature measured using neutron diffraction. Adopted from [73].

1.4.2 Effects of Pressure on Glassy Ge_xSe_{1-x}

Pressure-induced phase transformations have also attracted widespread interest in the condensed matter science community, both in crystalline and non-crystalline solids. The atomic rearrangements that occur at different length scales induced at high pressure have been observed to affect the macroscopic level material characteristics such as elastic and optical properties. Analogous to the polymorphism observed and well studied in crystalline materials, the existence of metastable configurations in an amorphous system is called polyamorphism [78]. The amorphous-amorphous transformations (AATs) have been detected in a variety of systems including oxide and chalcogenide glasses [76, 77, 79, 80, 81, 82, 83], amorphous Si [84] and Ge [85] and even vitreous H_2O [86]. AATs have been often observed in systems having directional bonding and low coordination numbers, such as tetrahedrally bonded systems that allow for a

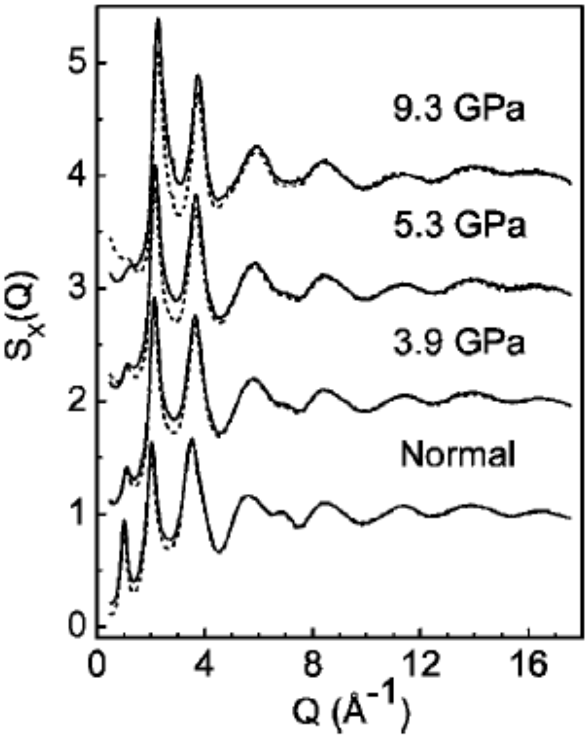

Figure 1.12: The total structure factor for $GeSe_2$ at different pressures measured by high energy X-ray diffraction. The dashed lines corresponds to the Fourier transforms of the total pair distribution functions. Adopted from [76].

large free volume in the system. More recently this phenomenon was also identified in a binary metallic glass [87]. The AATs can occur either in a sharp manner as in case of amorphous Si, or more gradually, as observed in oxide glasses, depending on the governing kinetics of the transition.

In contrast to the number of studies carried out for AATs of the oxide glasses, relatively fewer investigations have been reported for semiconducting chalcogenide glasses except the stoichiometric glass $GeSe_2$. This particular composition has been studied under pressure by means of X-ray and neutron diffraction, Raman scattering as well as acoustic measurements [76, 83, 75, 39]. The X-ray diffraction results showed a gradual decrease in the height FSDP with increasing pressure before it vanishes (Fig. 1.12), which can be seen as an indicative of a breakdown in the intermediate range order. In addition, the position of the principal peak shifts towards higher q vectors. Acoustic measurements of $GeSe_2$ under pressure showed a minimum observed in the shear-wave velocity, associated anomalous behavior in Poisson's ratio, along with discontinuities. This was related to the rigidity minimum occuring due to two competing densification mechanisms. This finding was recently confirmed by a direct volumetric study on a set of chalcogenide glasses including $GeSe_2$ under pressure [88]. In this work, the relaxation rate for $GeSe_2$ showed a pronounced maximum compared to the non-stoichiometric compounds at around 3.5-4.5 GPa, which was reported to be an indication of the existence of several active mechanisms for structural relaxation.

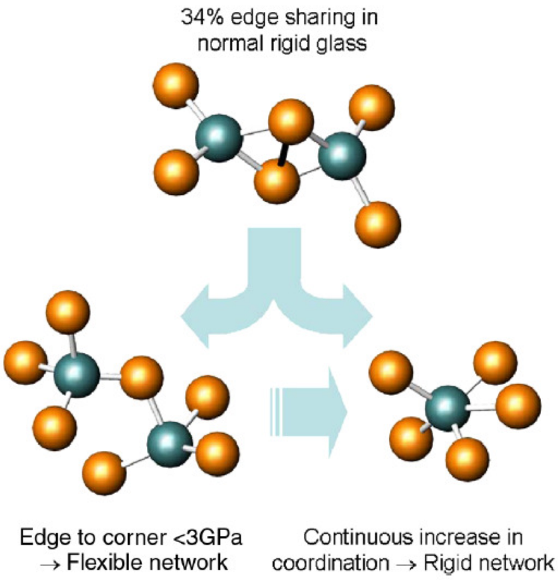
34% edge sharing in normal rigid glass
Edge to corner <3GPa → Flexible network
Continuous increase in coordination → Rigid network

Figure 1.13: Densification mechanisms suggested by acoustic measurements in $GeSe_2$.Se atoms are shown in orange an Ge atoms in blue. Adopted from [83].

In another study carried out with a combination of neutron diffraction and ab initio Molecular Dynamics (AIMD) simulations on the high pressure behavior of of $GeSe_2$, a conversion from edge- to corner-sharing tetrahedra was reported (Fig. 1.13) along with a continuous increase in the coordination number up to 8.5 GPa [89]. Furthermore, it was suggested that the homopolar bonds play a mediating role in the appearance of higher coordinated Ge polyhedra. This suggestion was speculated to be a signature for materials having homopolar bonds in which the fragility is promoted by the ES motifs [89, 75]. Another remark for this study is the deviation in the coordination numbers between the AIMD calculated and diffraction results at larger pressures. The discrepancy between simulations and the experiments was associated with the thermal history of the simulations (see section 2.5 for details). Recently, an EXAFS study has shown a semiconductor to metal transition between 10-15 GPa accompanied with a profound increase in the coordination number and Ge-Se distances [90]. Similar observations have been reported for GeS_2 under pressure in earlier EXAFS experiments [91] and atomic simulations [92] (see section 2.5 for details of atomic modeling of Ge-Se system). Another interesting composition in Ge-Se glasses is $GeSe_4$ since it is located at the rigidity percolation threshold. It was shown that during compression, unlike the continuous coordination increase observed in the stoichiometric compound

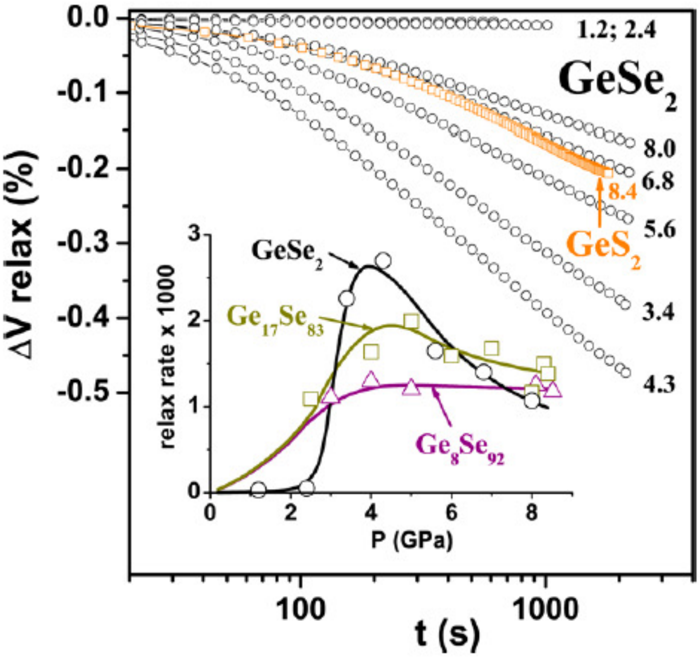

Figure 1.14: Specific volume relaxation of $GeSe_2$ at different pressures. The orange curve corresponds to the relaxation for GeS_2. The inset provides the pressure dependence of relaxation rate on different Ge-Se glasses. Reproduced from [88].

$GeSe_2$, the coordination number remains constant up to 8.6 GPa [93]. A more recent study suggests a transition from a low density amorphous semiconductor to a high density metallic amorphous between 10 and 15 GPa using X-ray diffraction (XRD) and electrical conductivity measurements [77].

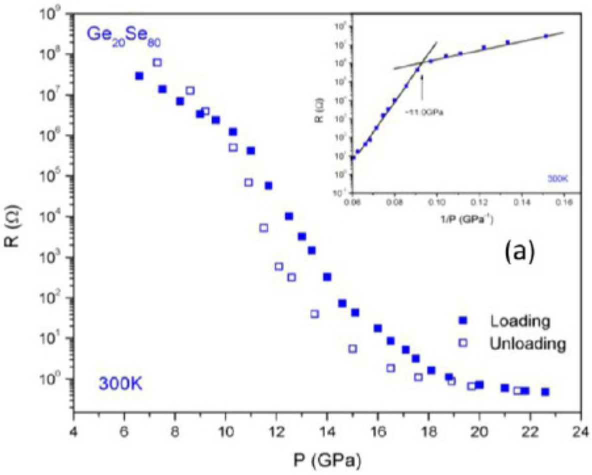

Figure 1.16: Electricial resistivity of glassy $GeSe_4$ under pressure. The inset shows the variation of the resistivity with reciprocal of pressure, showing a threshold around ∼ 11 GPa. Reproduced from [77].

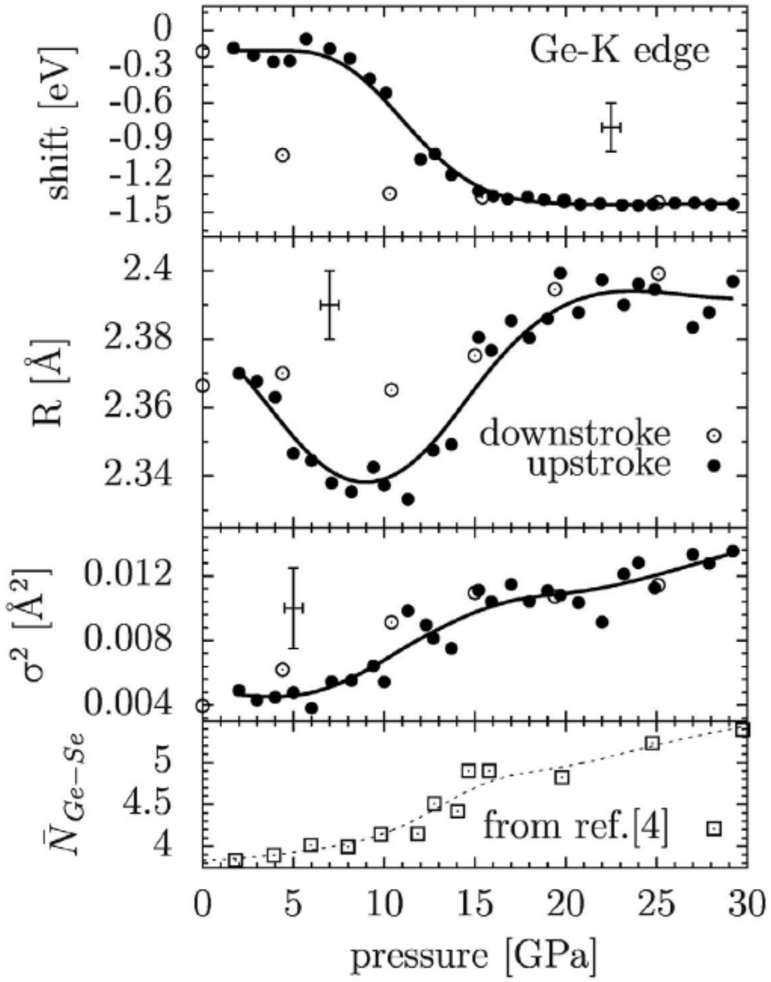

Figure 1.15: X-ray absorption spectroscopy results of $GeSe_2$ under pressure. The panels show the pressure dependencies of various properties (in descending order), band gap energy, Ge-Se distance, Debye Waller factor, and coordination number of Ge-Se. Reproduced from [90].

Additional evidence for a semiconductor to metal transition in $GeSe_4$ under pressure was given recently using a combination of neutron diffraction and *ab initio* simulations [94]. That work confirmed that the average coordination number shows no significant changes up to ~ 8 GPa and a that non-negligible fractions 5-fold Ge and 3-fold Se appear around 13 GPa. Nevertheless, some contradictory results with [77] were reported in the mean coordination number and Ge-Se distances. In Ref [94], these discrepancies were attributed to the differences in atomic models (in Ref. [77] ; empirical potential structural refinement and in ref [94] AIMD simulations were used).

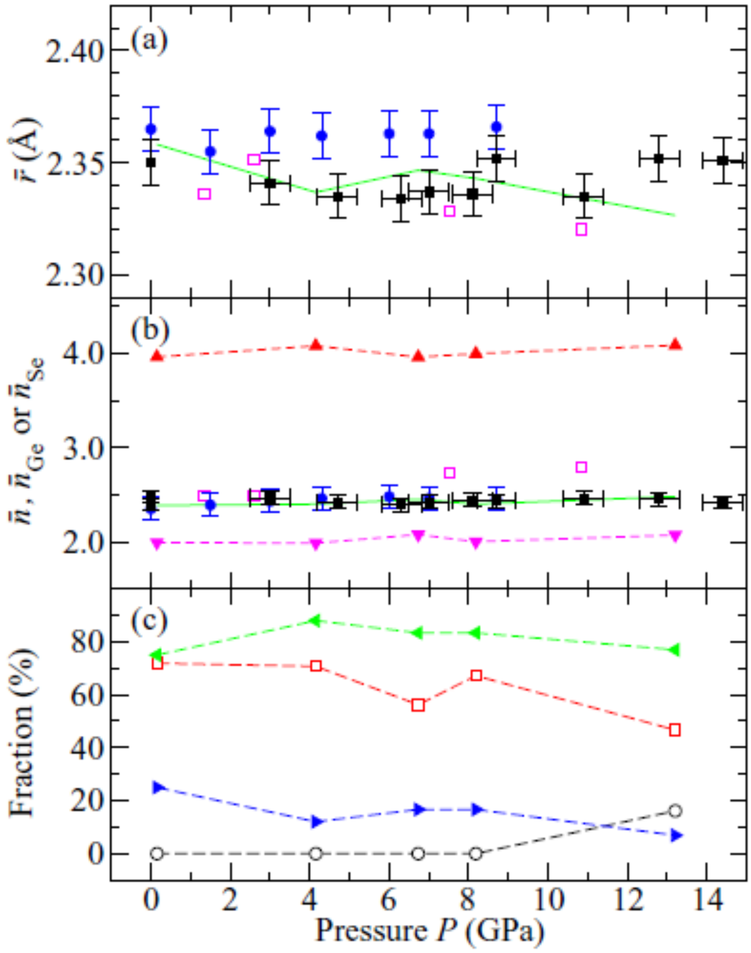

Figure 1.17: The pressure dependence of (a) the mean nearest neighbor distance $\bar{r}$ as measured in (i) the X-ray diffraction work of Skinner et al. [93] [(blue) solid circles with vertical error bars] and Kalkan et al. [77] [(magenta) open squares], (ii) the neutron diffraction work [(black) solid squares with error bars], and (iii) as calculated by ab initio Molecular Dynamics (AIMD) simulations [solid (green) curve]; (b) the mean coordination number $\bar{n}$ as measured in (i) the X-ray diffraction work of Skinner et al. [93] (blue) solid circles with vertical error bars] and Kalkan et al. [77] [(magenta) open squares], (ii) the present neutron diffraction work [(black) solid squares with error bars], and (iii) as calculated by AIMD [solid (green) curve], where the latter is broken down into its contributions from $\bar{n}_{Ge}$ [(red) upward-pointing triangles] and $\bar{n}_{Se}$ [(magenta) downward-pointing triangles]; and (c) the AIMD results for the fractions of Ge [(black) open circles] and Se [(red) open squares)] atoms involved in homopolar bonds, and the fractions of Ge atoms involved in corner-sharing [(green) leftward-pointing triangles] and edge-sharing [(blue) rightward-pointing triangles] tetrahedra. Reproduced from [94].

1.5 Motivations and Thesis Organization

Despite the experimental findings and simulations carried out regarding the pressure-induced structural changes in $Ge_{33}Se_{67}$ and $Ge_{20}Se_{80}$ glasses, a complete understanding of the underlying densification mechanisms leading to the AATs in Ge_xSe_{1-x} glasses is still lacking. Therefore, the motivation of this study is to cover a set of different compounds and investigate the structural and dynamic evolution under a combined change in composition and pressure. The main objective of this work is to provide, indeed, a comprehensive link between composition, pressure, and structural rigidity in Ge_xSe_{1-x} glasses using a combination of density functional theory (DFT) based molecular dynamics simulations, i.e. *ab initio* molecular dynamics (AIMD), X-ray diffraction (XRD), and X-ray absorption spectroscopy (XAS).

Indeed, glasses are so-called frozen-in liquids, and as it was mentioned earlier in this chapter, the molecular rigidity has a pronounced effect on the fragility of glass forming melts. For this reason, another goal of this study is to investigate the structural and dynamical properties of Ge-Se melts with detailed AIMD based compositional analyses before discussing the pressure effects on the glassy Ge_xSe_{1-x}. In this respect, this chapter covers a brief background information regarding the thermodynamic and kinetic aspects of glass formation, fragility, network rigidity and topological constraints, a brief overview of the chalcogenide glasses, and finally recent studies on the Ge-Se system.

In the next chapter 2, we will present the reasons of adopting AIMD for this thesis along with a quick review on the DFT. Furthermore, this chapter also includes a summary of the selected accomplishments in the atomic simulations of Ge-Se system. In the last part of Chapter 2, the details of the postprocessing of our simulations are given.

The experimental details of this thesis work in chapter 3. In particular, XAS theory, details of experimentation, and data reduction is explained along with brief descriptions of the other techniques used such as XRD and energy dispersive X-ray spectrum (EDXS).

In Chapter 4, we examine liquid Ge-Se using AIMD simulations. We discuss the dynamic anomalies, especially in viscosity and diffusivity which naturally affect the fragility of these liquids. A global link between topological constraints and fragility concept is provided which applies not only to the Ge-Se system but other network forming liquids. In Chapter 5, we report on pressure induced structural modifications in vitreous $\mathrm{Ge_xSe_{100-x}}$ (where $10 \leq \mathrm{x} \leq 25$) investigated using a combination of XAS, XRD and AIMD simulations. Our results show a polyamorphic transition from a tetrahedral to an octahedral phase for all the studied compounds accompanied with a semiconductor to metal transition under pressure. .the densification mechanisms are studied by examining neighbor distances and angle distributions under pressure. Chapter 6 focuses on vitreous $\mathrm{Ge_{20}Se_{80}}$ which is located at the rigidity percolation threshold. After having validated our AIMD simulations with experimental data over a broad pressure range, we show that the onset of polyamorphism is strongly related to network rigidity. We identify a parameter P_c which indicates the pressure at which the amorphous-amorphous transitions takes place. The composition dependence of this parameter shows that there is a direct correlation between ambient pressure connectivity of a tetrahedrally coordinated system with the polyamorphic transitions.

Finally, concluding remarks of and possible future directions for the subject of this study are given in Chapter 7.

Chapter 2

Theory

Abstract

In this chapter, an overview to the theoretical framework of the atomic simulations that were performed in order to investigate the structure and dynamics of Ge-Se liquids and glasses under pressure is given. The first section consists of the early history the density functional theory (DFT), and the main concepts of electronic structure. Subsequently, the derivation of the DFT along with important approximations in its use are given systematically. Finally, in the last section of this chapter, the Car-Parrinello Molecular Dynamics (CPMD) method and its essential features are briefly explained.

2.1 Density Functional Theory

2.1.1 Why Using the DFT Scheme ?

Atomic scale simulations have been used extensively over the last couple of decades to investigate materials properties in many different disciplines. Understanding the atomic scale properties of many body systems and linking them with macroscopic materials properties to be used in technological applications requires accurate and realistic descriptions of the models. Depending on the system in questions, specific input parameters, adequate system sizes, and convenient approximations are key factors in performing robust atomic scale simulations.

Classical molecular dynamics (CMD) has been proven to be a remarkable method for the description of a variety of systems [95]. In CMD, after having selected the specific ensemble of particles, one needs a description for the interaction between particles such as a classical inter-atomic potential having attractive and repulsive parts, which does not explicitly depend on the electronic structure of the system in question. With the use of these potentials, the forces acting on the interacting particles are calculated and the atoms are moved according to the Newton's law of motion using selected discrete time step. This is followed by the recalculation of the forces with the new positions of the particles after they are moved.

It is of paramount importance to note that the choice of the starting potentials has a strong effect on the accuracy of the model. There are a number of different parameters and fitting procedures that have been introduced to develop inter-atomic potentials for different organic and inorganic systems. Therefore, the success of CMD simulations relies on the accurate description of the bonding nature of the system in question. In particular, systems having large differences in electronegativity can be described with classic Coulomb charges due to the charge separation of the species. Oxide glasses and liquids are examples of systems for which the CMD yields accurate descriptions [96, 97, 98]. However, CMD fails to reproduce some structural features of chalcogenide glasses due to the similarities in electronegativities. Notably, the first CMD simulations of Ge-Se system reported by Vashista on $GeSe_2$ showed limitations in reproducing the Ge-Ge and Se-Se homopolar bondings which are shown experimentally with neutron diffraction [99, 70]. In the following years, Mauro and Varshneya tackled this issue using a new set of interatomic-potentials fitted to produced two and three body interactions using a ab-initio data. Even though some fraction of the Se-Se homopolar bonds were reproduced, this approach could not lead to the generation of Ge-Ge homopolar bonds [100]. Therefore, once can concluded that in order to perform accurate simulations of chalcogenide glasses having weak differences in electronegativity, and in particular Ge-Se system, the electronic structure has to be taken into account for a better description of the complex atomic interactions and to obtain a more realistic representation of the structural and dynamic properties. For this reason, the theoretical part of this thesis was solely built on the DFT based atomic simulations.

2.1.2 Historical Overview

In the early 20th century, quantum mechanics grew by leaps and bounds after the discovery of electrons by J. J. Thompson in 1897. Many scientist in the first three decades of this century studied the atomic structure (in which electrons and nuclei that are in continuous interaction with each other) of matter in order to understand the behavior of matter. Particularly in 1926, Erwin Schrödinger described the electronic wave behavior after the wave nature of the electrons had been suggested. Subsequently, the model suggested by Thomas and Fermi [101, 102] laid the base to the density functional theory (DFT). The importance of this model lies in the fact that it is the first theory that used the electron density as the fundamental variable to compute the electronic structure of an atom even though the model itself was too inaccurate. In the following years, Dirac contributed to this model with an additional exchange term [103]. In spite of Dirac's contribution, the inaccuracy remained and it was only in the mid sixties that Hohenberg, Kohn and Sham formulated the DFT rigorously[104, 105]. Since then, DFT has become a powerful tool to calculate the ground state properties of an atomic system in condensed matter physics, using a certain number approximations. Today, DFT is widely used in many different research fields to calculate interacting many-body problem and is becoming even more popular with the continuous rise in the performance of computer simulations. In the following sections, a brief step wise derivation of the DFT is provided.

2.1.3 Many-Body Equations

The behavior of an atomic system that consists of interacting electrons and nuclei can be shown in the form of a many-body Hamiltonian

$$\begin{aligned} H = & -\sum_i \frac{\hbar^2}{2m_e}\nabla_i - \sum_I \frac{\hbar^2}{2M_I}\nabla_I \\ & - e^2\sum_{i,I}\frac{Z_I}{|\mathbf{r}_i - \mathbf{R}_I|} + \frac{e^2}{2}\sum_{i\neq j}\frac{1}{|\mathbf{r}_i - \mathbf{r}_j|} + \frac{e^2}{2}\sum_{I\neq J}\frac{Z_I Z_J}{|\mathbf{R}_I - \mathbf{R}_J|} \end{aligned} \tag{2.1.1}$$

where m_e accounts for the electron mass, M_I and I represent the mass and charge of the nuclei while $\mathbf{r}_i$ and $\mathbf{R}_I$ are the positions of the electrons and nuclei, respectively. The first two terms in the Hamiltonian are the kinetic energy of the electrons and that of the ions. The remaining terms represent the interactions between electron-ion, electron-electron and ion-ion in the order of appearance. Therefore, equation 2.1.1 can be written in a more compact form

$$H = T_e(\mathbf{r}) + V_{eN}(\mathbf{r}, \mathbf{R}) + V_{ee}(\mathbf{r}) + T_N(\mathbf{R}) + V_{NN}(\mathbf{R}) \tag{2.1.2}$$

where T and V stand for the kinetic energy and the potential formed due to particle interactions, respectively. Due to the large mass difference between electrons and ions, it is convenient to consider the nuclei as being stationary in comparison with the electrons. Therefore, we can assume that the electrons instantaneously locate themselves adiabatically in the rearranged positions of nuclei. As a result, the kinetic energy term for nuclei, $T_N(\mathbf{R})$, can be neglected in the Hamiltonian. This simplifies the problem down to

$$H_e = T_e(\mathbf{r}) + V_{ext}(\mathbf{r}, \mathbf{R}) + V_{int}(\mathbf{r}) \tag{2.1.3}$$

where H_e is the electronic part of the Hamiltonian, V_{ext} is the external ion-electron potential and V_{int} is the internal electron-electron potential. The separation of ionic and electronic motion is called the *Born-Oppenheimer*(BO) or the adiabatic approximation.

2.1.4 The Schrödinger Equation and Many-Body Wavefunction

The time-independent Schrödinger equation is used to describe the quantum mechanics of the interacting particles. Within the BO approximation, the electronic Hamiltonian in equation 2.1.3 that accounts for the energy of a system can be converted to an eigenvalue-problem using the non-relativistic Schrödinger equation that satisfies the Pauli exclusion principle as follows

$$H_e\Psi = \varepsilon_e\Psi \tag{2.1.4}$$

where Ψ is the many-body electron wavefunction and ϵ_e is the eigen value. One can interpret the many-body wavefunction as the *probability amplitude* of finding an electron in a given position. Thus for a system containing N electrons, one can show that N electrons exist with unit probability as :

$$\int |\psi(\mathbf{r}_1, \mathbf{r}_2, \mathbf{r}_3 .....\mathbf{r}_N)|^2 d\mathbf{r}_1\mathbf{r}_2\mathbf{r}_3.....\mathbf{r}_N = 1 \tag{2.1.5}$$

Therefore the total number of electrons can be found using the single particle density, $n_0(\mathbf{n})$, with integration over entire space in the following form;

$$\int n_0(\mathbf{r})d\mathbf{r} = N \tag{2.1.6}$$

2.1.5 Hohenberg and Kohn Theorem

Although neglecting the electron-phonon coupling using BO approximation provides considerable simplification of the Hamiltonian, it is still impossible to solve equation 2.1.4 due to the large number of electrons in an atomic system (i.e. 10^{23}). This is where the Hohenberg-Kohn (HK) formalism [104] becomes useful. The essence of their approach is to describe an interacting many-body system with the ground state particle density $n(\mathbf{r})$ instead of using many-body wavefunction.The theory suggests an energy functional denoted as $E[n(\mathbf{r})]$ that is strictly a function of the ground state electron density $n(\mathbf{r})$,

$$E[n(\mathbf{r})] = \int V_{ext} n(\mathbf{r}) d^3\mathbf{r} + F[n(\mathbf{r})] \tag{2.1.7}$$

where V_{ext} is the external electrostatic potential caused by the nuclei as appears in equation 2.1.3. The HK theorem implies that if one is able to find the correct ground state density of a system, then it is possible to determine its properties. The universal energy functional $E[n(\mathbf{r})]$ can be expressed as a function of a particular electron density and at a given external potential, V_{ext}. The ground state electron density yields the global minimum of the universal energy functional. Furthermore, we have a new variation functional appearing in the HK theorem. In the work of Hohenberg and Kohn [104] the electron density was set to be *v-representable*, which means that for a certain local potential, $n(\mathbf{r})$ must be the ground state density. Within the next two decades this functional was reconstructed for *N-representable* densities in a Levy-Lieb form [106, 107, 108]

$$F[n(\mathbf{r})] = min < \Psi | T + V_{int} | \Psi > \tag{2.1.8}$$

in which the minimum is calculated over all the arbitrary anti-symmetric wavefunction that leads to the $n(\mathbf{r})$. Nevertheless the variation functional $F[n(\mathbf{r})]$ is not known. Therefore HK theorem could only be used to calculate the electronic energies if the exact form of this variation functional was known.

2.1.6 Kohn-Sham Formalism

A year after the HK theory was published, Kohn and Sham reformulated the HK formalism in order the tackle the issue of the variation functional $F[n(\mathbf{r})]$ being unknown. The main idea of the ansatz is to assume the ground state density of electrons of the an interacting system under consideration to be equal to that of a *non-interacting* system [105]. This assumption reduces the complexity of the many-body problem to a great deal so that one can treat the electrons of a system that *does not* interact. Therefore, the variation functional is defined as

$$F[n(\mathbf{r})] = T_0[n(\mathbf{r})] + E_H[n(\mathbf{r})] + E_{xc}[n(\mathbf{r})] \tag{2.1.9}$$

where $T_0[n(\mathbf{r})]$ represents the kinetic energy of the auxiliary non-interacting system while $E_H[n(\mathbf{r})]$ stands for the classical Coulomb potential of the electrons (also regarded as Hartree potential) and finally is the exchange-correlation energy E_{xc} of the electrons that also includes the energy difference between the kinetic energy of the auxiliary system and the original system under consideration. Thus one can express the KS energy functional as follows:

$$E_{KS}[n(\mathbf{r})] = T_0[n(\mathbf{r})] + \int n(\mathbf{r}) \left[V_{ext} n(\mathbf{r}) \frac{1}{2} V_H[n(\mathbf{r})] \right] d^3\mathbf{r} + E_{xc}[n(\mathbf{r})] \tag{2.1.10}$$

The kinetic energy term and the terms in the integral can be calculated whereas proper approximations must be performed for the last term which stands for the exchange-correlation energy that remains unknown. On the other hand, it was shown that the kinetic energy of the electrons of the auxiliary system may constitute a crucial part of the kinetic energy of in the Hamiltonian of an interacting system [109]. From 2.1.10, one can write :

$$\frac{\delta E_{KS}[n(\mathbf{r})]}{\delta n(\mathbf{r})} = \frac{\delta T_0[n(\mathbf{r})]}{\delta n(\mathbf{r})} + V_{ext}(\mathbf{r}) + V_H(\mathbf{r}) + \frac{\delta E_{xc}[n(\mathbf{r})]}{\delta n(\mathbf{r})} \tag{2.1.11}$$

Taking a step further, an effective potential $V_{eff}(\mathbf{r})$ that incorporates the external and Hartree effects along with the exchange correlation effects of the other electrons can be provided as follows;

$$V_{eff}(\mathbf{r}) = V_{ext}(\mathbf{r}) + V_H(\mathbf{r}) + \frac{\delta E_{xc}[n(\mathbf{r})]}{\delta n(\mathbf{r})} \tag{2.1.12}$$

The above equation can be solved through a set of single-particle Schrödinger wave equations of the *non-interacting* particles with the use of the variation principle [109] satisfying the conservation of the total number particles, and leads to the KS single-particle eigen-value equation,

$$\left[\frac{\hbar^2}{2} \nabla^2 + V_{eff}(\mathbf{r}) \right] \psi_i(\mathbf{r}) = \varepsilon_i \psi_i(\mathbf{r}) \tag{2.1.13}$$

The DFT ground state of an atomic system can be calculated by solving the above equation for single particles. It should be noted that the single particles do not correspond to the electrons of the original system but should be considered as the auxiliary particles. The equation should be solved *self consistently*, that is iterating the single particle states until the density of the original interacting system $n(\mathbf{r})$ is equal to the density of non-interacting system $n^*(\mathbf{r})$. The charge density that is used in the iterations can be expressed as

$$n(\mathbf{r}) = \sum_i |\psi_i(\mathbf{r})|^2 \tag{2.1.14}$$

However, the exact form of the $E_{xc}[n(r)]$ is not known. Some approximations are unavoidable to solve 2.1.13, which are briefly pointed out in the next section.

2.2 Practical Approximations

Over the past 50 years many approximations have been introduced for the exchange-correlation functional in the DFT scheme proposed by Kohn and Sham. In fact the very first approximation was suggested in the original paper in 1965 [105] which was developed further within 2 decades[110], based on local electronic density approximation (LDA). In the following years, a number of different functional including generalized gradient approach (GGA) [111], meta-GGA [112], hybrid functionals [113] and optimized effective potentials [114] have been proposed. In the following subsections the two most commonly used approximations for exchange-correlation functional will be given.

2.2.1 Local Density Approximation

The LDA is the simplest, yet one of the most appealing approximation for tackling the issue of unknown exchange-correlation potential. This approximation assumes that at any position in space the exchange-correlation function of a single particle is equal to that of the homogeneous electron gas, ignoring the spatial dependence of density (i.e. exchange-correlation is purely local). Therefore, the spatial variations in the electron density are not taken into account. The exchange correlation of the homogeneous electron gas is given by

$$\epsilon_{xc}^{LDA}(\mathbf{r}) = \epsilon_{xc}^{h}(\mathbf{r})[n(\mathbf{r})] \tag{2.2.1}$$

Therefore the exchange-correlation energy can be written as

$$E_{xc}^{LDA}[n(\mathbf{r})] = \int n(\mathbf{r})\epsilon_{xc}^{LDA}(\mathbf{r})d\mathbf{r} \tag{2.2.2}$$

The exchange part of the homogeneous gas can be calculated analytically through a Hartree-Fock method while the correlation part is obtained using Quantum Monte-Carlo simulations [115]. Despite the fact that it is a very straightforward approximation, LDA provides impressively good results for certain quantities such as lattice geometries and vibrational properties, especially for the materials in which the electronic density varies weakly with the position. However LDA method is not reliable when it comes to binding energies or band gaps of materials due to over-binding which underestimates the results as compared to experimental data.

2.2.2 Generalized Gradient Approximation

In the GGA method, the exchange correlation functional $E_{xc}^{GGA}[n(\mathbf{r})]$ is expressed via the rate of change of the particle density, ∇n.

$$E_{xc}^{GGA}[n(\mathbf{r})] = \int n(\mathbf{r})\epsilon_{xc}[n(\mathbf{r}), \nabla n(\mathbf{r})]d\mathbf{r} \tag{2.2.3}$$

In this form, the spatial gradient improvement of the functional leads to having a number of different possibilities of expressing the exchange-correlation term. Therefore, a variety of functionals have been proposed. The choice of the appropriate functional is essential according to the system under consideration. Some of the most widely used functionals are the Perdew-Burke-Erzenhof (PBE) [116] Perdew-Wang (PW)[117] and Becke's exchange and Lee, Yang and Parr correlation therefore, BLYP [118, 119].

2.2.3 Plane-Wave Basis Set

In order to solve the KS many-body problem mapped onto a singe-particle problem one needs to overcome the issue of infinite number of auxiliary (non-interacting) electrons within a potential. In other words, a wavefunction must be calculated for an infinite number of electrons which expands throughout the entire system. One can express the wave function within a periodic system using the Bloch's theorem as follows:

$$\psi_i = e^{[i\mathbf{k}\cdot\mathbf{r}]f_i(\mathbf{r})} \tag{2.2.4}$$

where **k** is a reciprocal vector. In the plane-wave expansion, one has the wave function expanded at each **k** point in a defined basis-set. Therefore, the above Bloch function can be rewritten in the following form

$$\psi_i = \frac{1}{\sqrt{\Omega}} \sum_{\mathbf{G}} c_{i,\mathbf{k}+\mathbf{G}} e^{i(\mathbf{k}+\mathbf{G})\cdot\mathbf{r}} \tag{2.2.5}$$

where **G** is the reciprocal space vector and Ω is the volume of the repeated cell. Principally, as stated above, an infinite number of plane waves are required to expand the wave functions over the entire system. Yet in practice, the plane-wave expansion can be truncated at a cut-off value E_{cut} which defines the maximum kinetic energy within the basis set shown below,

$$\frac{\hbar}{2m}|\mathbf{k}+\mathbf{G}|^2 \leq E_{cut} \tag{2.2.6}$$

Indeed, the smaller the selected E_{cut} the smaller the computational effort, but this reduces the accuracy of the calculation. In practice, cut-off energy should be increased until the total energy has converged, which could be done by a series of iterations or simulations.

2.2.4 Pseudopotentials

A rather large cut-off energy is required in order to take the high kinetic interactions between core and valence electrons into account, meaning a selection of a higher **G** vector to expand plane waves which in turn costs more computation time. The core electrons are highly localized due to their tight binding to nuclei, yielding steep oscillations in the wavefunctions around the core region. Yet the physical properties of a solid are governed mostly by the valence electrons is that the fast oscillations of the core region can be approximated. Therefore, the core electrons can be treated as "frozen" with respect to their effect on the material properties, and the ionic (the highly oscillated core region) potential that requires a high cut-off energy can be replaced by a *pseudopotential* which accounts for a unified potential between core and valence electrons and yield to a lower cut-off energy with good accuracy.

A number of different sorts of pseudopotentials are available in the literature (ultrasoft, atomic, empirical etc.). In this thesis, norm-conserving Troullier-Martins type pseudopotentials are used [120]. In the original work, four general conditions are imposed for constructing a norm conserving pseudopotential. Firstly, there must be no nodes in the pseudowavefunctions since any wiggling in the core region due to a node would deteriorate the smoothness. The second requirement to meet is that beyond a selected cut-off distance, r_c, the normalized atomic radial pseudo wavefunction should be equal to the normalized all electron wave function having an angular momentum, l. Thirdly, the charge enclosed below the cut-off radius should be equal as described below:

$$\int_0^{r_c} |R_l^{PP}(r)|^2 r^2 dr = \int_0^{r_c} |R_l^{AE}(r)|^2 r^2 dr \tag{2.2.7}$$

where R_l^{PP} and R_l^{AE} represent the pseudo wave and all electron wave function. Finally the eigen values of the pseudowavefunctions and all electrons wavefunctions must be equal.

2.3 Ab initio Molecular Dynamics

The ground state DFT calculations can be combined with molecular dynamics simulations which is a method that is based on computing the time dependent behavior of N-body atomic or molecular systems. These type of calculations are referred as *ab initio* molecular dynamics (AIMD). AIMD computer simulations has become a very powerful tool for studying condensed matter science within the last couple of decades and this success is particularly coupled with the continuous development of computer performances. The main idea behind AIMD simulation is: initially solving the electronic structure using DFT for each time step and then finding the forces acting to each atom in the system with the use of the Hellman-Feynman theorem;

$$\mathbf{F} = -\frac{\partial E[n_0(\mathbf{r})]}{\partial \mathbf{R}} \tag{2.3.1}$$

where $\mathbf{F}$ is the force, E is the energy, $\mathbf{R}$ is the ionic position and $n_0(\mathbf{r})$ is the ground state density. After the forces acting on ions are calculated, the atoms are moved according to Newton's equation of motion from time t to time $t + \delta t$. In this thesis, the equation of motion of atoms were integrated using the Verlet algorithm [121]:

$$x(t + \delta t) = 2x(t) - x(t - \delta t) + \delta^2 \ddot{x}(t) \tag{2.3.2}$$

where x is position, t is time, and δt is the time step for the integration in the simulation. One of the most widely used methods in AIMD is the Born-Oppenheimer molecular (BOMD) dynamics. As mentioned earlier in this chapter, the BO approximation is basically the separation of electronic and nuclear parts due to the large difference in their mass. Therefore in the BOMD method, in each time step, first the ground state electronic structure of the stationary nuclei are calculated and the nuclei are displaced according to the forces acting on them. The energy minimization is carried out by diagonalization of the Hamiltonian. Although the BOMD methods are widely used, one major drawback is that at each time step, the electronic state of the system should be brought down to the ground state for recalculation prior to the next time step and this requires increased simulation time. In this thesis, an alternative MD method to overcome this time constraint is used, i.e. the Car-Parrinello dynamics (CPMD) [122].

2.3.1 Car-Parrinello Molecular Dynamics

The main advantage of CPMD, requiring no self-consistent solution of KS equations at each time step, relies on the fact that the electronic ground state energy calculations are performed only once in the very first step and the wavefunctions are evolved from the initial ground state. In other words, the initial calculation of the ground state electronic orbitals can have a finite thickness that allows variations in the solution of the KS equations along with the evolving time. In contrast to the BOMD method in which the electronic structure calculation is carried out with stationary ions, CPMD method allows the coupled electronic orbitals and ionic movement, via a Lagrangian given by :

$$
\begin{aligned}
L = \mu \sum_i \int |\dot{\psi_i}|^2 d\mathbf{r} + \frac{1}{2} \sum_I M_I \dot{\mathbf{R}}_I^2 - E[(\psi_i), (\mathbf{R}_i)] \\
+ \sum_{i,j} \Lambda_{i,j} \left(\int \psi_i^*(\mathbf{r}) \psi_j(\mathbf{r}) d\mathbf{r} - \delta_{i,j} \right)
\end{aligned}
\tag{2.3.3}
$$

where ψ_i are the electronic orbitals, $\mathbf{R}_I$ and M_I are the ionic positions and masses, dot stands for the time derivative Λ are Lagrangian multipliers introduced for constraining the orthonormality, and μ is the fictitious electron mass. Thus, the equations of motions that consist of the real motion of nuclei and the fictitious electronic motion can be given as follows:

$$
\mu \ddot{\psi}(\mathbf{r}, \mathbf{t}) = -\frac{\partial E}{\partial \psi^*(\mathbf{r}, \mathbf{t})} + + \sum_i \Lambda_{i,j} \psi_j(\mathbf{r}, \mathbf{t}) \tag{2.3.4}
$$

, and

$$
M_I \ddot{\mathbf{R}} = \frac{\partial E}{\partial R_I} \tag{2.3.5}
$$

The understanding of the fictitious mass parameter μ is of a special importance in the CPMD method. One should be careful choosing a value for this parameter, as the adiabaticity between the two degrees of freedom has to be satisfied. To keep the wavefunctions very close to the BO surface any possible energy exchange between electrons and ions should be prevented. A smaller μ signifies higher frequencies that result in a decrease in the time step. On the other hand, an overestimation of this parameter causes departure from the BO surface. Generally μ is of the order of 10^2-10^3 m_e to ensure slowing down of the electron dynamics while keeping the time steps considerably shorter than that of BOMD method. The optimum conditions for adiabaticity are met when minimum electron frequencies are substantially larger than the maximum ion frequencies. In systems with a finite band gap energies, the minimum electron frequencies can be expressed as:

$$\omega_e^{min} \sim \left(\frac{E_{gap}}{\mu}\right)^{1/2} \tag{2.3.6}$$

, where E_{gap} is the electronic band gap. Indeed, the simulations of system having no gap between conduction and valence bands is troublesome with CPMD method. Nevertheless, this problem could be overcome overcome by using different thermostats for each degrees of freedom for the case of aluminum [123].

2.4 Our Simulations

In this thesis, CPMD simulations are used for investigating the structure and dynamics of liquid and vitreous $\mathrm{Ge_xSe_{1-x}}$ for various compositions (where x=0.10, 0.143, 0.17, 0.18, 0.20, 0.21, 0.22, 0.23, 0.25 and 0.33), and under pressure. As embedded in the CPMD code, we have utilized a DFT scheme to describe the electronic structure that evolves self-consistently with time. For exchange correlation energies, the BLYP-GGA approach was used. The Trouller-Martins type pseudopotential approximation is adopted. Our simulations were carried out in NVT ensembles (i.e. number of atoms, volume and temperature of the system are kept constant with a total of 250 atoms. The cell dimensions are determined according to the experimental densities available in the literature [46], or to their extrapolations which will be discussed in the following chapters [124]. The initial positions of the atoms were taken from the GeSe crystal and Ge atoms are replaced with Se atoms depending on the composition in question. The wavefunctions have been expanded at the Γ point of the supercell on a plane-wave basis set having a cut-off energy of 20 Ry. A time step of Δt= 0.1 fs is used to integrate equations of motion using the Verlet algorithm implemented in CPMD code. The fictitious electron mass was selected as 200 a.u. ensuring the adiabaticity. All compositions are heated to 2000 K and kept there for 22 ps to lose memory of initial positions. Subsequently, a number of different temperatures were visited before thermalizing the glassy structure at 300 K. Figure 2.1 shows the cooling sequence of our CPMD simulations.

Since glasses are thermodynamically metastable materials, it is of crucial importance to verify the final structure of the glassy state after cooling down to room temperature due to the fact that different energy basins could be reached depending on

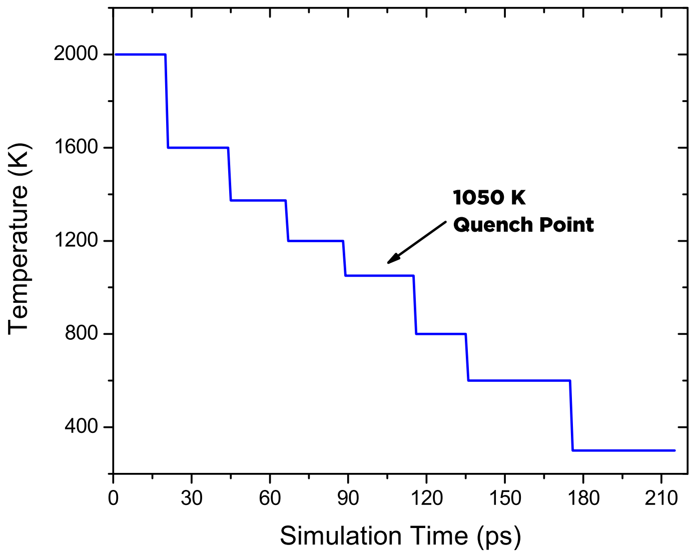

Figure 2.1: The cooling regime for obtaining glassy Ge_xSe_{1-x} with AIMD simulations. 1050 K represents the quenching point from the lowest liquid temperature attained.

the atomic configurations prior to quenching. Therefore, three independent quenches with 1050 K being the starting temperature were performed in order to have a statistical average of the 300 K trajectories. Fig. 2.1 a) shows the importance of averaging the structure over different quenching as reflected to the Ge-Ge partial pair distribution function $g_{Ge-Ge}(r)$. The first peak represents the Ge-Ge homopolar bonding as an example to which is given in the snapshot. These quenches are obtained with 2-4 ps difference from one another at 1050 K, thus having different atomic positions/energies before the temperature is lowered to 800 K, in other words, when the atomic motion starts to freeze). This leads to a diversity in bonding at 300 K. Particularly, Ge-Ge correlations are the most sensitive and show large differences between various quenches. This is not only due to their limited number in cells containing 250 atoms for Ge deficient compositions but also due to the fact that the system finds different basins in the potential energy diagram once quenched to a local minimum (Fig. 2.2 b).

In order to study AIMD generated glasses under pressure, the cell sizes were decreased under NVT conditions and the cell pressure were calculated from the average of the stress tensors through the useful parts of the trajectories (i.e. first 4 ps of 300 K trajectories were removed). The most energetically stable structure among the individual quenches were used to apply compression. It is important to emphasize that

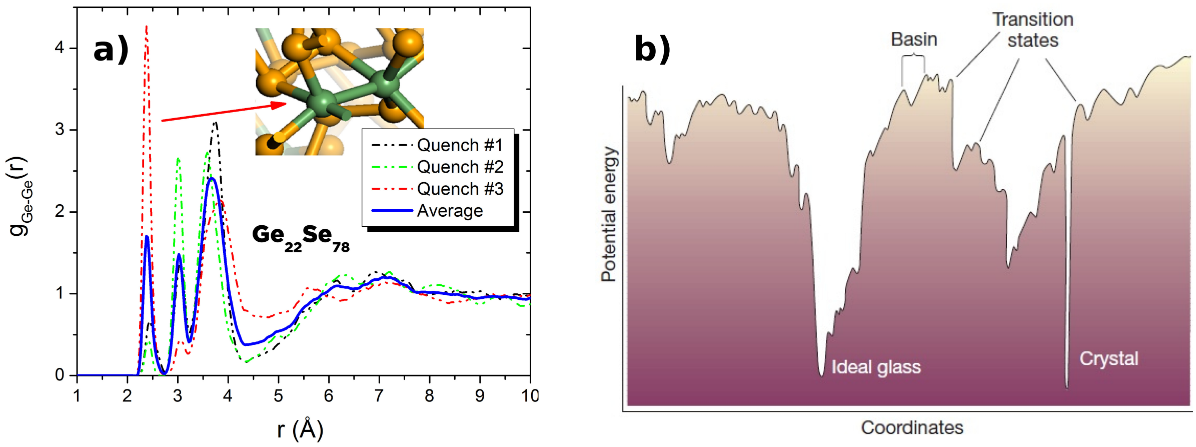

Figure 2.2: a) Ge-Ge partial pair distribution of $Ge_{22}Se_{78}$ at 300 K obtained by 3 quenches from 1050 K. The snapshot represents the Ge-Ge homopolar bonding where green atoms are Ge and yellow atoms are Se. b) Schematic Potential energy of a glass, defining basins, transition states, and minima. Adapted from [12] .

the compression of the cells were achieved in two ways: either annealed or cold compressed. In the former, the cells were compressed at 600K for 40 ps which was then followed by another 40 ps run at 300 K (within this method, a partial relaxation of the atomic structure was possible). In the latter, the compressions were directly performed at 300 K and pressure was increased using the last configurations of the previous pressure simulation. In this situation, glassy relaxation was reduced to its minimum.

2.5 Atomic Scale Simulations of Ge_xSe_{1-x}

Having built the framework of the DFT based atomic simulations, in this section, an overview to the important theoretical achievements on the AIMD modeling of Ge_xSe_{1-x} system will be given.

The first DFT based study on Ge-Se system was reported in 1995 [125]. In this work, the vibrational properties of glassy $GeSe_2$, the most studied composition of Ge-Se system, were investigated in a 63-atom model and compared to the experimental findings. The LDA scheme was used to describe the exchange-correlation energy. However, it was a non-self-consistent scheme in the sense that the electronic density of this system was approximated by a set of wave functions which were super-positioned around isolated atoms. The calculated vibrational density of states were in line with the experimental findings (Fig. 2.3). However, this work did not provide an understanding of the origin of the structural and the dynamic features that were observed. The

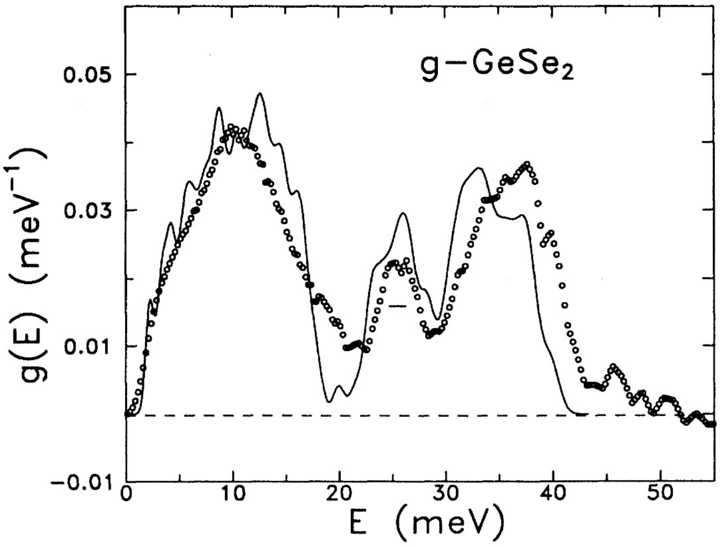

Figure 2.3: Calculated vibrational density of states (solid curve) for glassy $GeSe_2$ are compared to the experimental data (open circles). Adapted from [125] .

same authors contributed using the same theoretical model for an increased size (216 atoms) in glassy and liquid $GeSe_2$, showing some improvement in the structure [126]. In this work, the emphasis was given on the intermediate range order (IRO) and the electronic density of states, providing a discussion on the origin of the photo-induced phenomena observed in the glassy state (see section 1.4).

In 1998, the first self-consistent AIMD calculations were reported, again on the structure of liquid $GeSe_2$ [127]. Even though the improved description of the chemical bonding increased the agreement with the experimental findings,better models were still needed (Fig. 2.5). As the authors stated:

"This structural model is, nevertheless, still insufficient to explain the physical origin of the FSDP in the S_{CC} structure factor observed observed in the experiment. This defines an important open issue in the physics of disordered network-forming materials."

The issue of the absence of FSDP calculated with LDA was visited in different studies in the following years [128, 129]. In these contributions, Massobrio and co-workers compared LDA and PW-GGA schemes and showed that the choice of the exchange correlation functional was of special importance in the reproduction of the structure of liquid $GeSe_2$. The calculated structure factors using LDA and PW-GGA approaches were compared to the neutron diffraction experiments. The results showed that the (FSDP) in the Faber-Ziman structure factor of liquid $GeSe_2$ was successfully reproduced with the PW-GGA scheme. It was shown that the GGA approach gave a better

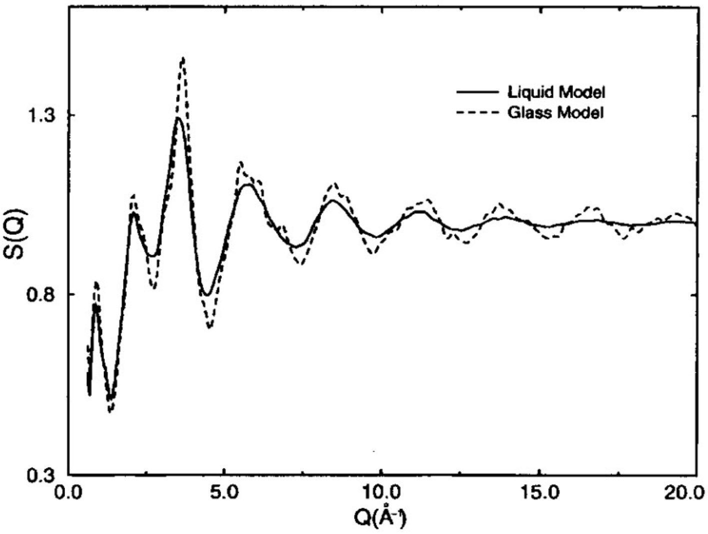

Figure 2.4: Computed structure factors for liquid (solid curve) and glassy (broken lines) $GeSe_2$. Note that the lack of the reproduction of the FSDP in $S_{CC}(\mathbf{k})$. Adapted from [126] .

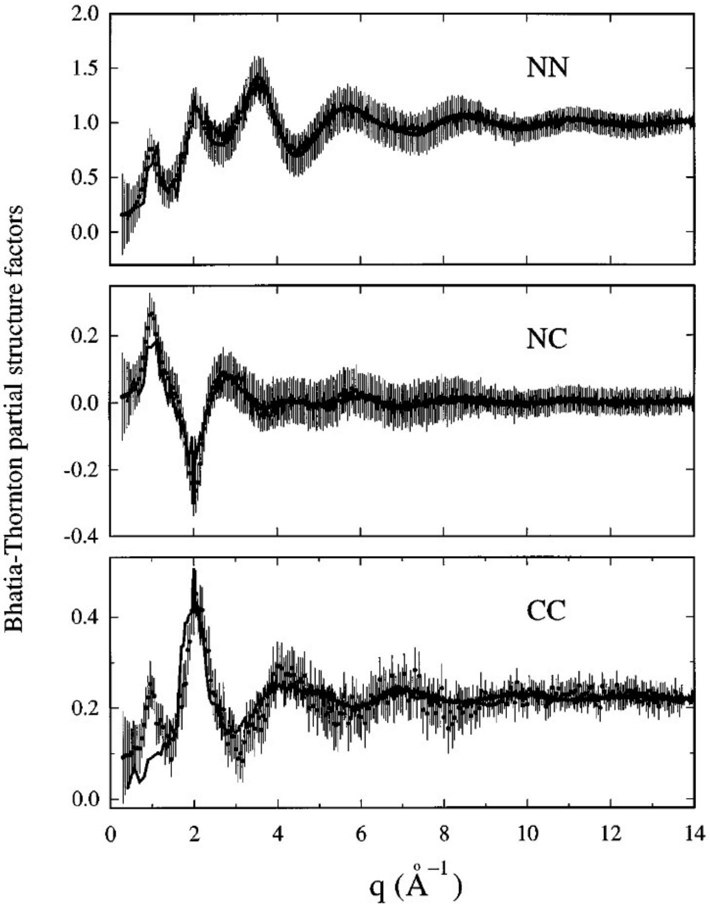

Figure 2.5: Calculated Bhatia-Thornton structure factors for liquid $GeSe_2$ (solid lines) compared to experiment (dots with error bars). Adapted from [127] .

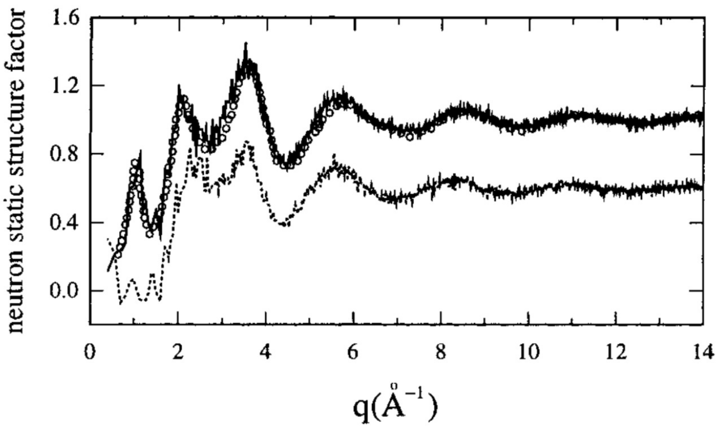

Figure 2.6: Calculated structure factors for liquid GeSe$_2$ using GGA (upper solid curve) and LDA (lower curve with dots) approaches compared to experimental findings (open circles). Adapted from [128] .

account on the ionicity of thy system reflected by the depletion of the charge density around the Ge sites and thus a larger accumulation around the Se atoms [128]. The lack of FSDP in the structure factor in LDA approach was correlated with the number of GeSe$_4$ tetrahedra, the main motifs in Ge-Se systems, due to comparable percentages of two, three, four, and five fold Ge environments [128]. These structural units were reproduced using PW-GGA functional thus giving a better agreement of the structure factor with the neutron diffraction data (Fig. 2.6). Although the GGA approach led to a better description of the short and the intermediate range ordering in liquid GeSe$_2$ over the LDA approach, the PW-GGA scheme still showed some deviations in the Ge-Ge correlations and the inter-atomic distances when compared to the experiment. This was attributed to the overestimation of the charge delocalization of the valence electrons along the bonds, in other words an overestimation of the metallic character. Therefore, the residual differences in Ge-Ge correlations exhibiting a less structured form as compared to experiments were argued to be the reason of the absence of the FSDP in the concentration concentration structure factor, S_{CC}, in the PW-GGA scheme.

In the following years, apart from GeSe$_2$, there were other contributions on the atomic simulations of Ge-Se system for different compositions such as GeSe, GeSe$_4$. After the success of the GGA approach over LDA, a next step to improve the accuracy of the simulations, in particular tackling the issue of assessing an accurate description of Ge-Ge correlations was achieved in 2009 [130]. The use of another GGA functional was proposed to overcome the difficulties faced with PW-GGA. In this published work, a BLYP functional was used as an alternative approach to PW. The authors chose to use BLYP given that this functional was giving better outcomes on properties such

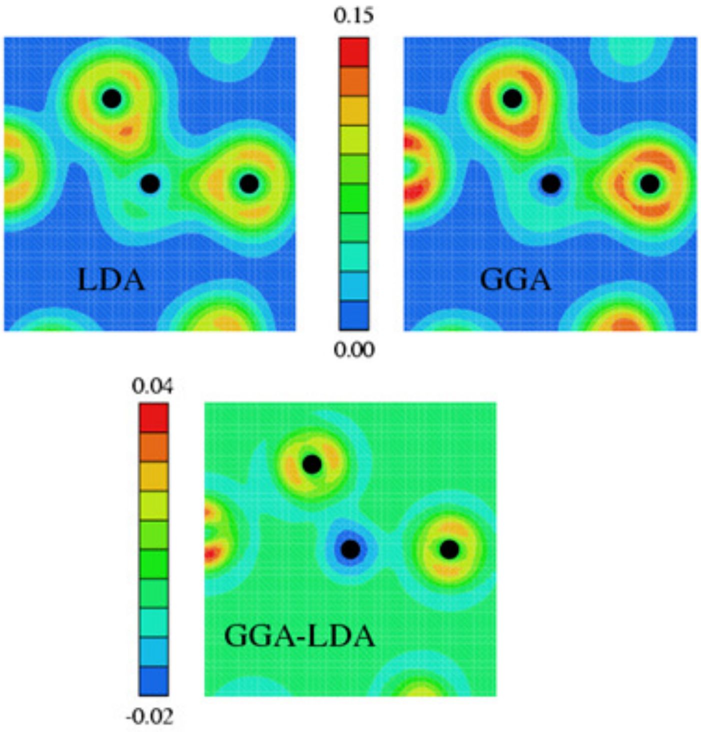

Figure 2.7: Contour plots of the electronic charge density for a tagged Se-Ge-Se trimer in liquid GeSe2 calculated using LDA (upper left) and GGA (upper right) approaches in atomic units. The lower panel shows the difference plot (GGA-LDA). Adapted from [128] .

as equilibrium geometries and vibrational frequencies [131]. In addition, the motivation of using BLYP functionals was due to the anticipation of a localized behavior of the electron density at the expense of the electronic delocalization effects that favor the metallic character, therefore casting a better picture for the Ge bonding environments as compared to PW (Fig. 2.7).

Using the same method with the previous study [129] (DFT with PW-GGA having 120 atoms at 1050 K) but this time with BLYP functional instead of PW showed some improvements in the structure of liquid $GeSe_2$. The BLYP approach made it possible to have a better accuracy in the short range order parameters such as coordination numbers, Ge-Ge correlations, tetrahedrality, and bond angle distributions over PW (Fig. 2.8). Increased tetrahedrality with better defined bond angle distribution (more symmetric around 109.5 ° for Se-Ge-Se) and were more accurate coordination numbers were obtained. The Ge-Ge correlations exhibited a better defined minimum for homopolar bonds as detected from the partial pair correlations Ge-Ge. Even though they were overestimated as compared to the experimental, they were better than those attained with the PW scheme, as expected. It was reported that due to the increased tetrahedrality, the diffusion coefficients were lower in the case of BLYP scheme. How-

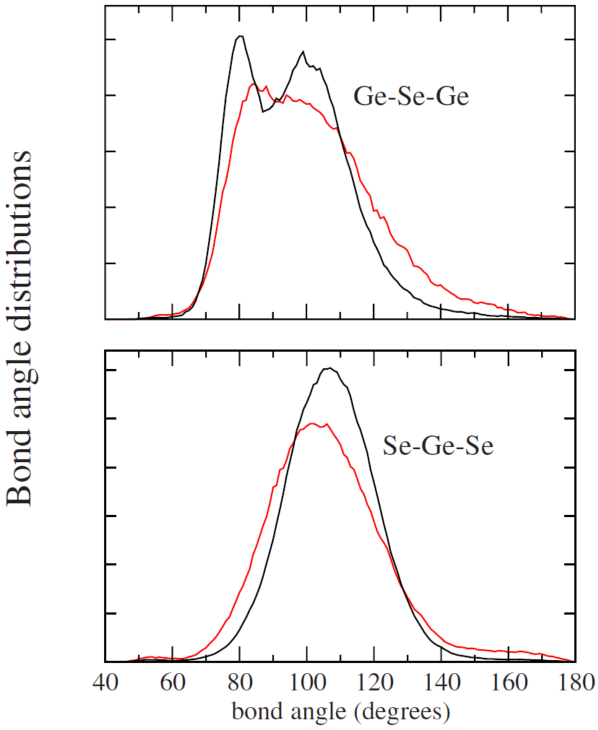

Figure 2.8: Ge-Se-Ge (upper) and Se-Ge-Se (lower) Bond angle distributions of liquid $GeSe_2$ with BLYP (black) and PW (red) schemes. Adapted from [130] .

ever, weak improvements were reported for the reciprocal space properties and the issue of intermediate range ordering remained somewhat unclear. Nevertheless, this work showed that the DFT models with the BLYP scheme yield better description of the structure of liquid $GeSe_2$. The same theoretical framework was used to study the effect of the BLYP functional on amorphous $GeSe_2$ [132, 133] and improvements of the short and intermediate range order were also reported in these studies.

Table 2.1: Calculated coordination numbers with PW and BLYP schemes compared to neutron diffraction experiment [70]. Note the bimodal distribution in the Ge-Se-Ge due to ES and CS contribution. Reproduced from [130].

	n_{Ge}	n_{Se}	n
BLYP	3.77 ± 0.02	2.11 ± 0.02	2.66 ± 0.02
PW	3.80 ± 0.02	2.25 ± 0.02	2.77 ± 0.02
Experiment	3.75 ± 0.3	1.98 ± 0.15	2.77 ± 0.20

Following the developments in the description of $GeSe_2$ with the use of the BLYP scheme, a step further at that time was to test the effect of system size. The same BLYP scheme used for 120 atoms was compared to a larger ensemble containing 480 atoms [134]. It was reported that the computation time was 10 times longer for the latter. This worked showed no drastic changes in the main features of the network. Nevertheless, increased chemical order in the short range and a slightly more accurate results in the small q wave-vectors of the structure factors were obtained.

In the same year, a note reported on the effect of residual pressure on the structure of glassy $GeSe_2$ using the same 120 atom BLYP DFT framework [135]. In this study, the authors compared the previous results with the extensively relaxed structures having less than 0.1 GPa internal stress within the simulation cells. The total simulation time was more than 500 ps at different temperatures. It was reported that lowering the residual pressure gives better agreement with the experiments, particularly for the partial coordination numbers and $S_{\mathrm{CC}}(\mathbf{k})$.

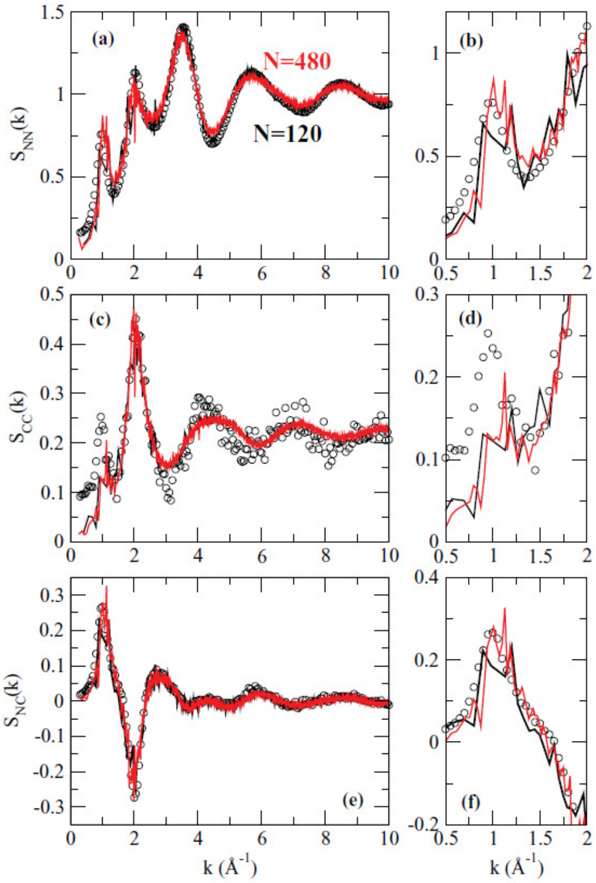

Figure 2.9: Partial Bhatia-Thornton structure factors calculated with 120 atoms (black) and 480 atoms (red) are compared experimental results (open circles). The right panels zoom to the low wave vector region of the spectrum. Adapted from [134].

Turning back from the theoretical studies on $GeSe_2$ to other compositions in the Ge-Se system, it is convenient to start with the stoichiometric compound GeSe. Unlike the complex bonding in $GeSe_2$, GeSe is rather more straightforward to describe in such a way that the structure factor does not exhibit the FSDP, which was argued to be correlated with the intermediate range order IRO [74], in contrast to what is observed in $GeSe_2$. Therefore, the local structure of the system is sufficient to describe the bonding nature. In early 2000, the liquid structure and dynamics of GeSe was investigated using DFT based molecular dynamics simulations [136, 137]. In these studies, it was reported that the structure consists of $GeSe_3$ and $SeGe_3$ units. Even though the reciprocal space properties compared well with the experiments, some discrepancies were reported in the pair distribution functions. About a decade after, the structure of GeSe liquid was revisited with the use of three different exchange-correlation functionals; PW91, PBE, and BLYP [138]. In this study, the BLYP scheme showed a higher number of tetrahedra with better account on Ge-Ge, which in turn resulted in lower diffusion coefficients (Fig. 2.10).

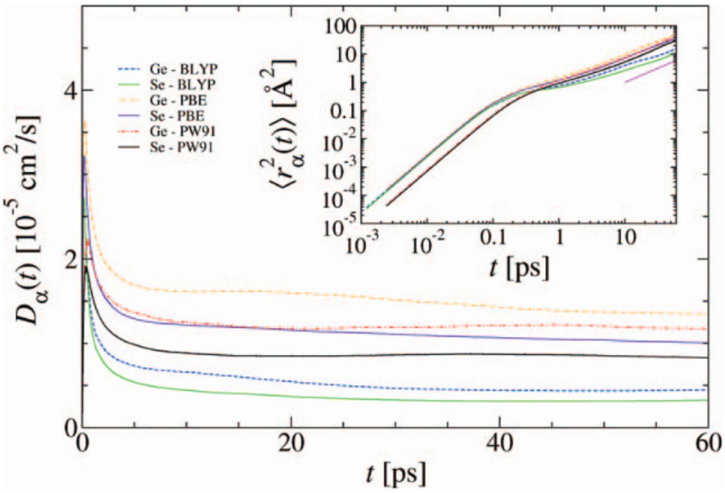

Figure 2.10: Comparison of calculated diffusion coefficients of liquid GeSe (Se and Ge species) using BLYP, PBE, and PW schemes. Adapted from [138].

Another interesting composition is $GeSe_4$ due to the fact that the network is optimally rigid (i.e. isostatic composition). The liquid structure of this composition was studied in 1998 [139]. The FSDP structure factor was well reproduced showing the IRO correlations. It was reported that the microstructure consists of $GeSe_4$ tetrahedra interconnected with Se chains or atoms. As for the IRO connections, nearly an equal amount of edge and corner sharing tetrahedral units were observed (49% and 51%, respectively). In the following years, glassy structure of $GeSe_4$ was compared to $SiSe_4$ using both AIMD and neutron diffraction [140]. The real and reciprocal space properties gave a satisfactory reproduction of experimental structural features, $S(\mathbf{k})$ and $g(r)$. The authors argued that the ES and CS connections of tetrahedra form three distinct motifs, and give giving rise to structural variability in Ge_xSe_{1-x} and Si_xSe_{1-x} systems. A more recent study compared the *ab initio* calculated nuclear magnetic resonance (NMR) chemical shifts of $GeSe_2$ and $GeSe_4$ with the experimental counterparts

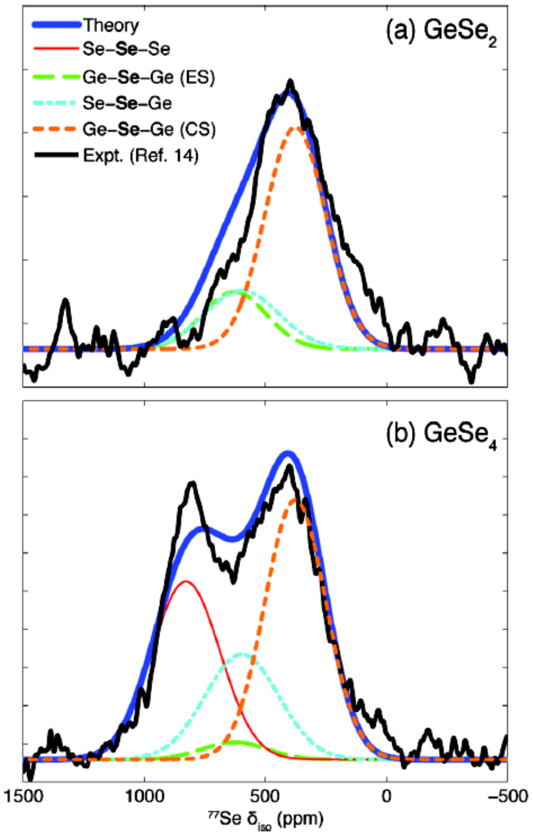

Figure 2.11: Calculated NMR chemical shifts in $GeSe_2$ (upper) and $GeSe_4$ (lower) compared to experiment. Adapted from [141].

[141]. This study showed contradictions with the earlier proposed phase separation theory [44] of the $GeSe_4$ network in which the system consists of $GeSe_2$ motifs and chains of Se. However, the results showed 20% of Se atoms are connected in Se-Se-Ge form, enhancing the cross linking of Se-Se-Se chains and Ge-Se-Ge tetrahedral units.

A complementary study using PBE and PW functionals confirmed the coexistence of $GeSe_4$ tetrahedra with Se_n chains where n reaches up to 12 in the PBE scheme [142]. It was reported again that the phase separation model does not apply to the network of $GeSe_4$ due to the important presence of Ge-Se-Se-Ge connections.

Size effects of the simulations were also tested for glassy $GeSe_4$ and GeS_4 compounds [143]. BLYP scheme was employed for the AIMD for 120 and 480 atom systems. In contrast to what is observed for liquid $GeSe_2$, the system size showed rather important differences in the Se or S environment. The nearest neighbor distances showed large discrepancies for the 120 and 480 atom cases. In particular, homopolar Ge-Ge bonds were found in 480 atoms, unlike the 120-atom case (Fig. 2.12). Moreover, it was also reported that GeS_4 shows a more intense FSDP as compared to $GeSe_4$ and this was attributed due to the fact that the former has larger size rings.

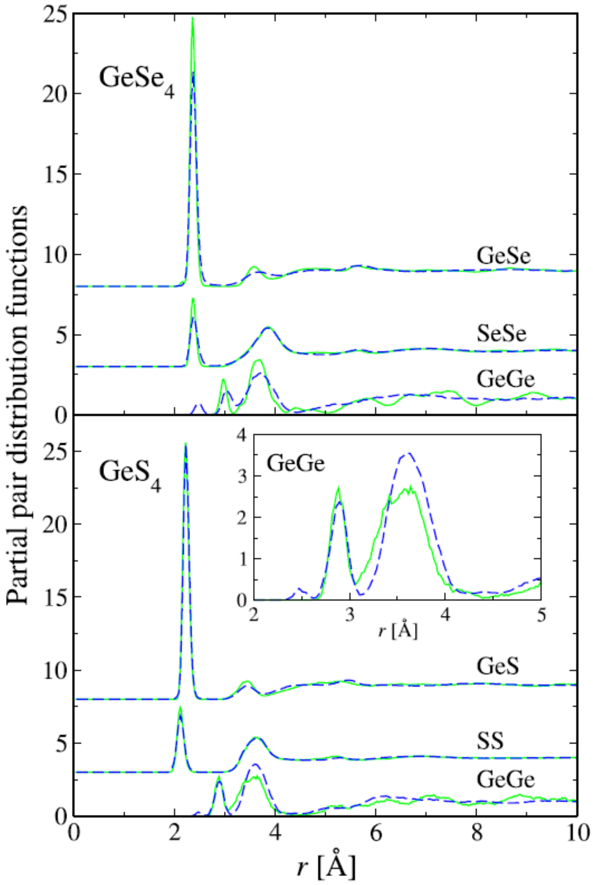

Figure 2.12: Computed partial pair distribution functions for $GeSe_4$ (upper) and GeS_4 (lower) for 120 (green continuous lines) and for 480 (blue broken lines). The inset highlights the Ge-Ge correlations and homopolar bonds observed in 480 atoms case. Adapted from [143].

Obtaining satisfactory results through years of methodological studies improving the structural models in Ge-Se system made it possible to investigate further the link between structural properties and the network connectivity. As explained in the earlier sections, Ge_xSe_{1-x} system progressively stiffens as the Ge concentration is increased due to the increased the average coordination number and the rigidity threshold is observed at $Ge_{20}Se_{80}$, where $< r >= 2.4$ and $n_d = n_c$. In what follows, the recent studies with the purpose of providing a general picture for the flexible to rigid transitions in Ge_xSe_{1-x} system will be mentioned.

The network properties of glassy Ge_xSe_{1-x} along with a set of oxide and chalcogenide glasses were investigated with the use of well established DFT based methods and BLYP functionals, in conjunction with rigidity theory [144]. One of the main outcomes of this study can be given as the role of Ge composition, in other words the network rigidity, on the variations of the angular constraints around Ge while those of Se almost remains the same. Furthermore, it was reported that the angles involv-

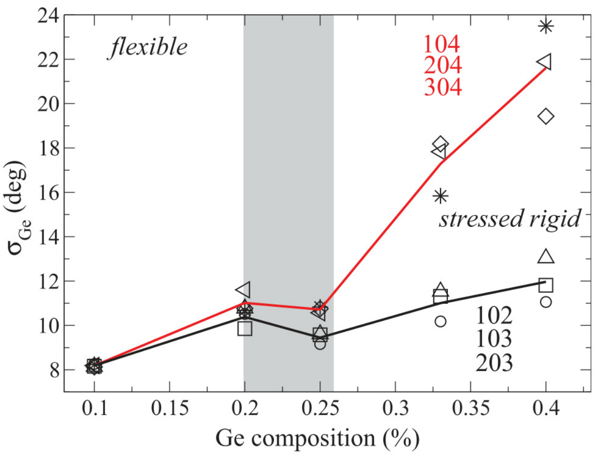

Figure 2.13: Comparison of the standard deviation of the Ge centered partial bond angle distributions, σ_{Ge}, within tetrahedra as a function of composition. The shaded zone corresponds to the reported IP phase for Ge-Se system [50]. Adapted from [144].

ing the fourth neighbor around germanium atoms change once the system enters the stressed rigid zone. In a more recent study, structural, electronic, and vibrational properties of $\mathrm{Ge_xSe_{1-x}}$ were investigated (120 atoms, BLYP functionals) [145]. Flexible, isostatic, and stressed rigid compositions were studied, with the focus given on the effect of Ge composition on the various properties of the system. The real and reciprocal space properties of the simulations compared well with the available experiments. Especially the concentration-concentration structure factor S_{CC} agreed well with $GeSe_2$. The increase in the height of FSDP in the number-number structure factor, S_{NN} with increasing Ge content was well reproduced (Fig 2.15). Furthermore, the validity of certain simple pair models such as random covalent network, chemically ordered network, chain-crossing etc.) was investigated. It was reported that none of those models were able to describe the network properties such as the bond statistics of bonding defects, in particular Ge-Ge homopolars. Another interesting result of this study was given as the atomic constraints analysis. Of special importance is the breaking of the angular constraints in the stressed rigid phases (Fig. 2.13), for this study it was $GeSe_2$ and Ge_2Se_3, in order to accommodate the stress caused by the increased cross-linking.

2.6 Data Processing

In this section, the details of the postprocessing of our simulations are given. The numerical analyses were performed by FORTRAN codes and also the Nmoldyn [146] program package. The graphical representations of the snapshots of the atomic trajec-

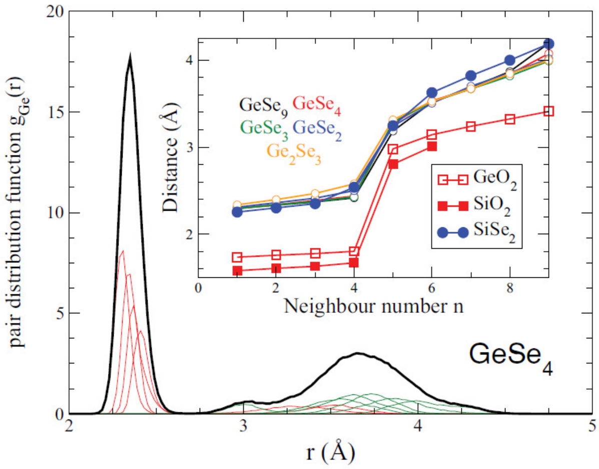

Figure 2.14: Neighbor distribution as a function of distance around a central Ge atom for glassy GeSe$_4$ (red: neighbors 1-4, green : neighbors 5-9). The black curve is the sum of all neighbor contributions. The inset shows the peak positions of each neighbor for different chalcogenide and oxide compounds. Adapted from [144].

tories were generated by using VMD [147] program packages.

2.6.1 Radial Distribution Function

Since the atoms in an amorphous materials do not have fixed positions as compared to their crystalline counterparts, what we have is more of a statistical information when it comes to finding the position of atoms. The radial distribution function (RDF), $g(r)$, is the probability of finding an atom within a spherical shell centered on agiven atom and having a radius r and a thickness δr :

$$g(r) = \rho 4\pi r^2 dr \tag{2.6.1}$$

, where ρ isdensity, i.e. the density of atoms per unit volume. The integral of $\rho 4\pi r^2 g(r)$ for a certain r gives the average coordination number over a particular distance, i.e. the first minimum of the $g(r)$ curve is taken to find the first shell coordination number.

In a system having multiple components, one can find the same probability of the individual pairs using partial pair-distribution function. Consider a system containing α and β species. One can use the following formulation to find the β atoms around α,

$$g_{\alpha\beta}(r) = \frac{N}{\rho N_\alpha N_\beta} \sum_{i=1}^{N_\alpha} \sum_{k=1}^{N_\beta} \langle \delta(r - |r_k - r_i|) \rangle \tag{2.6.2}$$

where N is the total number of atoms while N_α and N_β are the corresponding numbers of the different chemical species.

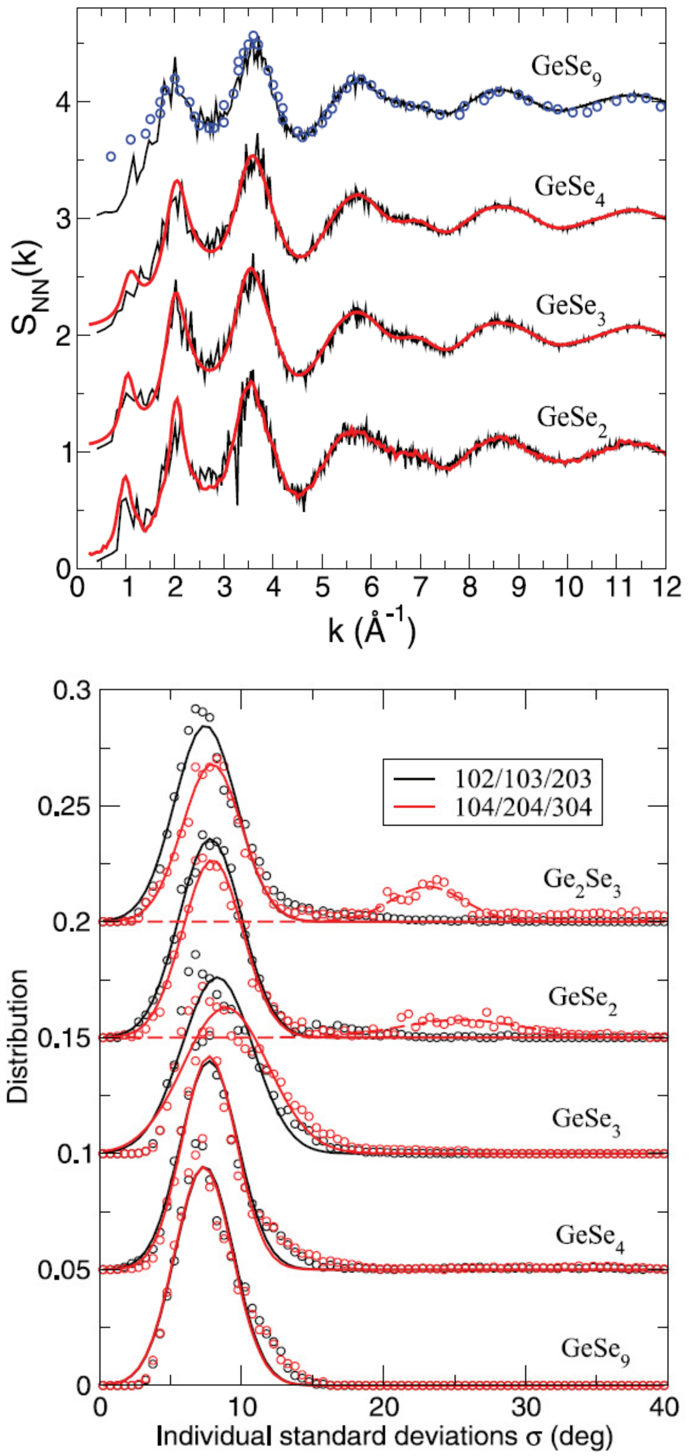

Figure 2.15: Calculated total structure factors of different Ge$_x$Se$_{1-x}$ compounds (black) are compared with the experimental results(red lines and blue circles) in the upper panel. The lower panel shows the distribution of the standard deviation of the Ge centered angular constraints. The continuous lines represent the Gaussian fits to the data points. The broken curves are the fits to calculate the population of the broken bond-bending constraints for the stressed rigid compositions. Reproduced from [145].

2.6.2 Structure Factor

Moving from real space to reciprocal space, the static structure factor of a system containing N atoms is described as:

$$S(\mathbf{k}) = \frac{1}{N}\langle\sum_{i=1}^{N}\sum_{j=1}^{N} exp(-i\mathbf{k}\mathbf{r}_i)exp(-i\mathbf{k}\mathbf{r}_j)\rangle \tag{2.6.3}$$

,where **k** is the reciprocal space vector.

An alternative way of describing the static structure factor is the Fourier transformation of the RDF;

$$S(\mathbf{k}) = 1 + 4\pi\rho\int_{0}^{\infty}\mathbf{r}^2 g(r)\frac{sin(\mathbf{kr})}{\mathbf{kr}}dr \tag{2.6.4}$$

The total structure factor of systems having different chemical species can be obtained by the Faber-Ziman relation:

$$S(\mathbf{k}) = \sum_{\alpha,\beta} c_\alpha b_\alpha c_\beta b_\beta \left[S_{\alpha\beta}^{\mathrm{FZ}}(\mathbf{k}) - 1\right] \tag{2.6.5}$$

,where $S_{\alpha\beta}^{\mathrm{FZ}}$ is the partial Faber-Ziman structure factor which an be obtained from the Fourier relation of the partial PDF. Here c_α and c_β represent the concentrations while b_α and b_β represent the coherent scattering length of the chemical species. Another approach to describe structure factor is using the Bhatia-Thornton formalism. For a case of binary AB$_\mathrm{x}$ system, the total structure factor is given by:

$$S(\mathbf{k}) = \frac{\langle b\rangle^2 S_{\mathrm{NN}}(\mathbf{k}) + 2\langle b\rangle(b_A - b_B)S_{\mathrm{NC}}(\mathbf{k}) + (b_A - b_B)^2 S_{\mathrm{CC}}(\mathbf{k})}{\langle b\rangle^2} - \frac{(c_A b_A^2 + c_B b_B^2)}{\langle b\rangle^2} + 1 \tag{2.6.6}$$

, where $\langle b\rangle = c_A b_A + c_B b_B$ with c_A and b_A representing the concentration and the scattering length of species A. Bhatia-Thornton partial structure factors $S_{\mathrm{NN}}(\mathbf{k})$ (number-number), $S_{\mathrm{NC}}(\mathbf{k})$ (number-concentration) and $S_{\mathrm{CC}}(\mathbf{k})$ (concentration-concentration) which are experimentally accessible using isotope substitution in neutron diffraction. For the Ge-Se system, the partial Bhatia-Thornton structure factors can be obtained by linear combination of the Faber-Ziman partial structure factors $S_{\mathrm{GeGe}}^{\mathrm{FZ}}(\mathbf{k})$, $S_{\mathrm{SeSe}}^{\mathrm{FZ}}(\mathbf{k})$, and $S_{\mathrm{GeSe}}^{\mathrm{FZ}}(\mathbf{k})$;

$$S_{\mathrm{NN}}(\mathbf{k}) = c_{\mathrm{Ge}}c_{\mathrm{Ge}}S_{\mathrm{GeGe}}^{\mathrm{FZ}}(\mathbf{k}) + c_{\mathrm{Se}}c_{\mathrm{Se}}S_{\mathrm{SeSe}}^{\mathrm{FZ}}(\mathbf{k}) + 2c_{\mathrm{Ge}}c_{\mathrm{Se}}S_{\mathrm{GeSe}}^{\mathrm{FZ}}(\mathbf{k}) \tag{2.6.7}$$

$$S_{\mathrm{NC}}(\mathbf{k}) = c_{\mathrm{Ge}}c_{\mathrm{Se}}[c_{\mathrm{Ge}}(S^{\mathrm{FZ}}_{\mathrm{GeGe}}(\mathbf{k}) - S^{\mathrm{FZ}}_{\mathrm{GeSe}}(\mathbf{k})) \\ -c_{\mathrm{Se}}(S^{\mathrm{FZ}}_{\mathrm{SeSe}}(\mathbf{k}) - S^{\mathrm{FZ}}_{\mathrm{GeSe}}(\mathbf{k}))]. \qquad (2.6.8)$$

$$S_{\mathrm{CC}}(\mathbf{k}) \;=\; c_{\mathrm{Ge}}c_{\mathrm{Se}}\{1 + c_{\mathrm{Ge}}c_{\mathrm{Se}}[(S^{\mathrm{FZ}}_{\mathrm{GeGe}}(\mathbf{k}) - S^{\mathrm{FZ}}_{\mathrm{GeSe}}(\mathbf{k})) \\ +(S^{\mathrm{FZ}}_{\mathrm{SeSe}}(\mathbf{k}) - S^{\mathrm{FZ}}_{\mathrm{GeSe}}(\mathbf{k}))]\}. \qquad (2.6.9)$$

where c_{Ge} and c_{Se} represent the Ge and Se concentrations, respectively. Due to very close values of the coherent scattering length of the chemical species Ge and Se (b_{Ge}=8.185 fm, b_{Se}=7.97 fm) and to the limited range of variation of $S_{\mathrm{NC}}(\mathbf{k})$ and $S_{\mathrm{CC}}(\mathbf{k})$, $S_{\mathrm{NN}}(\mathbf{k})$ is a very good approximation of the total structure factor, i.e. $|S_{\mathrm{T}}(\mathbf{k}) - S_{\mathrm{NN}}(\mathbf{k})| < 0.025$. Therefore, the considerations developed hereafter on $S_{\mathrm{NN}}(\mathbf{k})$ apply equally well to the total structure factor.

Using AIMD generated atomic trajectories, structure factor can be obtained in either way. Experimentally, structure factors can be obtained using neutron, X-ray, and electron diffraction. Comparing the structure factor calculated through the AIMD atomic trajectories with experiments is a good way to verify the robustness of the simulations.

2.6.3 Bond Angle Distribution

In network forming glasses, bond angle distribution (BAD) analyses could provide important information of the short range (i.e. tetrahedra) as well as of the medium range (connection of the structural units) ordering. In order to calculate the angle between two bonds, one should first define the bonding of the species with a meaningful cut-off value. Typically, the cut-off distance for BAD analyses, $r_{cut-off}$, are taken from the first minimum of the $g(r)$ (for this thesis, a value around 2.8-2.9 Å). For a given three atoms A, B, and C, the angle θ_{ABC} can be defined as;

$$\theta_{ABC} = arccos\left(\frac{(\mathbf{r_a} - \mathbf{r_b}) \cdot (\mathbf{r_a} - \mathbf{r_b})}{|\mathbf{r_a} - \mathbf{r_b}| \cdot |\mathbf{r_c} - \mathbf{r_b}|}\right) \qquad (2.6.10)$$

2.6.4 Constraint Counting

As mentioned in the previous chapter, the total number of constraints is a sum of both bond stretching (BS) and bond bending (BB) interactions of atoms. In MD based constraint counting method, we monitor the standard deviations of the atomic motions to check if the distances and/or angles deviate around a fixed value with small spatial excursions manifested by the restoring forces, in order to determine a particular constraint being intact. Fig.2.16 shows schematically the criterion of determination of intact and broken constraints. The distribution of the distances and angles of different neighbors are used in assigning the corresponding standard deviation of stretching σ_r or bending σ_b. Note that the standard deviation is an arbitrary number and depends strongly on temperature and pressure [144, 148]. Fig.2.17 illustrates the enumeration of neighbors. An atom is tagged as the central atom having the label 0, and depending on the distance between this central atom and the surrounding neighbors, they are labeled in an incremental fashion. By the same convention, in angular notation we examine the angle constituted by neighbors of the central atom. In Fig.2.17 one can see the illustration of that the angle number 102 stands for the angle between the first two closest neighbors of a central atom in a tetrahedron. Fig.2.18 provides an example of counting BB constraints in AIMD generated GeSe$_4$. In this analysis, σ_b was taken to

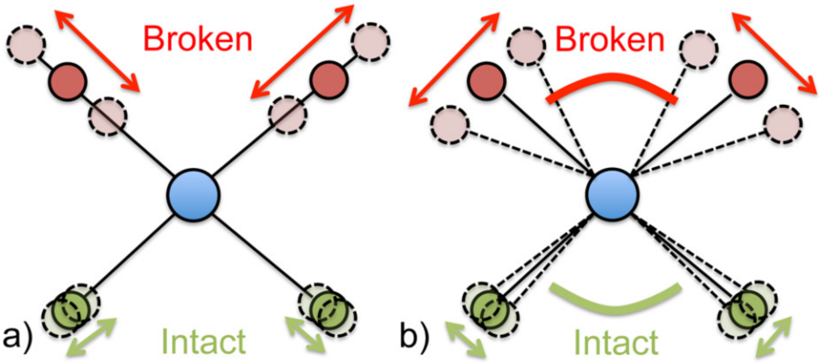

Figure 2.16: Schematics of MD based constraints counting method. a) Bond stretching b) bond bending constraints. The large excursions are set to be broken while the small excursions are enumerated as intact constraints. Adapted from[30].

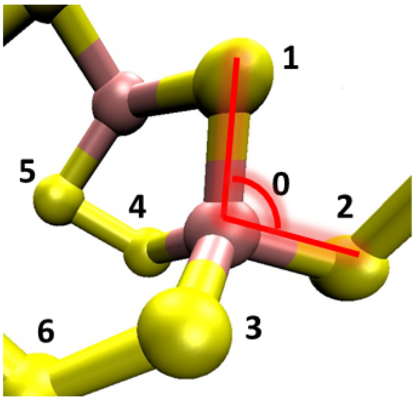

Figure 2.17: Enumerating the neighbors of a central atom labeled as 0. The angle that correspond to 102 is emphasized in red.

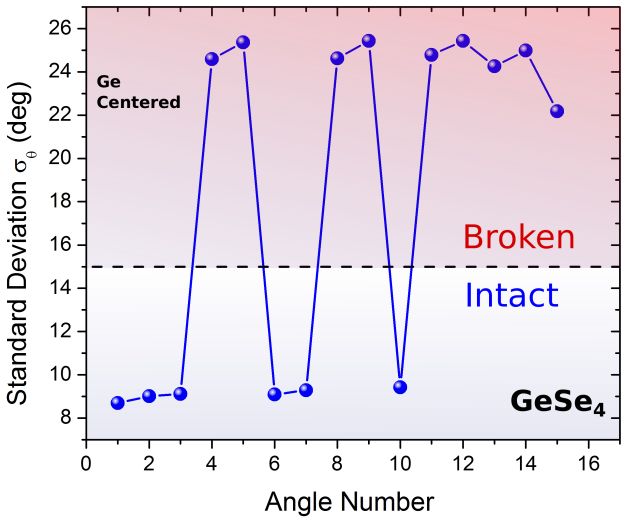

Figure 2.18: Standard deviation σ_θ of Ge centered partial bond angle distributions as a function of angle number. The horizontal dashed line indicates the fixed angular cut-off for σ_θ .

be 15° (the horizontal dashed line). One can identify 6 different angle numbers maintaining their average angular excursion throughout the whole simulation below the cut-off value, thus, they are counted as intact BB constraints. Consequently, we have 6 bond angles appearing to be intact, namely; 102, 103, 104, 203, 204, and 304. Yet only 5 of these angles are independent since the sixth one can be determined from the value of the 5 others. Therefore, we conclude that there are 5 BB constraints for Ge. Similarly, when the same neighbor analysis is applied to radial distributions, one can count the BS constraints.

2.6.5 Mean Square Displacement

In order to calculate atomic diffusion the simulation box, we first calculate the mean-square displacement (MSD) $\langle r_\alpha^2(t)\rangle$ of the chemical species α from the atomic trajectories of our simulations using:

$$\langle r_\alpha^2(t)\rangle = \frac{1}{N_\alpha}\langle\sum_{i=1}^{N_\alpha}|\mathbf{r}_i(t)-\mathbf{r}_i(0)|^2\rangle \tag{2.6.11}$$

where $\mathbf{r}_i(t)$ is the coordinate of the ith particle of the chemical species α at time t and N_α is the total number of particles of type α. Fig.2.19 illustrates the MSD behavior of a typical Lennard-Jones liquid [149] as a function of time. For high temperature, at the very early times, a ballistic motion of particles is manifested by a quadratic time dependence of the MSD, $\langle r_\alpha^2(t)\rangle \sim t^2$. This rapid motion of the tagged particles gives way to a linear dependence at longer times, in other words the diffusive behavior. As the temperature of the system is decreased, the atomic mobility and therefore the MSD is decreased. However, at the intermediate time scales, a plateau starts to build up as the temperature is decreased. This slow down in the atomic mobility corresponds to what is called the caging regime, in which the tagged particles are trapped by the surrounding neighbors and the mobility is largely diminished until the the particle leaves the cage and the MSD starts to increase again.

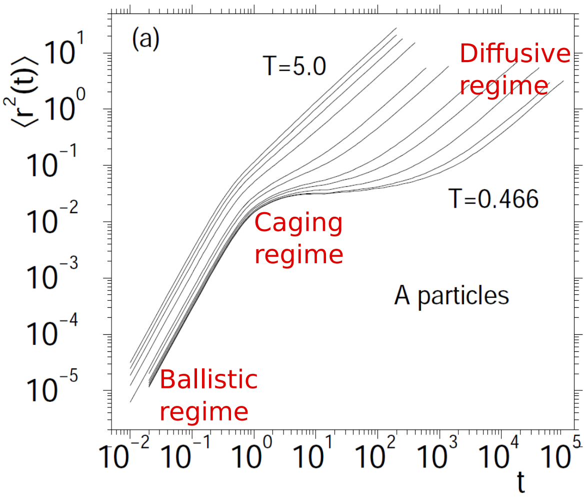

Figure 2.19: Time dependence of mean-square-displacement in a Lennard-Jones liquid at different temperatures. Three different mobility regimes are observed. Here the longest time attained in simulation corresponds to 30 ns in real time. Reproduced from[149].

Once the diffusive regime is reached at the long time limit, as seen from the log-log plot (Fig. 2.19), the diffusivity D_α of the chemical species α is given by the Einstein relation,

$$D_\alpha = \frac{< r_\alpha^2(t) >}{6t} \tag{2.6.12}$$

2.6.6 Intermediate Scattering Function

Additional insight into the real space dynamics and the transport mechanisms can be provided by the Van Hove correlation function [150, 151] which is a density-time correlation of particles. Given that there is a particle at the origin at time $t = 0$, the Van

Hove correlation is given as

$$G(\mathbf{r},t) = \frac{1}{N}\langle\sum_{i=1}^{N}\delta(\mathbf{r}+\mathbf{r}_i(0)-\mathbf{r}_j(t))\rangle \tag{2.6.13}$$

The van Hove correlation function can be divided into a self and a distinct part for the cases $i = j$ and $i \neq j$, respectively. The former gives indication about an average motion whereas the latter is directly related to unlike particle correlations that reduces to the static pair correlation function $g(r)$ at $t = 0$ [152]. For the self part, the probability of finding a particle of species α at the position **r** at time t is given by:

$$4\pi r^2 G_s^{\alpha}(r,t) = \frac{1}{N_\alpha}\langle\sum_{i=1}^{N_\alpha}\delta(\mathbf{r}+\mathbf{r}_i(0)-\mathbf{r}_i(t))\rangle \tag{2.6.14}$$

and $4\pi r^2$ results from the spherical integration of an isotropic media.

From MD simulations, the self intermediate scattering function $F(k,t)$ for the species α is:

$$F_s^{\alpha}(k,t) = \frac{1}{N_\alpha}\sum_{j=1}^{N_\alpha}\exp(i\mathbf{k}\cdot(\mathbf{r}_j(t)-\mathbf{r}_j(0))) \tag{2.6.15}$$

which is also the Fourier transform [152] of the Van Hove correlation function defined previously. Note that $F(k,t)$ can be also calculated directly. Fig.2.20 shows the time dependence of a Lennard-Jones mixture at the reciprocal vector corresponding the first peak position of the static structure factor of the same system. At high temperature, since atoms are more mobile, a ballistic type regime is followed by an exponential decay. As the temperature is lowered, a plateau builds up at the intermediate time scale associated with the cage motion. At longer times, a stretched exponent (Kohlrausch) behavior is observed, corresponding the particles leaving the cage.

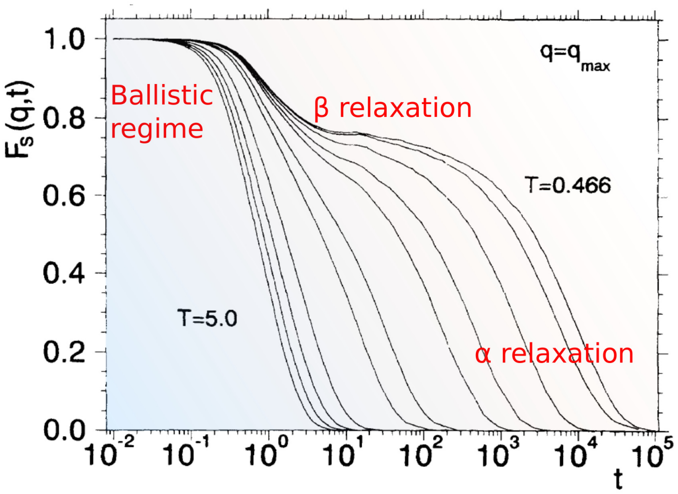

Figure 2.20: Self part of the intermediate scattering function for a Lennard-Jones liquid. Here the longest time attained in simulation corresponds to 30 ns in real time. Reproduced from [153].

Chapter 3

Experimental Techniques

Abstract

The atomic structure of amorphous systems can be studied by means of various different methods. Among them, synchrotron radiation is an excellent tool to probe the structure of condensed matter, thanks to the high brightness of the third generation light sources. In this respect, we performed X-ray absorption spectroscopy (XAS) along with simultaneous X-ray diffraction (XRD) experiments of $\mathrm{Ge_xSe_{1-x}}$ under pressure at BM23 at the European Synchrotron Radiation Facility (ESRF), Grenoble, France. In this chapter, a brief overview to the XAS theory will be given first. In what follows, experimental details of our XAS measurements including the high pressure equipment and the data analysis will be explained. The remaining sections of the chapter will provide information regarding the sample preparation and characterization with the use of energy dispersive X-ray spectroscopy (EDXS).

3.1 Phenomenology of XAS

XAS is one of the most novel characterization techniques to study local atomic structure in condensed matter science. In XAS, the probability of the absorption of an incident beam by a sample is measured. Depending on how the X-ray beams are absorbed near and above the core shell binding energy levels, one can extract crucial information on the coordination number and geometry, oxidation state, and inter-atomic distances. Therefore, XAS measurements are used in numerous scientific fields including material science, chemistry, biology and condensed matter physics.

When a sample is subjected to incident X-ray beams with a range of energy, the cross sectional absorbance decreases monotonously with increasing energy until an abrupt change at a distinct energy for each element, what is called the absorption edge. The absorption edge can be defined as the discontinuity in the linear absorption coefficient that takes place when the incident beam reaches an energy that is equal to the energy required to knock a core shell electron out of its orbital. Each absorption edge is named depending on the binding energy of atomic subshell such as K, L, M, and N which correspond to different quantum states.

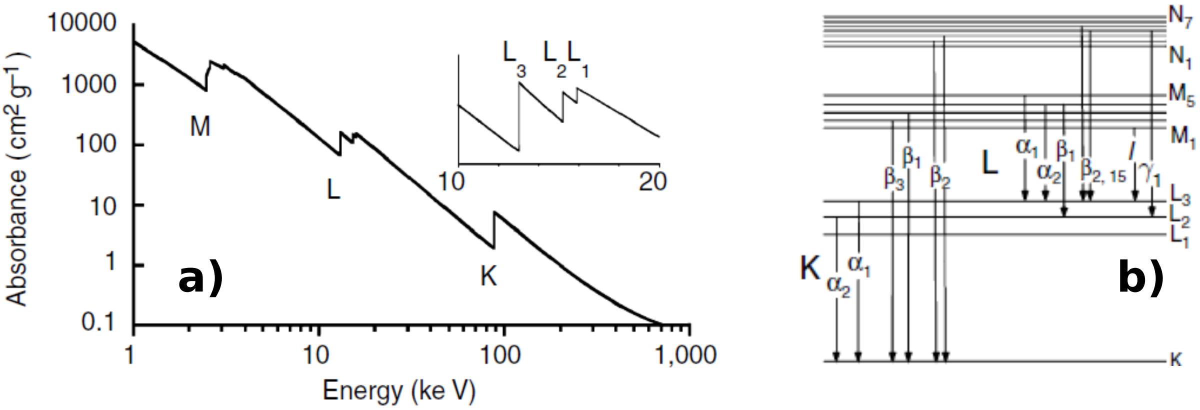

Figure 3.1: a) X-ray absorption spectrum of Pb element. Here K, L, and M radiations refer to different quantum number n being 1, 2, and 3,respectively. The inset shows L subshell radiations corresponding to $2s$ and $2p$ orbitals. b) X-ray emission lines of different shells. Adapted from [154]

.

In XAS, one measures the absorption coefficient $\mu(E)$ as a function incident X-ray radiation energy. A material absorbs the X-rays according to the following relation:

$$I = I_0 e^{-\mu t} \tag{3.1.1}$$

where I_0 is the incident beam intensity, t is thickness of the sample, μ is absorption coefficient, and I is the transmitted intensity through the sample. The absorption coefficient strongly depends on the atomic number Z and the incident X-ray energy E. These feature of absorbency enable good contrast between high Z and low Z elements allowing different applications, particularly for medical imaging purposes.

X-ray absorption is a process of transitions in different states. As an incident beam having an energy of $\hbar\omega$ hits a core electron of an atom, the photo-electron that is ejected has a momentum of $\hbar k$ where k is the wave vector and is given by :

$$k = \frac{2\pi}{\hbar}\sqrt{2m(\hbar\omega - E_b)} \tag{3.1.2}$$

where E_b accounts for the binding energy of an electron in a particular quantum shell. The variations of the kinetic energy of the photo-electron is manifested by different type of scattering interactions. A closer look into Fig. 3.1 a) reflects interesting interactions of the incident beam with the sample following diverse paths. Fig. 3.2 shows the X-ray Absorption Near Edge (XANES) and Extended X-ray Absorption Fine Structure (EXAFS) parts of the spectra at Se K edge for $Ge_{10}Se_{90}$.

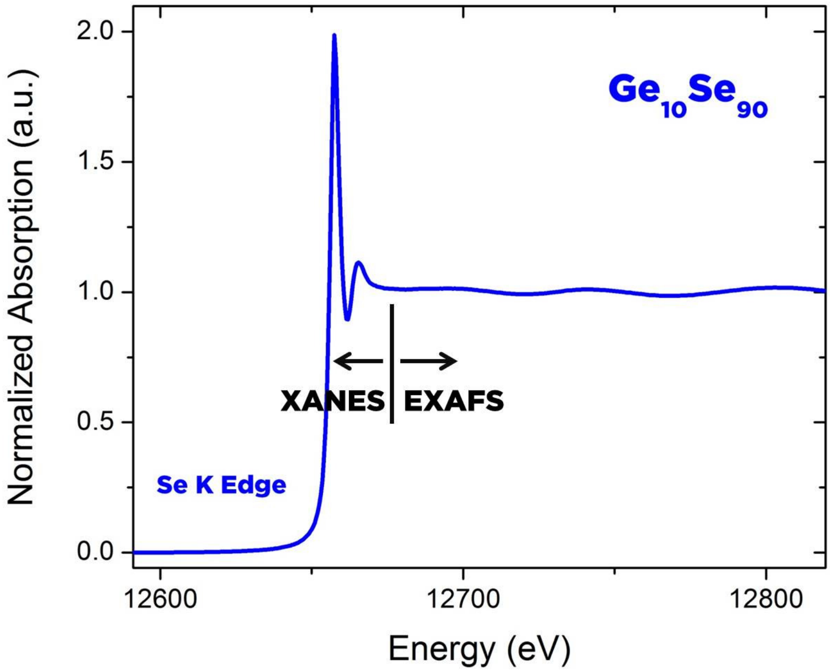

Figure 3.2: Se K edge absorption spectrum of $Ge_{10}Se_{90}$ showing the XANES (from the edge to $\sim$ 12.68 keV) and EXAFS parts separated by the vertical line.

3.2 XANES

XANES part of the absorption spectra corresponds to an energy range of about $\sim$ 50 meV above the absorption edge where the scattered photo-electrons from the neighboring atoms have low kinetic energy. The absorption edge is generally taken as the maximum in the first derivative of energy or by convention the half height of the peak. The unoccupied states are filled by the photo-electrons in this region, which gives rise to the change in the charge density of the initial and the final states. This feature of XANES is used in to distinguish the local coordination chemistry and the oxidation states of a selected absorber. Due to the complicated multiple scattering of the low kinetic energy photo-electrons interacting in the XANES region, there is no simplified equation for this part of the spectrum .Thus, the interpretation of XANES is generally qualitative in terms of coordination chemistry, band structure, and ionization states. Another important feature in the XANES region is the pre-edge interactions. These type of features are seen in most of the metals due $1s$ to $3d$ orbital transitions depending on dipole or quadripole selections [155]. Fig. 3.3 shows different scattering processes triggered by an incident X-ray beam on a sample.

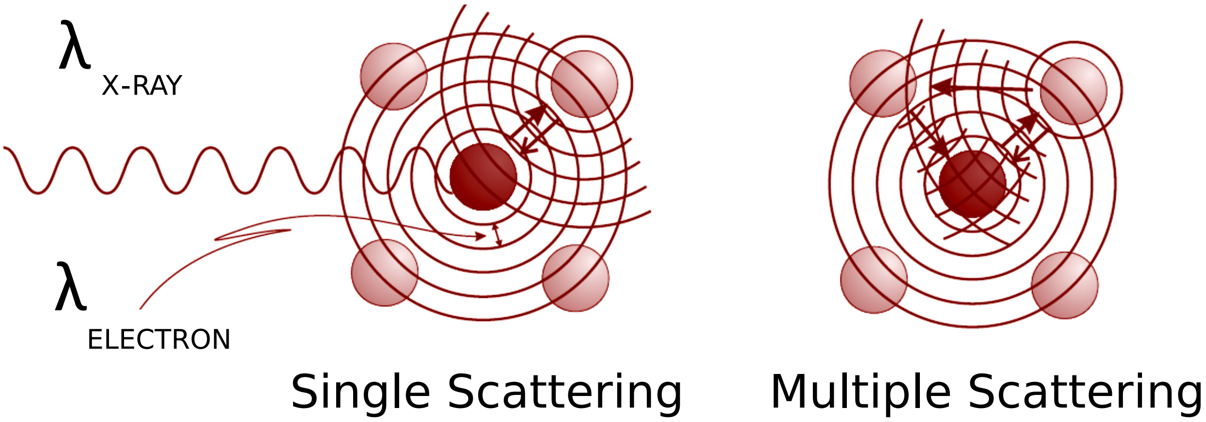

Figure 3.3: Schematic representation of single and multiple scattering of a photo-electron due to an incident X-ray beam. Reproduced from [156].

3.3 EXAFS

Unlike the XANES spectrum which is largely affected by the multiple scattering with low kinetic energy of photo-electron, the EXAFS part consists of the modulations of the absorption coefficient μ due to the interaction of the outgoing and the back-scattered waves of photo-electrons. The oscillations that can be seen in the marked EXAFS region in Fig. 3.2 occur due to the constructive and destructive interference of such interactions. As the X-ray energy increases, the resulting photo-electron has a greater kinetic energy and the EXAFS effects occurs mostly due to the single scattering event from an absorber to a scatterer and because of such effects, the absorption coefficient μ varies. In EXAFS, the signal measured in $\chi(\mathbf{k})$ represented as

$$\chi(\mathbf{k}) = \frac{\mu(E) - \mu_0(E)}{\Delta\mu_0(E)} \tag{3.3.1}$$

where μ_0 is the absorption coefficient in the absence of the EXAFS modulations. The value of EXAFS signal $\chi(\mathbf{k})$ depends on a number of parameters as follows [157, 158]

$$\chi(\mathbf{k}) = \sum_s \frac{N_s A_s(\mathbf{k}) S_0^2}{k R_{as}^2} exp(-2R_{as}/\lambda(\mathbf{k})) exp(-2k^2\sigma_{as}^2) \cdot sin(2kR_{as} + \phi_{as}(\mathbf{k})) \quad (3.3.2)$$

Here N_s coordination number of scattering atoms around the absorber. Of special importance is that the EXAFS signal responds inversely to the distance between absorber and scatterer, denoted as R_{as}. A_s and $\lambda(\mathbf{k})$ represent the energy dependence of the scattering and the mean free path of the photo-electron, respectively. The phase shift that depends on the scattering atom is given by $\phi(\mathbf{k})$. Finally, S_0^2 is the amplitude reduction parameter which has a value between 0 and 1 while σ_{as} is the Debye-Waller factor which reflects the variance of the multiple absorber-scatterer distance differences. This value can also be interpreted as the mean square displacements of the scatterer atoms in some cases. Note that in EXAFS measurements, the extracted distances are averaged, therefore σ_{as} holds important meaning of the errors of the fitting and variations in the structure. Fig. 3.4 shows some of the parameters appearing the equation 3.3.2 for different elements calculated by the FEFF [159] program package.

3.4 Data Analysis

In previous sections of this chapter it was mentioned that the rather complicated nature of XANES spectrum due to many multiple scattering of the photo-electron a simplified quantitative analysis for this part of the spectrum is lacking. Fortunately, for EXAFS part of the spectrum well established methods for data reduction can be found in the literature [161, 162]. The EXAFS signal, $\chi(\mathbf{k})$, is obtained after removing the background modeled by polynomial splines and then normalizing the magnitude of the oscillations to the edge jump. Figure 3.5 shows the normalization procedure for $Ge_{20}Se_{80}$ at the Ge K edge.

Since the EXAFS oscillations occur due to the damping of $sin(2kR_{as})$ term appearing in equation 3.3.2, the Fourier transform of the these oscillation frequencies with respect to k vector results in the inter-atomic distances between the absorber and the scatterer through various scattering path. The EXAFS signal $\chi(\mathbf{k})$ is generally weighted with a power of k and the oscillations are truncated using a window function. The truncation range is determined by the noise level of the weighted EXAFS signal. Subsequently, a Fourier transformation is applied from reciprocal to real

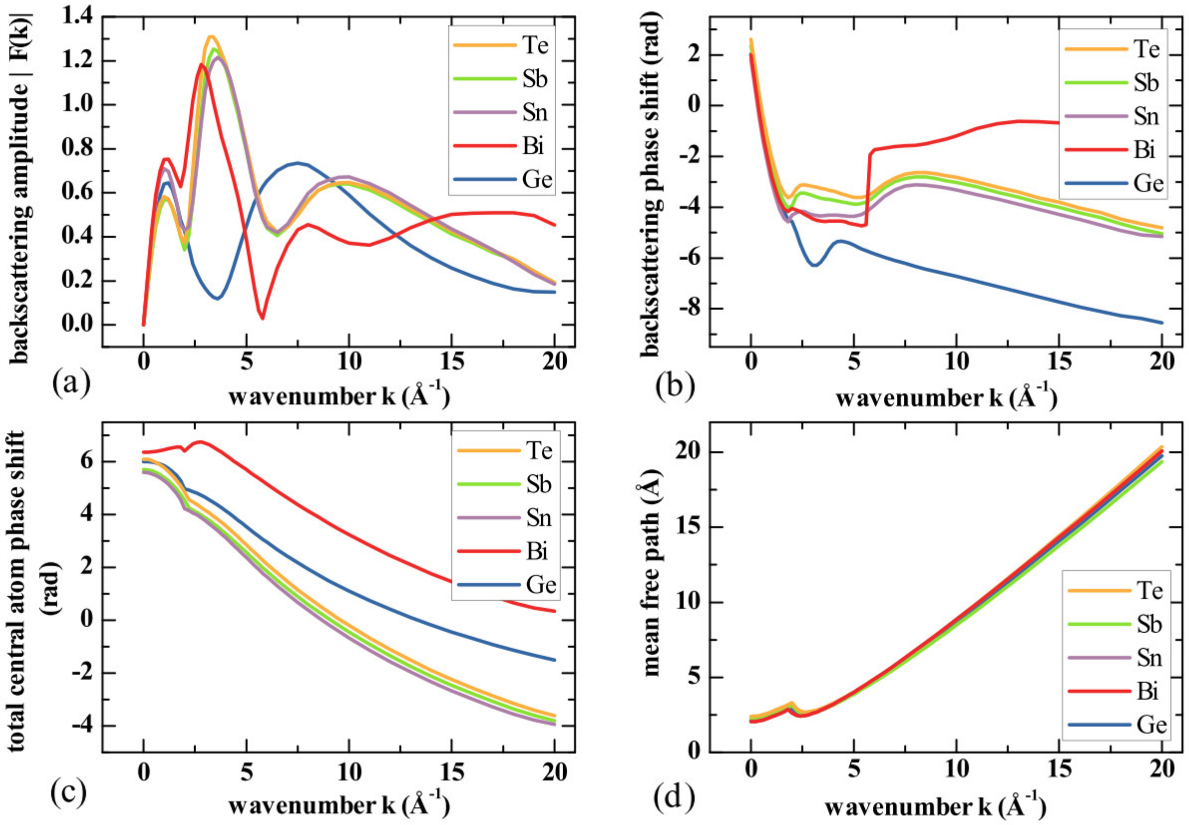

Figure 3.4: k dependence of EXAFS parameters calculated by FEFF. Adapted from [160]

space and a radial distribution function (RDF) of the first neighbors is obtained. With the application of another window function, the back Fourier transform is performed to the truncated RDF data and finally the filtered EXAFS signal is obtained. Fig. 3.6 illustrates the schematic of the EXAFS data refinement procedure.

In this thesis, XAS data were analyzed using the ATHENA and ARTEMIS programs of the IFEFFIT package [163, 164]. The parts of the analyses that are explained above were carried out using ATHENA. In order to account for the neighboring distances, the ARTEMIS program was used. Fig.3.7 illustrates an example of data reduction for $Ge_{20}Se_{80}$.

In the analysis of our data collected at BM23, the $\chi(\mathbf{k})$ signals were fitted in k space in an interval of 3.96 to 15.2 Å^{-1}. The first shell contribution was isolated by selecting a back transforming range between $1 \leq$R≤ 3 Å. A Hanning window function was used for the Fourier transformations. The fitting parameters amplitude reduction factor, S_0^2, and energy mismatch, E_0, were refined with initial predictions between 0.86 to 1 and 5 to 7, respectively. For XAS refinement of the short range structure, two methods were compared to obtain the best-fitting parameters ; in one method the first shell neighbor

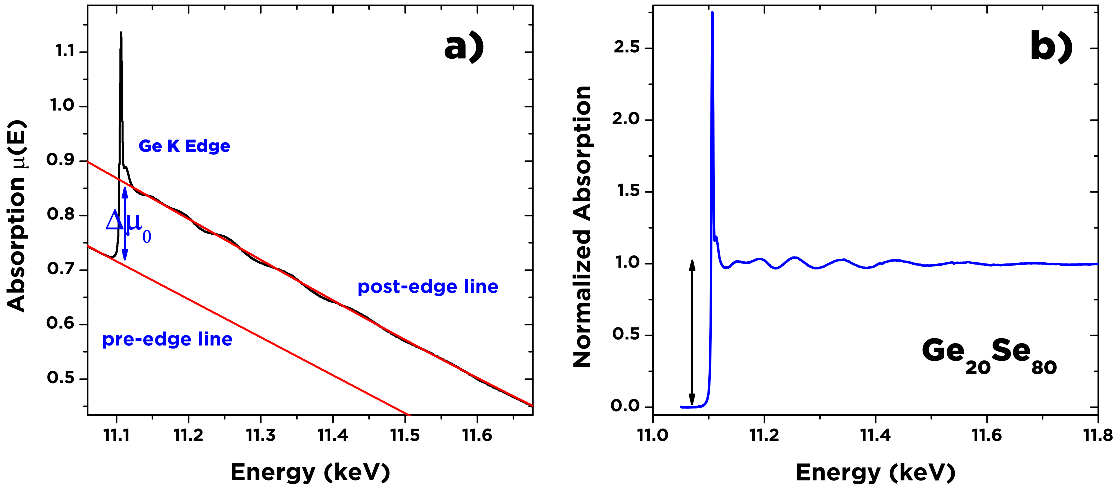

Figure 3.5: Measured absorption spectrum at Ge K edge for $Ge_{20}Se_{80}$ (black). a) Normalization of the measured $\mu(E)$ is done with the post and pre-edge lines having cubic spline fits (red). b) normalized absorption spectra with edge step equal to 1 (black arrows).

coordination numbers were fixed to n_{GeSe} = 4 and n_{SeGe} = 2 whereas in the other the coordination numbers found through *ab initio* calculations of Ge_xSe_{1-x} glasses under pressure are used. The details of AIMD results will be presented in the following chapters. The comparison revealed no significant differences in σ^2 values and Ge-Se distances (i.e. for the structural parameters in the refining of $Ge_{25}Se_{75}$, when n_{GeSe} is set to 4, the calculated best fit yields R_{GeSe} = 2.366(4) Åand σ^2_{GeSe} = 0.00429(3), which is identical to the case when n_{GeSe} = 3.87 determined by the *ab initio* simulations with a 3 % difference in S_0^2). Therefore, the former approach has been adopted in which the coordination numbers are fixed to n_{GeSe} = 4 and n_{SeGe} = 2 for the XAS data refinement

To this point, a short overview of X-ray absorption phenomenon was given, covering the essential parts of the physics behind the actual measurement along with the guideline to the data analysis. In the next sections of this chapter, the details of the XAS and XRD experiment, sample preparation and characterization will be described.

3.5 Experimental Details

The XAS and XRD experiments were carried out at BM23 at the European Synchrotron Radiation Facility (ESRF). Synchrotron light sources are extremely powerful facilities to for investigating structure and/or dynamics of matter in a variety of diverse disciplines. The synchrotron radiation is achieved by the trajectory of accelerated charged

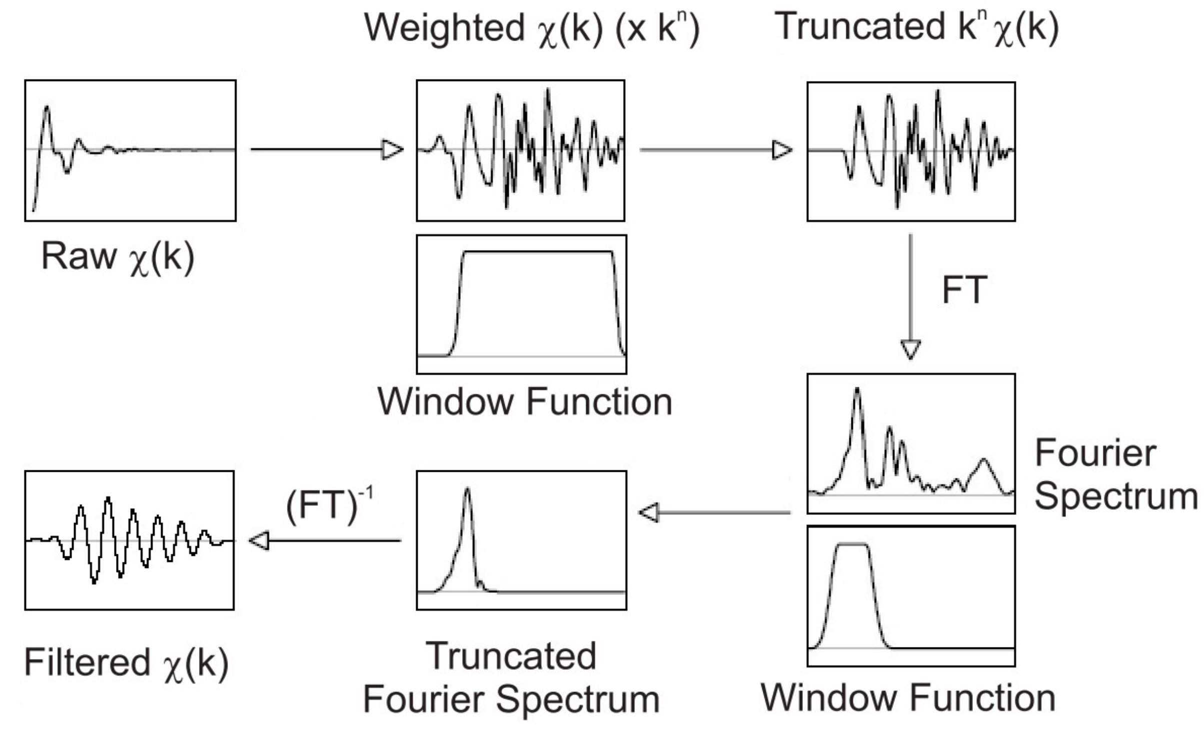

Figure 3.6: Schematic of the standard EXAFS data reduction. Reproduced from [156]

particles (electrons or positrons) in curved (bending magnet) or orbiting paths (undulators and wigglers).The main advantage of the synchrotron X-rays over conventional X-rays generated in laboratory X-ray tubes or rotating anodes is the orders of magnitude differences in the term what is called brightness. Brightness can roughly be described photon flux per unit area and unit time.

At the ESRF, BM23 offers XAS experiments within an energy range of 4 keV to 74 keV with bending magnets. The data collection can be performed both in transmission or florescence modes.The beamline optics in transmission mode is represented in Fig3.8. In our experiments, XAS data were collected at Ge K edge (11.1 keV) and Se K edge (12.66 keV) using ionization chambers. The X-ray beam spot size focused on the sample was about 5 x 5 μm^2.

To study the structural evolution of $\mathrm{Ge_xSe_{1-x}}$ under compression, pressure was applied using a gas driven membrane diamond anvil cells (DAC). Conical shape Boehler-Almax design diamond anvils having 300 μm culets were used. Rhenium gaskets were thinned down to 35 μm and holes of 120 μm diameter were drilled using laser beam. Fine pieces of the samples were placed inside the hole along with spheres of rubies. Ruby florescence method was used to measure the applied pressure. A droplet of paraffin oil was introduced the hole after the sample and the rubies were loaded to achieve hydrostatic pressure conditions, as the pressure transmitting medium. Fig.

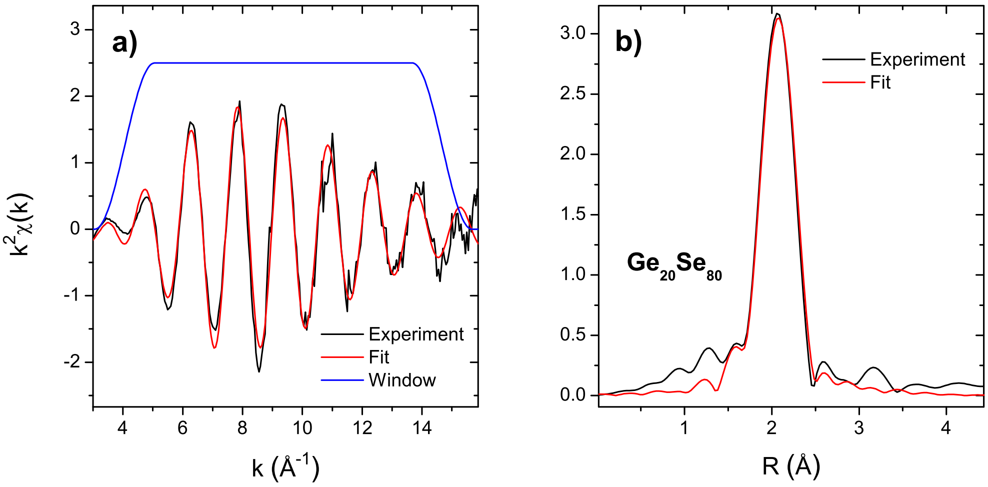

Figure 3.7: k^2 weighted EXAFS signals at the Ge K edge of amorphous $Ge_{20}Se_{80}$ (black), the calculated best fit (red) and the window function (blue) together with b) the Fourier transforms at ambient pressure. Note that the phase shifts are not corrected here

3.6 shows one half of a DAC and a zoom to the hole at the tip of the diamonds.

The simultaneous XRD patterns were collected with a MAR165 CCD detector having a 79 x 79 μm^2 pixel size which was placed at about 164 mm from the sample. An incident wavelength of 0.688 Å was selected through Si (111) monochromators as shown in the Fig.3.8. The XRD data reduction was carried out using FIT2D package [166].

3.6 Sample Preparation and Characterization

Samples that were used for this thesis work had been prepared at the University of Cincinnati. Amorphous Ge_xSe_{1-x} (where x=10, 17, 20, 22 and 25) samples were synthesized using 99.999% Ge and 99.999 % Se pieces mixed in the desired ratio and were sealed in evacuated quartz tubes. The quartz ampules were held vertically in a T-programmable box furnace for 192 h at 950 °C to ensure homogenization. The ampules were water quenched from 50 °C above the liquidus temperature. FT Raman profiling was performed on the as-quenched melts to confirm structural homogeneity [45]. The as-quenched melts were then heated in the box furnace at T_g+20 °C for 10 min and brought down to room temperature at a cooling rate of 3 °C/min. The produced amorphous Ge_xSe_{1-x} samples were kept in a glove box for further manipulation.

The chemical composition and homogeneity of the samples was verified within the limitations of energy dispersive X-ray spectroscopy (EDXS) analyses. EDXS character-

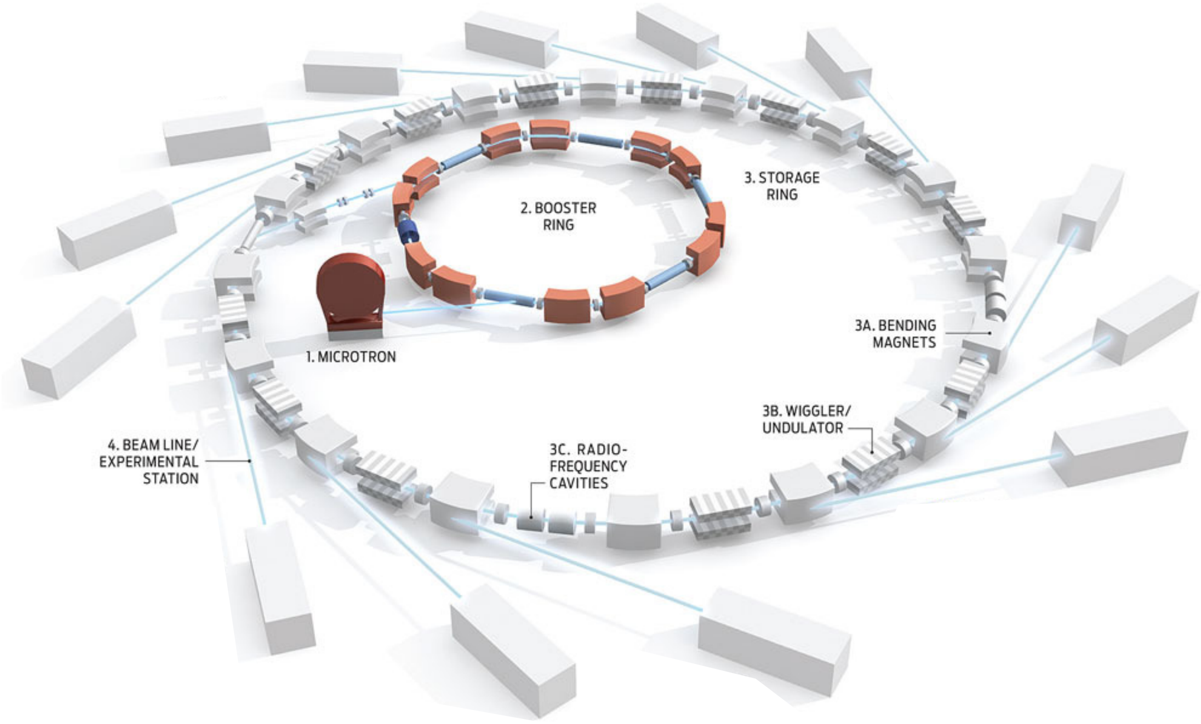
3. STORAGE RING
2. BOOSTER RING
1. MICROTRON
3A. BENDING MAGNETS
3B. WIGGLER/ UNDULATOR
4. BEAM LINE/ EXPERIMENTAL STATION
3C. RADIO-FREQUENCY CAVITIES

Figure 3.8: Schematics of a typical synchrotron ring showing its essential components. Adapted from [165]

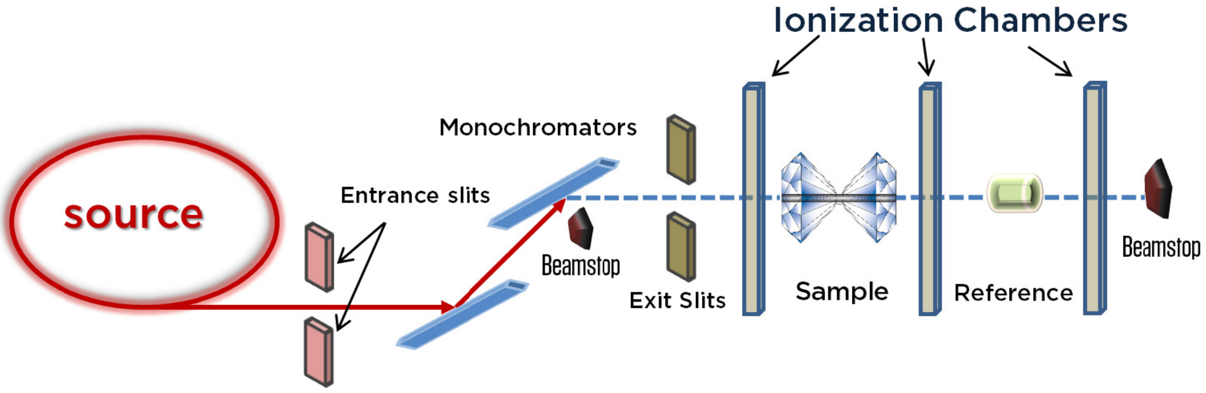
Ionization Chambers
Monochromators
Entrance slits
source
Beamstop
Exit Slits
Sample
Reference
Beamstop

Figure 3.9: Schematics of XAS beamline optics.

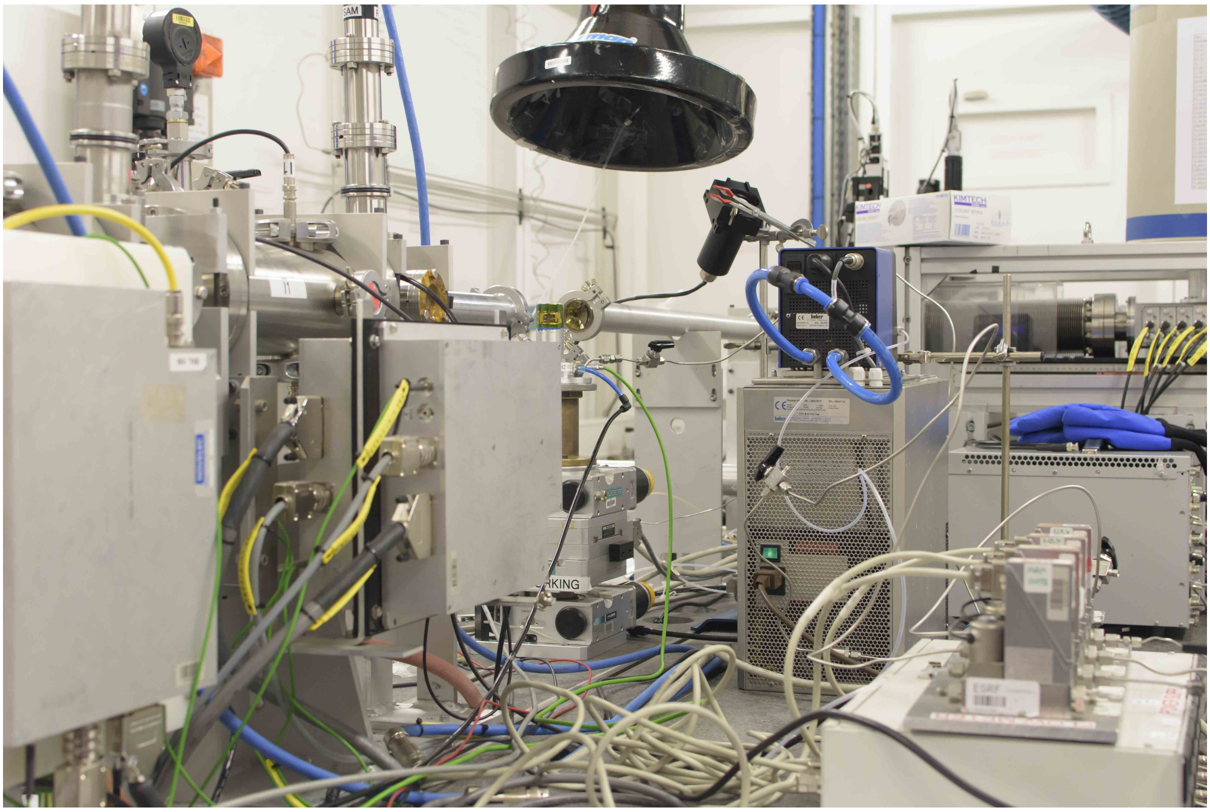

Figure 3.10: BM23 XAS beamline at ESRF, Grenoble, France.

ization is a rather simple yet a powerful method to perform qualitative and quantitative composition analysis on a material. The basic working principle of EDXS relies on the bombarding of a sample with focused electron beam in a scanning or transmission electron microscope. The electron beam that hits the material has several interactions at various depth of the sample from the surface, namely; back-scattering, secondary, auger electrons, and the emission of the characteristic X-rays of the elements in the sample. In EDXS, one records the relative intensities of these characteristic X-rays generated by filling holes of the ejected electrons due to the incident electron beam. Since the characteristic X-ray lines of elements depends on the atomic number Z, the energy of the incident beam should be chosen carefully in order to observe an element in the sample. Another important point is the control of the so-called parameter 'dead time', which is the time spent between the pulses which are not measured given in percentages with the following relation;

$$Deadtime = (1 - \frac{Outputrate}{InputRate}) \times 100 \tag{3.6.1}$$

A good range for dead time can be given as 20-40 $\%$, which can be controlled by the excitation voltage of the beam, spot size, and the level of the sample stage. The

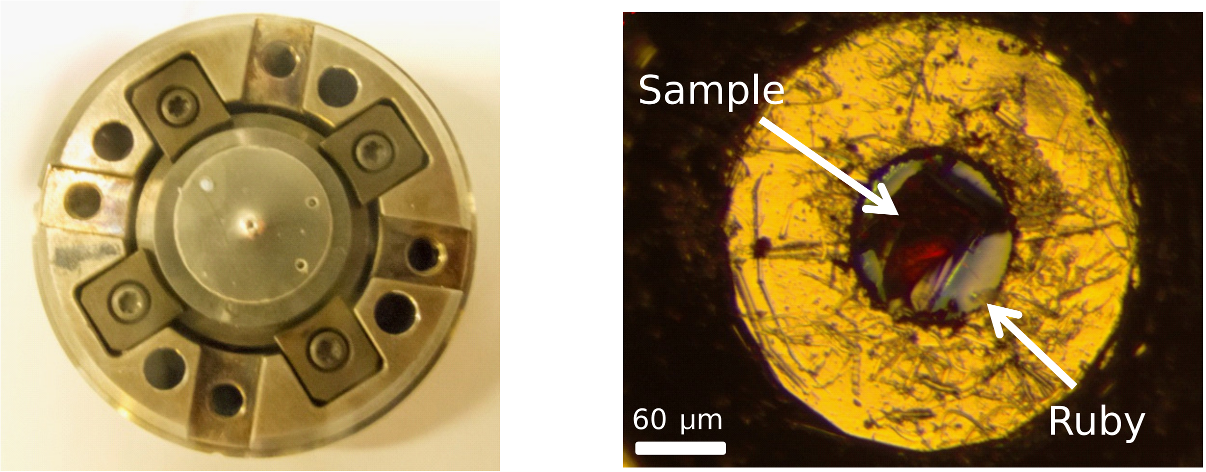

Figure 3.11: Lower half of the diamond anvil cell (DAC) having the rhenium gasket with a 120μm diameter hole (left). Inside the DAC with sample and ruby placed in the 35μm thick hole.

EDXS analyses of the above mentioned samples were performed using a field emission scanning electron microscope (FESEM) at the CEA, Grenoble, France prior to the X-ray absorption (XAS) and X-ray diffraction (XRD) experiments. An excitation voltage of 15 keV was used to generate characteristic L emission lines of Ge and Se elements that are located at 1.118 and 1.379 keV, respectively. Fig. 3.7 illustrates the EDXS spectra of $Ge_{25}Se_{75}$ with the corresponding image at which the spectra was collected. The average dead time for the measurements were 19 %. The characteristic lines for carbon is generally observed due to the carbon tape that is used to attach the sample to the sample holder in the microscope. Similarly, the O content appearing in the spectra is in the accepted range. The characteristic L radiations of the Ge and Se elements are observed at their respected positions. a series of EDXS spectra was collected from different parts of the samples and for this case, $Ge_{25}Se_{75}$, EDXS results showed Se:Ge ratio of 3.01 ± 0.02. The EDXS results showed no Si contamination due to melting in the quartz capillaries.

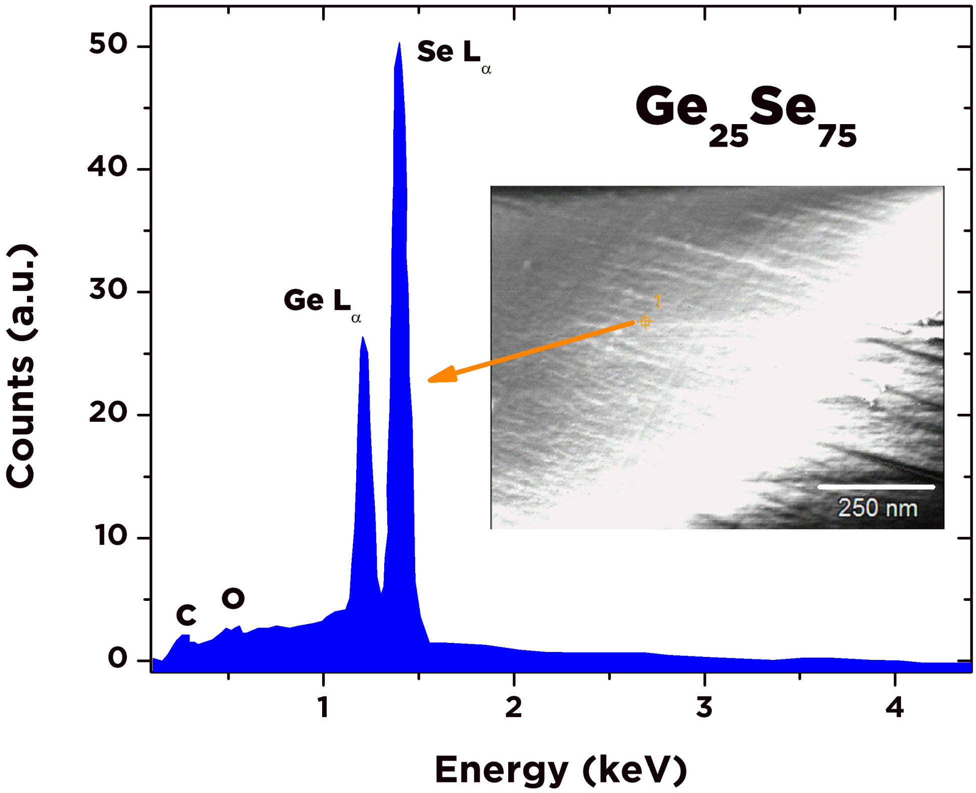

Figure 3.12: EDXS spectrum of $Ge_{25}Se_{75}$ at 15 keV. The inset shows the corresponding image where the spectrum was collected.

Chapter 4

Study of Liquid Ge-Se

Abstract

There are important differences in the way liquids relax as they approach the glass transition, i.e. rapid or slow variation in dynamic quantities under moderate temperature changes. In this chapter, we investigate the structure and dynamics of Ge-Se liquids using AIMD simulations. The focus is set on ten compositions (where $x \leq 33$ %) encompassing the reported elastic phase transitions. We examine diffusion coefficients, diffusion activation energies, glassy relaxation behavior and viscosity of these liquids from Van Hove correlation and intermediate scattering functions. We show that the relaxation behavior of the supercooled liquid is strongly correlated to the variation of rigidity with temperature and the spatial distribution of the corresponding topological constraints, which ultimately connect to the fragility minima. This enables us to extend the fragility concept to aspects of topology/rigidity, and to the degree of homogeneity of the atomic-scale interactions for a variety of structural glasses.

4.1 Introduction

The $\mathrm{Ge_xSe_{100-x}}$ system holds and important place among chalcogenide melts due the nature of the chemical bonding which can be substantially changed by composition or temperature even though the tetrahedral local structure remains predominant. These variations in the network structure lead to alterations in physical properties [167, 168] among which a substantial increase in the electrical conductivity [169] by about three orders of magnitude for Ge-rich compositions ($x \leq 33$ %) that is due to the progressive conversion of the bonding from covalent to metallic [138]. The non-monotonic trends in other properties such as enthalpy relaxation at the glass transition was shown in Chapter 1. Here, we investigate the dynamic and relaxation properties of Ge-Se supercooled liquids from molecular dynamics using AIMD. The computational details are given in section 2.4. In addition to the experimental glass densities, here we also performed simulations using the experimental liquid densities[124]. Fig. 4.1 shows the interpolation applied to the available data for Se rich compositions. In the following sections, after the verification of our simulations, a comprehensive investigation of dynamics in Ge-Se melts will be provided.

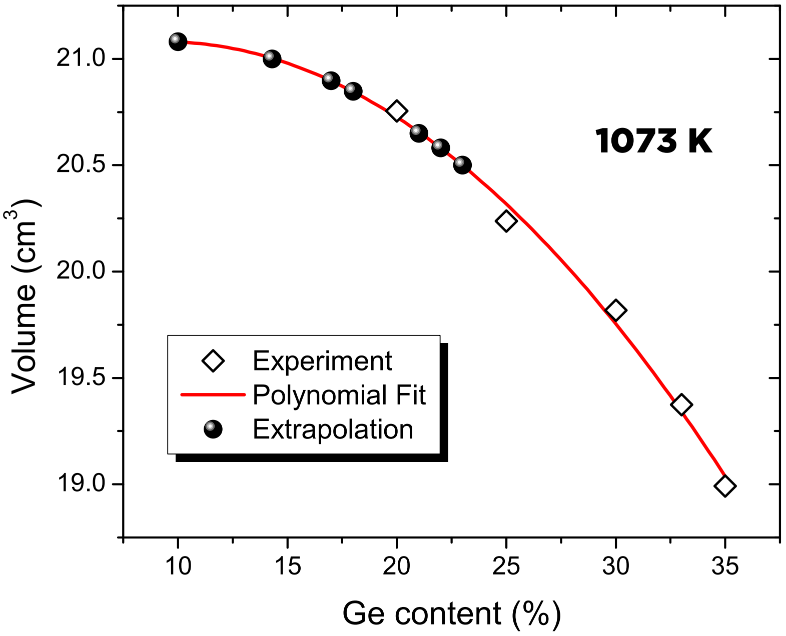

Figure 4.1: Composition dependence of molar volume of Ge-Se liquids at 1073 K. The red curve represents the polynomial fit applied to the experimentally measured data [124] (diamond symbols). Black symbols shows the extrapolated data for other compositions used in our simulations.

4.2 Structural Properties

In this section we verify the reliability of our simulations by comparing the obtained structural models to the available experimental findings, before proceeding with the detailed investigation of the dynamics. Fig. 4.2 shows the calculated static coherent structure factors $S(\mathbf{k})$ of selected compositions at several temperatures along with corresponding neutron scattering experimental result [170, 140, 171]. In the glassy state (Fig. 4.2a), a noticeably good agreement is observed between our simulations and the experimental findings at 300 K [73, 170, 140, 171]. Previous AIMD investigations on Ge-Se glasses [138, 132, 49, 170, 140, 171] show similar levels of accuracy when compared to experiments. The typical features of the neutron diffraction pattern such as the first sharp diffraction peak (FSDP) located at around k=1.0 Å^{-1}, the principal peak at k=2.10 Å^{-1} and the secondary principal peak at k=3.50 Å^{-1} and the high vector range of $S(\mathbf{k})$ (k=10-12 Å^{-1}) are very well reproduced. In the liquid state (Fig. 4.2b), the calculated and experimental structure factors are also in good overall agreement, especially for $\text{Ge}_{33}\text{Se}_{66}$ [73, 172]. For the latter, the intensity decrease of the FSDP upon raising the temperature to 1373 K is also rather well reproduced. Moreover, it should be noted that small changes in composition ($\text{Ge}_{22}\text{Se}_{78}$, Fig. 4.2b) do not yield considerable modifications in the diffraction pattern, this compound also matching the experimental curve of $\text{Ge}_{20}\text{Se}_{80}$. Finally, it is important to mention that there are almost no changes due to system size as the results for the present N=250 atoms system are comparable to results for N=120 (Fig. 4.2b) [173] or N=480 [134]. Fig. 4.3 shows the calculated total pair distribution function $g(r)$ (PDF) for selected compositions at 1050 K and 1373 K with their experimental counterparts [73, 140]. A decent agreement is found in the real space features of our structural models when compared to the experimental findings. The main peak of $g(r)$ which is located at 2.35 Å and due to Ge-Se correlations (2.36 Å [73], experimentally), and the second peak at around 3.85 Å which is associated with the Se-Se distances between the edges of $\text{GeSe}_{4/2}$ tetrahedra [145] are also very well reproduced. The detail of the partial contributions is very similar to those obtained with different system sizes [145, 173, 134, 174]. These results confirm the validity of the models generated with AIMD, allowing us to further analyze the system in terms of dynamic properties.

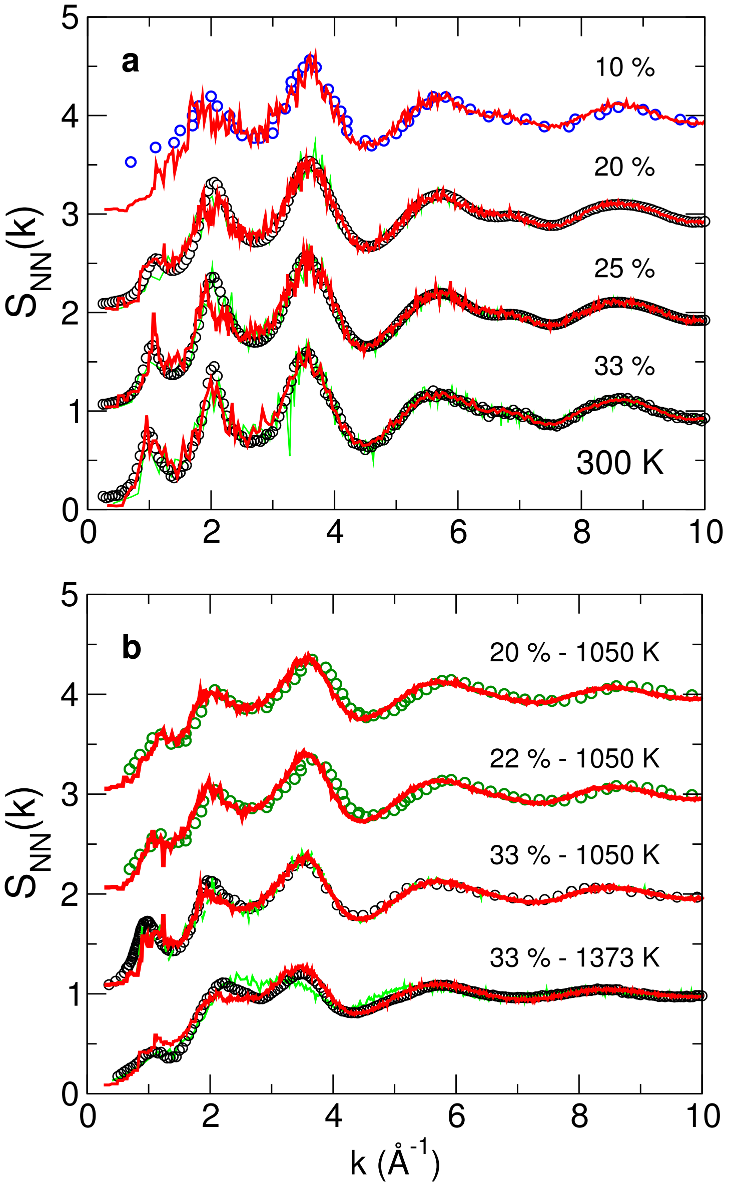

Figure 4.2: Calculated static structure factors $S(\mathbf{k})$ (red curves) for selected compositions at 300 K (a) and in the liquid state (b), and comparison with experimental neutron diffraction results in panel a: blue circles [170], black circles : $Ge_{20}Se_{80}$ [140], $Ge_{33}Se_{67}$ [171], and in panel b: Green circles $Ge_{20}Se_{80}$ [175], $Ge_{33}Se_{67}$ at 1050 K [172], and at 1373 K [176]. The yellow curve corresponds to a system with 120 atoms [173]. Note that the experimental data of $Ge_{20}Se_{80}$ have been duplicated in order to be compared with the simulated $Ge_{22}Se_{78}$.

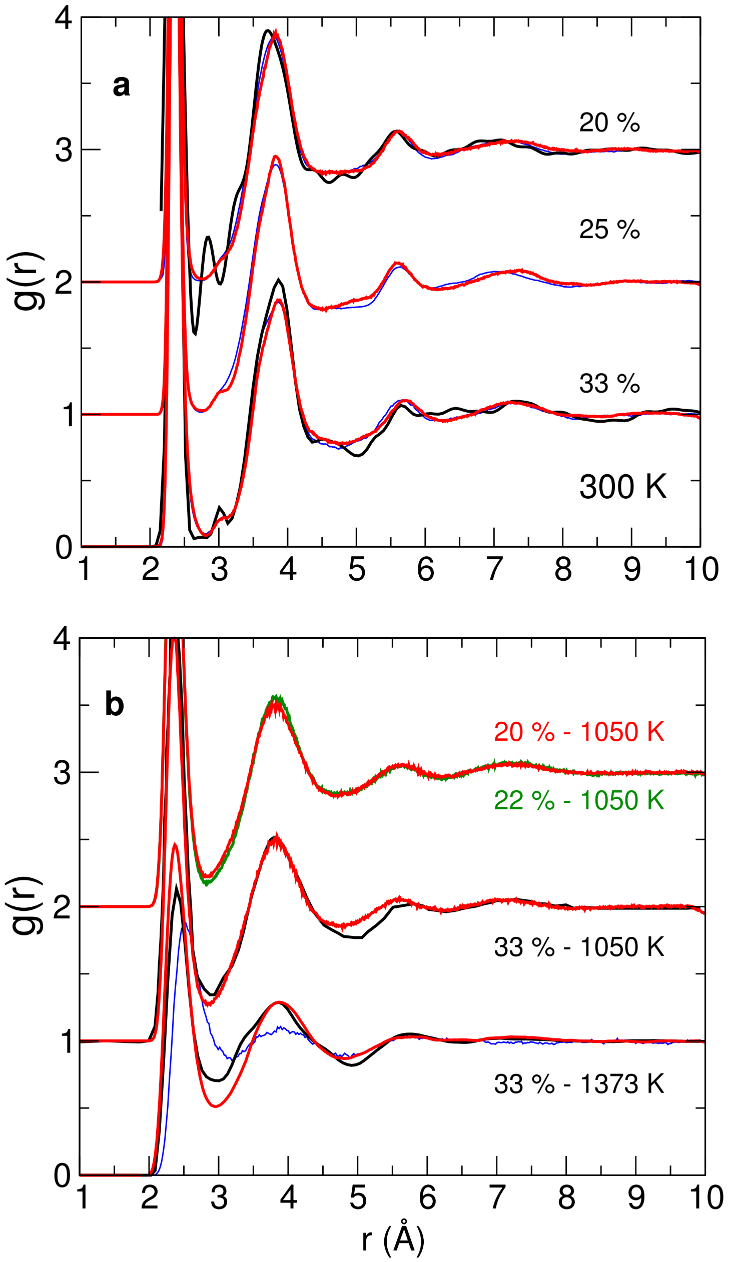

Figure 4.3: Calculated total pair distribution functions (red curves) for selected compositions at 300 K (a) and in the liquid state (b), compared to neutron diffraction experiment results (black lines): $Ge_{20}Se_{80}$ [73] and $Ge_{33}Se_{67}$ at 300 K [140], $Ge_{33}Se_{67}$ at 1050 K [172] and 1373 K [176]. The calculations are also compared to previous simulation results (blue curves) on 120 atom systems for 1373 K ($GeSe_2$) [175] and 300 K [140, 145].

4.3 Anomalous Dynamics and Relaxation

In order to investigate the dynamics of liquid $\mathrm{Ge}_x\mathrm{Se}_{100-x}$ we first calculate the mean square displacement (msd) $\langle r_\alpha^2(t)\rangle$ of the chemical species α (α=Ge,Se) from the atomic trajectories of our simulations. Fig. 4.4 shows the time dependence of the total msd at selected temperatures for liquid $\mathrm{Ge}_{20}\mathrm{Se}_{80}$. The mobility of the atoms decreases with decreasing temperature, as expected. At high temperatures two well-defined time regime can be identified, a ballistic regime at short times at which the msd is proportional to t^2, and a diffusive regime which correspond to the linear dependence on time at larger time values ($t >$5ps). This feature is detected for all compositions and at all $T >$1050 K. For the particular temperature of 1050 K, Fig. 4.4 shows that the diffusive regime appears at somewhat longer times (typically 10 ps), and this has been found for all temperatures, consistently with fact that the onset of the diffusive regime shifts to larger time values upon decreasing the temperature. In particular, the msd curve obtained at 1050 K shows that it is the lowest temperature in the liquid state at which the diffusive regime can be attained within the limits of our simulations (25-40ps). It should be noted that the structural and dynamic properties above 1050 K weakly vary between glass and liquid densities. On the other hand, the changes in dynamic properties are more prominent for the liquid densities at 1050 K. For this reason, the data presented here will be a combination of the two; in such a way that all the 1050 K properties are calculated using liquid densities, and glass densities are used for the rest of the data provided (see Appendix A for details).

For lower temperatures, a typical cage-like regime is observed [177] (msd$\simeq$0.3 Å) that extends to long times as the temperature is decreased. This behavior is due to the trapping of individual atoms by their neighbors environment, resulting in a constant value for the msd. The atoms can only leave this effective 'cage' after a sufficient time has passed, and a diffusive regime may be reached but beyond the time limit of our simulations. Fig. 4.5 shows the msd at 1050 K for the compositions studied. The typical features observed for $\mathrm{Ge}_{20}\mathrm{Se}_{80}$ at 1050 K can be identified for the other compositions as well. It can clearly be seen that the atoms of the compound $\mathrm{Ge}_{10}\mathrm{Se}_{90}$ are the most mobile while it is the least for that of $\mathrm{Ge}_{22}\mathrm{Se}_{78}$ in the diffusive regime. This picture contradicts a natural anticipation which correlates the increasing network structure should decrease overall mobility of the system. Therefore, we now turn to the diffusion coefficients to see the effect of composition on atomic mobility. Once the diffusive regime is reached in the long time limit, as seen from the log-log plot (Fig. 4.4), the diffusivity D_α of the chemical species α is given by the Einstein rela-

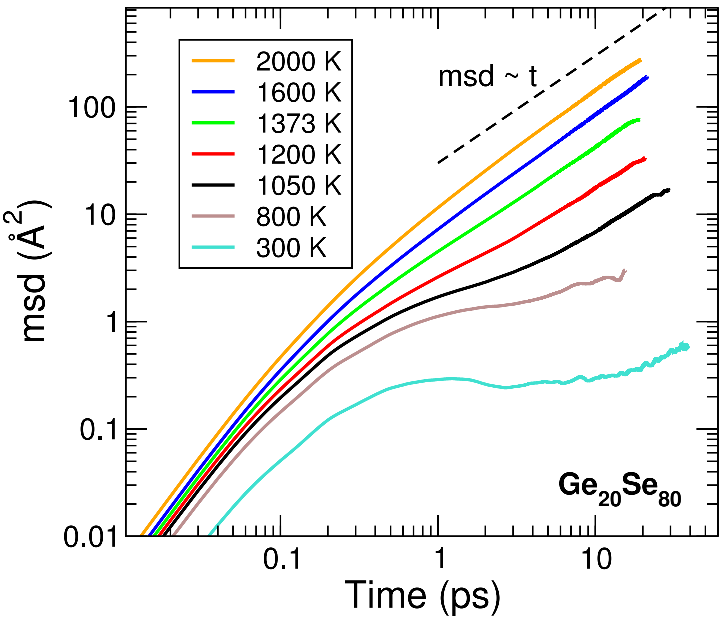

Figure 4.4: Total mean square displacement (msd) as a function of simulation time for $Ge_{20}Se_{80}$ at different temperatures. The broken line shows the behavior of $\langle r_\alpha^2(t)\rangle$ in the diffusive regime.

tion. The diffusion coefficients as a function of composition at selected temperatures are shown in Fig. 4.6. At all temperatures Se atoms are more mobile than Ge atoms due to their lighter atomic weight, except at 33 $\%$ Ge concentration which corresponds to the stoichiometric compound. A global decrease in the diffusivity is detected with the increase in Ge content, along with the stiffening of the network at both 1050 K and 1373 K, as the liquid becomes more and more cross-linked by the addition of four-fold Ge atoms. For higher temperatures, a smooth decrease of D_{Se} and D_{Ge} is found. Interestingly, we note that at 1050 K, within a small compositional range (18-22 %), the values of D_{Ge} and D_{Se} decrease even more, at least when compared to a linear extrapolation between 10 % and 33 % Ge. This effect is enhanced for Ge atoms. In order to have a better understanding of this anomalous diffusion behavior, one can evaluate the diffusion activation energies E_A using the calculated diffusivities for different temperatures and $D = D_0 \exp[-E_A/k_BT]$ for the low temperature data points. Fig. 4.7a shows the evolution of the average diffusion constant as a function of temperature for selected compositions. The calculated diffusivities behave according to an Arrhenius law. At 2000 K, a deviation from the Arrhenius behavior with the diffusion constants increasing more slowly than what is expected for a thermally activated process. This is a feature that has been previously also observed in liquid SiO_2 [178] and GeO_2 [179]. In addition, it is also clearly seen that $Ge_{22}Se_{78}$ has the steepest curve among all the compositions whereas the slope of the line for $Ge_{10}Se_{90}$ is the smallest, a first indica-

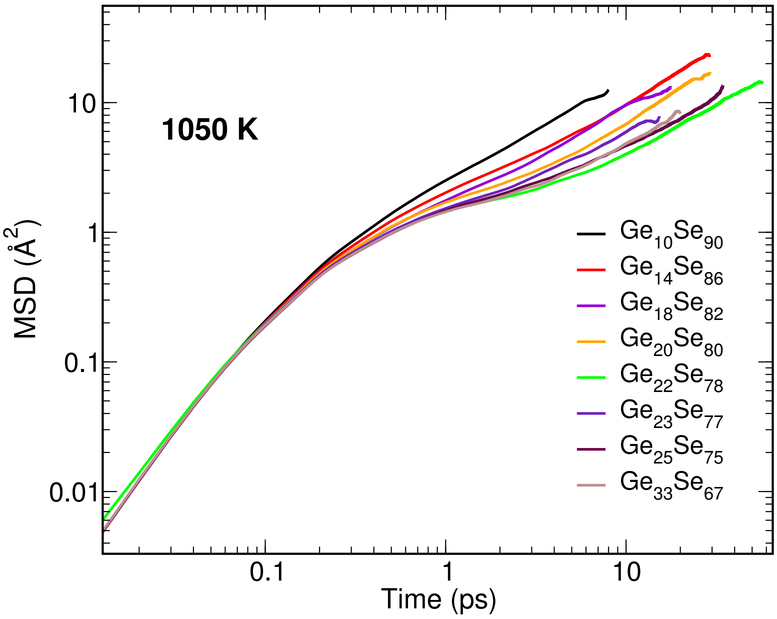

Figure 4.5: Total mean square displacement (msd) as a function of simulation time for different compositions at 1050 K.

tion that corresponding activation energies will depend on the Ge content. Fig. 4.7b shows the composition dependence of diffusion activation energy E_A. It is important to note that the non-monotonic trend in diffusivity at 1050 K is reflected in the behavior of E_A. As a result of the lower mobility of Ge atoms, the energy needed to activate Ge self-diffusion is higher than that of Se. The thermal energy barrier for diffusion rises almost linearly with increasing Ge content from Ge$_{10}$Se$_{90}$ to Ge$_{33}$Se$_{66}$,with an important increase in the same interval (18-22 %).These results signify a distinguished diffusion anomaly.

Additional insight into the real space dynamics and the transport mechanisms is provided by the Van Hove correlation function (equation 2.6.13). Fig. 4.8 shows the self part of the van Hove correlation function $G_s^{\alpha}(r, t)$ at different times for 1050 K. As opposed to the sharper peaks at earlier times, which behave as the Dirac $\delta(r)$ for $t = 0$ (equation (2.6.14), with the increase in time, the atoms have larger displacements and broader distributions. The probability to find a Se atom at a given time and position is, indeed, higher than that of a Ge atom, as expected, and the distances that Se atoms cover are larger than their Ge counterparts.

One can connect the diffusivity of the species with the jump probabilities of the atoms that have moved further than the first neighbour distances $r > r_0$ by integrating the van Hove self correlation function for each composition at a given time. Fig. 4.9 shows the composition dependence of such jump probabilities of the species where the

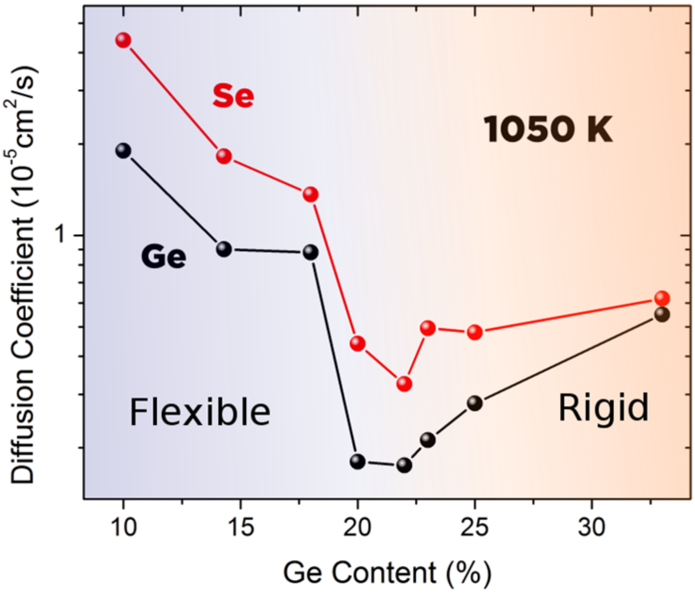

Figure 4.6: Calculated self diffusion coefficients D_{Se} (red) and D_{Ge} (black) as a function of composition at 1050 K.

hopping distance r_0=2.88 Å corresponds to the first minimum of the pair correlation function (Fig. 4.3). At 1373 K nearly all the particles are able to move over large distances due to the thermal excitation thus no particular anomaly is obtained, and the jump probability is $\simeq$80-100 % for nearly all compositions, consistently with the obtained trend for diffusivity. This situation contrasts with the composition dependence at the 1050 K isotherm. $Ge_{10}Se_{90}$, for which the underlying network consists of weekly interconnected chains [73, 180], has the highest jump probability for both Ge and Se species given that nearly all the atoms in the box have moved by more than 2.88 Å within 20 ps. Again, increasing Ge content results in a global decrease in jump probability analogous to the diffusion behavior exhibited in Fig. 4.6. It is important to note that the substantial slow down in the atomic mobility observed in the same interval 18-22 $\%$ in which the system exhibits an anomalous diffusion behavior. These results, together with the real space based dynamical analysis of our structural models, appeal for additional investigation in order to understand the mechanism driving this anomaly.

4.4 Role of with Molecular Rigidity on Fragility

A central result is the detection of the crucial role played by rigidity in the anomalous relaxation dynamics of Fig. 4.10, and the indication of a fragility minimum. Within

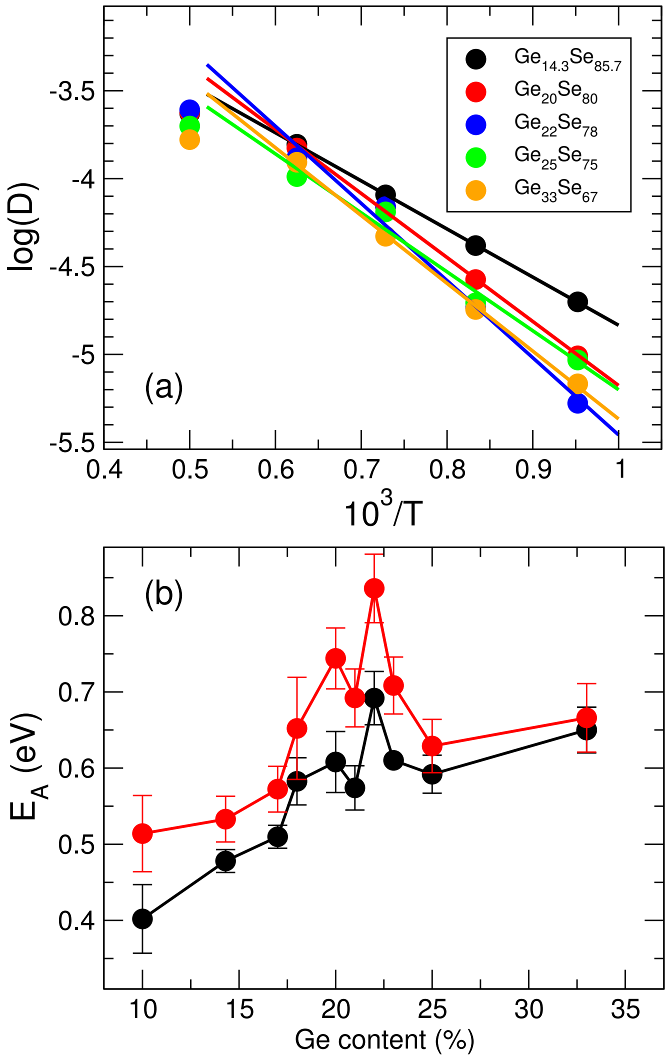

Figure 4.7: a) Arrhenius plot of the diffusion constant for selected compositions. The solid lines represent the Arrhenius fits. (b) Diffusion activation energy E_A of Ge (red) and Se (black) as a function of Ge content.

temperature-dependent rigidity theory, the assumption of an Adam–Gibbs form for the relaxation time, $\ln \tau_\alpha \propto 1/TS_c$, and the contribution of the number of topological degrees of freedom $f(x,T) = 3 - n_c(x,T)$ to the configurational entropy [181] $S_c(x,T)$ leads to the prediction of the fragility index M:

$$M = M_0[1 + \frac{\partial \ln f(x,T)}{\partial \ln T}]_{T=T_g} \qquad (4.4.1)$$

which depends only on the scaling of $f(x,T)$ with temperature. The validity and predictive power of equation 4.4.1 has been checked on a certain number of glasses by building structural models, establishing their constraint count, and comparing with a composition dependence of fragility measurements such as for borates [182] or phos-

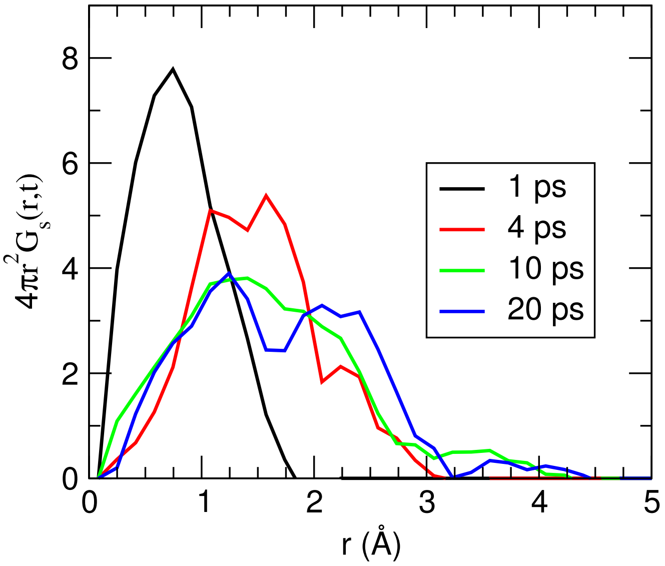

Figure 4.8: Self part of van Hove correlation function of Ge atoms, showing the atomic displacements at different simulation times.

phates [183]. MD-based constraint counting algorithms (see section 2.6.4 are used [184] to yield $n_c(x,T)$ from Ge/Se bond-stretching (BS) and bond-bending (BB) motions. These show that (i) for the 300K glasses, n_c follows exactly the mean-field estimate $n_c = 2 + 5x$ (Fig. 4.10 a [29]), leading to an isostatic condition ($n_c = 3$ for 20$\%$ Ge) that agrees with the experimentally measured threshold value [42], and, importantly, (ii) the calculated $n_c(x,T)$ displays a minimum change with temperature for 20–22$\%$ Ge. The obtained minimum change is robust. Following equation 4.4.1, this leads to a minimum for the liquid fragility with composition given the weaker variation of the term $dn_c/d\ln T$ at x ~22%, and coincides with $n_c = 3$. When the details of the constraint contributions are investigated, and their spatial distribution analyzed Fig.4.10, additional important features can be linked to the weak variation of n_c with temperature. First, for the composition at which the weakest change in n_c is found (22%), the BB constraints are nearly homogeneously distributed in the structure given that n_c BB maximizes to its nearly low temperature value (n_c^{BB}=5), which reduce the possible fluctuations. This contrasts significantly with all the other compositions (for example, 14.3 and 33%, Fig. 4.10c, which display a heterogeneous distribution of constraints broken by thermal activation. The variance of n_c BB is also a measure of the spread in the spatial distribution of atomic interactions leading to rigid constraints. For the compositions in the range 20–23%, one could extrapolate that homogeneity of stress (that is, interactions) will not only induce a cascade of dynamic anomalies as detected from the diffusivity minima and viscosity/relaxation time maxima located in the same range of compositions (Fig. 4.6) but also represents a more stable state at the

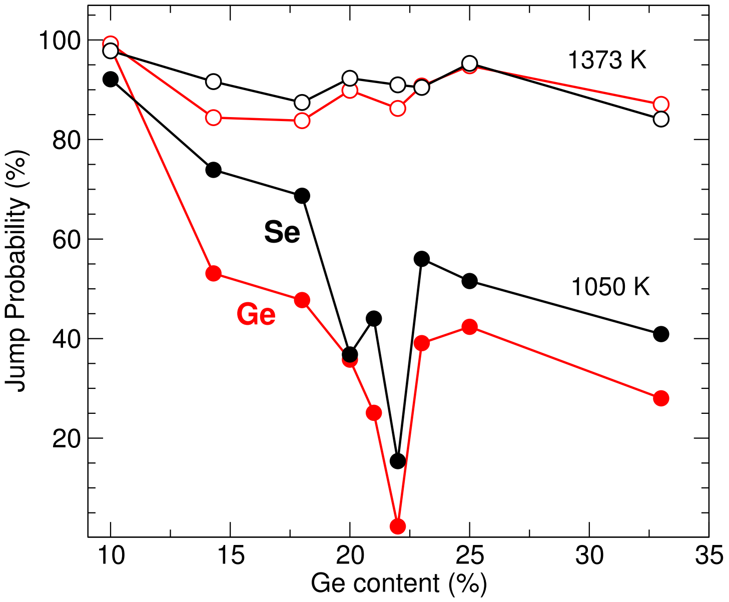

Figure 4.9: Composition dependence of the jump probabilities of atoms that have jumped r>2.88 Å within 20 ps at 1050K (filled circles) and 1373 K (open circles).

nanoscale. As a consequence, thermal changes must lead to minor changes of n_c with temperature, and ultimately will minimize fragility (equation 4.4.1). In this particular region of anomalous behavior, one furthermore detects weak effects on structure with chemical composition given that both the pair correlation function $g(r)$ in real space and the structure factor in reciprocal space exhibit small differences with Ge content . For instance, the structural properties of the 22% composition that appears to be so particular in terms of dynamic properties (Fig. 4.6), are found to be nearly identical to the 20% one, although their relaxation time differs by a factor 2 and their rigidity also varies substantially within a tiny compositional interval. This, ultimately, emphasizes the predominance of rigidity and its spatial distribution on the liquid relaxation properties, over aspects of structure.

It was already shown that rigidity of a glass forming network can be linked to its fragility. To do this, we investigate the viscosity of liquid $\mathrm{Ge_xSe_{100-x}}$ and first compare with experimental results [185, 186, 187]. The direct calculation of viscosity is out of reach given that the system size and the time scales of the AIMD simulations are too small in order to obtain a satisfying decay of the stress auto-correlation function in the Green-Kubo approach [152]. Therefore, we use the Einstein-Stokes (SE) relation in which the viscosity is given by

$$\eta = \frac{k_B T}{6\pi R D} \tag{4.4.2}$$

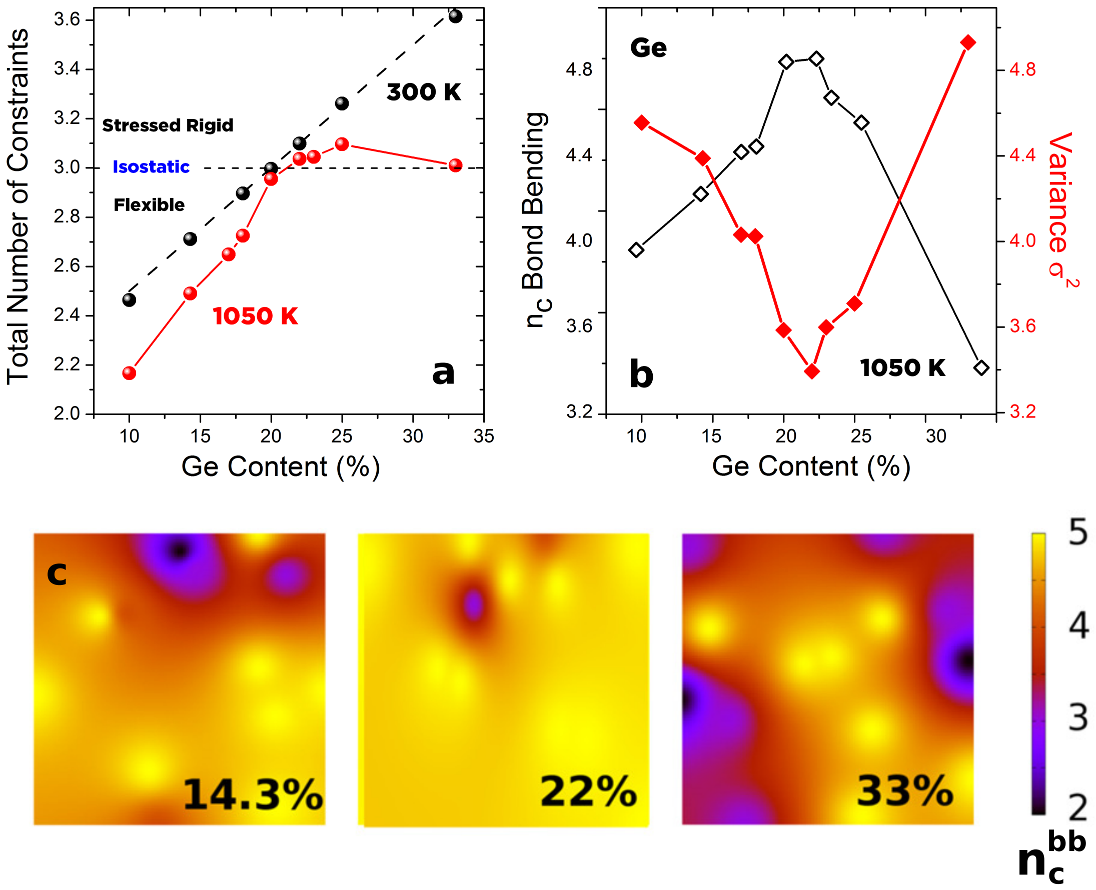

Figure 4.10: (a) Global MD constraint count of the liquid (1050 K), compared with a count in the glassy state (300 K). The broken line represents the Phillips–Thorpe constraint count $n_c = 2{+}5x$ [29]. (b) Contourplots of the Ge BB constraint distribution among the structure for selected compositions. They have been generated by focusing on the constraint distribution inside a slab of 3.2 ± 0.2 Å(c) Calculated Ge BB (black) and BS (red, right axis) constraint density as a function of Ge content. (d) Variance $\sigma^2_{n_c}$ of the Ge BB constraint population.

where k_B is the Boltzmann constant, T is temperature, D is the diffusion constant (Fig. 4.7), and $R = 0.5\rho^{-1/3}$ given that ρ is the density [137]. It is important to note that we have checked for the validity of the SE relation by verifying that the calculated diffusivity scales as T/τ_α. This is fulfilled for all investigated temperatures including the 1050 K one.

We plot the calculated viscosities (equation (4.4.2)), we represent these in an Angell plot, i.e. $\log_{10}\eta$ as a function of T_g/T, together with the experimental measurements (Fig. 4.11). Note that only a limited number of high temperature experimental measurements [185] can be compared directly to our simulations ($Ge_{20}Se_{80}$ and $Ge_{33}Se_{66}$). These show a rather good agreement, and Figure 4.12 provides a validation that the high temperature viscosity behavior is rather well reproduced from the AIMD structural models.

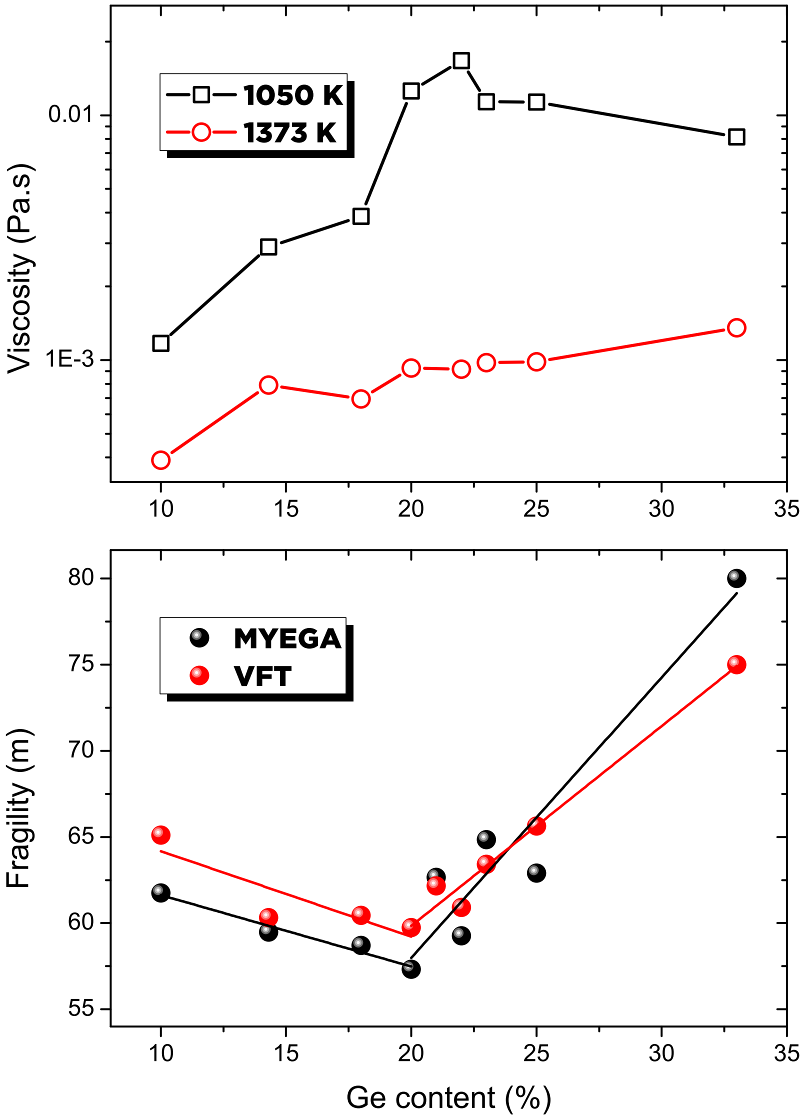

Figure 4.11: SE estimated viscosities at 1050 K (black) and 1373 K (red) as a function of Ge content (upper panel). Fitted fragility values using MYEGA (equation 4.4.3)(black) and VFT functional (equation1.2.4) forms (red), as a function of Ge content (lower panel).

When represented as a function of temperature, it turns out (Fig. 4.11a) that for 1050 K the obtained anomalous dynamics obtained from the diffusivity or the jump probability (Fig. 4.9) induces an behavior for η that is also non-monotonic with Ge content. The viscosity shows, indeed, a continuous increase as the liquid becomes more cross-linked but, interestingly, exhibits a clear maximum for 22-23 % Ge that is correlated to the minimum in diffusivity (Fig. 4.6).

The larger viscosities for such select Ge compositions can lead to lower fragilities $\mathcal{M}$. In order to access this quantity ($\mathcal{M}$), and although we do not have data close to the glass transition for obvious numerical reasons, we can use the Mauro-Yue-Ellison-Gupta-Allen (MYEGA) form that predicts the behavior of η with temperature in supercooled liquids from:

$$\log \eta(T,x) = \log \eta_{\infty}(x) + \frac{K(x)}{T} \exp\left(\frac{C(x)}{T}\right) \tag{4.4.3}$$

where we have used the value $\log_{10} \eta_{\infty}$=-4 [188]. This permits to extract the fragility $\mathcal{M}$ as a function of Ge content for the Ge-Se melts, i.e. the low temperature behavior close to the glass transition from the high temperature numerical data. Results are shown in Figure 4.11b but do not compare favorably to experimental measurements [189, 190, 187]. Indeed, the fitted values from the MYEGA equation (4.4.3) or from the Vogel-Fulcher-Tamman (VFT) equation $\eta = \eta_{\infty} \exp[A/(T-T_0)]$ lead to fragility values that are overestimated (Fig. 4.11b) by a factor 3, i.e. we find from the MYEGA fit $\mathcal{M}$=58 for $Ge_{18}Se_{82}$ but experimentally it is found $\mathcal{M}$=21 [189] for $Ge_{17}Se_{83}$. Despite these differences, a non-monotonic trend for $\mathcal{M}$ is obtained as a function of Ge content that is merely consistent with the trend obtained experimentally, i.e. a fragile to strong modification of Ge-Se melts is observed at Ge compositions found between 20 and 25 % Ge.

Given that other dynamic quantities exhibit for these composition an anomalous behavior, one can, finally, argue that the strong glass-forming Ge-Se liquids exhibit a reduced diffusivity and an increased viscosity for select compositions, these behaviors being accompanied by additional anomalies that are detected from the Van Hove correlation function and the intermediate scattering function.

This physical picture revealing the central role played by network rigidity is consistent with conclusions drawn from a compilation of fragility data on network glasses including chalcogenides and oxides for which the location of the isostatic composition is determined from calorimetric measurements [191, 189, 192, 193]. These liquid fragilities are plotted in Fig. 4.13, and show that once the composition is rescaled with respect to the centroid x_c of the isostatic composition interval (for example, x_c =22.5%

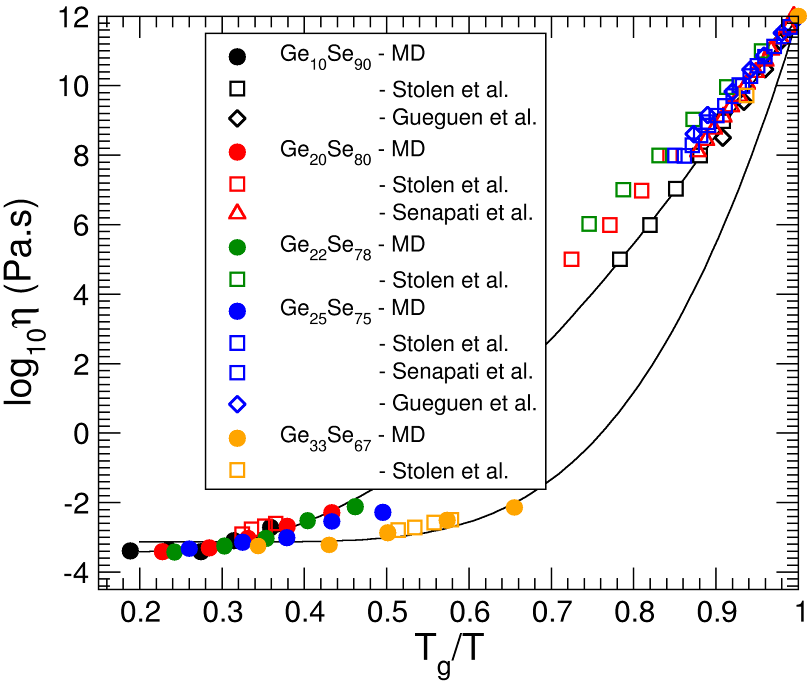

Figure 4.12: Comparison between the Stokes–Einstein calculated (filled symbols) viscosities at various Ge–Se compositions and experimental measurements of viscosity (open symbols) from Stolen et al. [185] Senapati et al [187] and Guegen et al. [186] Note that only Stolen et al. have investigated the high temperature region where numerical data can be directly compared. The solid lines correspond to fits using the Mauro–Yue–Ellison–Gupta–Allen (MYEGA) equation4.4.3 that describes with an increased accuracy the high temperature viscosities as compared with alternative fitting functionals (for example, Vogel–Fulcher–Tamman, VFT) 1.2.4.

in Ge_xSe_{100-x}; [193]), all data exhibit a minimum in M at $x \sim x_c$. This not only emphasizes that rigidity affects the fragility evolution of melts, a qualitative correlation that has been reported in the literature for quite some time (ref. 3) and reference therein), but from Fig. 4.10, one also realizes that the spatial distribution of atomic scale interactions/constraints is a key feature for the understanding of transport properties during the glass transition. This conclusion can be only drawn from a detailed inspection of constraints, accessed from MD on individual atoms. Although further detailed analysis on the constraint behavior of, for example, organic glass formers is necessary, these results may indicate that liquids with non-directional bonding and, therefore, with a more probable heterogeneous distribution of interactions will lead to a much more fragile behavior.

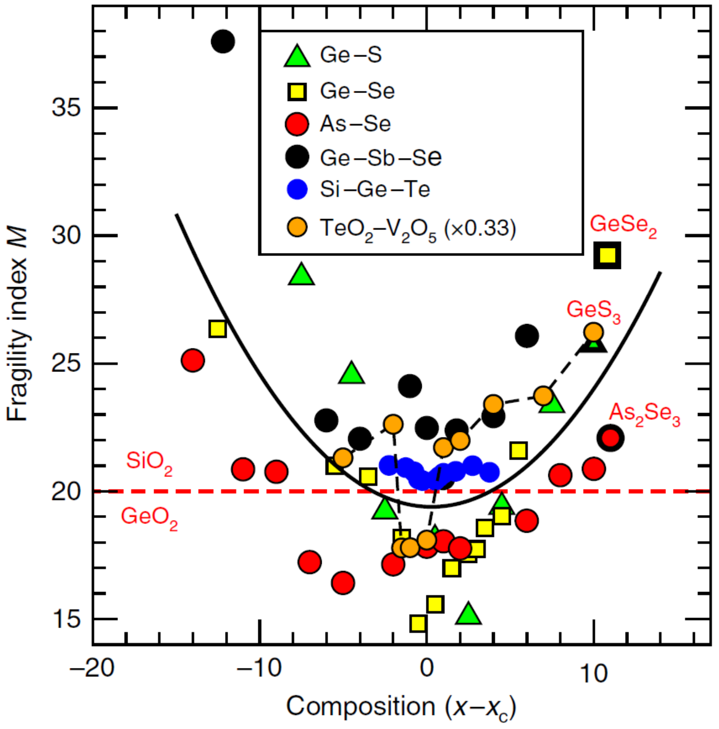

Figure 4.13: A summary of experimentally measured fragilities in glass network-forming melts. Experimental fragilities as a function of a rescaled composition corresponding to the centroid of the corresponding isostatic window (or Boolchand phase): Ge–S [191], Ge–Se [189], As–Se [192], Ge–Sb–Se [193], Si–Ge–Te. All display a minimum at or close to . Note that the minimum for Ge–Si–Te is clearly visible if represented on an appropriate scale [194]. The trend in composition for TeO_2–V_2O_5 is highlighted by a thin broken line (P. Boolchand, unpublished results). The solid line is a global quadratic fit to the whole data sets, and serves only as guide. Stoichiometric compounds are signaled.

4.4.1 Relaxation and interaction range

In this section we investigate the relaxation behavior of liquid Ge_xSe_{100-x} by examining the intermediate scattering function which is a quantity usually accessed with X-ray or neutron scattering [195, 196]. From MD simulations, the self intermediate scattering function $F(k,t)$ for the species α is given in equation 2.6.15 which is also the Fourier transform [152] of the Van Hove correlation function defined previously (equation 2.6.14). In Fig. 4.15, we represent the temperature dependence of $F_s(k,t)$ for a given composition at a fixed wave vector k=2.10 Å^{-1} that corresponds to the position [73] of the principal peak in the static structure factor $S(\mathbf{k})$. The salient features of $F_s(k,t)$ observed here for Ge-Se systems are comparable to those of other typical glass forming systems [151, 197, 198]. At higher temperatures (e.g. 1600 K), the relaxation process takes place in a single step Debye-like fashion. However, as the system is cooled down to lower T, the decay becomes more complex and cannot be fitted by a single exponential anymore, (e^{-t/τ_α}), where τ_α represents the structural relaxation time towards thermal equilibrium. At even lower temperatures, a typical β-relaxation plateau builds up [12], seen e.g. for t >1 ps at 800 K. This plateau extends to very long times and becomes of the order of the simulation time for 300 K. In fact, it is seen from the figure than 1050 K is the lowest temperature over which a full relaxation can be achieved on the 20-30 ps timescale, the time domain over which $F_s(k,t)$ becomes close to zero being associated with the α relaxation regime. Fig. 4.14 shows

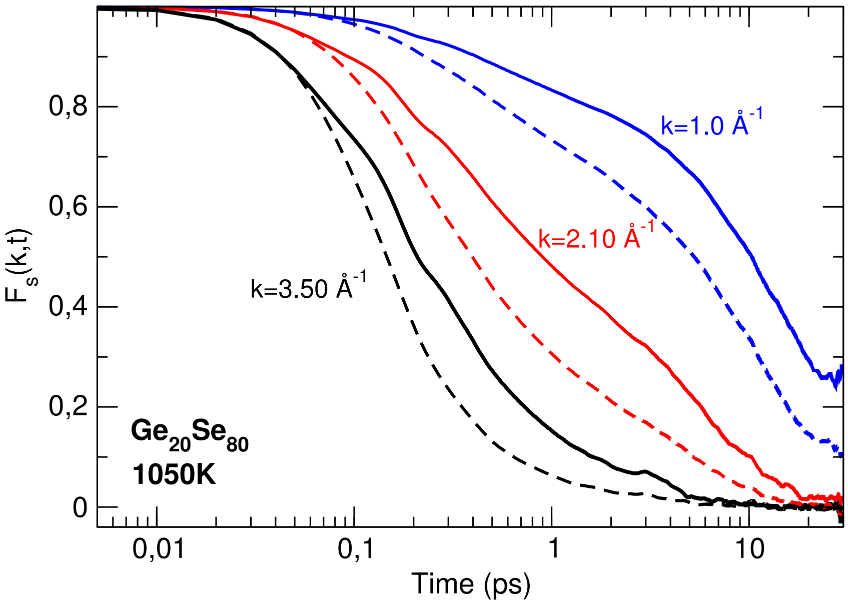

Figure 4.14: Reciprocal space vector dependence of $F_s(k,t)$ of Ge$_{20}$Se$_{80}$ at 1050 K for Ge (solid curves) and Se (broken curves).

the k vector dependence of $F_s(k,t)$ at 1050 K for a fixed composition (Ge$_{20}$Se$_{80}$). The represented values of the wave vector correspond to the positions of the FSDP (1 Å^{-1}), the principal peak (2.10 Å^{-1}, same as Fig. 4.15) and the secondary principal peak (3.50 Å^{-1}) of $S(\mathbf{k})$. As previously, one can notice a faster relaxation at a given time when the reciprocal lattice vector has a larger value, simply because smaller k involve relaxation on larger scales in real space which leads to larger relaxation times. The relaxation at k vectors of the principal and second principal peaks follow a nearly single step decay analogous to high temperature relaxation, whereas the FSDP related decay (k$\simeq$1.0 Å) obviously leads to a plateau behavior typical of a β-relaxation process. One then realizes that even after 30 ps of simulation time the system has not fully relaxed to $F_s(k,t)$=0 for k=1.0 Å^{-1}. Finally, in Fig. 4.16 we present the relaxation behavior investigated as a function of composition at 1050 K for selected compositions. It is seen

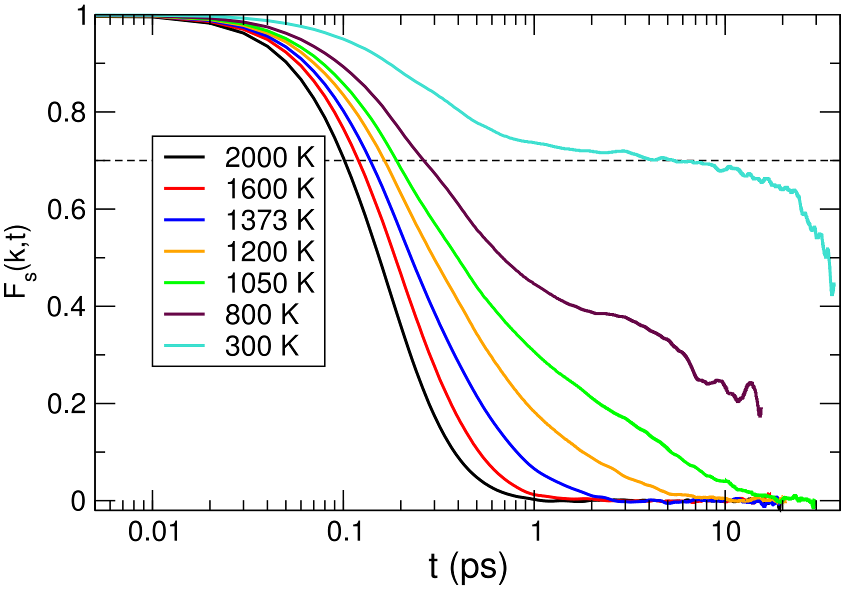

Figure 4.15: Reciprocal space vector dependence of $F_s(k,t)$ of $Ge_{20}Se_{80}$ at 1050 K for Ge (solid curves) and Se (broken curves).

that there is an enhanced slowing down of the relaxation that connects, indeed, with the anomalous diffusion interval mentioned earlier in this paper. In particular the $F_s(k,t)$ of $Ge_{22}Se_{78}$ exhibits a much slower dynamics and $F_s(k,t)$ is shifted to longer times, leading even to the presence of a β-relaxation plateau that is formed for both species, driven by a low diffusivity (Fig. 4.6) and jump probability (Fig. 4.9). In order to extract additional information from Fig. 4.14 and particularly, concerning the relaxation time, we fit the long-time behavior of $F_s(k,t)$ at low temperature (1050 K) by a stretched Kohlrausch-Williams-Watts (KWW) exponential decay $\exp[-(t/\tau_\alpha)^\beta]$ with τ_α the structural relaxation time and β the Kohlrausch exponent REF. The use of such a fitting form is justified by the fact that at this temperature the liquid obviously undergoes a complex relaxation dynamics that is certainly not of Debye type as in high temperature liquids. As mentioned above, an inspection of Figure 4.15 shows, indeed, that while a single exponential can account for the decay of $F_s(k,t)$ at high temperature, this is not possible in more viscous liquids as several relaxation steps are involved. For the α-relaxation process occurring in the long time limit when e.g. $F_s(k,t) < 1/e$, the use of the KWW fitting functional is, therefore, preferred. The value of the KWW parameter β <1 indicates that the decay of the spatial density correlations extends over a wide range in time [195, 196, 199, 200], and signals that the relaxation cannot be described by a simple exponential Debye relaxation. The analysis on the relaxation times as a function of composition at given temperature (1050 K) and selected k=2.1Å is summarized in Fig. 4.17. As the lighter Se atoms move faster than Ge atoms, they

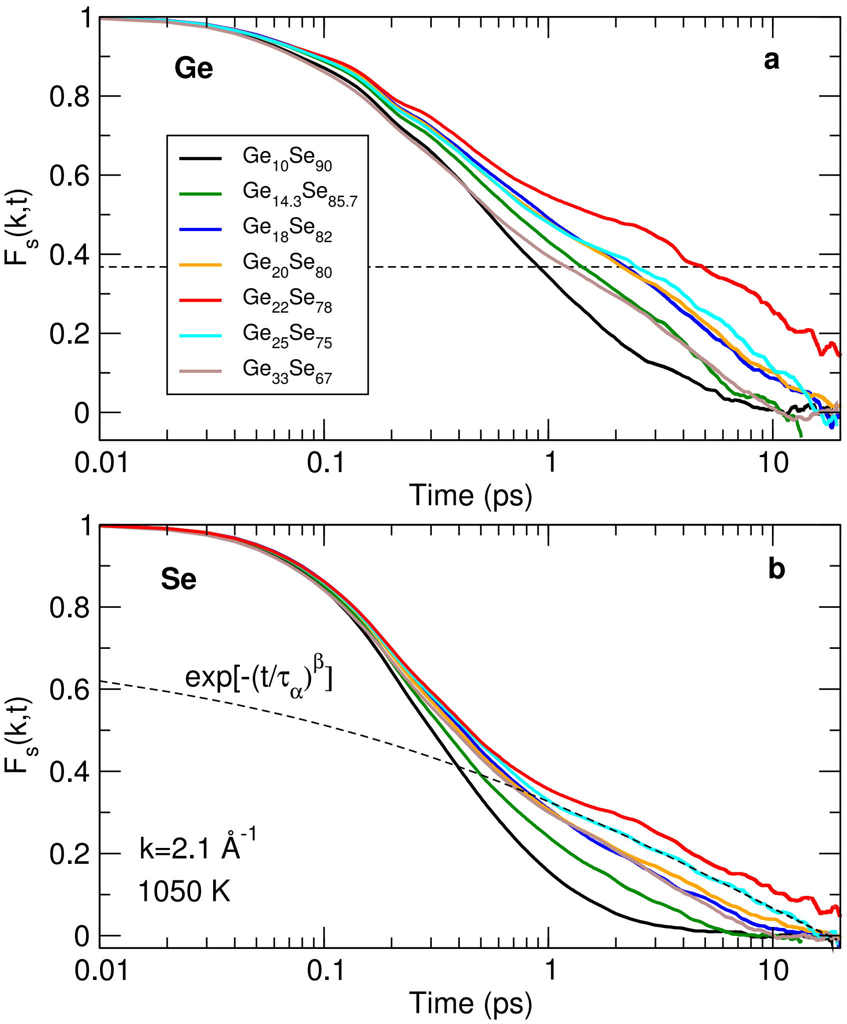

Figure 4.16: Self part of intermediate scattering function $F_s(k,t)$ of Ge (a) and Se (b) at 1050 K and k=2.10Å^{-1} for selected compositions. The horizontal solid line in panel a corresponds to the value e^{-1}, whereas the broken line in panel b shows the Kohlrausch fit at the long time limit of $F_s(k,t)$ for Ge$_{25}$Se$_{75}$

relax at shorter times. Again, with increasing Ge content a non-monotonic trend is detected that correlates with the one found for diffusion. In particular, the relaxation time for Ge species peaks at 22 %, in accordance with the minimum in jump probabilities of the atoms (Fig. 4.9). The same trend is observed at k=3.5Å^{-1}or Ge atoms (not shown). The results for τ_α obtained from the KWW fit are compatible with the simple estimate $F_s(k,\tau_\alpha) = 1/e$ (open circles, Fig. 4.16a) that is also used in the literature REF. Fig. 4.17a shows that the values obtained from this simple method (open symbols) are very close to those obtained from the KWW fit, and display the same behavior with Ge content. Results for the exponent β are shown in Fig. 4.17b and will discussed below given that β is also found to display a non-monotonic behavior with a deep minimum found at 22 % Ge.

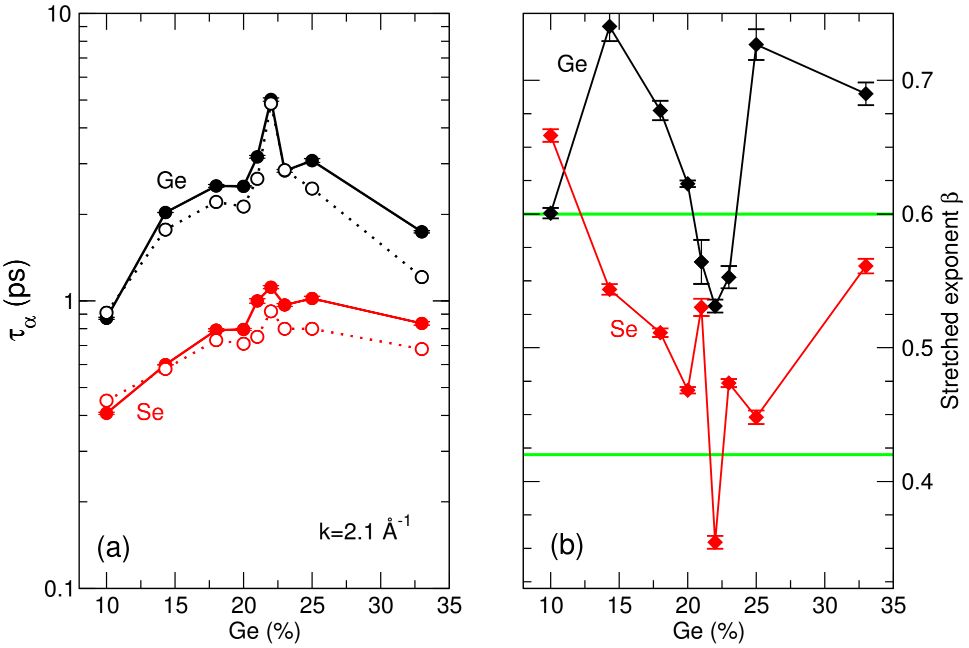

Figure 4.17: Fitted relaxation times τ_α (a) and stretched exponent β (b) of the (Ge,Se) species as a function of Ge content from the KWW fits. The open circles represents a simple estimate using $F_s(k, \tau_\alpha) = e^{-1}$. Error bars are of the size of the symbols. The green horizontal lines are predicted values for β from trap models of relaxation (3/7, 3/5) REF (see text for details).

Fig. 4.17b leads to additional information regarding the dimensionality of the relaxation. In the literature, the Kohlrausch exponent β is presented [199, 200] as the reflection of the degree of cooperativity of relaxation, the smaller the β the larger the collective behavior of atomic motion [151]. The important variation of β with Ge content indicates that substantial changes in the collective behavior manifest in the same region of interest at 18-22 %Ge. We note, indeed, that the variation of the Kohlrausch exponent $\beta(x)$ displays a trend that leads either to a broad minimum centered at $\simeq$ 22 % from the fit of the Se-related intermediate scattering function $F_s(k, t)$, or to a deep minimum between 18 and 25 % Ge for the Ge-related function. This evolution contrasts with previous experimental findings at low temperature for the exponent in the $\mathrm{Ge}_x\mathrm{As}_x\mathrm{Se}_{1-2x}$ ternary glasses measured in flexible measurements. Here, it has been found [201] that β steadily increases with Ge content to converge to a value of 0.60 for x >20 %.

At high temperatures (T > T_g), the single step Debye relaxation leads to a stretched exponent β $\simeq$1 but reduces as T decreases to T_g, i.e., $\beta(\mathrm{T} \rightarrow \mathrm{T}_g) < 1$. The reduction of β usually reflects the contraction of the configuration space available to the supercooled liquid, and its stabilization [151] due to structural arrest near T=T_g. Building on this statement, at a fixed network dimensionality one expects that an increase in the number of constraints or increase of Ge content will contract the configuration space given that floppy modes lead to tunneling states in the energy landscape [181], and this should lead to lower values for β. Fig. 4.17b obviously does not follow this anticipated behavior as the dimensionality is changing in a non-monotonic fashion with modifier content. Models of traps [202, 203] for tracer diffusion in a D-dimensional lattice show that β is related to the dimensionality d via:

$$\beta = \frac{D}{D+2} \tag{4.4.4}$$

and Phillips has shown that this relationship is satisfied for various molecular supercooled liquids and glasses [8] exhibiting either a 3D (β = 3/5) or a 2D relaxation (β = 1/2). In addition, for the case where an internal structural dynamics takes place, the dimensionality D must be replaced [8] by an effective one, D_{eff} that depends on the range of the interactions, short- or long-range. For instance, it has been shown that the relaxation of an industrial sodium borosilicate glass decays with a KWW function and a stretching exponent β= 3/7=0.42 that corresponds exactly to the value predicted by diffusion-trap models for a relaxation dominated by long-range pathways [204]. Conversely, for a relaxation dominated by short-range interactions, β has been predicted to be equal to 3/5=0.60 [8]. A recent MD study on energy relaxation [205] has shown that the potential energy relaxation in model silicates also follows a stretched exponential decay with this particular stretching exponent of β=3/5.

In the present Ge-Se system, Fig. 4.17b exhibits a non-monotonic behavior for both the Se- and Ge-based relaxation dynamics encoded in $\beta(x)$. Both species show, indeed, a larger value for β for Se-rich or Ge-rich compositions, with β $\simeq$0.6-0.70 and β $\simeq$0.60 for Ge and Se, respectively. This value (β=0.60) corresponds to the situation in which all the relaxation channels are active [8], and this is typically observed for the stress relaxation in glasses [206, 207], and for energy relaxation [205], while being also recovered here. In fact, flexible glasses achieve energy release from low-frequency modes, whereas Ge-rich glasses display an increased stress due to the higher bond density. However, for the same range of compositions (20-23 %) where all dynamic anomalies are detected, β shows a minimum that becomes close to the value of β=0.42 for the Se-related parameter, and such stretched exponents are typical of long-range pathways for relaxation [8] that is usually embedded in volume relaxation [204]. One is, thus, led to believe that Ge-Se compositions found in the region 18-23 % display a rather different dynamics, associating long-range interactions and volume relaxation rather than short-range and energy relaxation.

4.5 Summary and Conclusions

Ge_xSe_{100-x} liquids and glasses are ideal candidate systems for testing the predictions of flexible to rigid transitions. The numerical characterization of their structural, electronic and vibrational properties has been reported in detail both in the glassy and liquid state, and the general picture in a structural evolution made of a progressive cross-linking of $GeSe_{4/2}$ tetrahedra into the basic network of Se chains that is found in elemental selenium that leads to a fully 3D network structure at the stoichiometric composition (33 %). However, despite these contributions, not much has been achieved regarding dynamical properties on $GeSe_2$. In fact, we are not aware of any previous work on simulated dynamic properties in a fashion similar to the numerical studies of e.g. silica [178] (see however [208]). Much less is also known on such properties on non-stoichiometric chalcogenides although many different experimental studies have emphasized the crucial role of composition on glass relaxation, enthalpic changes at the glass transition [42] and fragility [185]. In the present contribution we have used *ab initio* Molecular Dynamics (AIMD) simulations to investigate in detail the effect of Ge content on dynamic properties of Ge_xSe_{100-x} melts by focusing on nine compositions with x $\leq$33 %. These compositions belong to the elastic phases predicted by Rigidity Theory, i.e. a flexible Se-rich phase which contains local deformation modes, a Ge-rich phase which is stressed rigid and locked by an important bond density, and a compositional interval, the intermediate phase (20-25 %), that has been revealed from a series of optical and calorimetric measurements.

Having validated the structural models obtained by AIMD in the liquid and glassy state by comparing with available experimental data from neutron diffraction, we have then investigated the dynamic properties of the melts by calculating diffusivities, activation energies for diffusivity, relaxation times, etc. All indicate that melts at the lowest equilibrated temperature (1050 K) already contain features of the low temperature elastic phases and the rigidity status of the underlying network. This result seems in line with a previous study on different glass-forming liquids [209], showing that the fragility of supercooled liquids should be linked with the elastic properties of the corresponding glass, quantified from the non-ergodicty parameter accessed from inelastic x-ray scattering. Using the connection with dimensionality and relaxation pathways established by Phillips [8], we have finally shown that the behavior of the Kohlrausch exponent β may reflect that the relaxation is also driven by the nature of the underlying interactions. Specifically, for compositions belonging to the intermediate phase (20-25 %), the Se-related relaxation degree yields $\beta \simeq 3/7$, a value that is typical of long-range pathways for volume relaxation. On the contrary, for Se-rich or Ge-rich compositions, one has rather $\beta \simeq 3/5$ and this indicates dynamics driven by short-range interactions.

Chapter 5

Pressure Induced Polyamorphism in Vitreous Ge-Se

Abstract

Pressure induced structural modifications in vitreous $\mathrm{Ge_xSe_{100-x}}$ (where 10 $\leq$x$\leq$ 25) are investigated using XAS along with supplementary (XRD) experiments and ab initio molecular dynamics (AIMD) simulations. Universal changes in distances and angle distributions are observed when scaled to reduced densities. All compositions are observed to remain amorphous under pressure values up to 42 GPa. The Ge-Se interatomic distances extracted from XAS data show a two-step response to the applied pressure; a gradual decrease followed by an increase at around 15-20 GPa, depending on the composition. This increase is attributed to the metallization event that can be traced with the red shift in Ge K edge energy which is also identified by the principal peak position of the structure factor. The densification mechanisms are studied in details by means of AIMD simulations and compared to the experimental results. The evolution of bond angle distributions, interatomic distances and coordination numbers are examined and lead to similar pressure-induced structural changes for any composition.

5.1 Introduction

Compression-induced structural modifications in glasses are of high importance due to the fact that macroscopic properties such as conductivity or compressibility are directly affected by the local atomic rearrangements of the phases despite the fact that chemical composition remains the same. In addition, it is still an unsolved issue weather these polyamorphic transitions can be considered as an extension of the liquid-liquid transitions. The effect of pressure on chalcogenide glasses, in particular in the Ge-Se system are discussed in section 1.4.2. Despite the experimental findings and simulations carried out regarding the pressure-induced structural changes in $GeSe_2$ and $GeSe_4$ glasses, a complete understanding of the underlying densification mechanisms leading to the AATs in Ge_xSe_{100-x} glasses is still lacking. Here we report results of a comprehensive study of the polyamorphic transitions in vitreous Ge_xSe_{100-x} with a detailed description of the structural modifications using a combination of X-ray absorption spectroscopy (XAS), XRD and *ab initio* molecular dynamics (AIMD) simulations under pressure up to 41.4 GPa. Our results provide a thorough insight of the atomic packing rearrangements triggered during the AAT over a range of compositions including flexible and optimally rigid networks.

5.2 XRD

XRD results for $Ge_{25}Se_{75}$ with increasing pressure as an example for all compositions are shown in Fig. 5.1 a). A strong diamond diffraction peak due to diamond anvil is observed at q=3.04 Å^{-1}, which was subtracted through the empty cell measurement from the measured XRD spectra of the samples in order to find the peak positions reliably. The q range of the diffractograms allows one to distinguish the typical features of Ge_xSe_{1-x} glasses; namely the first sharp diffraction peak (FSDP) located $\sim$ 1.0 Å^{-1} which has been attributed to Ge-Ge correlations [171] and the first principal peak (PP) at $\sim$ 2.0 Å^{-1} in agreement with the values found using neutron or X-ray diffraction in previous studies of Ge-Se glasses under pressure. With increasing pressure, the FSDP loses its intensity and vanishes around 4 GPa due to the collapse of the network structure whereas the PP notably gains intensity, sharpens and shifts to higher q values. It has been argued that the intensity of the principal peak in glasses can be attributed to the development of the extended range ordering during densification controlled by Ge-Se and Se-Se correlations[210].

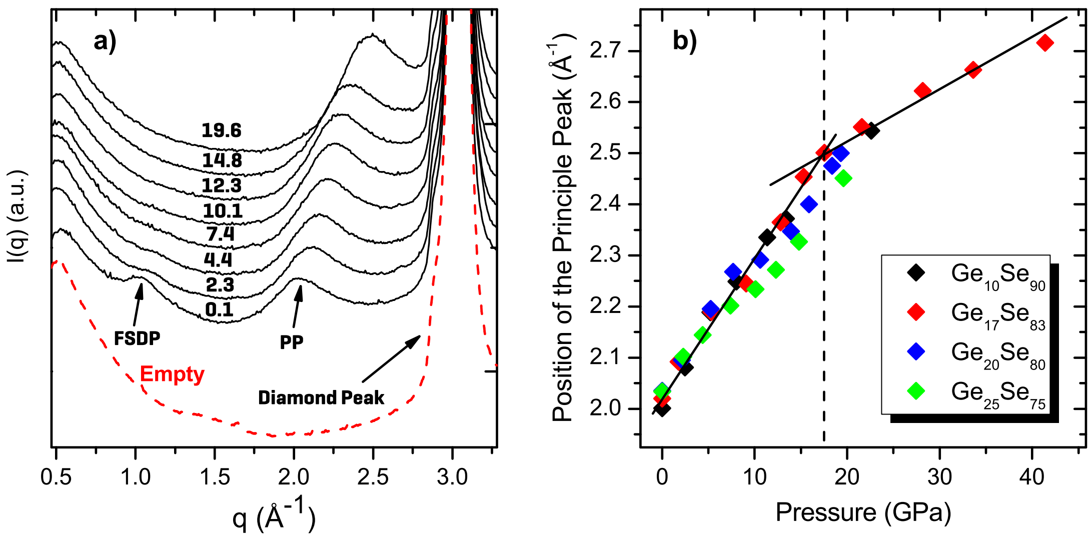

Figure 5.1: a) X-ray diffraction patterns of $Ge_{25}Se_{75}$ with increasing pressure (written on the continuous curves in GPa unit) and of the measured empty cell (red dashed line). b) The pressure dependence of the principal peak position of the XRD patterns for Ge_xSe_{1-x}. The black solid lines are guides to the eye, marking the high and low pressure regimes while the dashed lines indicate the transition in $Ge_{17}Se_{83}$ glass.

No sign of crystallization was observed up to a maximum pressure of 41.4 GPa for $Ge_{17}Se_{83}$ and up to 20 GPa for the other compositions studied. The PP positions that have been found through Gaussian peak fits as a function of increasing pressure are given in the Fig. 5.1 b). It can be seen that at ambient pressure the position of the PP increases as the network stiffens (i.e. increasing Ge content). A more detailed analysis shows that two different trends exist in the densification of $Ge_{17}Se_{83}$ which could be traced with the linear line . A rather fast increase of the PP position with a slope of 0.0267 ± 0.0015 Å^{-1}GPa^{-1} and a slow down having a slope of 0.0098 ± 0.0008 Å^{-1}GPa^{-1} after $\sim$ 15 GPa. This change in slope indicates the existence of a pressure induced transition with structural modifications.

5.3 EXAFS

X-ray absorption near edge structure (XANES) spectra at Ge and Se K edge for vitreous Ge_xSe_{1-x} at ambient pressure are shown in Fig. 5.2 a) and 2 b), respectively. The spectrum for each composition is shifted by 0.25 at the μ(E) axis. At the Ge K edge, a prominent absorption peak implying the transition between 1*s* orbital and the unoccupied states (the white line) to be located at ~ 11.107 keV with a shoulder peak found at ~ 11.113 keV. The intensity of the shoulder peak is observed to decrease and eventually vanish under pressure (not shown). Similarly at Se K edge, a strong absorption peak is located at ~ 12.657 keV followed by a shoulder at ~ 12.665 keV. Fig. 5.2 c) and d) shows the EXAFS spectra of $Ge_{17}Se_{83}$ glass at selected pressures at Ge K and Se K edges, respectively. The changes in the oscillations with increasing pressure can be seen clearly. The evolution of the average Ge-Se interatomic distance for

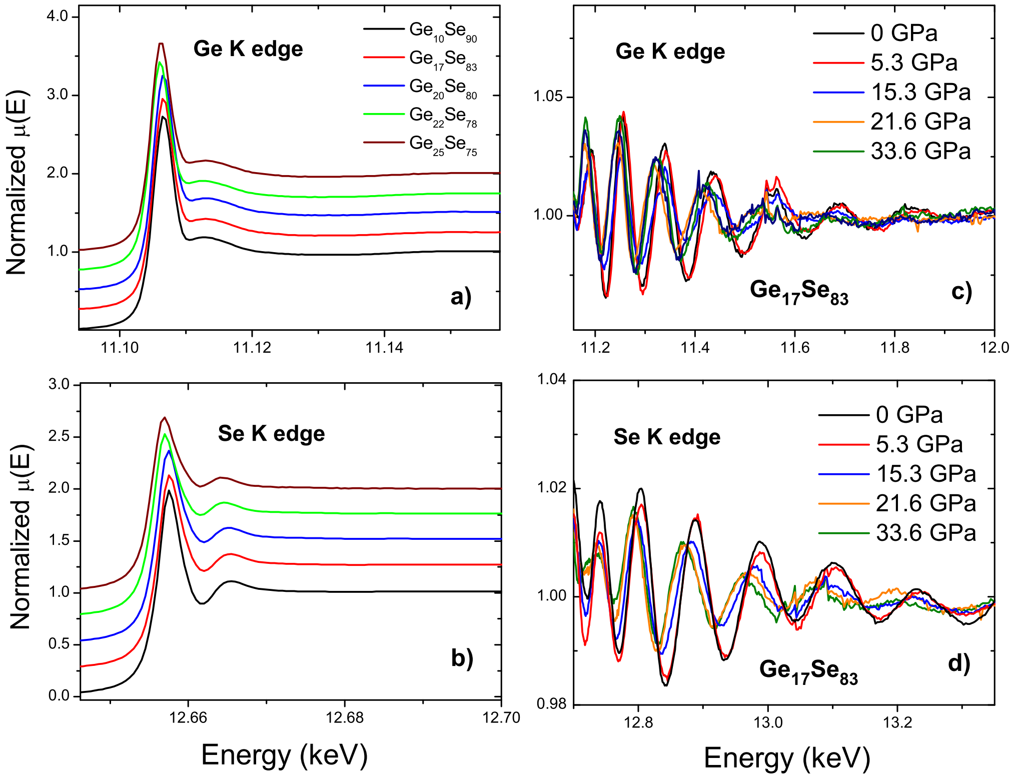

Figure 5.2: Normalized X-ray absorption spectra at the a) Ge K edge and b) at the Se K edge of amorphous Ge_xSe_{1-x} at ambient pressure. EXAFS oscillations of $Ge_{17}Se_{83}$ at the c) Ge K edge and d) at the Se K edge under selected pressure points collected using DAC.

$Ge_{17}Se_{83}$ and $Ge_{20}Se_{80}$ as a function of increasing pressure extracted from EXAFS data is compared with the AIMD results for $Ge_{18}Se_{82}$ in Fig. 5.3 a). Here we provide selected compositions to represent the structural response in terms of the average Ge-Se bond length. For $Ge_{17}Se_{83}$ at pressures below 13 GPa the average Ge-Se bond length shortens by about 0.02 Å. This bond compression is followed by an abrupt increase in Ge-Se bond length that is observed in the pressure range 15 GPa $\leq$ P $\leq$ 20 GPa resulting in an elongation of about 0.09 Å. An increment of 0.00725 Å^2 in the variance parameter σ^2 accompanies the sudden change in the Ge-Se bond length associated with the higher disorder in the distribution of the first shell neighbors. After reaching a maximum around 22 GPa, the average bond length decreases with a parabolic dependence on pressure. Thereby, this compression suggests that the high pressure modification has already been achieved with the sudden increase in the Ge-Se interatomic distance corresponding the slope change in the PP position of XRD pattern. Similarly for $Ge_{20}Se_{80}$ a bond compression is followed by a sudden increase in the Ge-Se distance at around 17 GPa and continues to increase up to $\sim$ 20 GPa, reaching a value of $\sim$ 2.44 Å. This result is inline with the previous study on $Ge_{20}Se_{80}$[77]. In contrast to $Ge_{17}Se_{83}$, due to lack of pressure points at P $\geq$ 20 GPa, the decrease of Ge-Se in the high density amorphous (HDA) phase is not observed. Nevertheless, further increase in the applied pressure should lead to a bond compression in the high-pressure structural motifs as shown for $Ge_{17}Se_{83}$. At this stage, in the light of XRD and EXAFS results under pressure, evidence of a threshold behavior in the structural response of $Ge_{17}Se_{83}$ to the applied pressure is detected around 17 GPa both in reciprocal and real space. The AIMD results of $Ge_{17}Se_{83}$ agree well with the experimental under pressure, providing a very similar trend. Note that the Ge-Se distance at ambient pressure is underestimated compared to the values extracted from EXAFS. These minor differences that occur due to the local dependence of the exchange correlation kernel f_{xc} on the electronic density are generally accepted in AIMD simulations as noted in earlier studies [211, 49]. Detailed investigations on different bond lengths upon compression are discussed in following sections. The average Ge-Se distance decreases under pressure values up to $\sim$ 10 GPa. Subsequent to this decrease, a dramatic bond elongation is observed upon further compression and around 15 GPa, the average Ge-Se bond length recovers to its ambient pressure value. This increment is followed by a similar rate of change until 22 $\sim$ GPa and eventually a drop in the slope of the curve is observed towards 32 GPa. Invariably, other flexible compositions that are generated by AIMD have shown a similar behavior under pressure ; an initial bond compression in the low density amorphous (LDA) phase in the early stages of densification followed by an evident transition monitored by an increase in the average Ge-Se bond length.

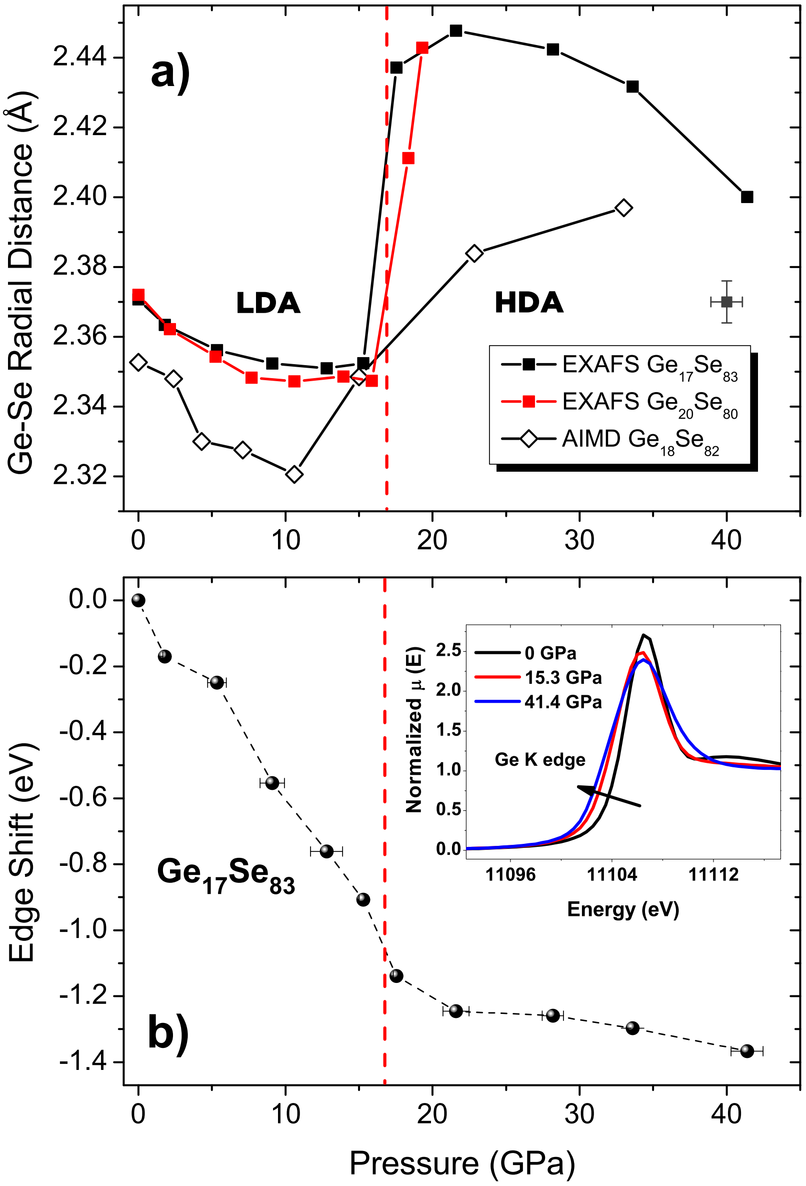

Figure 5.3: a) Evolution of the Ge-Se interatomic distance as a function of increasing pressure. The filled symbols represent $Ge_{17}Se_{83}$ (black) and $Ge_{20}Se_{80}$ (red). The open diamond symbols are AIMD results for $Ge_{18}Se_{82}$. The estimated error bars are shown separately in the graph. The red dashed line corresponds to the intercept of low and high pressure regimes shown by the pressure dependence of the PP position in Fig. 5.1 b). b) Energy decrease in the Ge K absorption edge position with increasing pressure of $Ge_{17}Se_{83}$. In the inset, the XANES spectra of selected pressures are compared to illustrate the edge shift.

Fig. 5.3 b) reveals the pressure dependence of the energy variation in Ge K edge position of $Ge_{17}Se_{83}$. A gradual shift in the edge position towards lower energies of about ∼-1.4 eV is followed by a rather slower decrease at P $\geq$ 20 GPa. The negative shift in the edge position is attributed to the semiconductor to metal transition which was shown in chalcogenides under pressure with EXAFS[90, 91] and electrical conductivity[77] measurements. In the inset of Fig. 5.3 b) the clear change of the red shift is demonstrated at selected pressures. The closing of the band gap is valid for all compositions under consideration. In contrast with the Ge K-edge shift towards lower energies, Se K-Edge XANES spectra revealed no significant change in the edge position upon compression for all compositions, as observed in earlier studies on the stoichiometric compound $GeSe_2$ [90]. Another feature observed in Ge K edge XANES for the compositions under consideration is the area decrease in the shoulder peak of the white line. Previous studies have interpreted as the angular variations between tetrahedra [90, 212]. On the other hand, the shoulder peak in the Se K edge XANES spectra is observed to shift to higher energies (i.e. increasing about ∼ 6.5 eV up to 19.3 GPa for $Ge_{20}Se_{80}$) which may be an indication of the changes in the inter-layer Se-Se correlations.

5.4 Equation of State

We have analyzed the structural changes in terms of AIMD simulations in order to track the alterations in the atomic arrangements responding to the applied pressure. In Fig. 5.4 we provide the calculated volume change of glassy Ge_xSe_{1-x} AIMD trajectories as a function of pressure and compare them with experimental measurements where available. The results show that the equation of state of AIMD generated amorphous Ge_xSe_{1-x} are very well reproduced. The simulation data were fitted by both second and third-order isothermal Birch Murnaghan (BM) equation of state (EoS) ; for for $Ge_{20}Se_{80}$ the fits yields a bulk modulus B_0 of 10.51 ± 0.31 GPa and 11.04 ± 0.76 GPa with the first pressure derivative B_1 being 4.25 ±0.15, respectively. These results agree well with the experimental values with B_0 = 10.4 ±0.14 GPa and B_1 = 6.0 ±0.11 for $Ge_{20}Se_{80}$[93]. As for $Ge_{25}Se_{85}$, a second-order BM fit gives a B_0 of 10.64 ± 0.18 GPa. Note that these values were obtained by fitting to all pressure points. It has been shown earlier that LDA phase has a smaller bulk modulus compared to that of high density amorphous (HDA) phase [77]. In this respect a value of 9.44 ± 0.02 GPa is obtained for $Ge_{20}Se_{80}$ when a second-order BM EoS is fitted in a range of 0 to 9.7 GPa,where the LDA to HDA transition is detected. We will discuss the issue further

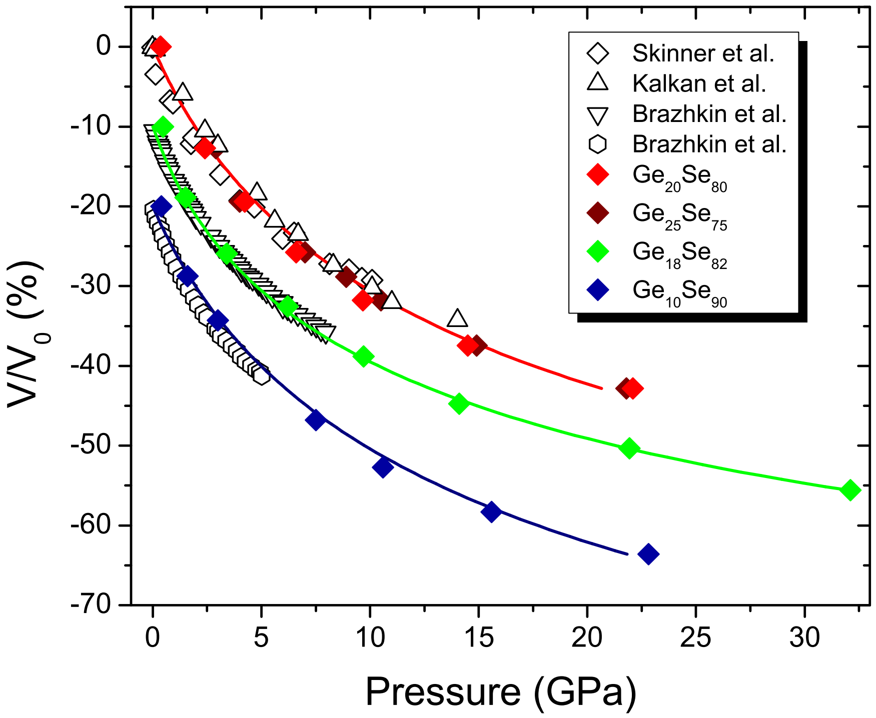

Figure 5.4: The pressure-volume equation of state for amorphous Ge$_x$Se$_{1-x}$. The results obtained by AIMD (filled diamond symbols) are compared to the measured data of Ge$_{20}$Se$_{80}$ [77, 93], Ge$_{17}$Se$_{83}$ and Ge$_8$Se$_{92}$[88] (open symbols) The solid lines represent third-order Birch-Murnaghan equation of state fits to the simulation data and the corresponding data are presented with 10% internal displacement in the reduced volume axis.

the following sections. Similarly a LDA bulk modulus is calculated as 11.09 ± 0.23 GPa for Ge$_{18}$Se$_{82}$ which is in good agreement with the result obtained by a direct volumetric stduy for a similar composition Ge$_{17}$Se$_{83}$ yielding a bulk modulus of 11 GPa[88].

5.5 Pair Distribution Functions

The computed real space properties of Ge$_{25}$Se$_{75}$ are presented in Fig 6. The evolution of coordination numbers with increasing pressure scaled to reduced densities, the density at a given pressure point, ρ, divided by the density at ambient pressure, ρ_0, is shown in Fig 6 a). The coordination numbers at ambient pressure calculated by AIMD follow the 8-N rule; Ge having 4 and Se having 2 neighbors in the first shell, and effectively agrees well with the relation: $\bar{n} = 2 + 2x$, where x is Ge mole fraction for all the compositions studied (eg. $\bar{n}_{Ge_{20}Se_{80}} = 2.4$ and $\bar{n}_{Ge_{10}Se_{90}} = 2.2$). During compression $\bar{n}$ changes slightly in the early stages of densification. However, a distinguishable coordination change takes place at around ρ/ρ_0 ~1.4. The coordination of Se atoms markedly increases which is accompanied by the increase of Ge coordination at $\rho/\rho_0 \sim 1.6$. These changes are connected to the transition of the low-pressure to high-pressure modification. During this stage Ge atoms reach an octahedral coordination (with a considerable fraction of five fold Ge) while the Se coordination increases and majority of the atoms become 3-fold coordinated (again with some fraction of 4-fold Se). At about 22 GPa the average coordination of Ge and Se atoms reach to 4.87 and 2.59, respectively. The calculated pressure dependence of the partial pair distribution

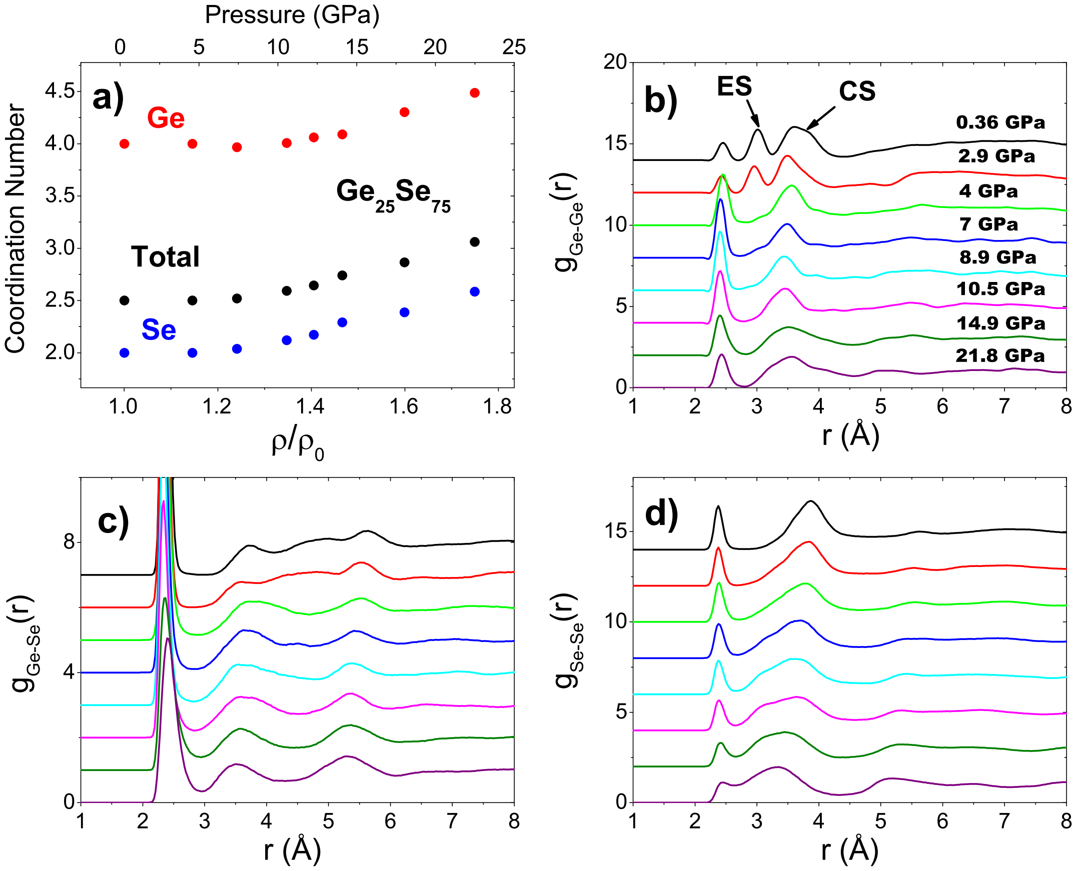

Figure 5.5: AIMD results of $Ge_{25}Se_{75}$. a) The reduced density dependence of the coordination number. Here, the cut-off distances for the calculation of the coordination numbers are defined by the position of the first minimum of the total pair distribution functions, $r = 2.85$ Å. The gradual increase in the coordination of Ge and Se atoms becomes pronounced around $\rho/\rho_0 = 1.4$. The calculated partial pair distribution functions b), c) and d) as a function of pressure. Note that the evolution of Ge-Se bond length could also be traced in a trend similar to what is observed in Fig. 5.3

functions (g_{ij} where $i, j =$ Ge,Se) of $Ge_{25}Se_{75}$ are shown in the other panels of Fig. 5.5. The typical features of the pairs that were shown earlier with neutron diffraction in Ge-Se glasses [73] are well reproduced. For the case of g_{GeGe}, three main peaks are noticed at ambient pressure at 2.46 Å 3.02 Å and 3.61 Å respectively. These values agree with earlier findings[49]. The first peak is associated with the homopolar Ge-Ge bonds. These homopolar bonds are absent at ambient pressure for the other compositions studied that are generated by AIMD simulations due to the fact that they are Ge deficient as compared to $Ge_{25}Se_{75}$ (not shown). However during the quenching of the liquid state, some of these features may be trapped and preserved in the glassy state. Thus for the simulations of the Ge deficient compositions, the independent quenches which contained no 'wrong bonds' were used for cold compression. Nevertheless, for $Ge_{18}Se_{82}$, homopolar Ge-Ge bonds were unavoidable, leading to a partial coordination number $n_{GeGe} \sim 0.09$ for each quench to ambient pressure. The second peak of g_{GeGe} is assigned to the edge sharing (ES) tetrahedra distances whereas the third peak indicates the corner sharing (CS) bonding distances.

During compression, the first peak associated with homopolar Ge-Ge bonding distance remains nearly the same below 3 GPa and notably increases until reaching a maximum at around 9 GPa. Up to this point the homopolar Ge-Ge bonding has an overall shortening of about 0.06 Å. Further densification causes a decrease in the intensity. Unlike the first peak, the ES peak loses intensity upon compression while shifting to shorter distances, and at 4 GPa, it completely vanishes. For the case of the CS tetrahedra distances, again a two stage behavior is observed ; a shift to shorter distances in the peak position until 10.5 GPa followed by an increase upon further compression.

The main feature of the g_{GeSe} is the strong peak located at 2.36 Å which was also found at the same distance for the stoichiometric compound $GeSe_2$ by previous neutron diffraction[73] and EXAFS[90] studies. This peak defines the Ge-Se correlation distances within a tetrahedron. Upon compression significant changes take place in the peak shape and position. In particular, the intensity of the peak slightly decreases at around 3 GPa. This decrease is followed by a substantial intensity loss at 4 GPa to nearly half of the value of the peak at ambient pressure which is then followed by a gradual intensity loss until 8.9 GPa. Another significant drop is observed at this stage, corresponding to the rapid coordination increase and the peak broadens evidently. The evolution of peak position of the first peak of g_{GeSe} with increasing pressure is remarkable. A bond compression similar to what is observed in the Ge-Se pairs in $Ge_{17}Se_{83}$ extracted from EXAFS signals is present below 8.9 GPa. Up to this point the Ge-Se interatomic distance decreases of about 0.04 Å. Subsequent to this drop, a marked increase in the Ge-Se distance can be traced accompanying the rapid coordination increase indicating the high pressure modification transition. At the highest pressure, Ge-Se distance reaches $\sim$ 2.40 Å . Finally g_{SeSe} e•xhibits two main peaks at the ambient pressure. The first peak is located at 2.37 Å defining the homopolar Se-Se bond whereas the second is found at 3.85 Å and corresponds to the distances associated with the edge distances of tetrahedra. The intensity of the homopolar peak decreases with increasing pressure. The bond length again starts to increase strongly after 8.9 GPa in a similar manner to Ge-Se bond length. On the other hand the second peak shifts to shorter distances under compression. The distance corresponding to the edges of tetrahedra decreases gradually to reach a minimum value of 3.40 Å at 21.8 GPa. The detailed analysis on the atomic trajectories have shown that this distance correspond to as the edges of an octahedron. A shoulder peak at around $\sim$ 3.05 Å evolves until 10.5 GPa and then merges with the main peak that corresponds to the octahedra edges. This peak is associated with the distance of three or four fold Se-Se correlations connecting separate four or five atom rings that consist of one or more Ge atom that will eventually transform into octahedra. Note that even at 21.8 GPa a full octahedral state is not achieved.

5.6 Neighbor Distances and Bond Angle Distributions

The pressure modifications reflected on the interatomic distances that are shown for $Ge_{25}Se_{75}$ are representative for the other compositions under consideration. The partial pair distribution functions respond in a similar way to the applied pressure. In particular AIMD results showed that the ES peak of the g_{GeSe} vanishes for all compositions and homopolar Ge-Ge peak appear while the CS peak shifts to shorter distances. Moreover, the average Ge-Se bond length evolution extracted for $Ge_{20}Se_{80}$ and $Ge_{10}Se_{90}$ is inline with Fig. 5.3 a) : a gradual bond compression followed by a significant increase around $\sim$ 15 GPa. To get further insight on the densification mechanism, we now turn to the detailed investigation of the neighbor distance variations under compression. Fig. 5.6 a) shows the computed evolution of the average distance decomposed into the neighbors around a Ge atom of selected composition as a function of reduced density. As the applied pressure increases the bond length of the second shell neighbors, the fifth and the sixth neighbors, decrease in a parabolic behavior for all compositions. On the other hand, the first shell neighbors display smaller variations. An intriguing feature is that the distance evolution of the second shell neighbors starts to decrease more rapidly around $\rho/\rho_0 = 1.4$, where they effectively become the part of the first shell. Consequently these results show that the transition from the low pressure to the high pressure modification is triggered by the merging of the second shell neighbors which is followed by a substantial increase in the coordination number at a certain threshold and evidently this mechanism applies to all the compositions under consideration. We now turn to bond angle distributions (BAD) to provide further

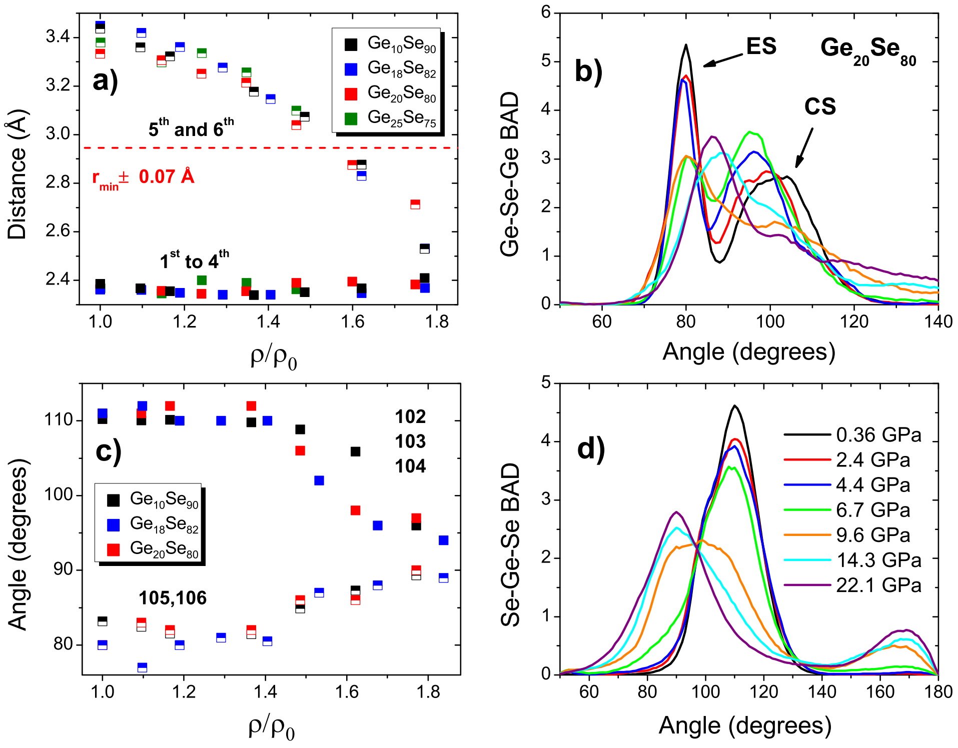

Figure 5.6: a) Calculated interatomic distances evolution of selected compositions as a function of ρ/ρ_0 the filled squares shows the average distances within the first shell consisting of 4 neighbors while the half filled circles show the average distances of the 5th and the 6th neighbors. The dashed red line corresponds to the minimum r_{min} of the pair correlation function, and serves to split the first from the second shell of neighbors. b) Computed bond angle distributions Ge-Se-Ge with increasing pressure for $Ge_{20}Se_{80}$ c) Reduced density dependence of the angle distributions split into neighbor number of the selected compositions obtained from CPMD simulations. Here 0 stands for a central Ge atom in a tetrahedron and the numbers 1,2,3,4,5 and 6 represent the neighbors (i.e. 102 indicates the angle between the first and 2nd neighbor of the central Ge atom labeled 0. d) Computed bond angle distributions Se-Ge-Se with increasing pressure for $Ge_{20}Se_{80}$. The color code in panel b) is the same as in panel d).

insight into the densification of Ge_xSe_{1-x}. Fig. 5.6 shows the variations in the BAD of $Ge_{20}Se_{80}$ under pressure. Here $Ge_{20}Se_{80}$ illustrates the common behavior observed in all compositions generated by AIMD. Fig. 5.6 b) shows that at ambient pressure, two main peaks are present in the Ge-Se-Ge BAD located at ∼80° and 100 ° that are associated with ES and CS tetrahedra, respectively. During compression, the former loses intensity in contrast to the increment in that of the latter. At around 9.6 GPa the peaks merge and further compression leads to a broad peak centered at 90° with a shoulder at 100° as the system globally transforms from a tetrahedral to an octahedral coordination. A closer look into the atomic trajectories indicates that the shoulder peak at 100° is associated with the Ge-Se-Ge angles in the rings that contain five atoms. Fig. 5.6 c) exhibits the Se-Ge-Se BAD under pressure. A strong peak centered at ∼ 110° defining the tetrahedra. The intensity of this peak reduces during the low pressure modifications analogous to the intensity loss as the Ge content increases [49]. An explicit intensity drop occurs from 6.7 GPa to 9.6 GPa and the peak position moves to ∼ 100 °. This change is connected to the marked increase in the coordination number. Further compression yields to the continuation of the shift towards smaller angles reaching to the octahedral angle, 90°(confirmed by the emergence of a smaller peak around 170-180 degrees). Fig 8 d) demonstrates the changes in BAD decomposed to the neighbor contributions around a Ge atom under pressure for selected compositions. The average BAD of the first shell neighbors, 102, 103 and 104 contributions, that are around ∼ 110° at ambient pressure remains nearly at the same angle with slight fluctuations until ρ/ρ_0 ∼1.4. During this pressure interval the average second shell contributions, 105 and 106, move around ∼ 80°. Remarkably, again, further densification after ρ/ρ_0 ∼1.4 induces a coalescence in the BAD of the first and the second shell neighbor contributions, reaching to 90°. At $\rho/\rho_0 > 1.4$, the increment in the BAD of the 105 and 106 contributions are somewhat similar. On the other hand a rather parabolic decrease is observed starting from ρ/ρ_0 ∼1.4 for the first shell neighbor contributions to BAD of $Ge_{10}Se_{90}$ unlike the compositions with higher Ge content for which the BAD in the first shell decays more rapidly to octahedral angle.

5.7 Octahedrality and Coordination Numbers

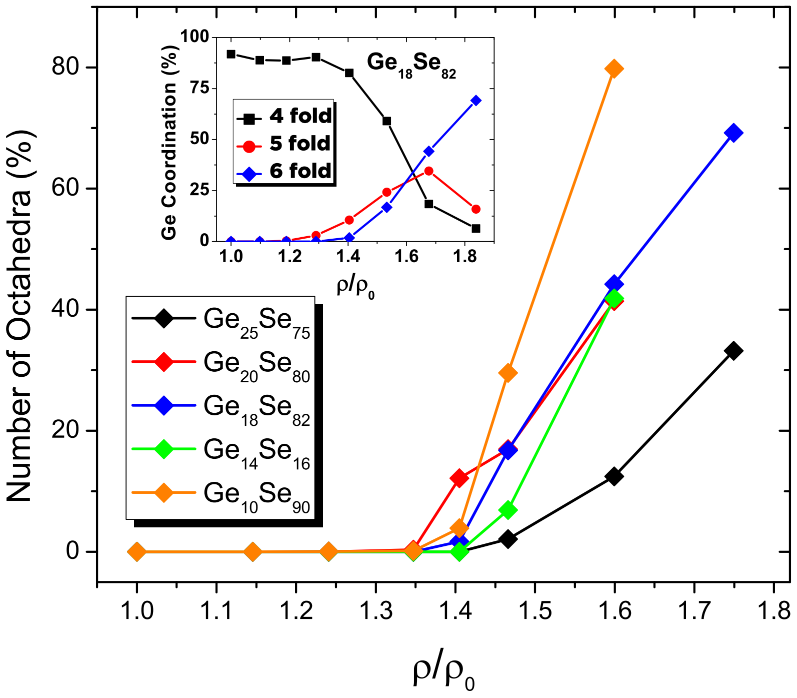

Figure 5.7: Evolution of 6 fold coordinated Ge atoms as a function of reduced density. The inset shows the changes of various Ge environment in $Ge_{18}Se_{82}$ over the whole pressure range of the AIMD simulations.

The tetrahedral to octahedral conversion can be traced by looking at the coordination geometry around a Ge atom. Fig. 5.7 shows the evolution towards octahedrality as a function of reduced density for Ge_xSe_{1-x}. The inset of the figure exhibits the interplay between 4, 5 and 6 folded Ge atoms in $Ge_{18}Se_{82}$ under compression. The tetraheldral configuration at ambient pressure is maintained at a constant value for all the compositions under consideration during the low-pressure modifications. Indeed, the percentage of 4 fold coordinated Ge atoms is maximum for the isostatic composition $Ge_{20}Se_{80}$. The small variations from a perfect tetrahedral connection observed in the other compositions are due to 2- or 3- folded atoms. Upon compression, around $\sim \rho/\rho_0$= 1.2 an increase in the amount of 5 fold coordinated Ge atoms is detected, while the Ge-Se bond compression still takes place. The onset of the LDA to HDA phase transformation is located at $\sim \rho/\rho_0$=1.4 for all compositions, manifested by the nucleation of the octahedra. The simultaneous decrease in the number of tetrahedral connections accompanying the appearance of 6 fold coordinated Ge atoms can be observed in the inset of Fig. 5.7. A fully octahedral coordination is not achieved within the compression range of our simulations, reaching up to 32 GPa for $Ge_{18}Se_{82}$. Another very interesting observation can be deduced from of Fig 9 is the composition dependence of the rate of change in LDA to HDA transformation. The rate of increase of percentage of the octahedraly connected Ge atoms decreases as Ge content increases. In other words, the AAT becomes more diffuse as the network stiffens. Finally we show the AIMD computed average coordination number normalized to the value at ambient pressure (eg. $n = 2.2$ $Ge_{10}Se_{90}$ at $\rho/\rho_0 \sim= 1$) as a function of reduced density in Fig. 5.10. Again, the trend in the average coordination numbers is the same for all compositions studied; a marked increase in the coordination after ρ/ρ_0 >1.4, signifying the LDA to HDA transformation. A transition zone is suggested in Fig. 5.9 below which only the low-pressure modifications take place. This result demonstrates a universal behavior in the densification mechanisms for target Ge_xSe_{1-x}, and indicates the transition from a low density amorphous to high density amorphous around ρ/ρ_0 >1.4 regardless of the Ge content.

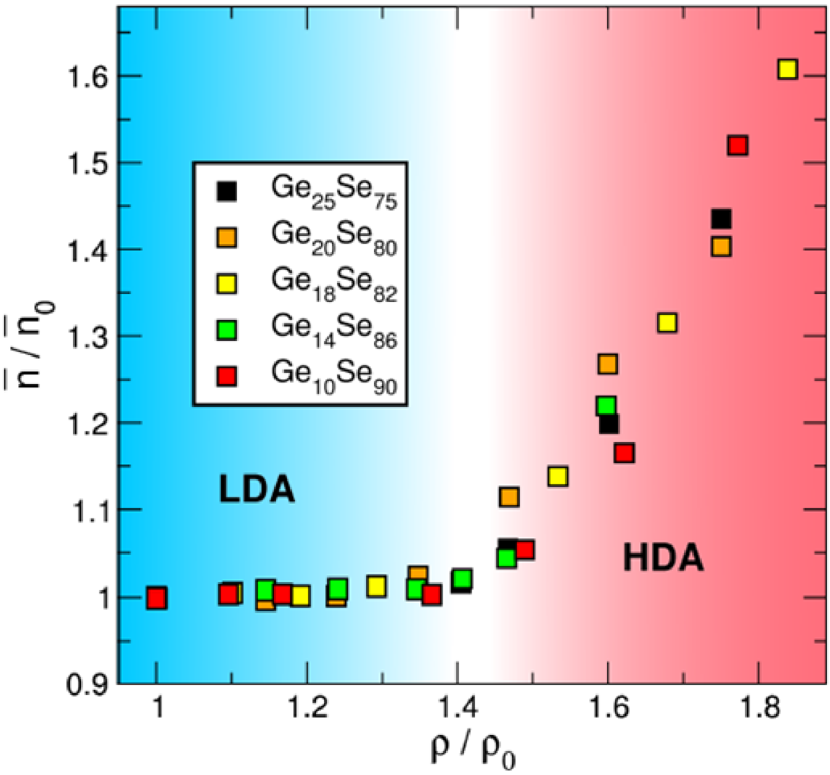

Figure 5.8: Normalized total coordination number as a function of the reduced density for the selected compositions of Ge_xSe_{1-x} obtained from CPMD calculations. Here the y axis represents the total coordination number at a given ρ divided by the total coordination number at ambient pressure. A global behavior is clearly observed for all the compositions with a marked increase in the coordination number starting around $\rho/\rho_0 = 1.4$.

5.8 Discussion

Our XRD measurements show no sign of crystallization under pressure, thus the amorphous nature of the structure is preserved up to 20 GPa for all compositions, in particular up to 41.4 GPa for $Ge_{17}Se_{83}$. However an in the intensity of the PP upon increasing pressure is observed. The intensity of the PP has been related to extended range ordering in previous studies[210]. In addition to this, the vanishing of the FSDP in the early stages of low-pressure modifications indicates the collapse of the IRO, as reported earlier[75]. A significant observation out of our XRD analyses is the shift in the PP position under pressure. We have detected a two step behavior appearing around 15 GPa for $Ge_{17}Se_{83}$ agreeing well with what was observed for $Ge_{20}Se_{80}$ in a previous study [77]. Note that in order to distinguish the two-step slope in the PP position, one should have sufficient number of pressure points in the HDA region.

The EXAFS data gave us access to crucial structural information. The average bond length calculated through the Fourier transform of the EXAFS signal give values between 2.366 Å and 2.372 Å for Ge-Se and 2.354 Å and 2.366 Å for Se-Se correlations within the first shell neighbors which are in line with the previous scattering and absorption experiments. We did not focus on the Se-Se distances due to the fact that the pressure modification are reflected dominantly on Ge-Se interatomic distances in Ge deficient Ge_xSe_{1-x}. One of the main results is the evolution of the average Ge-Se distance under pressure. The bond compression in LDA phase is followed by a sudden increase in the Ge-Se bond length. The pressure at which this jump occur corresponds to the slope change observed in the PP position, suggesting existence of another densification mechanism taking place in the structure. The Ge-Se bond elongation can be inferred as the tetrahedral to octahedral transformation. We support this argument with the AIMD results on the interplay between percentage of the 4 and 6 fold coordinated Ge atoms. Therefore we have shown a clear evidence for the transition from LDA to HDA phase occurring within an interval of 15-20 GPa. Moreover, within the compression range of our simulations, a considerable amount of 5 folded Ge was found in the network. From the EXAFS data, a bond compression in the HDA phase is identified with the average Ge-Se bond length shortening after 20 GPa for $Ge_{17}Se_{83}$. Even though this bond shortening is not reproduced in the pressure range for the AIMD of $Ge_{18}Se_{82}$, the observed slowing down in the increment of the average Ge-Se bond length with increasing pressure coincides with the decrease in the amount of 5 folded Ge atoms. Thus the degree of octahedrality continues to increase during the compression of HDA phase along with simultaneous drop of 4 and 5 folded Ge atoms after a certain threshold. A semiconductor to metal transition is identified with the negative shift in Ge K absorption edge (about -1.4 eV) under pressure. Similar results have been shown regarding the closing of the band gap with optical and XANES experiments as well as *ab initio* simulations. Note that the negative edge shift occurs for all the compositions and the metallization event may not necessarily coincide with the increase in the average Ge-Se bond length due to the fact that the half of the gap closure is already achieved during the low-pressure modifications[91].

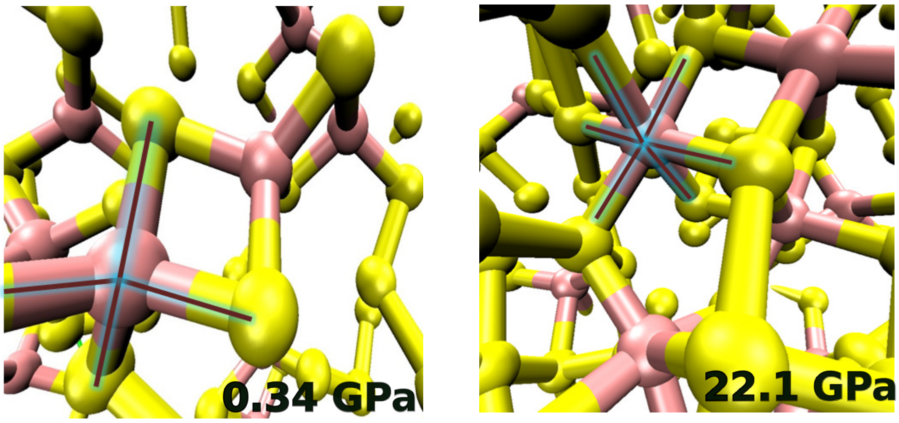

Figure 5.9: Atomic configurations of $Ge_{20}Se_{80}$ for LDA (right panel) and HDA (left panel) phases where Ge atoms are pink and Se atoms are yellow. The bars are drawn to highlight tetrahedral (right panel) and octahedral (left panel) coordination environment of a selected Ge atom.

Our experimental results have shown that the pressure effects are reversible, except for $Ge_{17}Se_{83}$. Unfortunately, a detailed explanation as to how decompression affects the real and reciprocal space properties can not be done due to the lack of data points. Nevertheless, we can speculate on $Ge_{25}Se_{75}$ for which we have two data points during decompression, 5.35 and 0 GPa, respectively (not shown). The PP in XRD pattern and the edge position in XANES as well as also the Ge-Se distance are observed to be recovered at ambient pressure after decompression, showing a hysteresis. Earlier studies have shown the existence of such hysteresis for various chalcogenides under pressure, the width of which depending on the extend of compression, using EXAFS, XRD and *ab initio* atomic simulations[82, 77, 91, 92]. As for the case of the differences between uncompressed and decompressed states of $Ge_{17}Se_{83}$ at ambient pressure may be due to an artifact in reading the decompressed pressure particularly for that measurement, since the decompressed properties in real and reciprocal space correspond to that of the region between 4-7 GPa.

We also provide information as to how the LDA to HDA transformation kinetics are affected with Ge content. Unlike the first order phase transformations observed in crystals, the AATs can have jump-like (analogous to first order transformations) or rather sluggish kinetics of transformation depending on the the stress level between the high pressure nuclei and the parent phase. Simple amorphous systems such as *a*-Si and *a*-Ge, as well as amorphous H_2O, have been shown (ref [213] and references therein) to exhibit sharp AATs, whereas network forming oxide and chalcogenide glasses such as GeO_2 and GeS_2 have been identified with the wide range AATs under pressure[92]. Our AIMD simulations demonstrates similar outcomes. The rate of AAT which is governed by the tetrahedral to octahedral transformation is observed to be inversely proportional to Ge content, in other words the network rigidity in amorphous Ge_xSe_{1-x}.

The pressure modifications that take place during the AAT mainly involve the convergence of the second shell neighbors with the first shell neighbors, as shown by our atomic simulations. This change is accompanied with the bond angle distributions of the related neighbors. In particular, the second shell neighbors defining the ES and CS Ge-Se-Ge angles merge with the tetrahedral angle of the first shell neighbors, eventually reaching to the octahedral angle. Furthermore, these structural modifications take place at a unique threshold when scaled to reduced densities, at ρ/ρ_0 =1.4. Consequently, these changes are reflected on average the coordination numbers. Another main result of this study is the universal behavior detected in the average coordination number during the transition from LDA to HDA phase in vitreous Ge_xSe_{1-x}. Although detailed thermodynamic studies are required to elucidate the physical origin of the threshold ρ/ρ_0 =1.4. At the present stage, we can only speculate that the coordination changes leading to redistribution of the stress that has been accumulated during the bond compression in the LDA phase ultimately leads to an octahedral configuration which corresponds to a different basin in the energy landscape.

5.9 Conclusions

In this work, we have investigated the pressure-induce polyamorphism in vitreous Ge_xSe_{1-x} using a combination of EXAFS, XANES, XRD experiments along with *ab initio* simulations. We have identified the LDA to HDA phase transition with the elongation in the average Ge-Se bond length using both EXAFS and AIMD simulations. Our results show that the convergence of the second shell neighbors to the first shell gives rise to the marked coordination change can be seen as signature of the AAT. The main outcome of our work is the universal threshold parameter at which the LDA phase starts to give high density octahedrally coordinated phase. The transformation is found to be taking place in a range of pressure values. The pressure range of the transformation is shown to be dependent on the network rigidity. The observed structural changes seem to be reversible within the limitation of decompression data. Although our work contributes to the understanding of the polyamorphism in many aspects, further thermodynamic evidences are required to have a full grasp of the underlying physics.

Chapter 6

Polyamorphism and Rigidity

Abstract

Density driven amorphous to amorphous transformations are generally observed in glasses having tetrahedral environments. Here, we report on the evolution in structural changes of the isostatic composition $Ge_{20}Se_{80}$, investigated by AIMD simulations at pressures up to ~ 50 GPa and compared to the X-ray and neutron scattering experiments in the literature where available. A good agreement with the experimental results are observed with no sign of crystallization. After having validated our results with the experimental findings on $Ge_{20}Se_{80}$, we present results for other compositions encompassing the elastic phase transition of Ge-Se system. We discuss that the rigidity concept can be extended further to explain polyamorphic transitions.

6.1 Introduction

Network-forming glasses may undergo structural changes with the applied pressure which lead alterations in their physicochemical properties. Chalcogenide glasses having enhanced structural variability due to the bonding environment compared to oxide glasses results in discrepancies in their structural response to the applied pressure. In the case of binary chalcogenides, little is understood as to the nature of the polyamorphic transitions. In this chapter, we further investigate the polyamorphic transitions by using AIMD simulations. We select the composition at the rigidity percolation threshold, $Ge_{20}Se_{80}$, for which the number of constraints is equal to number of degrees of freedom (i.e isostatic system). A detailed comparison is made with available experimental results. Subsequently we will provide information regarding the pressure response of other compositions such as $Ge_{10}Se_{90}$, $Ge_{14}Se_{86}$, $Ge_{18}Se_{82}$, $Ge_{22}Se_{78}$, and $Ge_{25}Se_{75}$. The link between ambient pressure rigidity of the system and the pressure induced transformations will be discussed.

6.2 Reciprocal Space Properties

Fig. 6.1 shows the AIMD calculated total structure factors for $Ge_{20}Se_{80}$ during compression compared to neutron ($S_N(k)$) (Bouzid et al.[94]) and X-ray ($S_X(k)$ (Kalkan et al. [77]) diffraction experiments. The calculated structure factors show a good agreement with experimental findings over the entire pressure range. It can be noticed from the simulations that the amorphous nature of the system is preserved until 49.2 GPa, in agreement with the XRD results shown in the previous chapter for $Ge_{18}Se_{82}$, indicating no crystallization up to 42 GPa, experimentally. The typical ambient pressure features of the reciprocal space (the FSDP at k $\sim$ 1.15 $Å^{-1}$, PP at k $\sim$2.05 $Å^{-1}$, and PP2 at $\sim$ 3.62 $Å^{-1}$) are well reproduced along with the oscillation in higher k vectors (8-12 $Å^{-1}$) when compared to neutron diffraction results. The FSDP broadens and loses intensity as the pressure is increased and completely vanishes at around 7 GPa, as reported earlier for other chalcogenide systems under pressure. Meanwhile the PP shifts to higher k values and a peak sharpening observed which is coupled with an intensity increase. Similar observations can be made for the PP2. It is worth noting that the X-ray results show a more pronounced sharpening effect upon compression which was argued to be related to the higher resolution function used as compared to the neutron diffraction results (ref [94] and therein). At higher pressures starting from 20 GPa, a peak located around k $\sim$ 5 $Å^{-1}$ starts to build up and becomes more pronounced as the pressure is increased. At pressures above 32 GPa, this peak is well separated from the PP2. The main contribution to the appearance of this peak is provided by the Se-Se partial structure factors and also its feature is enhanced by the drop in the intensity of Ge-Se partial structure factor around k $\sim$ 4.6 $Å^{-1}$ which are not shown here.

Important structural information can be found by investigating the behavior of the PP under pressure. Fig. 6.2 shows the AIMD calculated evolution of the PP during compression and compared to XRD measurements carried out by Kalkan et al. [77] with the corresponding decompression data. The PP position shifts to higher q vectors in the below 13 GPa with a slope of 0.0278 ± 0.002 $Å^{-1}GPa^{-1}$. Subsequently, a slower rate of increase is observed at higher pressures with a slope of 0.00861± 0.0008 $Å^{-1}$.

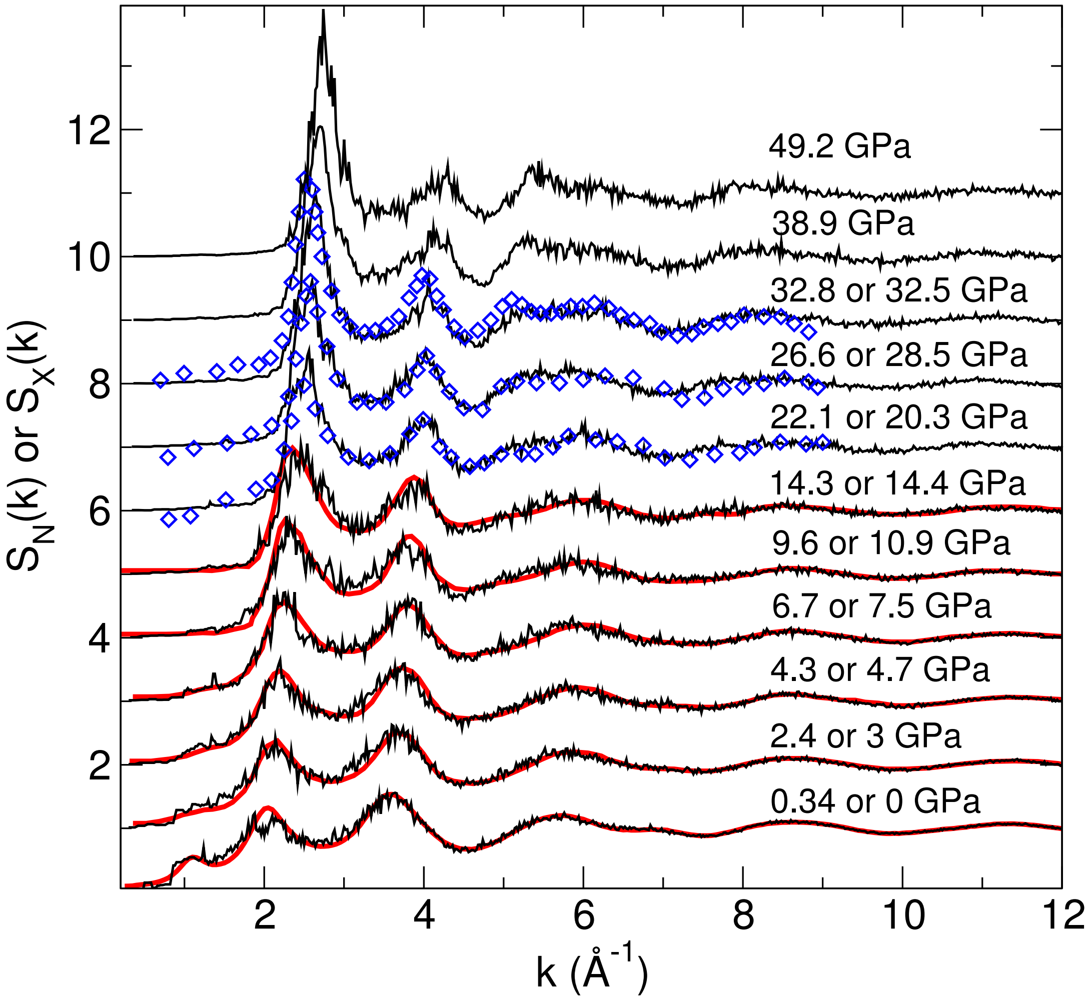

Figure 6.1: Pressure dependence of the total structure factor for $Ge_{20}Se_{80}$. AIMD computed results (black curves) are compared to neutron diffraction (red curves) [94] and X-ray [77] diffraction (blue diamonds) results. Here, the first pressure value indicated corresponds to the simulations while the second is for the experimental pressure points.

These results are in line with the work by Kalkan et al. [77] where the slopes of the low and high pressure regimes were given as 0.024 ± 0.001 $\text{Å}^{-1}\text{GPa}^{-1}$ and 0.011 ± 0.001 $\text{Å}^{-1}\text{GPa}^{-1}$, respectively. As it was mentioned in the previous chapter the change in slope is indicative of the existence of a pressure induced transition in structural modifications.

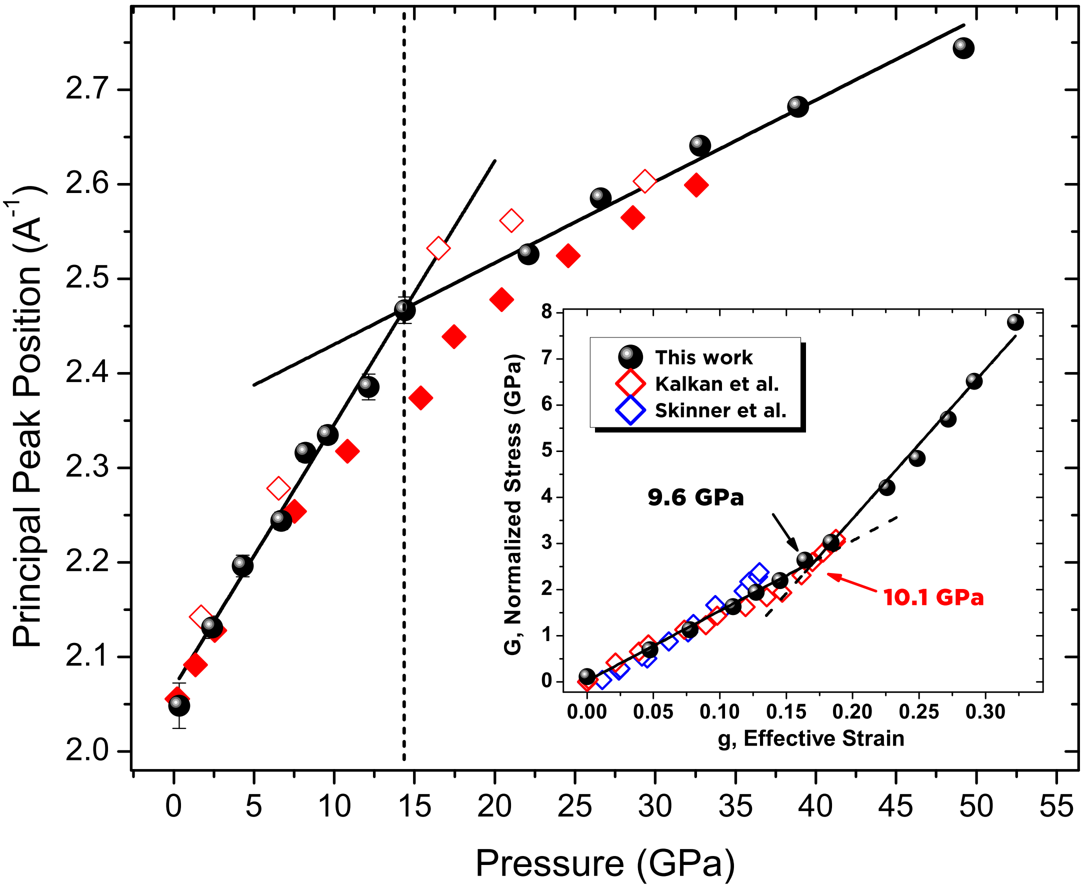

Figure 6.2: Computed pressure dependence of the principal peak position of the total structure factor (black spheres) compared to the experimental results of Kalkan [77] et al during compression (filled red diamond symbols) and decompression (open red diamond symbols). The solid black lines are the linear fits marking two different pressure while dashed vertical line is a guide to the eye for critical pressure. The inset shows the calculated normalized stress G as a function of normalized strain g (see text for details) compared to X-ray diffraction experiments by Kalkan et al.[77] (open red diamond symbols) and Skinner et al. [93] (open blue diamond symbolds).

Following the work of Jeanloz [214], the equation of state that was shown in the previous chapter can be further analyzed. Defining a normalized stress $G = P/(3(1 + 2g)^{3/2)})$ and an effective strain $g = 1/2[(V/V_0^{2/3})]$ which are expressed as the applied pressure P and volume of the simulation cells at ambient pressure V_0 and at a given pressure point V. The corresponding $G - g$ behavior of Ge$_{20}$Se$_{80}$ are shown in the inset of Fig. 6.2 where the AIMD calculated results were compared to the XRD measurements of Skinner et al. [93] and Kalkan et al. [77]. A similar two step behavior is also valid in the $G - g$ plot at 9.6 GPa for simulation results, which is quite close to the experimental value (10.1 GPa [77]).

One advantage of such $G - g$ plot can be given as characterizing low and high pressure behaviors by relating the the discontinuities of the isothermal compressibility κ_T which can be found using the relation $dG/dg \sim (\kappa_T + P)$. The compressibility values for the LDA and HDA phases were found as 0.10(4) $\times$ 10^{-9} Pa and 0.005 10^{-9}, respectively. These values agree well with the experimentally obtained values which are in the range of 0.05-0.10 $\times$ 10^{-9} for LDA [93, 77, 215] while the value for HDA was determined to be of about 2 times smaller [77].

6.3 Real Space Properties

We now turn to the real space properties. Fig. 6.3 shows evolution of the computed total pdf under pressure for Ge$_{20}$Se$_{80}$ compared to neutron diffraction (ND) results of the ref. [94]. It appears that there is a good agreement between our simulations and the ND measurements at ambient pressure. The first peak located at $\sim$ 2.36 Å and the second peak at $\sim$ 3.85 Å are well reproduced. It should be noted that the intensity of the first peak at ambient pressure is slightly overestimated in simulations compared to the experiment. An overall agreement between ND and AIMD results can be observed for the pressure behavior of the pdf. Upon compression the first peak loses intensity and shows a peak broadening. The position of this peak follows a similar trend to what is observed in Ge-Se bond length under pressure (see Fig. 5.3). The changes in this peak is directly reflected on the total coordination numbers (Fig. 6.5). The second peak continuously move to lower r values while losing its intensity along with a similar peak broadening. Fig. 6.4 shows the evolution of the partial pdf under pressure calculated with AIMD simulations. At ambient pressure one notices an absence of Ge-Ge homopolar bonds. This agrees with calculated coordination numbers (Fig. 6.5) where $\bar{n} = 2.4$ at ambient pressure with $\bar{n}_{\text{Ge}} = 4$ and $\bar{n}_{\text{Se}} = 2$, indicating predominant Ge(Se$_{1/2}$)$_4$ units in the structure. The homopolar Ge-Ge bonds appear with increasing

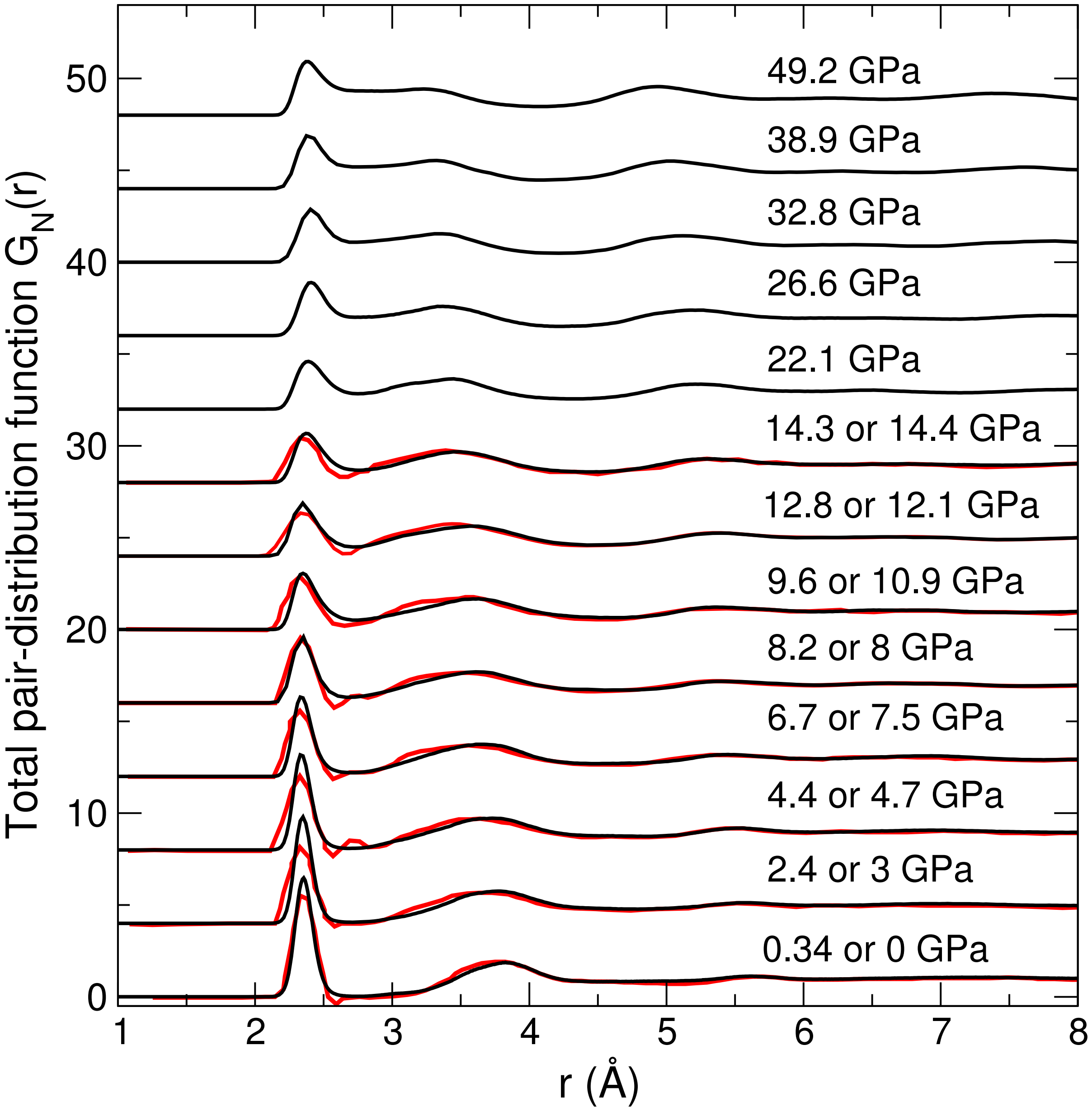

Figure 6.3: Pressure dependence of computed (black curves) total pair distribution function for $Ge_{20}Se_{80}$ are compared to neutron diffraction experiments [94] (red curves).

pressure and reaches a maximum intensity at around 15 GPa. Above this value a decrease in intensity is observed which is reflected to the Ge-Ge homopolar fraction (inset of Fig. 6.6). It can be seen that the peak corresponding the Ge-Ge inter-atomic distance forming the ES tetrahedral connection (at around 3 Å) loses intensity and completely vanishes at 12.1 GPa while the peak corresponding CS broadens as the pressure is increased. Turning to $g_{\mathrm{GeSe}}(r)$,one can notice that the position of the first peak located at $\sim$ 2.35 Å behaves similar to what is observed for $\mathrm{Ge_{18}Se_{82}}$ under pressure. The second peak located at around $\sim$ 3.66 Å at ambient pressure agrees well with the previous AIMD results [145], which can be attributed to the distances of a cros-linking Ge atom with a Se chain. The intensity of this peak was reported to increase with increasing Ge content [145]. In other words, increasing network connectivity yields an increase in the intensity of the secondary peak in $g_{\mathrm{GeSe}}(r)$. Our simulations agree with that previous study in the sense that for $P > 7$ GPa, the secondary peak gains intensity which is inline with the increased network rigidity and shifts to lower r values. Another interesting feature is that the peak that appears at $\sim$ 5.5 Å and again shifts to lower r values with an increase in its peak intensity. Finally, examining $g_{\mathrm{GeSe}}(r)$ shows that the first peak associated with the homopolar Se-Se bonds is located at 2.36 Å , consistent with the previous works. With increasing pressure this peak loses intensity and broadens. The secondary peak that is located at 3.85 Å again moves to smaller r values as the pressure is increased, eventually merging with the Se-Se homopolar peak. This indicates that at high pressures, there is a high structural variety for Se-Se type of bonding including motifs such as edge correlations of octahedral units, homopolar bonds, and connections with the next nearest neighbor as the fifth and sixth neighbors approaches to the first shell.

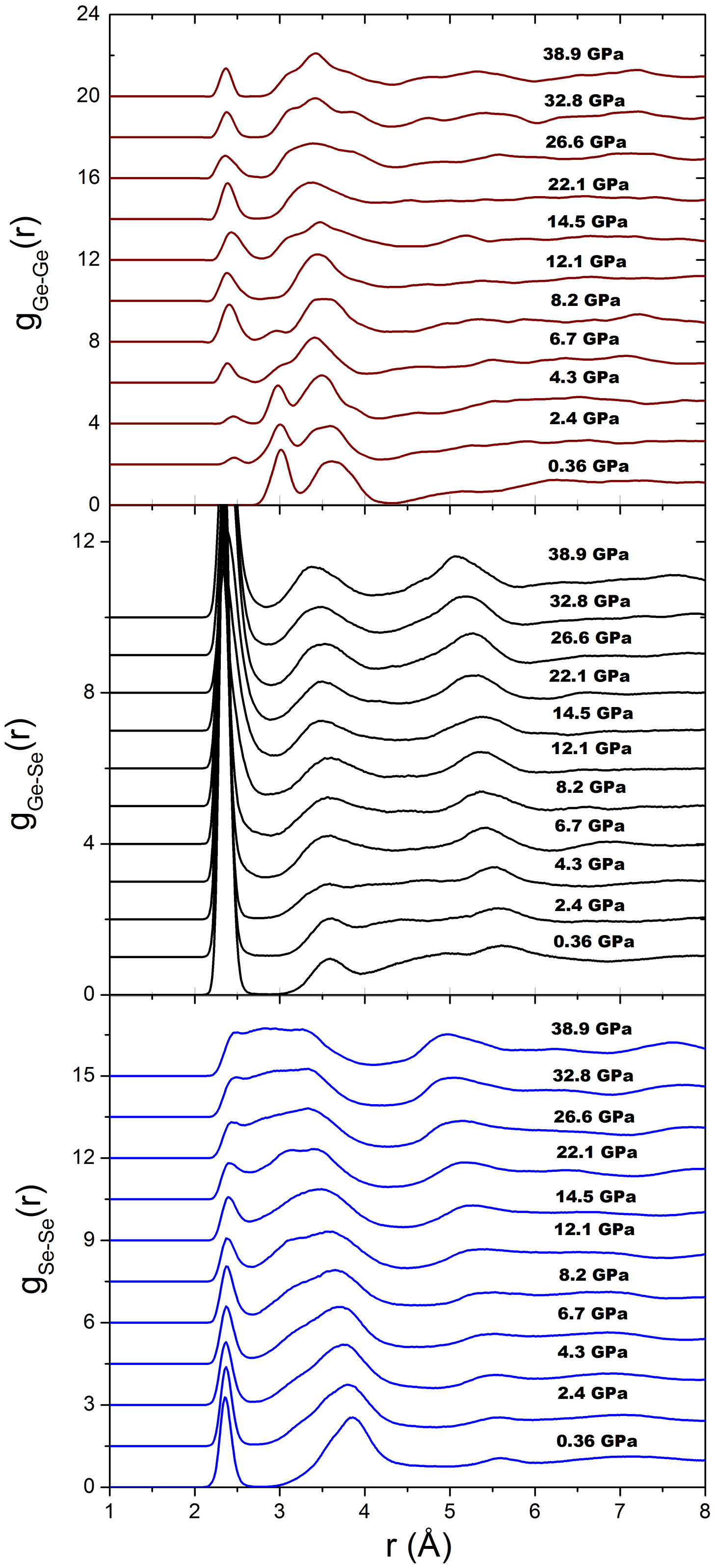

Figure 6.4: The calculated pressure dependence of partial pair distribution functions for $Ge_{20}Se_{80}$ (from upper panel to lower $g_{GeGe}(r)$, $g_{GeSe}(r)$, and $g_{SeSe}(r)$).

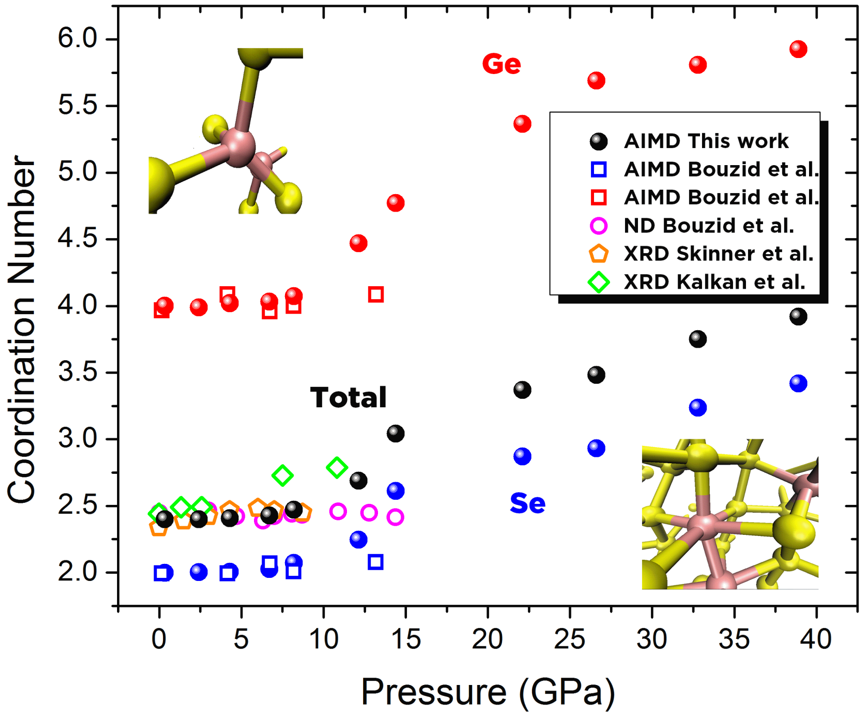

Figure 6.5: Computed pressure dependence of computed coordination number for $Ge_{20}Se_{80}$ (filled spheres) are compared to AIMD and ND work of Bouzid et al. [94] (open squares and magenta open circles, respectively), XRD work of Skinner et al. [93] (orange open pentagons) and XRD work of Kalkan et al. [77] (green open diamons). On the top left and bottom right snapshots of typical structural units are represented for LDA and HDA phases

.

Fig. 6.5 shows the coordination numbers for $Ge_{20}Se_{80}$. Again, our AIMD results are compared to experimental and simulation works available in the literature for this particular composition. The ambient pressure values for $\bar{n}$, $\bar{n}_{Ge}$, and $\bar{n}_{Se}$ are in line with the mean field calculations (see the previous chapter) and also consistent with the previous studies [93, 94, 77, 145]. Upon pressure, the mean coordination numbers almost remains constant P =9.6 GPa for our simulations with nearly no changes in the partials $\bar{n}_{Ge}$, and $\bar{n}_{Se}$, which corresponds to the deflection point of the $G - g$ curve presented in Fig.6.2. Above this value,a drastic increase is observed for $\bar{n}_{Ge}$ and $\bar{n}_{Se}$ indicating the LDA to HDA phase transformation. The rate of increase in coordination numbers is smaller at P > 22 GPa in such a way $\bar{n}_{Ge}$ and $\bar{n}_{Se}$ almost linearly approach to 6 and 4, respectively. The discrepancies between the AIMD results in the work by Bouzid et al. [94] may be due to the different glass production prior to the cold compression in the simulations. Furthermore, there are differences in the total average coordination number $\bar{n}$ between XRD and ND measurements. The XRD work by Kalkan et al. shows an increase in $\bar{n}$ at around $\sim P$ = 7.5 GPa, reaching a similar value with our simulations at around 12 GPa while the coordination numbers found by ND measurements are almost constant up to $\sim P$ = 15 GPa. It was argued that the increase in the XRD measured mean coordination number $\bar{n}$ can be due to the analysis which were done by employing empirical potential structure refinement method [94]. It should be noted that our simulation results shown in Fig. 6.5 are consistent with the statement in work of Skinner et al. [93] that there is no significant change in the coordination number at pressures up to 8.6 GPa.

6.3.1 Discussions and Conclusions

Fig. 6.6 shows the calculated bond statistics as a function of pressure for $Ge_{20}Se_{80}$. The average Se-Se and Ge-Se bond fractions show three regimes. At pressures below 8 GPa remaining constant at around 35$\%$ and 65 $\%$, respectively, which is followed by a continuous increase for Se-Se and decrease for Ge-Se up to 22 GPa. From this pressure point, no significant change is observed. At ambient conditions the majority of the bonds consists of Ge-Se connections. The Se-Se connections have some 30 $\%$ fraction. As shown already in Fig. 6.4, there exists no Ge-Ge bonding at ambient pressure and the fraction of Ge-Ge bonds does not exceed 2 $\%$ over the entire pressure range. The constant value of coordination number at low pressures (i.e. LDA phase) is reflected on the Ge-Se and Se-Se fractions which varies weakly below 5 GPa. Subsequently there are dramatic changes in such a way that Ge-Se fraction decreases to ~55 $\%$ while Se-Se fraction follows an inverse behavior, increasing to a value close to 45 $\%$ at around 22 GPa. A plateau value in Ge-Se and Se-Se fractions are observed for the pressure points above 22 GPa. This may explain the linear coordination increase for both species at pressures above 22 GPa observed in Fig. 6.5.

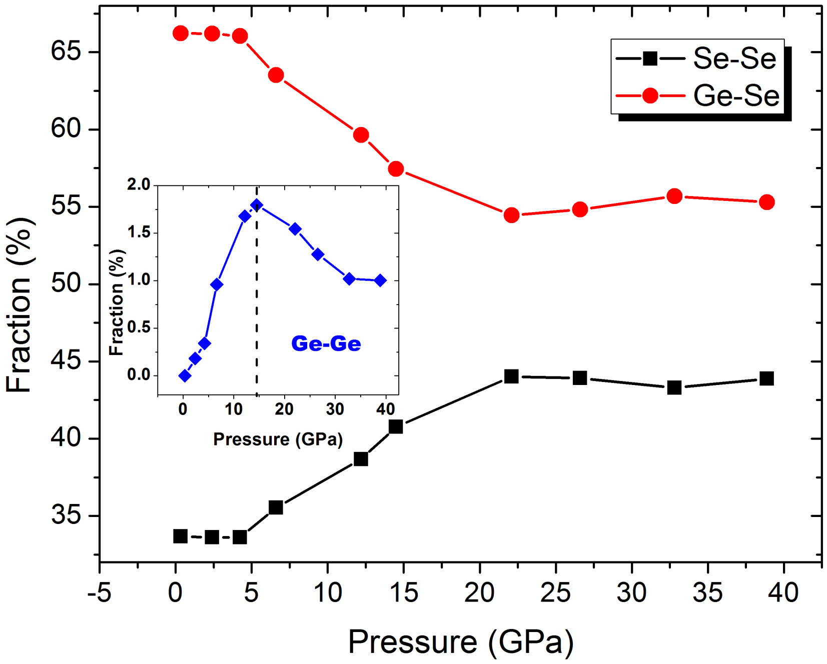

Figure 6.6: Calculated fraction of Ge-Se and Se-Se bonds as a function of pressure for $Ge_{20}Se_{80}$. Cut-off values for each pressure point was taken from the minimum of the corresponding pdf. (i.e 2.8 Å at ambient pressure). The inset shows the faction of Ge-Ge homopolar bonds.

It appears that the network predominantly consists of octahedral geometry, thus the applied pressure above this point only increases the coordination by the Ge-Se and Se-Se bond compression in HDA phase, weakly affecting on the Ge-Se and Se-Se bond fractions. In this respect, a contrast between LDA and HDA phase can be noticed; in the pressure ranges that lead to bond compression, although the Ge-Se and Se-Se bond fractions remain the same (predominant skeleton of the network being either tetrahedral or octahedra, respectively) the coordination of LDA phase does not increase as compared to what is observed in HDA phase, due to the open structure of LDA phase.

At this stage, can we give further insight to the LDA to HDA transformations that shows certain thresholds in different properties ? To address this question, we computed the evolution of the Ge-Se bond length under pressure for a number of compositions spanning flexible-rigid-stressed rigid transitions. A critical pressure parameter, P_c, is introduced. For each composition under consideration, the value of P_c is taken from the onset pressure value after which average Ge-Se bond length starts to increase, indicating the LDA to HDA transformation. Fig.6.7 shows the evolution of

P_c as a function of composition. One can see the evolution of the Ge-Se bond length versus pressure for all the compositions studied under pressure by AIMD. The most flexible compound of our simulations $Ge_{10}Se_{90}$ shows the highest P_c among the other compositions. Increasing Ge content decreases the critical pressure up to 22 %, the centroid of the so called intermediate phase for Ge-Se systems [42, 50, 145]. After this minimum, the critical pressure increases as the network becomes stressed rigid.

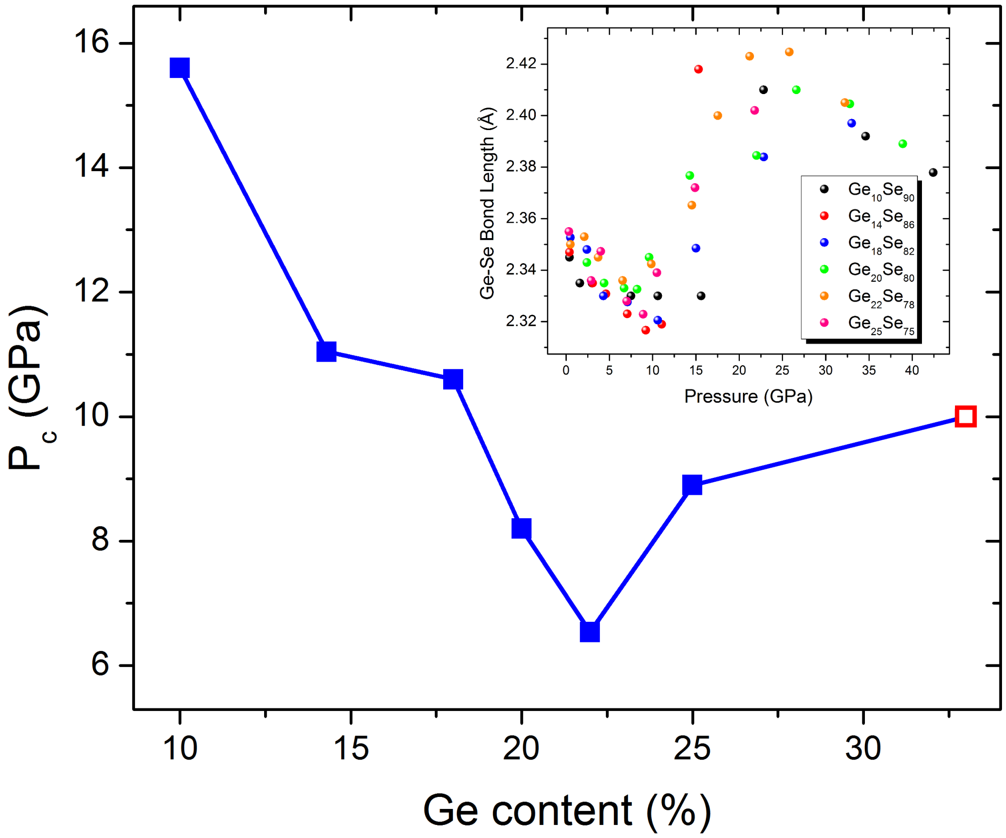

Figure 6.7: Composition dependence of the critical pressure found by the onset of the Ge-Se bond length increase. The inset shows the pressure dependence of the AIMD calculated Ge-Se bond length for a number of compositions ranging the rigidity transitions. The open red square data is taken from the EXAFS work of Properzi et al.[90]

Indeed, our results show that the ambient pressure network rigidity affects the AATs. A flexible network structure can be made rigid by two means; increasing the composition of the higher coordinated species (in our case increasing Ge content) or by applying pressure which will introduce an increment to the coordination number. Notably, among the flexible and isostatic compositions, less compression is needed for

AAT. For stressed rigid compositions such as $Ge_{33}Se_{67}$), the densification mechanism is rather different in such a way that there is a continuous increase in coordination of the rigid network while simultaneously an edge to corner sharing tetrahedral transition takes place suggested by acoustic measurements [83]. Another interesting finding is that the composition dependence of the critical pressure at which AATs takes place resembles that of the diffusivity behavior at 1050 K in the liquid state. This may indicate a possible correlation between liquid-liquid transitions and AAT even though it is still not clear if the the observed low temperature polyamorphic transition is an extension of the reported liquid liquid transition between two stable liquid states.

In summary, we studied the $Ge_{20}Se_{80}$ system under pressure up to 50 GPa using AIMD simulations. A detailed comparison of our simulations to the experimentally measured quantities by ND and XRD showed a good level of reproduction. The Ge-Se and Se-Se fractions showed three step behavior, providing an insight to the different regimes observed in average coordination numbers. A global connection between ambient network rigidity and the AAT is made by introducing P_c. It is interesting to see the link topological constraints in in this on P_c and composition. This work is under progress.

Chapter 7

General Conclusions and Future Directions

Chalcogenide glasses have attracted much attention over the past couple of decades on only due to their numerous optical applications ranging from night vision detectors to bio-sensors but also for their interesting network properties. In this work, we studied the structure and dynamics of the liquid and glassy $\mathrm{Ge_xSe_{100-x}}$ system as an archetype to the chalcogenide glasses using a combination of AIMD simulations and scattering experiments. The wide glass forming range of the Ge-Se system (for $x \leq 0.43$) enabled us to investigate many compositions spanning the flexible-rigid-stressed rigid elastic phase transitions.

We performed Car-Parrinelo AIMD in NVT conditions of 250 atoms to generate our structural models for liquid and glassy states. High performance super-computers were used to perform AIMD simulations to produce glassy structures with a total of several hundreds of picoseconds (simulation time) for each compound under consideration. Number of post analyses were made in order to study structural and dynamic properties of the atomic trajectories. Our simulation results show a good reproduction of the liquid and the glassy states both at ambient and high pressure conditions when compared to the available scattering experiments.

The experimental part of this work consist of measurements based on synchrotron X-ray radiation at BM23-ESRF and electron beam techniques at CEA, both located in Grenoble, France. The specimens were synthesized at the University of Cincinnati, US. Amorphous Ge-Se samples were produced using well established homogenization and melt quenching method in quartz tubes sealed under vacuum . We conducted simultaneous X-ray absorption at Ge and Se K edges and X-ray diffraction experiments under pressure. Diamond anvil cells containing nanocrystalline diamonds were used to employ pressure with paraffin oil acting as pressure transmitting media to achieve hydrostatic compression.

This research provides a systematical composition-pressure-rigidity approach to the prototypical Ge-Se networks. Our results contributes valuable information to general concepts such as rigidity, fragility and polyamorphism. Our results can be summarized in two parts : liquid Ge-Se with purely computational approach and vitreous Ge-Se under pressure with combined experimental and computational approach. In what follows, we present the highlights of our results :

-The Liquid State

After verifying the robustness of our structural model in liquid states by comparing with experiments available, we investigated the dynamics of Ge-Se liquids. We evidenced dynamic anomalies at 1050 K, which is the lowest temperature at which the liquid dynamics were attained in our simulations. In particular, the analysis in real space dynamic properties such as diffusion coefficients, diffusion activation energies, and viscosities showed an anomalous behavior at the rigidity percolation threshold in such a way that atomic mobility reaches a local minimum where average number of constraints n_c= 3. Furthermore, the reciprocal space properties were investigated by the intermediate scattering factor are the q vector corresponding to the PP for the structure factor. Relaxation times and stretched exponent values for both species showed similar anomalies around the same composition interval (18-22 $\%$ Ge). In order to elucidate this anomaly, we employed MD based constraint counting methods. The results showed that the BB constraints of Ge species reaches to a maximum for the compositions displaying the most sluggish dynamics. Moreover, the variance of these constraints yield a minimum at 22 $\%$ Ge at 1050 K. One of the most remarkable outcome of this part of the study comes from a more detailed analysis on the constraints. We showed that the topological distribution of the Ge BB constraints plays a key role in the dynamic anomalies observed. We further made a link between the distribution of the BB constrains of the higher coordinated species and fragility of network forming liquids. We show a global feature of the fragility minima observed in many network forming systems, which is related to the spatial distributions of the BB constraints at compositions leading to isostatic networks.

-Future directions for the liquid state

Having shown that AIMD simulations can provide detailed insight into the glassy dynamics of chalcogenides [208, 216, 217], there is probably much to learn from the investigation of dynamic heterogeneities. At present, such studies on structural glass-forming liquids have been restricted [218, 219] to liquid silica, and, for this reason, investigation of other typical network formers is desirable. While similar features with fragile liquids have, indeed, been emphasized, an investigation of off-stoichiometric liquids such as Ge-Se or As-Se can provide interesting insights because an appropriate alloying will allow to tune physical properties in a continuous fashion. Studying the compositional dependencies of dynamic heterogeneities and the possible detection of anomalies would be an interesting and promising extension of the present work. Work in this direction is in progress.

-The Glassy State

AIMD simulations reproduced the evolution of experimentally measured quantities in both real and reciprocal space for $\mathrm{Ge_xSe_{100-x}}$ glasses at ambient pressure and temperature. Our simulation results show no significant differences with previous simulations having 120 or 480 atom cells in NVT conditions. Our MD based constraint counting results at ambient pressure agrees very well with the mean field constraint counting where $n_c = 2 + 5\mathrm{x}$ where x is Ge mole fraction. (i.e. $\mathrm{Ge_{20}Se_{80}}$ has $n_c = 3$ and $\bar{n} = 2.4$ at 300 K). These convincing results obtained by AIMD simulations enabled us to study Ge-Se system with our structural models under pressure.

One of the main results of this work is the identification of polyamorphic phase transformations from a low density amorphous (LDA) phase, in which tetrahedra are the predominant structural units to a high density amorphous (HDA) phase with octahedral geometry under compression in all compounds studied. In particular, these transformations showed structural and electronic evidences. Notably, the average Ge-Se bond length extracted from EXAFS experiment and also calculated from AIMD simulations showed an initial bond compression at pressures below $\sim$ 10 GPa. This bond compression is followed by an abrupt increase corresponding the LDA to HDA transformation. Furthermore, the electronic evidence comes from the red shift detected from the measured XANES spectra which is associated with a semiconductor-metal transition which are in accordance with previous conductivity measurements. As for the densification mechanisms, we show that the tetrahedral motifs in the first shell neighbors are preservedup to a critical pressure at which the fifth and sixth neighbors effectively become a part of the first shell, corresponding to the angular adaptation from 109.5 to 90 degrees (i.e. tetrahedral to octahedral geometry).

We furthermore investigated the link between the network rigidity of the starting composition and the kinetics of amorphous-amorphous transition (AAT). We monitored the rate of increase of the fraction of the octahedrally coordinated Ge atoms as the signature of the AAT as a function of pressure. (i.e. reduced density). It appears that as the compounds having higher Ge content shows a more sluggish transformation while the more flexible compounds (i.e. $\mathrm{Ge_{10}Se_{90}}$) display a first order like transformation resembling single element semiconductor systems such as Si or Ge.

Perhaps the most striking result of this research is the global threshold value observed in the coordination number increase as a function of pressure. We showed that there is a threshold value around reduced density $\rho/\rho_0 \sim 1.4$ for $\mathrm{Ge_xSe_{100-x}}$ (where x ≤ 25). This global value must be related with a redistribution of stress which has been accumulated during the bond compression in the LDA phase thus ultimately leads to an octahedral HDA arrangement corresponding to a different basin in the energy landscape for each composition studied. We finally report on a critical pressure value, P_c indicating the onset of LDA to HDA transformation extracted from Ge-Se bond length evolution under pressure. The results showed that for the isostatic and flexible compounds, critical pressure follows a somewhat similar trend to the diffusivity at 1050 K, decreasing as the rigidity increases yet yields a minimum at 22 %.

-Future directions for the glassy state

As a continuation of our XAS study which is built mostly upon the Ge K edge EXAFS part of the spectra, we are planning investigate the Se K edge in detail. In particular, the FEFF simulations on our atomic trajectories can provide additional insight on this subject (see the preliminary result in B). A pressure-composition-energy-absorption map is to be done for the Se K edge.

For what concerns the dynamics of vitreous $\mathrm{Ge_xSe_{100-x}}$, we already simulated the vibrational spectra under pressure (see B). Furthermore, for the $\mathrm{Ge_{18}Se_{82}}$ $\mathrm{Ge_{25}Se_{85}}$ compounds we conducted an inelastic X-ray scattering (IXS) experiment under pressure up to 20 GPa. We plan to combine experimental and simulation results in order to have a better understanding of the relation between the vibrational fingerprints of the rigidity transitions, as the network connectivity increases with the applied pressure. We also measured IXS spectrum of the Ge_3Se_{97}, which is an ultra flexible compound to identify the floppy phonon modes. Analysis of this experiment will be done in the close future. Moreover, one can have an access to the non-ergodicity parameter from the IXS data. In this respect we calculated this parameter at ambient conditions from the intermediate scattering function of the Se species as a function of composition (see B). This work is in progress.

There is much to learn from the atomic simulations of chalcogenide glasses using the well established AIMD methods. As mentioned in this thesis and in previous works on the Ge-Se systems under pressure, different methods of simulation can yield discrepancies in different set of simulations. To address this issue, we are currently working on is the effect of thermal history of the compression on the structural and dynamic evolution of Ge-Se glasses. We accumulated some preliminary results on the $Ge_{10}Se_{90}$ system (see B). Detailed analyses are to be performed.

Appendix A

Liquid State

Fig. A.1 shows a comparison of the self diffusion coefficients of Ge and Se species at 1050 K in simulation cells prepared using experimental liquid and glass densities,respectively. The diffusion anomaly mentioned in Chapter 4 is more prominent for case of liquid densities. Nevertheless, the overall trend is conserved in such a way that the elastic phase transition yields the minimum value in diffusivity for each case.

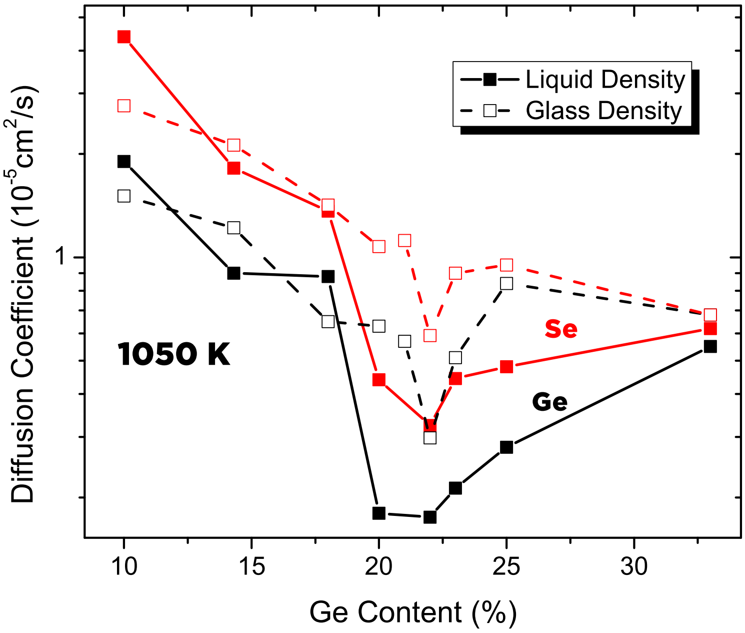

Figure A.1: Calculated self diffusion coefficients D_{Se} (red) and D_{Ge} (black) using glass and liquid densities as a function of composition at 1050 K.

One reason of the dynamic quantities having slightly different numbers can be attributed to the stress developing in the simulation cells. Fig. A.2 shows the stress evolution during the simulation time at 1050 K. As can be seen the average stress is less than 0.25 GPa. In the case of glass densities, the stress levels can be 3 times higher at 1050 K.

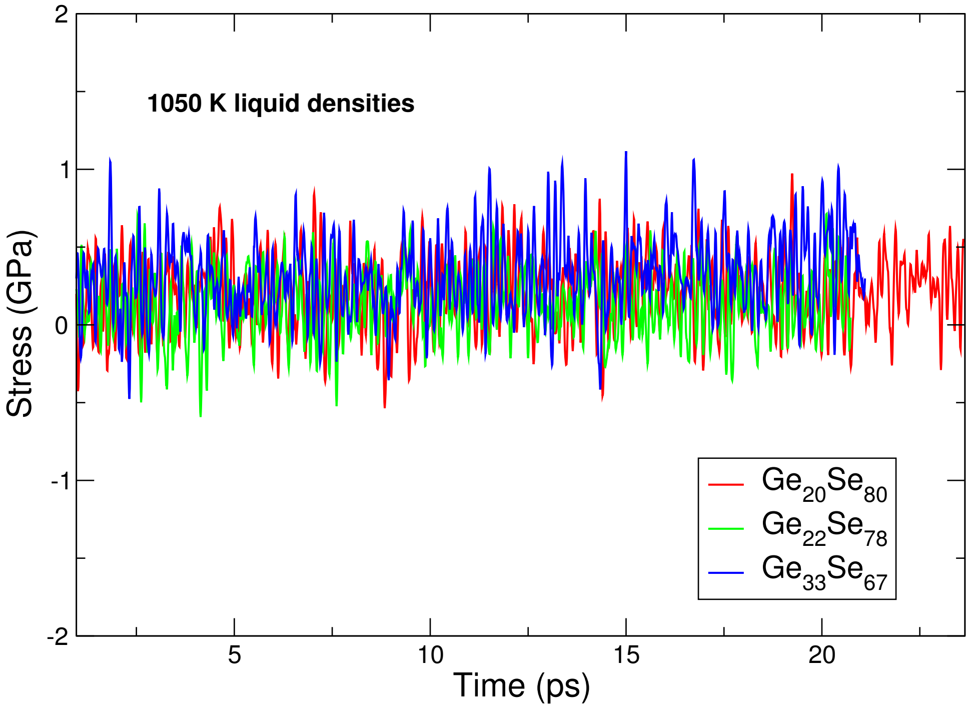

Figure A.2: Stress evolution in the simulation cells having liquid densities as a function of simulation time for selected compositions at 1050 K.

One can have a cross checking of the simulations by having a statistical average even at the liquid densities. For the compositions in the region 20-25%, we have realized a certain number of additional tests of validation in order to check that the results do not depend on e.g. system size or initial configuration. Here we present verification on the results found by using the glass densities. Five independent configurations have been chosen in the high temperature liquid and cooled to the isotherm of 1050 K over the same time interval (20 ps). All led to similar results in terms of constraints, either total number of interaction or related numbers (BS or BB) with a minimal spread between configurations. Fig. A.3 shows the calculated values for such configurations which validate e.g. the data point of 22% represented in Fig. 4.10 2b. In addition, the calculated pair correlation function for the five independent configurations at 1050 K of the 22% system lead to identical results (Fig. A.4), and corresponding g(r) are very close to the 20% system.

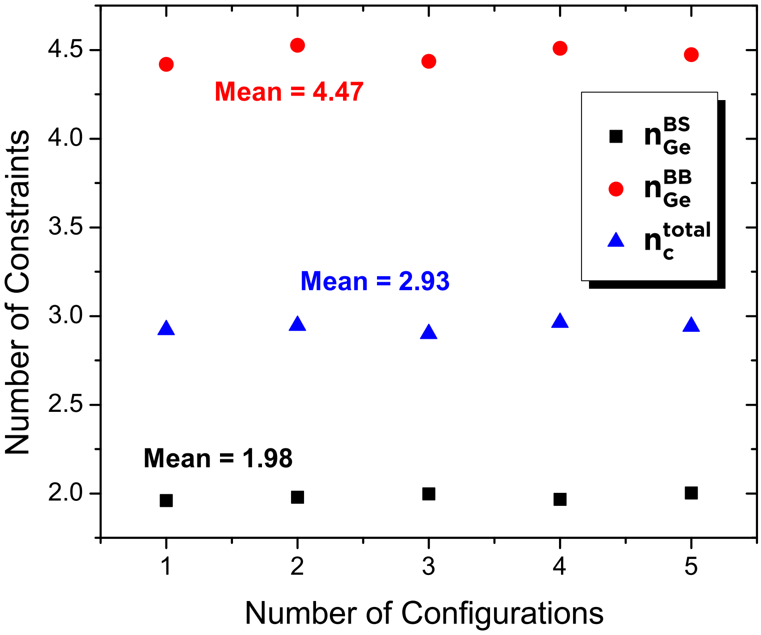

Figure A.3: A Number of constraints n_c Total and Ge related constraints calculated for five independent configurations at 1050 K for the 22% system for cells having glass densities.

Note that the simulation cells having glass density has higher internal stress during the simulation time. Even though this does not induce a change in the coordination numbers, thus the BS constraints, when compared to the cells having liquid densities at 1050 K, some of the angular constraints soften due to higher pressure within the cells. Therefore, in case of 22%, one finds BS constraints being 1.98 for glass and liquid densities while BB constraints differs (4.47 using glass, 4.85 using liquid densities, respectively). Despite this discrepancies, calculations show the trend observed in Fig. 4.10 b is retained when computed using glass densities over the entire composition range of this study.

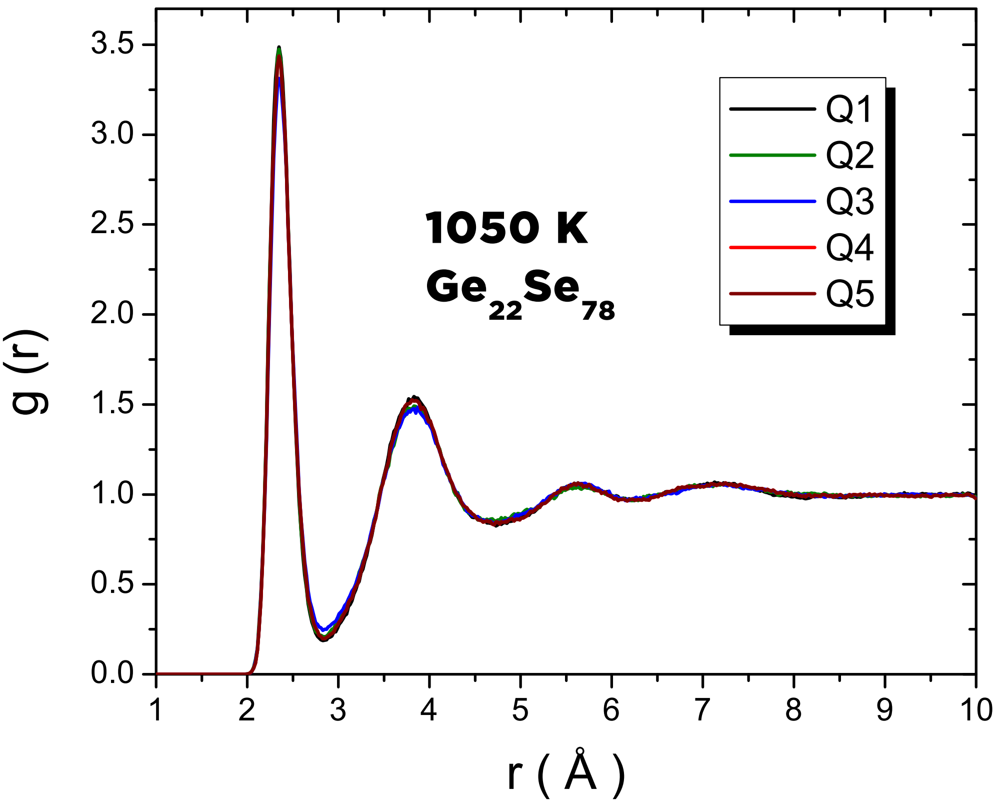

Figure A.4: Total pair distribution functions of the 22% system at 1050 K for five independent configurations for cells having glass densities.

Appendix B

Glassy State

The diffusive or vibrational properties of a material can be studied with the velocity autocorrelation function $Z(t)$. Taking $\mathbf{v}(r)$ as the velocity for atoms in a system, then $Z(t)$ can be defined as

$$Z(t) = \frac{\langle \mathbf{v}(0) \cdot \mathbf{v}(t) \rangle}{\langle \mathbf{v}(0) \cdot \mathbf{v}(0) \rangle} \tag{B.0.1}$$

where (t) is time. The Fourier transform of $Z(t)$ gives the vibrational density of states (VDOS) ;

$$F(\omega) = \frac{1}{\sqrt{2\pi}} \int\limits_{-\infty}^{\infty} dt e^{i\omega t} Z(t) \tag{B.0.2}$$

Fig. B.1 compares the AIMD calculated VDOS spectra with the inelastic neutron scattering. There is a good overall agreement between our simulations and the experimental findings.

Fig. B.2 shows the pressure dependence of VDOS/E- E plot of Ge$_{14}$Se$_{86}$ and Ge$_{18}$Se$_{82}$. The vibrational modes of the glasses are observed to evolve strongly below 12 GPa. The peak associated with the floppy modes (low frequency) around 5 meV arising from the under-constrained atomic configurations (n_c < 3 or $\bar{n} < 2.4$) gradually shifts to higher frequencies during compression. The interplay of the peak around 25 meV which corresponds to the atomic motion of Se atoms that link ES tetrahedra is observed. One can see that the vibrational spectra is directly affected by the network connectivity. These results under pressure is coherent with the compositional study done using inelastic neutron study on Ge-Se and Ge-As-Se alloys in ref [220].

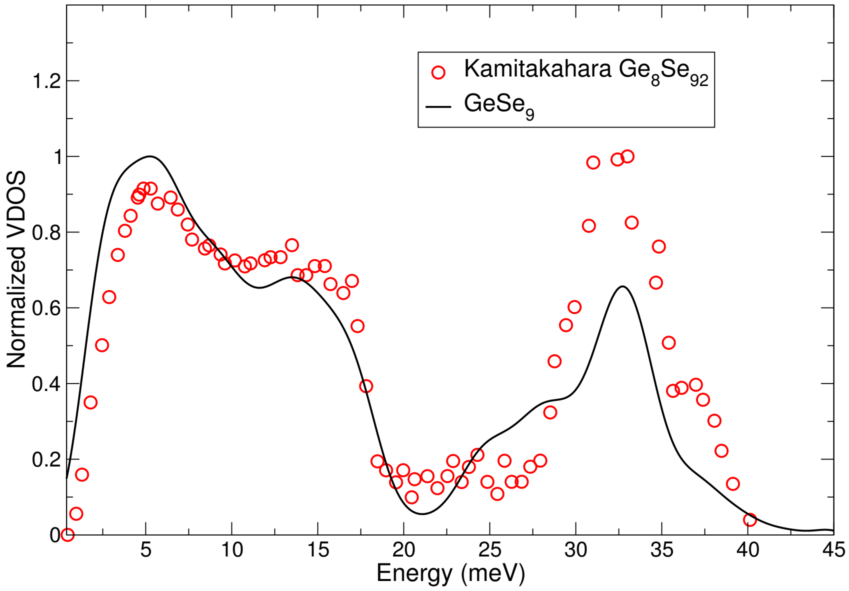

Figure B.1: Calculated vibrational density of states for $Ge_{10}Se_{90}$ at 300 K compared to inelastic neutron scattering measurement Ge_8Se_{92} (ref. [220]).

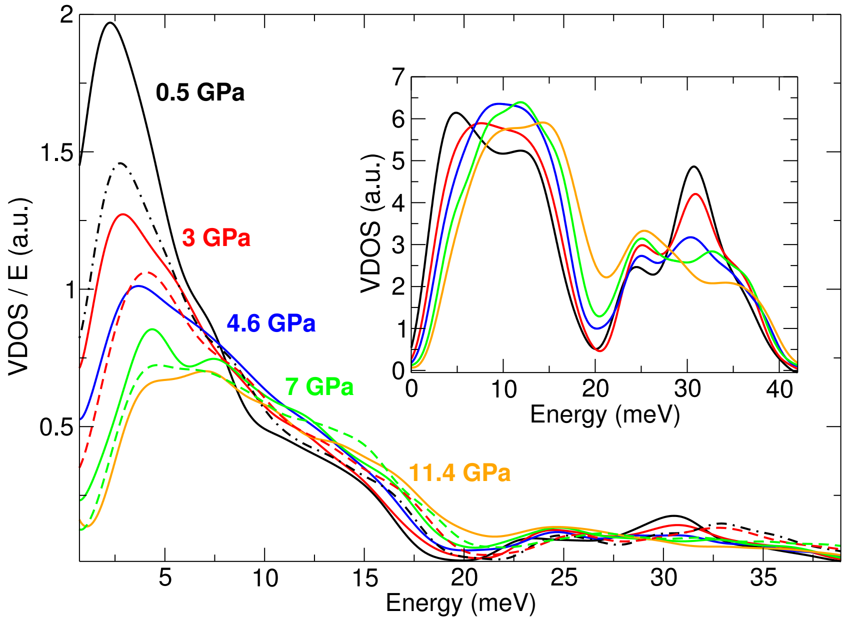

Figure B.2: Calculated energy normalized VDOS as a function of energy for $Ge_{14}Se_{86}$ (continuous lines) and for $Ge_{18}Se_{82}$ under pressure (broken lines) at 300 K. The inset shows the total VDOS as a function of energy for $Ge_{14}Se_{86}$.

Fig. B.3 shows the preliminary results on the comparison of the FEFF calculated XANES spectra at Ge K-edge for glassy $Ge_{25}Se_{75}$ with the XAS experiment carried out at BM23, ESRF. Even though the calculated spectra do not show a good agreement as far as normalized absorption intensities and shoulder peak positions, the trend of the

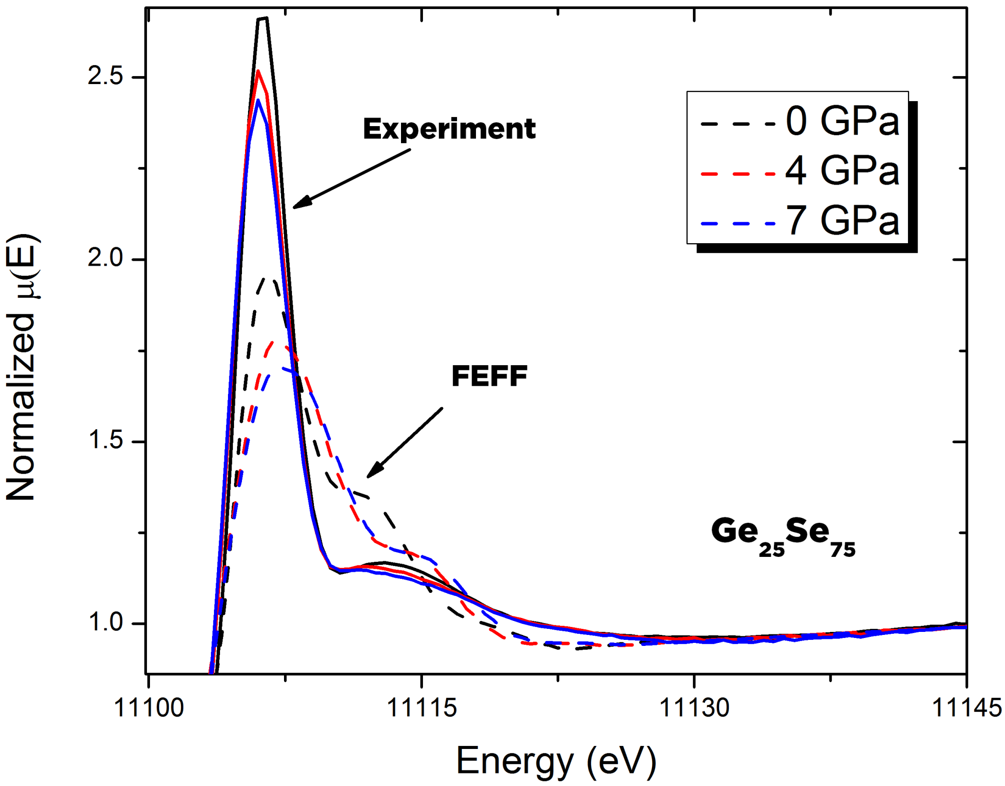

Figure B.3: Experimental XANES spectra (continuous curves) for $Ge_{25}Se_{75}$ under pressure at Ge K edge compared to FEFF calculations using the AIMD simulated atomic trajectories (broken curves).

response to the applied pressure is well produced. Further optimization is needed for future studies. Fig. a) B.4 shows intermediate scattering function of the Se species at 300 K and ambient pressure. Fig. b) B.4 shows the evolution of the non-ergodicity parameter obtained through the average value of the β relaxation plateau as a function of composition. It appears the network rigidity has a direct effect on the non ergodicity parameter in such a way that the most flexible compound $Ge_{10}Se_{90}$ has the lowest and the most rigid compound $Ge_{33}Se_{67}$ has the highest value. Moreover, increasing Ge content results in an increase in this parameter. However, a rather constant behavior is observed at the rigidity percolation threshold and the reported intermediate phase. We plan to confirm these values from the IXS experiment once the analysis are done.

All data regarding the Ge-Se system under pressure are produced by applying the cold compression method explained in Chapter 2. We also employed another thermal

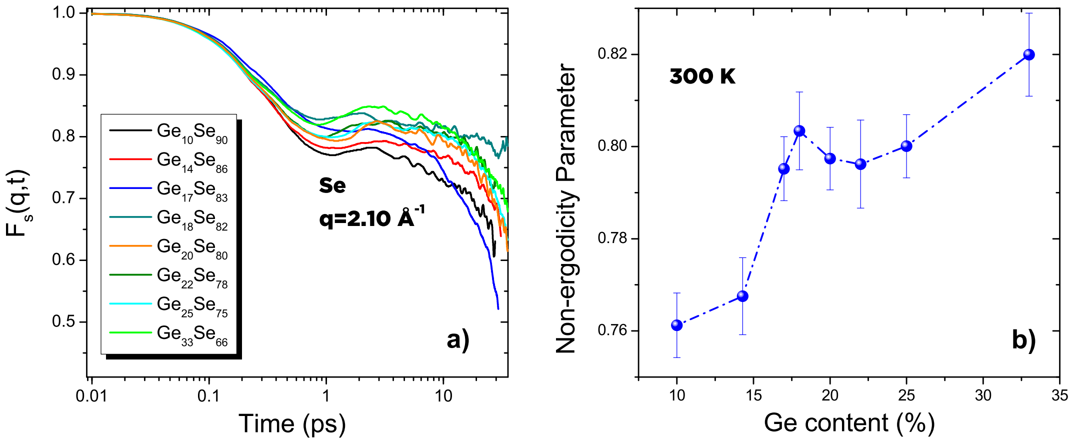

Figure B.4: a) Calculated intermediate scattering functions for selected compositions of Ge_xSe_{100-x} at 300 K. b) The non-ergodicity parameter as a function composition.

path for the application of pressure to our structural models generated by AIMD. For this, after obtaining the energetically best glass trajectory upon quenching, we applied pressure after heating the system at 600 K and relaxing it for about 40ps. This step was then followed by a cooling down to 300 K for another 30-40 ps. Fig. B.5 shows preliminary results on the effect of thermal history on the bond angle distribution for $Ge_{10}Se_{90}$ under pressure. Indeed, the results show that there are differences in the structural evolution under pressure, even though the simulated quantities at ambient pressure are nearly the same. An important result from the Ge-Se-Ge BAD can be given as the interplay between ES and CS tetrahedral connections. It appears that a more relaxed structure yields fewer ES connections. This results may be linked to the fact that ES connections are reported to be a fragility promoting feature in chalcogenide systems [[75] and therein]. Thus increased relaxation times may result in the decrease of the fraction of these connections. Furthermore, another interesting finding comes from Se-Ge-Se BAD at 10.4 GPa. The tetrahedral angle is preserved for both compression methods below 10 GPa. On the other hand, one can notice a shoulder at 90° degree and a tail around 180° degrees indicating an octahedral geometry for the annealed compression which are absent for the case of cold compression. This difference may be related with overcoming a thermal energy barrier of the annealed compression more easily compared to the cold compression case. Moreover, this result provides important insight to the differences between ND experiments and AIMD simulation in the work of Wezka et al. [89] where the coordination number of the $Ge_{33}Se_{67}$ system increases at pressures above 8 GPa, whereas the coordination number measured from ND remains nearly the same. Given that the thermal activation barrier can be surpassed more easily in the case of annealed compression, the LDA to HDA phase transition may occur which manifests itself with the coordination increase due to tetrahedral to octahedral geometry.

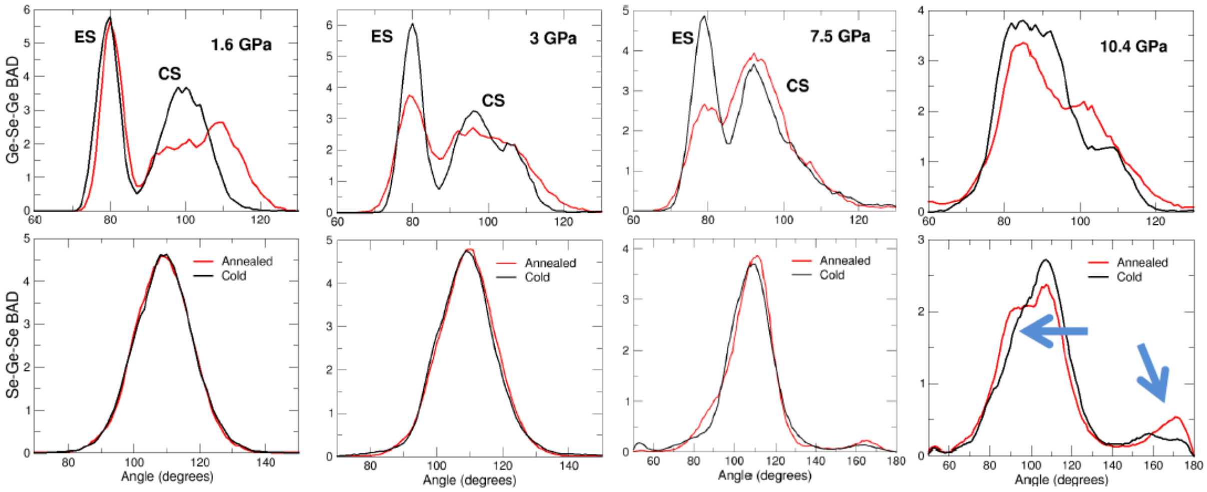

Figure B.5: Calculated average Ge-Se-Ge and Se-Ge-Se bond angle distributions of (BAD) $Ge_{10}Se_{90}$ under pressure at annealed or cold compression conditions.

Fig. B.6 shows the effect of pressure on the electronic band gap of $Ge_{20}Se_{80}$. The measured XANES spectra showed a red shift for Ge K edge (as shown for $Ge_{17}Se_{83}$ in Fig. 5.3) under pressure. The semiconductor to metal transition in $Ge_{20}Se_{80}$ is also confirmed by the work of Bouzid et al. [94] using AIMD simulations.

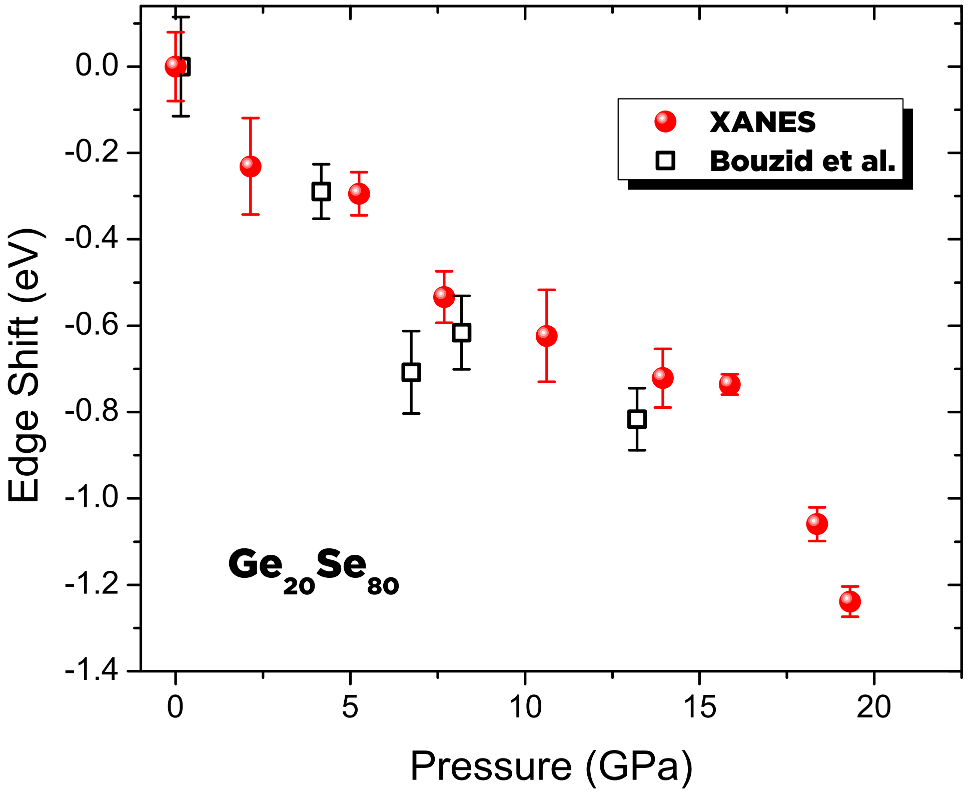

Figure B.6: Measured pressure dependence of Ge K edge shift energy in XANES spectra of $Ge_{20}Se_{80}$ compared to AIMD simulations from the ref [94].

Appendix C

List of Scientific Contribution

C.0.2 Publications in International Journals

1. *Revealing the role of molecular rigidity on the fragility evolution of glass forming liquids*
   C. Yildirim, J.Y. Raty, and M.Micoulaut
   Published in **Nature Communications**, doi:10.1038/ncomms11086

2. *Universal amorphous-amorphous transition in* Ge_xSe_{100-x} *glasses under pressure*
   C. Yildirim, M.Micoulaut, P. Boolchand, I. Kantor, O. Mathon, J.P. Gaspard, T. Irifune, and J.Y. Raty,
   Published in **Scientific Reports**, doi:10.1038/srep27317

3. *Anomalous diffusion and non-monotonic relaxation processes in liquid Ge-Se*
   C. Yildirim, J.Y. Raty, and M.Micoulaut
   Published in **Journal of Chemical Physics**, doi:10.1063/1.4953077

4. *Decoding embedded transitions: polyamorphism and stressed rigidity*
   C. Yildirim, J.Y. Raty, and M.Micoulaut
   Manuscript under preparation.

C.0.3 Oral Presentation

1. Glass & Optical Materials Division and Deutsche Glastechnische Gesellschaft Joint Annual Meeting - Madison, WI, May 2016

2. (**Invited**) Glass & Optical Materials Division and Deutsche Glastechnische Gesellschaft Joint Annual Meeting - Miami, FL, May 2015

3. PhD Days, Liege, Belgium, April 2016
4. International Doctoral School of Functional Materials Meeting, Bordeaux, France, March 2016
5. PhD Days, Liege, Belgium, April 2015
6. International Doctoral School of Functional Materials Meeting, Koblenz, Germany, March 2015
7. PhD Days, Liege, Belgium, April 2014
8. International Doctoral School of Functional Materials Meeting, Spa, Belgium, March 2015

C.0.4 Poster Presentations and Scientific Visits

1. **Poster presentation** at International Doctoral School of Functional Materials Meeting, *Structure and Dynamics of* Ge_xSe_{100-x} *Glasses under pressure*, Koblenz, Germany, March, 2015
2. **Poster presentation** at International Doctoral School of Functional Materials Meeting, *Revealing the Role of Constraints on the Fragility of Glass Forming Liquids*, Bordeaux, France, March, 2015
3. **Beamline user** at European Synchrotron Radiation Facility -Grenoble, France, Energy Dispersive XAS ID 24 Experiment on liquid-liquid transitions in ZnSe at Extreme Pressure and Temperature , HC-2787, April 2016
4. **Beamline user** at European Synchrotron Radiation Facility -Grenoble, France, Inelastic Scattering II beamline ID 28 Experiment on vibrational modes of Ge-Se glasses under pressure, HC-2195, February 2016
5. **Beamline user** at European Synchrotron Radiation Facility -Grenoble, France, BM 23 Experiment on amorphous phase transitions and densification mechanism Ge-Se glasses under pressure,HC-1862, July 2015
6. **Beamline user** at European Synchrotron Radiation Facility -Grenoble, France, Energy Dispersive XAS ID 24 Experiment on structural changes of liquid ZnSe at high temperature and pressure, HC-1608, October 2014

7. **Beamline user** at European Synchrotron Radiation Facility -Grenoble, France, Energy Dispersive XAS ID 24 Experiment on Experiment on layered multiband superconductors $LnO_{0.5}F_{0.5}BiS_2$ (Ln=La and Ce),HC-1304,April 2014

Bibliography

[1] A Leo Oppenheim. *Ancient Mesopotamia: portrait of a dead civilization*. University of Chicago Press, 2013.

[2] William Houlder Zachariasen. The atomic arrangement in glass. *Journal of the American Chemical Society*, 54(10):3841–3851, 1932.

[3] M. Reiner. The Deborah Number. *Phys. Today*, 17(M):62, 1964.

[4] Yu Wang, Xiaobing Ren, Kazuhiro Otsuka, and Avadh Saxena. Evidence for broken ergodicity in strain glass. *Phys. Rev. B - Condens. Matter Mater. Phys.*, 76(13):2–5, 2007.

[5] K. Binder and A. P. Young. Spin glasses: Experimental facts, theoretical concepts, and open questions. *Rev. Mod. Phys.*, 58(4):801–976, 1986.

[6] Ludger Santen and Werner Krauth. Absence of thermodynamic phase transition in a model glass former. *Nature*, 405(6786):550–551, 2000.

[7] RG Palmer. Broken ergodicity. *Advances in Physics*, 31(6):669–735, 1982.

[8] James Charles Phillips and Michael F Thorpe. *Phase transitions and self-organization in electronic and molecular networks*. Springer Science & Business Media, 2006.

[9] Jean-Luc Garden, Hervé Guillou, Jacques Richard, and Lothar Wondraczek. Non-equilibrium configurational prigogine–defay ratio. *Journal of Non-Equilibrium Thermodynamics*, 37(2):143–177, 2012.

[10] Prabhat K. Gupta and John C. Mauro. The laboratory glass transition. *J. Chem. Phys.*, 126(22), 2007.

[11] B Jerome and J Commandeur. Dynamics of glasses below the glass transition. 1997.

[12] Pablo Debenedetti and Frank Stillinger. Supercooled liquids and the glass transition. *Nature*, 410(6825):259–267, 2001.

[13] Charles Austen Angell and W Sichina. Thermodynamics of the glass transition: Empirical aspects*. *Annals of the New York Academy of Sciences*, 279(1):53–67, 1976.

[14] Charles Austen Angell. Structural instability and relaxation in liquid and glassy phases near the fragile liquid limit. *Journal of non-crystalline solids*, 102(1):205–221, 1988.

[15] C Austen Angell. Formation of glasses from liquids and biopolymers. *Science*, 267(5206):1924–1935, 1995.

[16] Walter Kauzmann. The nature of the glassy state and the behavior of liquids at low temperatures. *Chemical Reviews*, 43(2):219–256, 1948.

[17] EA DiMarzio and JH Gibbs. Chain stiffness and the lattice theory of polymer phases. *The Journal of Chemical Physics*, 28(5):807–813, 1958.

[18] C A Angell, K L Ngai, G. B. McKenna, P. F. McMillan, and S W Martin. Relaxation in glassforming liquids and amorphous solids. *J. Appl. Phys.*, 88(6):3113, 2000.

[19] Ian M Hodge and James M O'Reilly. Nonlinear kinetic and thermodynamic properties of monomeric organic glasses. *The Journal of Physical Chemistry B*, 103(20):4171–4176, 1999.

[20] Luca Leuzzi and Th M Nieuwenhuizen. *Thermodynamics of the glassy state*. CRC Press, 2007.

[21] George W Scherer. Editorial comments on a paper by gordon s. fulcher. *Journal of the American Ceramic Society*, 75(5):1060–1062, 1992.

[22] WT Laughlin and Donald R Uhlmann. Viscous flow in simple organic liquids. *The Journal of Physical Chemistry*, 76(16):2317–2325, 1972.

[23] John C Mauro, Yuanzheng Yue, Adam J Ellison, Prabhat K Gupta, and Douglas C Allan. Viscosity of glass-forming liquids. *Proceedings of the National Academy of Sciences*, 106(47):19780–19784, 2009.

[24] Gerold Adam and Julian H Gibbs. On the temperature dependence of cooperative relaxation properties in glass-forming liquids. *The journal of chemical physics*, 43(1):139–146, 1965.

[25] Prabhat K Gupta and John C Mauro. Composition dependence of glass transition temperature and fragility. i. a topological model incorporating temperature-dependent constraints. *The Journal of chemical physics*, 130(9):094503, 2009.

[26] Jr C Phillips. Topology of covalent non-crystalline solids i: Short-range order in chalcogenide alloys. *Journal of Non-Crystalline Solids*, 34(2):153–181, 1979.

[27] J. C. Phillips and M.F Thorpe. Constraint theory, vector percolation and glass formation. *Solid State Commun.*, 53(8):699–702, 1985.

[28] Michael F Thorpe. Continuous deformations in random networks. *Journal of Non-Crystalline Solids*, 57(3):355–370, 1983.

[29] H He and Michael F Thorpe. Elastic properties of glasses. *Physical Review Letters*, 54(19):2107, 1985.

[30] Mathieu Bauchy, Mohammad Javad Abdolhosseini Qomi, Christophe Bichara, Franz Joseph Ulm, and Roland J M Pellenq. Nanoscale structure of cement: Viewpoint of rigidity theory. *J. Phys. Chem. C*, 118(23):12485–12493, 2014.

[31] Mathieu Bauchy, Mohammad Javad Abdolhosseini Qomi, Christophe Bichara, Franz-Josef Ulm, and Roland J-M Pellenq. Rigidity transition in materials: hardness is driven by weak atomic constraints. *Physical review letters*, 114(12):125502, 2015.

[32] Morten M Smedskjaer, John C Mauro, and Yuanzheng Yue. Prediction of glass hardness using temperature-dependent constraint theory. *Physical review letters*, 105(11):115503, 2010.

[33] D Selvanathan, WJ Bresser, P Boolchand, and B Goodman. Thermally reversing window and stiffness transitions in chalcogenide glasses. *Solid state communications*, 111(11):619–624, 1999.

[34] D Selvanathan, WJ Bresser, and P Boolchand. Stiffness transitions in si x se 1- x glasses from raman scattering and temperature-modulated differential scanning calorimetry. *Physical Review B*, 61(22):15061, 2000.

[35] P Boolchand, P Chen, M Jin, B Goodman, and WJ Bresser. 129 i and 119 sn mössbauer spectroscopy, reversibility window and nanoscale phase separation in binary gexse 1- x glasses. *Physica B: Condensed Matter*, 389(1):18–28, 2007.

[36] DG Georgiev, P Boolchand, H Eckert, M Micoulaut, and K Jackson. The self-organized phase of bulk p x se 1- x glasses. *EPL (Europhysics Letters)*, 62(1):49, 2003.

[37] P Boolchand, DG Georgiev, and M Micoulaut. Nature of glass transition in chalcogenides. *J. Optoelectron. Adv. Mater*, 4(4):823, 2002.

[38] S Chakravarty, DG Georgiev, P Boolchand, and M Micoulaut. Ageing, fragility and the reversibility window in bulk alloy glasses. *Journal of Physics: Condensed Matter*, 17(1):L1, 2004.

[39] Fei Wang, S. Mamedov, P. Boolchand, B. Goodman, and Meera Chandrasekhar. Pressure raman effects and internal stress in network glasses. *Phys. Rev. B*, 71:174201, May 2005.

[40] K Rompicharla, DI Novita, Ping Chen, P Boolchand, M Micoulaut, and W Huff. Abrupt boundaries of intermediate phases and space filling in oxide glasses. *Journal of Physics: Condensed Matter*, 20(20):202101, 2008.

[41] C. Bourgel, M. Micoulaut, M. Malki, and P. Simon. Molar volume minimum and adaptative rigid networks in relationship with the intermediate phase in glasses. *Phys. Rev. B*, 79:024201, Jan 2009.

[42] Xingwei Feng, W. J. Bresser, and P. Boolchand. Direct evidence for stiffness threshold in chalcogenide glasses. *Phys. Rev. Lett.*, 78:4422–4425, Jun 1997.

[43] Ogur.z Gulbiten. AN INVESTIGATION OF DYNAMIC PROCESSES In the Graduate College. 2014.

[44] Pierre Lucas, Ellyn A. King, Ozgur Gulbiten, Jeffery L. Yarger, Emmanuel Soignard, and Bruno Bureau. Bimodal phase percolation model for the structure of ge-se glasses and the existence of the intermediate phase. *Phys. Rev. B*, 80:214114, Dec 2009.

[45] Siddhesh Bhosle, Kapila Gunasekera, Punit Boolchand, and Matthieu Micoulaut. Melt Homogenization and Self-Organization in Chalcogenides-Part I. *Int. J. Appl. Glas. Sci.*, 3(3):189–204, 2012.

[46] Siddhesh Bhosle, Kapila Gunasekera, Punit Boolchand, and Matthieu Micoulaut. Melt homogenization and self-organization in chalcogenides-part ii. *International Journal of Applied Glass Science*, 3(3):205–220, 2012.

[47] S Bhosle, K Gunasekera, Ping Chen, P Boolchand, M Micoulaut, and C Massobrio. Meeting experimental challenges to physics of network glasses: Assessing the role of sample homogeneity. *Solid State Communications*, 151(24):1851–1855, 2011.

[48] Deassy I. Novita and P. Boolchand. Synthesis and structural characterization of dry $\mathrm{AgPo_3}$ glass by raman scattering, infrared reflectance, and modulated differential scanning calorimetry. *Phys. Rev. B*, 76:184205, Nov 2007.

[49] M Micoulaut, Ali Kachmar, M Bauchy, S Le Roux, C Massobrio, and M Boero. Structure, topology, rings, and vibrational and electronic properties of ge x se 1- x glasses across the rigidity transition: A numerical study. *Physical Review B*, 88(5):054203, 2013.

[50] P Boolchand, X Feng, and WJ Bresser. Rigidity transitions in binary ge–se glasses and the intermediate phase. *Journal of Non-Crystalline Solids*, 293:348–356, 2001.

[51] Stefano Cazzato. Relaxation Dynamics in Amorphous Chalcogenides probed by InfraRed Photon Correlation Spectroscopy. *PhD Diss.*

[52] Allison A Wilhelm, Pierre Lucas, Diana L DeRosa, and Mark R Riley. Biocompatibility of te–as–se glass fibers for cell-based bio-optic infrared sensors. *Journal of materials research*, 22(04):1098–1104, 2007.

[53] Crystal A Vargas, Allison A Wilhelm, Jeremy Williams, Pierre Lucas, Kelly A Reynolds, and Mark R Riley. Integrated capture and spectroscopic detection of viruses. *Applied and environmental microbiology*, 75(20):6431–6440, 2009.

[54] Zhiyong Yang, Allison A Wilhelm, and Pierre Lucas. High-conductivity tellurium-based infrared transmitting glasses and their suitability for bio-optical detection. *Journal of the American Ceramic Society*, 93(7):1941–1944, 2010.

[55] XH Zhang, Y Guimond, and Y Bellec. Production of complex chalcogenide glass optics by molding for thermal imaging. *Journal of Non-Crystalline Solids*, 326:519–523, 2003.

[56] Bruno Bureau, Xiang Hua Zhang, Frederic Smektala, Jean-Luc Adam, Johann Troles, Hong-li Ma, Catherine Boussard-Plèdel, Jacques Lucas, Pierre Lucas, David Le Coq, et al. Recent advances in chalcogenide glasses. *Journal of non-crystalline solids*, 345:276–283, 2004.

[57] B Seddon. Chalcogenide glasses: A review of their preparation, properties and 191 applications. *J. Non-Cryst. Solid*, 184:44–50, 1985.

[58] Mihai A Popescu. *Non-Crystalline Chalcogenicides*, volume 8. Springer Science & Business Media, 2001.

[59] Valentina F Kokorina. *Glasses for infrared optics*, volume 13. CRC press, 1996.

[60] DR Uhman and NJ Kreidl. Glass science and technology, vol. 1, glass-forming systems, 1983.

[61] JA Savage. Infrared optical materials and their antireflection coatings. *Bristol: Hilger, 1985*, 1, 1985.

[62] AR Hilton, CE Jones, and M Brau. Non-oxide iva-va-via chalcogenide glasses. i. glass-forming regions and variations in physical properties. *Physics and Chemistry of Glasses*, 7(4):105, 1966.

[63] N Mehta. Applications of chalcogenide glasses in electronics and optoelectronics: A review. *Journal of Scientific and Industrial Research*, 65(10):777, 2006.

[64] Punit Boolchand. *Insulating and semiconducting glasses*, volume 17. World scientific, 2000.

[65] K Shimakawa, A Kolobov, and SR Elliott. Photoinduced effects and metastability in amorphous semiconductors and insulators. *Advances in Physics*, 44(6):475–588, 1995.

[66] AM Andriesh. Photoinduced phenomena in chalcogenide glass semiconductors. In *Physics and Applications of Non-Crystalline Semiconductors in Optoelectronics*, pages 17–30. Springer, 1997.

[67] Gerald Lucovsky. Optic modes in amorphous as 2 s 3 and as 2 se 3. *Physical Review B*, 6(4):1480, 1972.

[68] J Stuke and Wilhelm Brenig. Amorphous and liquid semiconductors(proceedings of the 5 th international conference on amorphous and liquid semiconductors). 1974.

[69] WJ Bresser, P Boolchand, P Suranyi, and JP De Neufville. Direct evidence for intrinsically broken chemical ordering in melt-quenched glasses. *Physical Review Letters*, 46(26):1689, 1981.

[70] Philip S Salmon and Ingrid Petri. Structure of glassy and liquid gese2. *Journal of Physics: Condensed Matter*, 15(16):S1509, 2003.

[71] R Azoulay, H Thibierge, and A Brenac. Devitrification characteristics of ge x se 1- x glasses. *Journal of Non-Crystalline Solids*, 18(1):33–53, 1975.

[72] P Boolchand, J Grothaus, WJ Bresser, and P Suranyi. Structural origin of broken chemical order in a ge se 2 glass. *Physical Review B*, 25(4):2975, 1982.

[73] Philip S Salmon. Structure of liquids and glasses in the ge–se binary system. *Journal of Non-Crystalline Solids*, 353(32):2959–2974, 2007.

[74] S Susman, DL Price, KJ Volin, RJ Dejus, and DG Montague. Intermediate-range order in binary chalcogenide glasses: The first sharp diffraction peak. *Journal of Non-Crystalline Solids*, 106(1-3):26–29, 1988.

[75] Philip S Salmon and Anita Zeidler. Networks under pressure: the development of in situ high-pressure neutron diffraction for glassy and liquid materials. *Journal of Physics: Condensed Matter*, 27(13):133201, 2015.

[76] Q Mei, CJ Benmore, RT Hart, E Bychkov, PS Salmon, CD Martin, FM Michel, SM Antao, PJ Chupas, PL Lee, et al. Topological changes in glassy ge se 2 at pressures up to 9.3 gpa determined by high-energy x-ray and neutron diffraction measurements. *Physical Review B*, 74(1):014203, 2006.

[77] Bora Kalkan, Ranga P Dias, Choong-Shik Yoo, Simon M Clark, and Sabyasachi Sen. Polyamorphism and pressure-induced metallization at the rigidity percolation threshold in densified gese4 glass. *The Journal of Physical Chemistry C*, 118(10):5110–5121, 2014.

[78] Paul F McMillan. Polyamorphic transformations in liquids and glasses. *Journal of Materials Chemistry*, 14(10):1506–1512, 2004.

[79] Tomoko Sato and Nobumasa Funamori. Sixfold-coordinated amorphous polymorph of sio 2 under high pressure. *Physical review letters*, 101(25):255502, 2008.

[80] M Vaccari, G Aquilanti, S Pascarelli, and O Mathon. A new exafs investigation of local structural changes in amorphous and crystalline geo2 at high pressure. *Journal of Physics: Condensed Matter*, 21(14):145403, 2009.

[81] VV Brazhkin, Y Katayama, K Trachenko, OB Tsiok, AG Lyapin, Emilio Artacho, M Dove, G Ferlat, Y Inamura, and H Saitoh. Nature of the structural transformations in b 2 o 3 glass under high pressure. *Physical review letters*, 101(3):035702, 2008.

[82] Murat Durandurdu and DA Drabold. Simulation of pressure-induced polyamorphism in a chalcogenide glass gese 2. *Physical Review B*, 65(10):104208, 2002.

[83] Sytle M Antao, Chris J Benmore, Baosheng Li, Liping Wang, Evgeny Bychkov, and John B Parise. Network rigidity in gese 2 glass at high pressure. *Physical review letters*, 100(11):115501, 2008.

[84] Dominik Daisenberger, Mark Wilson, Paul F McMillan, Raul Quesada Cabrera, Martin C Wilding, and Denis Machon. High-pressure x-ray scattering and computer simulation studies of density-induced polyamorphism in silicon. *Physical Review B*, 75(22):224118, 2007.

[85] A Di Cicco, A Congeduti, F Coppari, JC Chervin, F Baudelet, and A Polian. Interplay between morphology and metallization in amorphous-amorphous transitions. *Physical Review B*, 78(3):033309, 2008.

[86] O Mishima, LD Calvert, and E Whalley. An apparently first-order transition between two amorphous phases of ice induced by pressure. *Nature*, 314(6006):76–78, 1985.

[87] HW Sheng, HZ Liu, YQ Cheng, J Wen, PL Lee, WK Luo, SD Shastri, and E Ma. Polyamorphism in a metallic glass. *Nature materials*, 6(3):192–197, 2007.

[88] Vadim V Brazhkin, Eugene Bychkov, and Oleg B Tsiok. Direct volumetric study of high-pressure driven polyamorphism and relaxation in the glassy germanium chalcogenides. *The Journal of Physical Chemistry B*, 2015.

[89] Kamil Wezka, Assil Bouzid, Keiron J Pizzey, Philip S Salmon, Anita Zeidler, Stefan Klotz, Henry E Fischer, Craig L Bull, Matthew G Tucker, Mauro Boero, et al. Density-driven defect-mediated network collapse of gese 2 glass. *Physical Review B*, 90(5):054206, 2014.

[90] L Properzi, A Di Cicco, L Nataf, F Baudelet, and T Irifune. Short-range order of compressed amorphous gese2. *Scientific reports*, 5, 2015.

[91] M Vaccari, G Garbarino, G Aquilanti, M-V Coulet, A Trapananti, S Pascarelli, M Hanfland, E Stavrou, and C Raptis. Structural changes in amorphous ges 2 at high pressure. *Physical Review B*, 81(1):014205, 2010.

[92] Murat Durandurdu. High-density amorphous phase of ges 2 glass under pressure. *Physical Review B*, 79(20):205202, 2009.

[93] LB Skinner, CJ Benmore, S Antao, E Soignard, SA Amin, E Bychkov, E Rissi, JB Parise, and JL Yarger. Structural changes in vitreous gese4 under pressure. *The Journal of Physical Chemistry C*, 116(3):2212–2217, 2011.

[94] Assil Bouzid, Keiron J Pizzey, Anita Zeidler, Guido Ori, Mauro Boero, Carlo Massobrio, Stefan Klotz, Henry E Fischer, Craig L Bull, and Philip S Salmon. Pressure-induced structural changes in the network-forming isostatic glass gese 4: An investigation by neutron diffraction and first-principles molecular dynamics. *Physical Review B*, 93(1):014202, 2016.

[95] Godehard Sutmann. *Classical molecular dynamics*, volume 10. Citeseer, 2002.

[96] BWH Van Beest, Gert Jan Kramer, and RA Van Santen. Force fields for silicas and aluminophosphates based on ab initio calculations. *Physical Review Letters*, 64(16):1955, 1990.

[97] Bertrand Guillot and Nicolas Sator. A computer simulation study of natural silicate melts. part ii: High pressure properties. *Geochimica et Cosmochimica Acta*, 71(18):4538–4556, 2007.

[98] Yves Guissani and Bertrand Guillot. A numerical investigation of the liquid–vapor coexistence curve of silica. *The Journal of chemical physics*, 104(19):7633–7644, 1996.

[99] I Petri and PS Salmon. The topology of gexse1-x (0< x< 0.4) glasses. *Physics and Chemistry of Glasses*, 43:185–190, 2002.

[100] John C Mauro and Arun K Varshneya. Multiscale modeling of gese2 glass structure. *Journal of the American Ceramic Society*, 89(7):2323–2326, 2006.

[101] L H Thomas. The calculation of atomic fields. *Proc. Camb. Philos. Soc.*, 23(5):542, 1927.

[102] Enrico Fermi. Un metodo statistico per la determinazione di alcune priorieta dell'atome. *Rend. Accad. Naz. Lincei*, 6(32):602–607, 1927.

[103] P. a. M. Dirac. Note on Exchange Phenomena in the Thomas Atom. *Math. Proc. Cambridge Philos. Soc.*, 26(03):376, 1930.

[104] W Hohenberg, P ; Kohn. Inhomogenour electron gas. *Phys. Rev. Lett.*, 136(3B):B864, 1964.

[105] L J Kohn, W and Sham. Self-consistent equations including exchange and correlation effects. *Phys. Rev. Lett.*, 140(4A):A1133, 1965.

[106] M Levy. Universal variational functionals of electron densities, first-order density matrices, and natural spin-orbitals and solution of the v-representability problem. *Proc. Natl. Acad. Sci. U. S. A.*, 76(12):6062–5, 1979.

[107] Mel Levy. Electron densities in search of Hamiltonians. *Phys. Rev. A*, 26(3):1200–1208, 1982.

[108] E H Lieb. Density Functionals for Coulomb-Systems. *Int. J. Quantum Chem.*, 24(3):243–277, 1983.

[109] R. O. Jones and O. Gunnarsson. The density functional formalism, its applications and prospects. *Rev. Mod. Phys.*, 61(3):689–746, 1989.

[110] J. P. Perdew and Alex Zunger. Self-interaction correction to density-functional approximations for many-electron systems. *Phys. Rev. B*, 23(10):5048–5079, 1981.

[111] D Langreth and Mehl M J. Beyond the local-density approximation in calculations of ground-state electronic properties. *Phys. Rev. B*, 28(4):28, 1983.

[112] Axel D. Becke. A new inhomogeneity parameter in density-functional theory. *J. Chem. Phys.*, 109(6):2092–2098, 1998.

[113] Axel D Becke. A new mixing of Hartree-Fock and local-density-functional theories. *J. Chem. Phys.*, 98(2):1372–1377, 1993.

[114] Stephan Kümmel and Leeor Kronik. Orbital-dependent density functionals: Theory and applications. *Rev. Mod. Phys.*, 80(1):3–60, 2008.

[115] D M Ceperley and B J Alder. Ground state of the electron gas by a stochastic model. *Phys. Rev. Lett.*, 45(7):566–569, 1980.

[116] John P. Perdew, Kieron Burke, and Matthias Ernzerhof. Generalized Gradient Approximation Made Simple. *Phys. Rev. Lett.*, 77(18):3865–3868, 1996.

[117] John Perdew, Kieron Burke, and Yue Wang. Generalized gradient approximation for the exchange-correlation hole of a many-electron system. *Phys. Rev. B*, 54(23):16533–16539, 1996.

[118] A. D. Becke. Density-functional exchange-energy approximation with correct asymptotic behavior. *Phys. Rev. A*, 38(6):3098–3100, 1988.

[119] Chengteh Lee, Weitao Yang, and Robert G. Parr. Development of the Colle-Salvetti correlation-energy formula into a functional of the electron density. *Phys. Rev. B*, 37(2):785–789, 1988.

[120] N Troullier and J. L. Martins. Efficient pseudopotentials for plane-wave calculations. *Phys. Rev. B*, 43(3), 1993.

[121] L Verlet. Computer "experiments" on classical fluids. I. Thermodynamical properties of Lennard-Jones molecules. *Phys. Rev. Lett.*, 159(1):98–103, 1967.

[122] R. Car and M. Parrinello. Physical review letters 25. *Phys. Rev. Lett.*, 55(22), 1985.

[123] Peter E. Blochl and M. Parrinello. Adiabaticity in first-principles molecular dynamics. *Phys. Rev. B*, 45(16):9413–9416, 1992.

[124] J Ruska and H Thurn. Change of short-range order with temperature and composition in liquid ge x se 1- x as shown by density measurements. *Journal of Non-Crystalline Solids*, 22(2):277–290, 1976.

[125] R. L. Cappelletti, Mark Cobb, D. A. Drabold, and W. A. Kamitakahara. Neutron-scattering and *ab initio* molecular-dynamics study of vibrations in glassy gese_2. *Phys. Rev. B*, 52:9133–9136, Oct 1995.

[126] Mark Cobb, RL Cappelletti, and DA Drabold. Structure, dynamics and electronic properties of liquid and glassy gese 2. *Journal of non-crystalline solids*, 222:348–353, 1997.

[127] Carlo Massobrio, Alfredo Pasquarello, and Roberto Car. Microscopic structure of liquid GeSe_2: The problem of concentration fluctuations over intermediate range distances. *Phys. Rev. Lett.*, 80:2342–2345, Mar 1998.

[128] Carlo Massobrio, Alfredo Pasquarello, and Roberto Car. Intermediate range order and bonding character in disordered network-forming systems. *Journal of the American Chemical Society*, 121(12):2943–2944, 1999.

[129] Carlo Massobrio, Alfredo Pasquarello, and Roberto Car. Short-and intermediate-range structure of liquid gese 2. *Physical Review B*, 64(14):144205, 2001.

[130] Matthieu Micoulaut, Rodolphe Vuilleumier, and Carlo Massobrio. Improved modeling of liquid gese$_2$: Impact of the exchange-correlation functional. *Phys. Rev. B*, 79:214205, Jun 2009.

[131] Benny G Johnson, Peter MW Gill, and John A Pople. The performance of a family of density functional methods. *The Journal of chemical physics*, 98(7):5612–5626, 1993.

[132] Carlo Massobrio, Matthieu Micoulaut, and Philip S Salmon. Impact of the exchange-correlation functional on the structure of glassy gese 2. *Solid State Sciences*, 12(2):199–203, 2010.

[133] Luigi Giacomazzi, Carlo Massobrio, and Alfredo Pasquarello. Vibrational properties of vitreous gese2 with the becke? lee? yang? parr density functional. *Journal of Physics: Condensed Matter*, 23(29):295401, 2011.

[134] Matthieu Micoulaut, Sébastien Le Roux, and Carlo Massobrio. Investigation of size effects on the structure of liquid gese2 calculated via first-principles molecular dynamics. *The Journal of chemical physics*, 136(22):224504, 2012.

[135] Assil Bouzid and Carlo Massobrio. Note: Accounting for pressure effects on the calculated equilibrium structure of glassy gese2. *The Journal of chemical physics*, 137(4):046101, 2012.

[136] FHM Van Roon, C Massobrio, E de Wolff, and SW De Leeuw. Structure of liquid gese: A first principle study. *The Journal of Chemical Physics*, 113(13):5425–5431, 2000.

[137] Jean-Yves Raty, VV Godlevsky, Jean-Pierre Gaspard, C Bichara, M Bionducci, R Bellissent, R Céolin, JR Chelikowsky, and Ph Ghosez. Distance correlations and dynamics of liquid gese: An ab initio molecular dynamics study. *Physical Review B*, 64(23):235209, 2001.

[138] Sébastien Le Roux, Assil Bouzid, Mauro Boero, and Carlo Massobrio. The structure of liquid gese revisited: A first principles molecular dynamics study. *The Journal of chemical physics*, 138(17):174505, 2013.

[139] MJ Haye, C Massobrio, Alfredo Pasquarello, A De Vita, SW De Leeuw, and R Car. Structure of liquid ge x se 1- x at the stiffness threshold composition. *Physical Review B*, 58(22):R14661, 1998.

[140] Carlo Massobrio, Massimo Celino, Philip S Salmon, Richard A Martin, Matthieu Micoulaut, and Alfredo Pasquarello. Atomic structure of the two intermediate phase glasses sise 4 and gese 4. *Physical review B*, 79(17):174201, 2009.

[141] Mikhail Kibalchenko, Jonathan R Yates, Carlo Massobrio, and Alfredo Pasquarello. Structural composition of first-neighbor shells in gese2 and gese4 glasses from a first-principles analysis of nmr chemical shifts. *The Journal of Physical Chemistry C*, 115(15):7755–7759, 2011.

[142] Kateryna Sykina, Eric Furet, Bruno Bureau, Sébastien Le Roux, and Carlo Massobrio. Network connectivity and extended se chains in the atomic structure of glassy gese 4. *Chemical Physics Letters*, 547:30–34, 2012.

[143] Assil Bouzid, Sébastien Le Roux, Guido Ori, Mauro Boero, and Carlo Massobrio. Origin of structural analogies and differences between the atomic structures of gese4 and ges4 glasses: A first principles study. *The Journal of chemical physics*, 143(3):034504, 2015.

[144] M. Bauchy and M. Micoulaut. Atomic scale foundation of temperature-dependent bonding constraints in network glasses and liquids. *J. Non. Cryst. Solids*, 357(14):2530–2537, 2011.

[145] M. Micoulaut, A. Kachmar, M. Bauchy, S. Le Roux, C. Massobrio, and M. Boero. Structure, topology, rings, and vibrational and electronic properties of ge$_x$se$_{1-x}$ glasses across the rigidity transition: A numerical study. *Phys. Rev. B*, 88:054203, Aug 2013.

[146] Konrad Hinsen, Eric Pellegrini, Sławomir Stachura, and Gerald R. Kneller. NMoldyn 3: Using task farming for a parallel spectroscopy-oriented analysis of molecular dynamics simulations. *J. Comput. Chem.*, 33(25):2043–2048, 2012.

[147] W. Humphrey, A. Dalke, and K. Schulten. VMD - Visual Molecular Dynamics. *J. Mol. Graph.*, 14:33–38, 1996.

[148] Mathieu Bauchy. Topological constraints and rigidity of network glasses from molecular dynamics simulations. *Am. Ceram. Soc. Bull.*, 91(4):1–11, 2012.

[149] Walet Kob. Computer simulations of supercooled liquids and glasses. *J. Phys. Condens. Matter*, 11:85–115, 1999.

[150] Leon V a N Hove. Space and Time and Born. *Phys. Rev.*, 95(1), 1954.

[151] Walter Kob and Hans C. Andersen. Testing mode-coupling theory for a supercooled binary Lennard-Jones mixture. II. Intermediate scattering function and dynamic susceptibility. *Phys. Rev. E*, 52(4):4134–4153, 1995.

[152] Jean-Pierre Hansen and Ian R McDonald. *Theory of simple liquids*. Elsevier, 1990.

[153] Walter Kob and Hans C Andersen. Scaling behavior in the β-relaxation regime of a supercooled lennard-jones mixture. *Physical review letters*, 73(10):1376, 1994.

[154] J. E. Penner-Hahn. X-ray Absorption Spectroscopy. *Compr. Coord. Chem. II*, pages 159–186, 2003.

[155] Tami E. Westre, Pierre Kennepohl, Jane G. DeWitt, Britt Hedman, Keith O. Hodgson, and Edward I. Solomon. A multiplet analysis of Fe K-edge 1s ??? 3d pre-Edge features of iron complexes. *J. Am. Chem. Soc.*, 119(27):6297–6314, 1997.

[156] Wojciech Gawelda. Time-Resolved X-Ray Absorption Spectroscopy of Transition Metal Complexes. *PhD Diss.*, 3673, 2006.

[157] PA Lee and JB Pendry. Theory of the extended x-ray absorption fine structure. *Phys. Rev. B*, 11(8):2795–2811, 1975.

[158] Stern E A, Sayers D E, and Lytle F W. Extended x-ray-absorption fine-structure technique. III. Determination of physical parameters. *Phys. Rev. B*, 11(12), 1975.

[159] a. L. Ankudinov, J. J. Rehr, and S. D. Conradson. Real-space multiple-scattering calculation and interpretation of x-ray-absorption near-edge structure. *Phys. Rev. B*, 58(12):7565–7576, 1998.

[160] Julia Maria Van Eijk. Structural Analysis of Phase-Change Materials using X-Ray Absorption Measurements. *PhD Diss.*, 2010.

[161] Adriano Filipponi and Andrea di Cicco. X-ray-absorption spectroscopy and n-body distribution functions in condensed matter. II. Data analysis and applications. *Phys. Rev. B*, 1(21):135–149, 2015.

[162] Adriano Filipponi, Andrea Di Cicco, and Via Madonna. X-ray-absorption spectroscopy and n-body distribution functions in condensed matter. I.Theory. *Phys. Rev. B*, 52(21):122–134, 1995.

[163] M. Newville. IFEFFIT: interactive XAFS analysis and FEFF fitting. *J. Synchrotron Radiat.*, 8(2):322–324, 1988.

[164] B. Ravel and M. Newville. ATHENA, ARTEMIS, HEPHAESTUS: Data analysis for X-ray absorption spectroscopy using IFEFFIT. *J. Synchrotron Radiat.*, 12(4):537–541, 2005.

[165] spectrum.ieeee.org.

[166] AP Hammersley. FIT2D: an introduction and overview. *Eur. Synchrotron Radiat. Facil. Intern. Rep. ESRF97HA02T*, 68, 1997.

[167] AN Sreeram, AK Varshneya, and DR Swiler. Molar volume and elastic properties of multicomponent chalcogenide glasses. *Journal of non-crystalline solids*, 128(3):294–309, 1991.

[168] S Asokan, MVN Prasad, G Parthasarathy, and ESR Gopal. Mechanical and chemical thresholds in iv-vi chalcogenide glasses. *Physical review letters*, 62(7):808, 1989.

[169] Tatsuya Okada, Takahide Satoh, Masayuki Matsumura, and Satoru Ohno. Electrical properties of liquid ge–se alloys. *Journal of the Physical Society of Japan*, 65(1):230–236, 1996.

[170] N Ramesh Rao, PSR Krishna, Saibal Basu, BA Dasannacharya, KS Sangunni, and ESR Gopal. Structural correlations in ge x se 1- x glasses–a neutron diffraction study. *Journal of non-crystalline solids*, 240(1):221–231, 1998.

[171] Ingrid Petri, Philip S Salmon, and Henry E Fischer. Defects in a disordered world: The structure of glassy gese 2. *Physical review letters*, 84(11):2413, 2000.

[172] Ian T Penfold and Philip S Salmon. Structure of covalently bonded glass-forming melts: A full partial-structure-factor analysis of liquid gese 2. *Physical review letters*, 67(1):97, 1991.

[173] Matthieu Micoulaut, Rodolphe Vuilleumier, and Carlo Massobrio. Improved modeling of liquid gese 2: Impact of the exchange-correlation functional. *Physical Review B*, 79(21):214205, 2009.

[174] M Micoulaut and C Massobrio. Improving the structural description of high-temperature liquid gese2 from ab initio molecular dynamics simulations. *Journal of Optoelectronics and Advanced Materials*, 11(12):1907, 2009.

[175] C Massobrio, FHM Van Roon, Alfredo Pasquarello, and SW De Leeuw. Breakdown of intermediate-range order in liquid gese2 at high temperatures. *Journal of Physics: Condensed Matter*, 12(46):L697, 2000.

[176] Ingrid Petri, Philip S Salmon, and W Spencer Howells. Change in the topology of the glass forming liquid gese2 with increasing temperature. *Journal of Physics: Condensed Matter*, 11(50):10219, 1999.

[177] Hans Sillescu. Heterogeneity at the glass transition: a review. *Journal of Non-Crystalline Solids*, 243(2):81–108, 1999.

[178] Jürgen Horbach and Walter Kob. Static and dynamic properties of a viscous silica melt. *Physical Review B*, 60(5):3169, 1999.

[179] M Micoulaut, Y Guissani, and B Guillot. Simulated structural and thermal properties of glassy and liquid germania. *Physical Review E*, 73(3):031504, 2006.

[180] Bruno Bureau, Johann Troles, Marie Le Floch, Frédéric Smektala, and Jacques Lucas. Medium range order studied in selenide glasses by 77 se nmr. *Journal of non-crystalline solids*, 326:58–63, 2003.

[181] Gerardo G Naumis. Energy landscape and rigidity. *Physical Review E*, 71(2):026114, 2005.

[182] John C Mauro, Prabhat K Gupta, and Roger J Loucks. Composition dependence of glass transition temperature and fragility. ii. a topological model of alkali borate liquids. *The Journal of chemical physics*, 130(23):234503, 2009.

[183] Christian Hermansen, John C Mauro, and Yuanzheng Yue. A model for phosphate glass topology considering the modifying ion sub-network. *The Journal of Chemical Physics*, 140(15):154501, 2014.

[184] M Micoulaut, J-Y Raty, C Otjacques, and C Bichara. Understanding amorphous phase-change materials from the viewpoint of maxwell rigidity. *Physical Review B*, 81(17):174206, 2010.

[185] Svein Stølen, Tor Grande, and Hege-Britt Johnsen. Fragility transition in gese 2–se liquids. *Physical Chemistry Chemical Physics*, 4(14):3396–3399, 2002.

[186] Yann Gueguen, Tanguy Rouxel, Pascal Gadaud, Cedric Bernard, Vincent Keryvin, and Jean-Christophe Sangleboeuf. High-temperature elasticity and

viscosity of ge x se 1- x glasses in the transition range. *Physical Review B*, 84(6):064201, 2011.

[187] Udayan Senapati and Arun K Varshneya. Viscosity of chalcogenide glass-forming liquids: an anomaly in the 'strong'and 'fragile'classification. *Journal of non-crystalline solids*, 197(2):210–218, 1996.

[188] Qiuju Zheng, John C Mauro, Adam J Ellison, Marcel Potuzak, and Yuanzheng Yue. Universality of the high-temperature viscosity limit of silicate liquids. *Physical Review B*, 83(21):212202, 2011.

[189] K Gunasekera, S Bhosle, P Boolchand, and M Micoulaut. Superstrong nature of covalently bonded glass-forming liquids at select compositions. *The Journal of chemical physics*, 139(16):164511, 2013.

[190] J Gump, I Finkler, H Xia, R Sooryakumar, WJ Bresser, and P Boolchand. Light-induced giant softening of network glasses observed near the mean-field rigidity transition. *Physical review letters*, 92(24):245501, 2004.

[191] Shibalik Chakraborty and P Boolchand. Topological origin of fragility, network adaptation, and rigidity and stress transitions in especially homogenized non-stoichiometric binary ge x s100–x glasses. *The Journal of Physical Chemistry B*, 118(8):2249–2263, 2014.

[192] Sriram Ravindren, K Gunasekera, Z Tucker, A Diebold, P Boolchand, and M Micoulaut. Crucial effect of melt homogenization on the fragility of non-stoichiometric chalcogenides. *The Journal of chemical physics*, 140(13):134501, 2014.

[193] Kapila Gunasekera, P Boolchand, and M Micoulaut. Elastic phases of ge x sb x se100–2 x ternary glasses driven by topology. *The Journal of Physical Chemistry B*, 117(34):10027–10034, 2013.

[194] K Gunasekera, P Boolchand, and M Micoulaut. Effect of mixed ge/si cross-linking on the physical properties of amorphous ge-si-te networks. *Journal of Applied Physics*, 115(16):164905, 2014.

[195] Florian Kargl, A Meyer, MM Koza, and H Schober. Formation of channels for fast-ion diffusion in alkali silicate melts: A quasielastic neutron scattering study. *Physical Review B*, 74(1):014304, 2006.

[196] B Ruta, G Baldi, Y Chushkin, Benoit Rufflé, L Cristofolini, Adriano Fontana, M Zanatta, and Francesco Nazzani. Revealing the fast atomic motion of network glasses. *Nature communications*, 5, 2014.

[197] Jürgen Horbach and Walter Kob. Relaxation dynamics of a viscous silica melt: The intermediate scattering functions. *Physical Review E*, 64(4):041503, 2001.

[198] Neil A Morgan and Frank J Spera. Glass transition, structural relaxation, and theories of viscosity: A molecular dynamics study of amorphous caal 2 si 2 o 8. *Geochimica et Cosmochimica Acta*, 65(21):4019–4041, 2001.

[199] HZ Cummins, Gen Li, YH Hwang, GQ Shen, WM Du, J Hernandez, and NJ Tao. Dynamics of supercooled liquids and glasses: comparison of experiments with theoretical predictions. *Zeitschrift für Physik B Condensed Matter*, 103(3):501–519, 1997.

[200] G Neville Greaves and Kia L Ngai. Reconciling ionic-transport properties with atomic structure in oxide glasses. *Physical Review B*, 52(9):6358, 1995.

[201] Roland Bohmer and Charles Austen Angell. Elastic and viscoelastic properties of amorphous selenium and identification of the phase transition between ring and chain structures. *Physical Review B*, 48(9):5857, 1993.

[202] R. Friedberg and J. M. Luttinger. Density of electronic energy levels in disordered systems. *Phys. Rev. B*, 12:4460–4474, Nov 1975.

[203] Peter Grassberger and Itamar Procaccia. The long time properties of diffusion in a medium with static traps. *The Journal of Chemical Physics*, 77(12):6281–6284, 1982.

[204] Roger C Welch, John R Smith, Marcel Potuzak, Xiaoju Guo, Bradley F Bowden, TJ Kiczenski, Douglas C Allan, Ellyn A King, Adam J Ellison, and John C Mauro. Dynamics of glass relaxation at room temperature. *Physical review letters*, 110(26):265901, 2013.

[205] Yingtian Yu, Mengyi Wang, Dawei Zhang, Bu Wang, Gaurav Sant, and Mathieu Bauchy. Stretched exponential relaxation of glasses at low temperature. *Physical review letters*, 115(16):165901, 2015.

[206] Marcel Potuzak, Roger C Welch, and John C Mauro. Topological origin of stretched exponential relaxation in glass. *The Journal of chemical physics*, 135(21):214502, 2011.

[207] John C Mauro and Morten M Smedskjaer. Unified physics of stretched exponential relaxation and weibull fracture statistics. *Physica A: Statistical Mechanics and its Applications*, 391(23):6121–6127, 2012.

[208] M Bauchy, M Micoulaut, M Boero, and C Massobrio. Compositional thresholds and anomalies in connection with stiffness transitions in network glasses. *Physical review letters*, 110(16):165501, 2013.

[209] Tullio Scopigno, Giancarlo Ruocco, Francesco Sette, and Giulio Monaco. Is the fragility of a liquid embedded in the properties of its glass? *Science*, 302(5646):849–852, 2003.

[210] Philip S Salmon, Richard A Martin, Philip E Mason, and Gabriel J Cuello. Topological versus chemical ordering in network glasses at intermediate and extended length scales. *Nature*, 435(7038):75–78, 2005.

[211] M Celino, S Le Roux, G Ori, Benoit Coasne, A Bouzid, M Boero, and C Massobrio. First-principles molecular dynamics study of glassy ges 2: Atomic structure and bonding properties. *Physical Review B*, 88(17):174201, 2013.

[212] G Chen, F Inam, and DA Drabold. Structural origin of the intermediate phase in ge–se glasses. *Applied Physics Letters*, 97(13):131901, 2010.

[213] VV Brazhkin and AG Lyapin. High-pressure phase transformations in liquids and amorphous solids. *Journal of Physics: Condensed Matter*, 15(36):6059, 2003.

[214] Raymond Jeanloz. Finite-strain equation of state for high-pressure phases. *Geophysical Research Letters*, 8(12):1219–1222, 1981.

[215] Jean-Pierre Guin, Tanguy Rouxel, Jean-Christophe Sanglebœuf, Isabelle Melscoët, and Jacques Lucas. Hardness, toughness, and scratchability of germanium–selenium chalcogenide glasses. *Journal of the American Ceramic Society*, 85(6):1545–1552, 2002.

[216] Gabriele C Sosso, Joerg Behler, and Marco Bernasconi. Breakdown of stokes–einstein relation in the supercooled liquid state of phase change materials. *physica status solidi (b)*, 249(10):1880–1885, 2012.

[217] Gabriele C Sosso, Jader Colombo, Jorg Behler, Emanuela Del Gado, and Marco Bernasconi. Dynamical heterogeneity in the supercooled liquid state of the phase change material gete. *The Journal of Physical Chemistry B*, 118(47):13621–13628, 2014.

[218] Michael Vogel and Sharon C Glotzer. Spatially heterogeneous dynamics and dynamic facilitation in a model of viscous silica. *Physical review letters*, 92(25):255901, 2004.

[219] Ludovic Berthier. Efficient measurement of linear susceptibilities in molecular simulations: Application to aging supercooled liquids. *Physical review letters*, 98(22):220601, 2007.

[220] W. A. Kamitakahara, R. L. Cappelletti, P. Boolchand, B. Halfpap, F. Gompf, D. A. Neumann, and H. Mutka. Vibrational densities of states and network rigidity in chalcogenide glasses. *Phys. Rev. B*, 44:94–100, Jul 1991.